BULLETIN OF THE
MINERAL RESEARCH AND EXPLORATION

CONTENTS

Research Articles

Bulletin of the Mineral Research and Exploration

BULLETIN OF THE
MINERAL RESEARCH AND EXPLORATION

CONTENTS

Magnetic anisotropy of a sub-ophiolitic metamorphic sole (Mersin ophiolite, Türkiye)

Buğra ÇAVDAR[a,b]*[iD], Antony MORRIS[b][iD], Mark ANDERSON[b][iD], Luca MENEGON[c][iD] and Osman PARLAK[d][iD]

[a]General Directorate of Mineral Research and Exploration, Mineral Research and Exploration Department, 06530, Ankara, Türkiye
[b]University of Plymouth, School of Geography, Earth and Environmental Sciences, Drake Circus, PL4 8AA, Plymouth, United Kingdom
[c]University of Oslo, Department of Geosciences, The Njord Centre, 1048, Blindern, Norway
[d]Çukurova University, Faculty of Engineering, Department of Geological Engineering, 01380, Adana, Türkiye

Research Article

ABSTRACT

The Mersin ophiolite of southern Turkey is a well-exposed, Late Cretaceous, Neo-Tethyan supra-subduction zone ophiolite. It is underlain by metamorphic sole rocks inferred to have formed at the top of a down-going plate during subduction. These have a well-developed foliation and lineation observable in the field (defined by the preferred orientations of hornblende and plagioclase crystals). Here we present the first magnetic fabric data reported from the Mersin ophiolite with such settings. Anisotropy of low field magnetic susceptibility ellipsoids in sampled amphibolites have clustered, NW-plunging minimum principal axes representing poles to a SE-dipping magnetic foliation that aligns with the macroscopic metamorphic foliation plane seen in the field. Maximum AMS principal axes define a SE-plunging magnetic lineation that is parallel to the macroscopic metamorphic lineation. Oblate magnetic fabrics at specimen-level and an overall triaxial fabric at locality-level in these rocks are consistent with the development of the dominant metamorphic fabric by a combination of pure shear flattening and simple shearing during the formation and exhumation of the Mersin sole rocks. These observations are compatible with a recent tectonic model for the evolution of the ophiolite based on paleomagnetic data that invokes flattening and exhumation of the down-going slab in an incipient subduction zone during supra-subduction zone spreading.

1. Introduction

Magnetic fabric analysis has proved to be a valuable tool in understanding the structural evolution of rocks in a wide variety of geological settings (Tarling and Hrouda, 1993; Martín Hernández et al., 2004; Parés, 2015). Anisotropy of magnetic susceptibility (AMS) reflects the shape- or crystallographic-preferred orientations of minerals and grains in rock (Tarling and Hrouda, 1993; Borradaile and Jackson, 2004), or the distribution anisotropy of ferromagnetic grains (Stephenson, 1994), providing quantitative constraints on petrofabric development even in weakly deformed

rocks. Described by a second-order tensor, AMS is represented by a susceptibility ellipsoid specified by the magnitude and orientation of its principal axes (k_{max}, k_{int} and k_{min}, corresponding to its maximum, intermediate, and minimum susceptibility axes, respectively). AMS in a rock results from contributions from all its constituent minerals but is usually dominated by the signal from ferromagnetic phases when present because of their high susceptibilities.

Much attention has been given to using AMS to understand the development of fabrics in sedimentary and igneous rocks, and such studies have therefore

dominated the literature on magnetic fabrics. For example, k_{max} axes are a reliable proxy for extension directions in weakly deformed sedimentary rocks that lack macroscopic strain markers (Borradaile and Hamilton, 2004; Mattei et al., 2004) and for magmatic flow directions in volcanic (Morris, 2000; Cañón Tapia, 2004) and plutonic rocks (Bouchez, 1997; Staudigel et al., 1999; Morris et al., 2019). In contrast, AMS has been relatively underutilised as a tool in the analysis of metamorphic rocks, although several studies have successfully used magnetic fabric analysis to provide new insights into the kinematics of fabric development in higher-grade rocks such as mylonites (Bascou et al., 2002) and migmatites (Ferré et al., 2003, 2004; Kruckenberg et al., 2010).

Here we present the first AMS data reported from the metamorphic sole of an ophiolite as part of a wider magnetic project on the tectonic history of the Mersin ophiolite of southern Türkiye (Omer, 2014; Morris et al., 2017). These amphibolite-grade rocks have well-defined macroscopic fabrics (Parlak et al., 1996) that developed during their evolution as they have subducted beneath a Neotethyan supra-subduction zone seafloor spreading system and later

exhumed and accreted to the base of the overlying Mersin ophiolite (Parlak et al., 1995). We show that AMS in these rocks provides an accurate proxy for the orientation of the macroscopic foliation and lineation observed in the field and indicates an important flattening component. These new magnetic fabric constraints on fabric development are consistent with a recent tectonic model for the evolution of the Mersin ophiolite (Morris et al., 2017), based on net tectonic rotation analysis of paleomagnetic data that predicts shearing and flattening of the sole rocks in an incipient subduction zone system.

2. The Mersin Ophiolite and its Metamorphic Sole

The Mersin ophiolite outcrops over a 1500 km² area in southern Türkiye (Figure 1a) and consists of a Late Cretaceous ophiolite underlain by metamorphic sole rocks that overlie the Mersin Mélange (Figure 1b; Parlak and Delaloye, 1996, 1999; Parlak and Robertson, 2004; Parlak et al., 2013). The ophiolitic suite consists mainly of the mantle and lower crustal sequences, including tectonised harzburgites and ultramafic and mafic cumulate gabbros (Parlak et al., 1996). Thin, fine-grained basaltic dykes occasionally
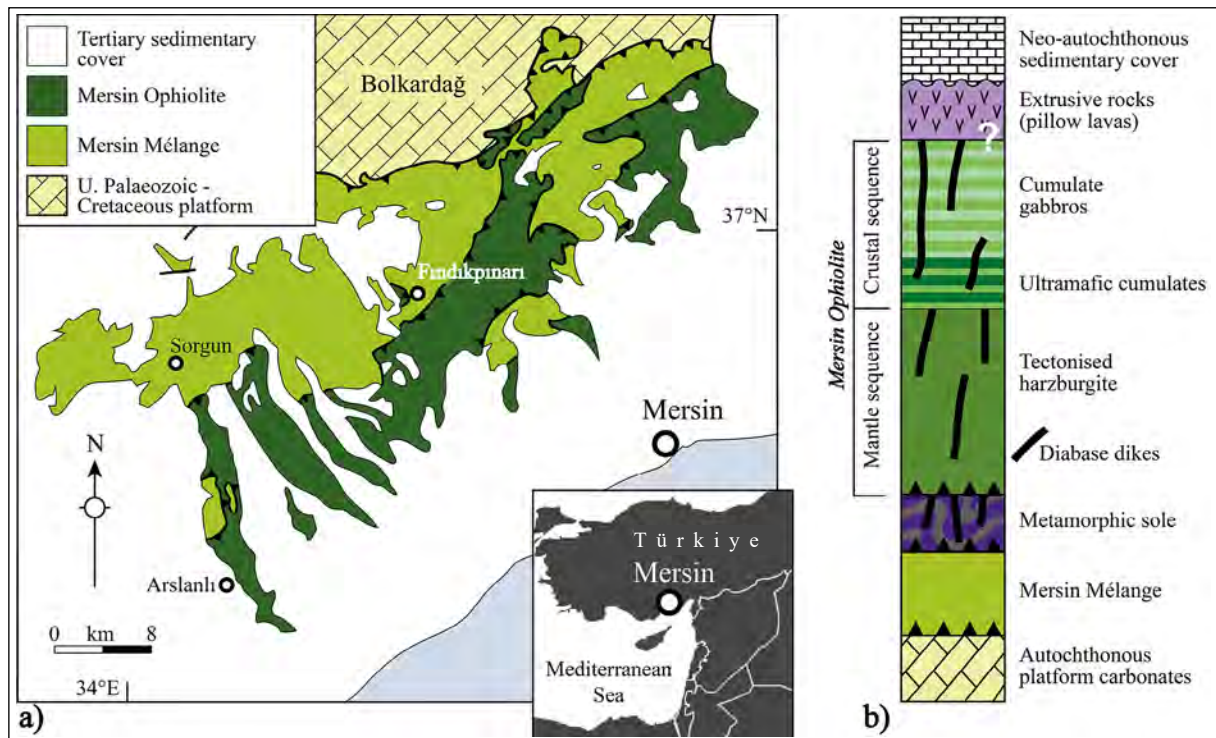
Figure 1- Summary of the geology of the Mersin ophiolite of southern Türkiye and location of the study near the village of Fındıkpınarı; a) the simplified geological map is after Tekin et al. (2016), b) the tectonostratigraphic column is after Parlak et al. (1996).

intrude the gabbros at a high angle to the cumulate layering. Basalts and associated deep marine sediments are structurally isolated from the main ophiolitic body (Parlak et al., 1996).

Key sections through the metamorphic sole and mantle sequence are exposed in the Fındıkpınarı valley area (Figure 1a). Here, the sole has sharp tectonic contact with the overlying mantle sequence (Figure 2a). It consists predominantly of amphibolites, amphibolitic schists, epidote-amphibolite schists, quartz-mica schists, calcschists, and marble. Over a thickness of about 50-70 m from top to base, it displays a typical inverted metamorphic zonation from upper amphibolite (top) to greenschist facies (base) (Parlak et al., 1996). The upper part of the Fındıkpınarı section is dominated by amphibolites, with phyllitic rocks and foliated metabasalts (accompanied by subordinate lenses of amphibolite) becoming more frequent towards the base. Intense deformation fabrics within the metamorphic sole are inferred to have formed along with the upper interface of a subducting slab. A pervasive SE-dipping metamorphic foliation (mean dip direction/dip = 146°/45°; Figure 2b) is associated with a mostly NW-SE-trending lineation (mean azimuth/plunge= 133°/46°) within the foliation plane, defined principally by alignment of elongate amphibole crystals.

The metamorphic sole and tectonised harzburgite are both occasionally cut by undeformed doleritic dykes that compositionally resemble evolved island-arc tholeiites derived from a mantle wedge that underwent previous melt extraction and subsequent metasomatism (Dilek et al., 1999). Dykes intruding the metamorphic sole clearly post-date shearing and metamorphism. ^{40}Ar–^{39}Ar age constraints (Dilek et al., 1999; Parlak and Delaloye, 1996, 1999) indicate that cooling of the metamorphic sole through amphibolite facies conditions (mean age= 92.7 Ma), intrusion of dykes into the mantle sequence (91.0 Ma), and intrusion of dykes through the sole (mean age= 89.6 Ma) were broadly synchronous events. Paleomagnetic analysis of the metamorphic sole-hosted dykes, those in the mantle sequence, and the overlying lower crustal cumulate gabbros reveals that each unit underwent large clockwise net tectonic rotations around similar NE-trending, shallowly plunging inclined axes. However, dykes in the sole experienced only about 45° rotation compared to about 120-125° rotation of the overlying mantle-hosted dykes and cumulate gabbros (Morris et al., 2017). These data support a model involving rotation of the Mersin oceanic crust and related mantle rocks in the footwall of a Neotethyan oceanic detachment fault system (Morris et al., 2017), with a later phase of footwall rotation occurring around the same ridge-parallel axis after accretion of the metamorphic sole rocks to the base of the footwall.

3. Sampling and Methods

We sampled amphibolites and some mica schists of the metamorphic sole of the Mersin ophiolite at 11
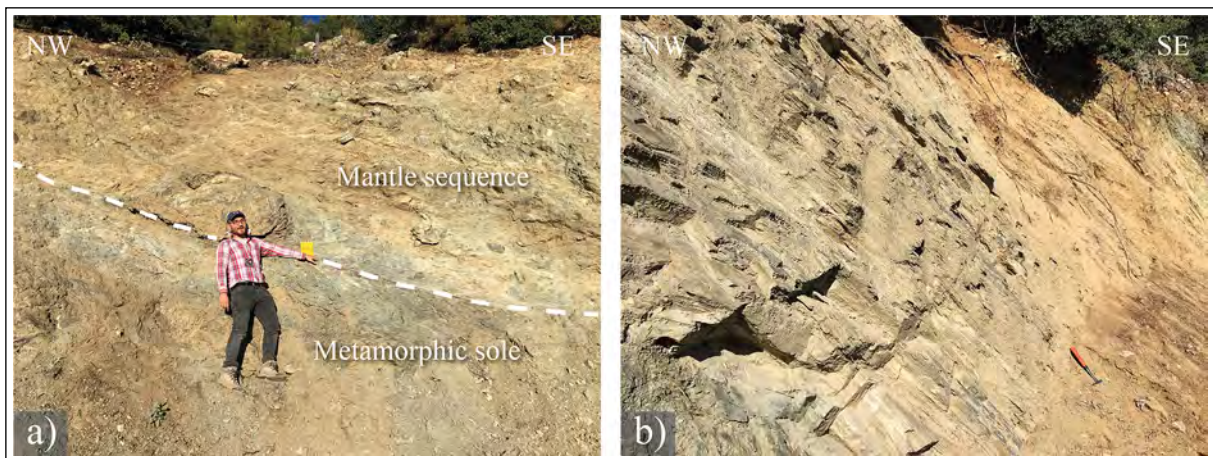
Figure 2- Field photographs of the metamorphic sole of the Mersin ophiolite exposed along the road-cut section near Fındıkpınarı; a) the tectonic contact between the metamorphic sole and the overlying mantle sequence of the ophiolite, b) amphibolites of the metamorphic sole showing the pronounced SE-dipping metamorphic foliation (hammer for scale).

sites distributed along a 650 m long road cut section near the village of Fındıkpınarı (Figure 1a, Table 1). At each site, oriented hand samples were collected and then drilled in the laboratory to obtain an average of eight standards (11 cm^3) cylindrical specimens per site for AMS analyses. Sampling was restricted to exposures that showed well-developed planar foliations. The orientations of foliations and lineations were measured to an accuracy of ± 5°.

Table 1- Site locations with the metamorphic sole rocks of the Mersin ophiolite.

Site	Lithology	UTM location
BC02	Amphibolite	36S 619297E, 4083374N
BC03	Amphibolite	36S 619238E, 4083392N
BC04	Amphibolite	36S 619251E, 4083390N
BC07	Amphibolite	36S 619330E, 4083355N
BC08	Amphibolite	36S 619097E, 4083484N
BC09	Amphibolite	36S 618959E, 4083576N
BC10	Amphibolite	36S 618915E, 4083598N
BC11	Micaschist/ Amphibolite	36S 618910E, 4083608N
BC12	Amphibolite	36S 618870E, 4083667N
BC13	Amphibolite	36S 618848E, 4083764N
BC14	Micaschist	36S 618836E, 4083777N

The anisotropy of low-field magnetic susceptibility of 96 specimens was measured using an AGICO-KLY-3S Kappabridge instrument. AMS tensors and associated eigenvectors and eigenvalues were calculated at specimen-level using AGICO SUSAR software. The shape of the AMS ellipsoid is defined by the relative magnitude of the principal susceptibility axes and can be: 1) isotropic ($k_{min} = k_{int} = k_{max}$) with no preferred alignment; 2) oblate ($k_{min} << k_{int} \approx k_{max}$) defining a planar magnetic fabric (foliation); 3) prolate ($k_{min} \approx k_{int} << k_{max}$) defining a linear magnetic fabric (lineation); or 4) triaxial ($k_{min} < k_{int} < k_{max}$). The magnitude of anisotropy is described using the corrected anisotropy degree, P_J (Jelínek, 1981), where $P_J = 1.0$ indicates an isotropic fabric and, e.g., $P_J = 1.05$ indicates 5% anisotropy. The shape parameter (T) describes the shape of the ellipsoid (-1.0<T<1.0), with positive/negative values of T indicating oblate/prolate fabrics, respectively (Jelínek, 1981). Statistical analysis of the data at the locality level was achieved

using the bootstrap method of Constable and Tauxe (1990).

Rock magnetic experiments were performed on representative powdered samples to investigate the nature of the ferromagnetic minerals contributing to the AMS. Curie temperatures were determined from the high-temperature (20-700°C) variation of magnetic susceptibility, measured using an AGICO KLY-3S Kappabridge coupled with an AGICO CS-3 high-temperature furnace apparatus. These data were analysed using AGICO Cureval8 software. Isothermal remanent magnetisation (IRM) acquisition experiments were conducted on representative samples using a Molspin pulse magnetiser to apply peak fields up to 800 mT with resulting IRMs measured using an AGICO JR6A fluxgate spinner magnetometer. Scanning electron microscopy and optical microscopy of oriented thin sections were used to further constrain the source of the AMS.

4. Findings

4.1. Rock Magnetic Properties

Bulk low field susceptibility values of the metamorphic sole rocks range between 0.38 x 10^{-3} SI and 7.85 x 10^{-3} SI (mean= 1.15 x 10^{-3} SI; Figure 3), suggesting that paramagnetic minerals dominate the AMS signal (Tarling and Hrouda, 1993) with a minor contribution from ferromagnetic minerals (Figure 3). This is confirmed by the temperature variations of low field magnetic susceptibility (Figure 4) that are dominated by a hyperbolic paramagnetic decay curve following the Curie-Weiss Law (Tarling and Hrouda, 1993), followed by a more rapid decrease in susceptibility at around 560-580°C, suggesting the presence of magnetite. Paramagnetic/ferromagnetic separation based on hyperbola fitting performed using AGICO Cureval8 software (green dashed lines in Figure 4) suggests that 90% of the susceptibility signal is due to paramagnetic minerals. Susceptibilities are systematically higher during the cooling cycle in these experiments and typically display an additional inflection at ~500°C that is not present during the heating cycle.

This suggests the production of new magnetite from a paramagnetic precursor mineral resulting from alteration during heating. IRM acquisition
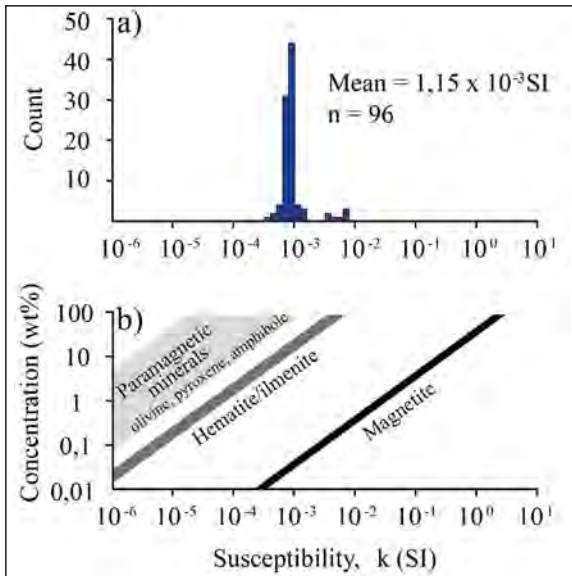
Figure 3- a) Histogram of low-field magnetic susceptibilities for amphibolites of the metamorphic sole of the Mersin ophiolite, b) relationship between bulk susceptibility and mineral concentrations (wt percent, Tarling and Hrouda, 1993). Note that low susceptibilities indicate less than 0.1 wt percent magnetite in most of these rocks and a major contribution from paramagnetic silicate minerals.

curves (Figure 4) reach saturation in most samples by applied fields of 300 mT, suggesting the presence of fine-grained, acicular magnetite. However, some samples (e.g. BC0303A and BC0401B in Figure

4) do not saturate in the maximum applied field of 800 mT suggesting the presence of high coercivity hematite. Maximum IRM intensities are typically less than 400 mAm^{-1}, consistent with the presence of only minor quantities of ferromagnetic minerals in these rocks. These values are also lower than those typically reported from mafic igneous rocks, e.g. within the overlying ophiolite, where IRM$_{800mT}$ values of ~50 Am^{-1} are observed (Omer, 2014; Morris et al., 2017), suggesting a reduction in the concentration of ferromagnetic phases during metamorphism of the original basaltic protoliths of the amphibolites (Parlak et al., 1996). This probably reflects the destruction of primary igneous magnetite during alteration, mobilising iron that became incorporated into newly formed amphibole crystals, as reported recently from the Thetford Mines ophiolite, Canada (Di Chiara et al., 2020). It is also noted that magnetite minerals can also be produced by the breakdown of pyrite at 370°C.

4.2. Magnetic Anisotropy Results

Specimen-level AMS data and derived parameters are provided in Table 2. Corrected anisotropy degrees (P$_J$) range from 1.01 to 1.13, with a mean value of 1.04 (indicating 4% anisotropy). There is a statistically significant positive correlation between P$_J$ and log$_{10}$ susceptibility (Figure 5a), excluding data from site
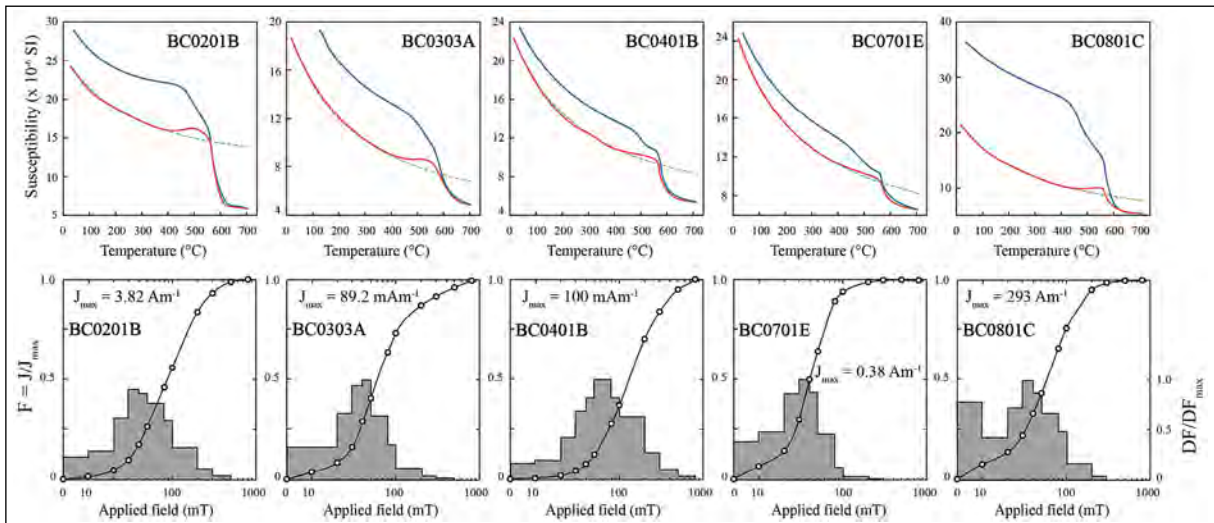
Figure 4- Representative plots showing the variation of low-field magnetic susceptibility with temperature (upper row) and isothermal remanent magnetisation acquisition curves (lower row) for metamorphic sole rocks of the Mersin ophiolite. Note that histograms in the lower row indicate the rate of change in acquired magnetization. The bar charts of BC0201B, BC0701E and BC0801C samples suggest that the saturation is reached around 300 mT of the applied field. However, BC0303A and BC0401B samples do not still saturate in the field of 800 mT, indicating the presence of high coercivity hematite.

Table 2- Anisotropy of magnetic susceptibility (AMS) results from the metamorphic sole rocks of the Mersin ophiolite.

Site	Specimen	Lithology	Mean susceptibility (SI)	Normalised k_{max}	Normalised k_{int}	Normalised k_{min}	Corrected anisotropy degree, Pj	Shape parameter, T	AMS principal axes (geographic coordinates)		
									k_{max}	k_{int}	k_{min}
BC02	BC0201A1	Amphibolite	9.40E-04	1.0314	0.935	1.121	1.0336	0.956	259/22	099/67	352/07
BC02	BC0201A2	Amphibolite	7.81E-04	1.0298	0.9366	1.118	1.0336	0.926	081/18	235/70	349/08
BC02	BC0201B1	Amphibolite	1.03E-03	1.0279	0.9403	1.111	1.0318	0.919	265/15	078/75	174/02
BC02	BC0201B2	Amphibolite	6.87E-04	1.0278	0.9396	1.112	1.0326	0.902	264/12	086/78	354/01
BC02	BC0202A	Amphibolite	1.55E-03	1.0186	0.8981	1.211	1.0832	0.344	233/15	108/65	329/20
BC02	BC0202B	Amphibolite	1.38E-03	1.021	0.9106	1.179	1.0684	0.432	099/53	242/31	343/18
BC02	BC0203A	Amphibolite	9.11E-04	1.008	0.9665	1.063	1.0255	0.417	162/49	071/01	341/41
BC02	BC0203B1	Amphibolite	9.00E-04	1.0086	0.9647	1.066	1.0268	0.427	208/24	070/59	307/18
BC02	BC0203B2	Amphibolite	9.26E-04	1.008	0.9653	1.065	1.0267	0.405	209/22	071/61	306/17
BC02	BC0203C1	Amphibolite	7.64E-04	1.0097	0.9644	1.066	1.0259	0.486	167/47	071/05	337/42
BC02	BC0203C2	Amphibolite	9.06E-04	1.0066	0.9686	1.059	1.0248	0.366	169/49	074/04	340/41
BC02	BC0204A	Amphibolite	8.48E-04	1.0332	0.9258	1.14	1.0409	0.873	043/05	137/42	308/47
BC02	BC0204B	Amphibolite	8.85E-04	1.0414	0.9117	1.17	1.0468	0.925	213/05	118/44	308/45
BC02	BC0204C	Amphibolite	8.65E-04	1.0412	0.9145	1.164	1.0443	0.955	048/12	150/43	306/44
BC03	BC0301A	Amphibolite	7.48E-04	1.0083	0.9763	1.043	1.0154	0.64	116/49	225/16	327/37
BC03	BC0301C	Amphibolite	7.32E-04	1.0074	0.9767	1.042	1.0159	0.573	116/46	225/17	330/39
BC03	BC0301D	Amphibolite	6.93E-04	1.008	0.9765	1.042	1.0155	0.621	125/46	230/13	331/40
BC03	BC0301E	Amphibolite	7.63E-04	1.0055	0.9823	1.032	1.0121	0.562	119/47	225/14	327/40
BC03	BC0301F	Amphibolite	7.64E-04	1.004	0.9815	1.034	1.0145	0.374	117/44	223/16	327/42
BC03	BC0301G	Amphibolite	3.82E-04	1.0077	0.9743	1.047	1.018	0.536	121/43	225/15	329/44
BC03	BC0301H	Amphibolite	7.64E-04	1.0029	0.9848	1.028	1.0123	0.323	117/45	228/19	334/38
BC03	BC0301I	Amphibolite	6.78E-04	1.0077	0.9778	1.04	1.0146	0.631	121/47	223/11	323/41
BC03	BC0301J	Amphibolite	7.49E-04	1.0026	0.9843	1.03	1.0132	0.273	094/36	206/27	323/42
BC03	BC0301K	Amphibolite	4.29E-04	1.011	0.9697	1.055	1.0192	0.676	130/53	231/08	327/36
BC03	BC0301L	Amphibolite	7.17E-04	1.0078	0.9762	1.043	1.016	0.596	141/53	234/03	326/37
BC03	BC0301M	Amphibolite	7.31E-04	1.0058	0.9792	1.038	1.0151	0.488	130/53	235/11	333/35
BC03	BC0302A	Amphibolite	7.45E-04	1.0066	0.9807	1.035	1.0127	0.627	122/56	226/10	322/33
BC03	BC0302B	Amphibolite	7.62E-04	1.0086	0.9768	1.042	1.0145	0.691	124/54	227/09	324/35
BC03	BC0302C	Amphibolite	8.29E-04	1.0123	0.9691	1.056	1.0186	0.748	121/54	223/09	320/35
BC03	BC0302D	Amphibolite	7.67E-04	1.0088	0.9761	1.043	1.0151	0.684	121/54	226/11	323/34
BC04	BC0401A1	Amphibolite	7.98E-04	1.0089	0.9718	1.052	1.0193	0.571	139/45	236/07	333/44
BC04	BC0401A2	Amphibolite	8.23E-04	1.0095	0.9692	1.057	1.0213	0.557	145/45	242/07	339/44
BC04	BC0401B1	Amphibolite	8.35E-04	1.0099	0.968	1.059	1.022	0.561	136/46	237/10	336/42
BC04	BC0401B2	Amphibolite	7.96E-04	1.0071	0.9764	1.043	1.0165	0.542	144/50	236/02	327/40
BC04	BC0401C1	Amphibolite	7.92E-04	1.0124	0.9652	1.064	1.0224	0.658	144/43	236/02	328/47
BC04	BC0401C2	Amphibolite	7.98E-04	1.0096	0.9678	1.059	1.0226	0.536	157/45	063/05	328/44
BC04	BC0401D1	Amphibolite	7.78E-04	1.009	0.9693	1.057	1.0217	0.527	149/48	240/01	331/42

Table 2- continued

BC04	BC0401D2	Amphibolite	7.47E-04	1.011	0.9696	1.055	1.0194	0.672	163/50	062/09	324/39
BC04	BC0401E1	Amphibolite	8.17E-04	1.0094	0.9715	1.052	1.0191	0.598	153/50	061/01	330/40
BC04	BC0401E2	Amphibolite	8.42E-04	1.012	0.9642	1.066	1.0238	0.611	145/48	237/02	329/42
BC04	BC0401E3	Amphibolite	6.39E-04	1.0128	0.96	1.074	1.0272	0.583	138/47	237/08	334/42
BC04	BC0401F1	Amphibolite	8.11E-04	1.0131	0.9623	1.069	1.0246	0.641	138/46	235/06	331/43
BC04	BC0401F2	Amphibolite	8.48E-04	1.0064	0.9755	1.045	1.018	0.463	150/47	243/03	336/43
BC04	BC0401F3	Amphibolite	6.08E-04	1.0136	0.9589	1.076	1.0275	0.606	133/45	233/10	333/43
BC04	BC0401G1	Amphibolite	8.66E-04	1.0095	0.9685	1.058	1.022	0.541	151/45	243/01	334/45
BC04	BC0401G2	Amphibolite	7.98E-04	1.0119	0.9672	1.06	1.0209	0.671	155/47	062/03	329/43
BC04	BC0401G3	Amphibolite	5.36E-04	1.0108	0.9645	1.066	1.0247	0.548	139/45	235/06	331/44
BC07	BC0701B1	Amphibolite	9.31E-04	1.0297	0.9323	1.127	1.038	0.85	212/48	108/12	008/40
BC07	BC0701B2	Amphibolite	7.55E-04	1.0211	0.9518	1.088	1.0271	0.846	211/48	111/10	012/40
BC07	BC0701B3	Amphibolite	8.22E-04	1.0341	0.9244	1.143	1.0414	0.882	185/54	278/03	010/36
BC07	BC0701C1	Amphibolite	8.62E-04	1.0265	0.9417	1.108	1.0317	0.889	201/52	101/07	006/37
BC07	BC0701C2	Amphibolite	9.40E-04	1.0313	0.9256	1.141	1.0431	0.809	153/61	276/17	013/23
BC07	BC0701C3	Amphibolite	8.19E-04	1.0288	0.9316	1.129	1.0396	0.811	164/43	264/11	005/45
BC07	BC0701D1	Amphibolite	8.81E-04	1.0339	0.9236	1.145	1.0425	0.864	154/62	268/12	003/25
BC07	BC0701D2	Amphibolite	8.67E-04	1.0275	0.9375	1.117	1.035	0.854	139/32	252/31	015/42
BC07	BC0701D3	Amphibolite	8.14E-04	1.0285	0.9366	1.118	1.0348	0.877	164/49	270/14	011/38
BC07	BC0701E1	Amphibolite	7.96E-04	1.0364	0.9161	1.161	1.0476	0.84	160/51	270/15	011/35
BC07	BC0701E2	Amphibolite	8.75E-04	1.0294	0.9377	1.116	1.0329	0.929	184/52	277/03	009/38
BC07	BC0701E3	Amphibolite	8.81E-04	1.0358	0.9203	1.152	1.0439	0.877	175/62	270/03	002/27
BC08	BC0801A1	Amphibolite	7.68E-04	1.016	0.9569	1.079	1.027	0.696	096/47	191/05	286/43
BC08	BC0801A2	Amphibolite	8.27E-04	1.0182	0.9502	1.092	1.0315	0.683	112/44	017/05	282/46
BC08	BC0801B	Amphibolite	7.47E-04	1.016	0.9582	1.077	1.0258	0.716	086/42	187/12	289/46
BC08	BC0801C1	Amphibolite	7.57E-04	1.0173	0.9568	1.079	1.026	0.756	098/44	193/05	289/46
BC08	BC0801C2	Amphibolite	5.63E-04	1.0151	0.959	1.075	1.0258	0.688	099/45	192/03	286/45
BC09	BC0901A	Amphibolite	6.40E-04	1.009	0.968	1.059	1.023	0.5	115/45	206/02	298/45
BC09	BC0901B	Amphibolite	5.35E-04	1.0069	0.9723	1.051	1.0207	0.44	132/46	038/04	304/44
BC09	BC0901C	Amphibolite	6.64E-04	1.0082	0.9693	1.057	1.0226	0.471	112/40	213/13	317/47
BC09	BC0902A1	Amphibolite	4.75E-03	1.013	0.8751	1.273	1.1118	0.222	100/48	203/12	303/40
BC09	BC0902A2	Amphibolite	3.14E-03	1.0123	0.8636	1.304	1.1241	0.205	108/46	211/12	312/41
BC09	BC0902B	Amphibolite	1.28E-03	1.0067	0.9731	1.05	1.0202	0.438	083/34	194/27	313/43
BC09	BC0902C	Amphibolite	3.33E-03	1.0438	0.8269	1.383	1.1294	0.495	115/42	222/18	329/43
BC10	BC1001A	Amphibolite	1.11E-03	1.0346	0.8978	1.203	1.0676	0.638	176/28	074/21	313/54
BC10	BC1001B	Amphibolite	9.35E-04	1.0268	0.9163	1.163	1.057	0.595	100/39	206/19	316/45
BC10	BC1002A	Amphibolite	7.59E-04	1.0301	0.9352	1.121	1.0346	0.914	045/23	299/33	162/48
BC10	BC1002B	Amphibolite	7.69E-04	1.0295	0.935	1.122	1.0356	0.885	027/36	282/19	170/48
BC10	BC1002C	Amphibolite	8.44E-04	1.0251	0.9466	1.098	1.0283	0.924	003/41	264/10	164/48

Table 2- continued

BC10	BC1002D	Amphibolite	7.21E-04	1.0275	0.9388	1.114	1.0337	0.874	027/36	282/20	168/47
BC10	BC1002E	Amphibolite	7.81E-04	1.029	0.9374	1.117	1.0337	0.907	027/35	283/19	170/49
BC10	BC1002F	Amphibolite	9.40E-04	1.0221	0.9501	1.092	1.0277	0.861	005/43	265/11	163/45
BC10	BC1002G	Amphibolite	1.13E-03	1.0236	0.9486	1.095	1.0278	0.896	007/43	266/11	164/45
BC11	BC1101A1	Micaschist/ Amphibolite	6.96E-04	1.0274	0.9383	1.115	1.0343	0.864	040/30	289/32	163/43
BC11	BC1101A2	Micaschist/ Amphibolite	9.78E-04	1.0441	0.8866	1.226	1.0693	0.746	025/39	274/24	161/42
BC11	BC1101B	Micaschist/ Amphibolite	1.06E-03	1.0506	0.8795	1.242	1.0699	0.814	026/41	275/23	164/41
BC11	BC1101E	Micaschist/ Amphibolite	8.26E-04	1.0483	0.8761	1.25	1.0756	0.749	026/37	274/26	158/42
BC12	BC1201A	Amphibolite	6.15E-03	1.0141	0.905	1.197	1.0809	0.282	110/51	212/09	310/37
BC12	BC1201B	Amphibolite	6.31E-03	1.0154	0.9109	1.182	1.0736	0.322	109/42	212/13	315/45
BC12	BC1201C	Amphibolite	6.69E-03	1.0166	0.9045	1.196	1.0789	0.326	115/47	216/10	315/41
BC12	BC1201D	Amphibolite	7.85E-03	1.0204	0.8974	1.211	1.0822	0.371	109/50	212/11	311/37
BC13	BC1301A	Amphibolite	7.88E-04	1.0249	0.9415	1.109	1.0336	0.819	119/18	217/23	355/61
BC13	BC1301B	Amphibolite	8.48E-04	1.0247	0.942	1.108	1.0333	0.818	113/15	210/27	357/59
BC13	BC1301C	Amphibolite	8.55E-04	1.0283	0.9338	1.124	1.0379	0.823	111/15	210/31	359/55
BC14	BC1401A	Micaschist	7.63E-04	1.0271	0.9329	1.126	1.04	0.772	127/03	219/31	032/59
BC14	BC1401B	Micaschist	4.15E-04	1.0186	0.9485	1.096	1.0328	0.675	293/12	196/32	041/55
BC14	BC1402A	Micaschist	8.80E-04	1.0278	0.9359	1.12	1.0363	0.839	253/12	158/22	009/64
BC14	BC1402B	Micaschist	8.97E-04	1.0283	0.9359	1.12	1.0358	0.857	255/05	164/18	360/72
BC14	BC1402C	Micaschist	7.92E-04	1.018	0.9419	1.11	1.0401	0.567	269/06	177/23	012/66
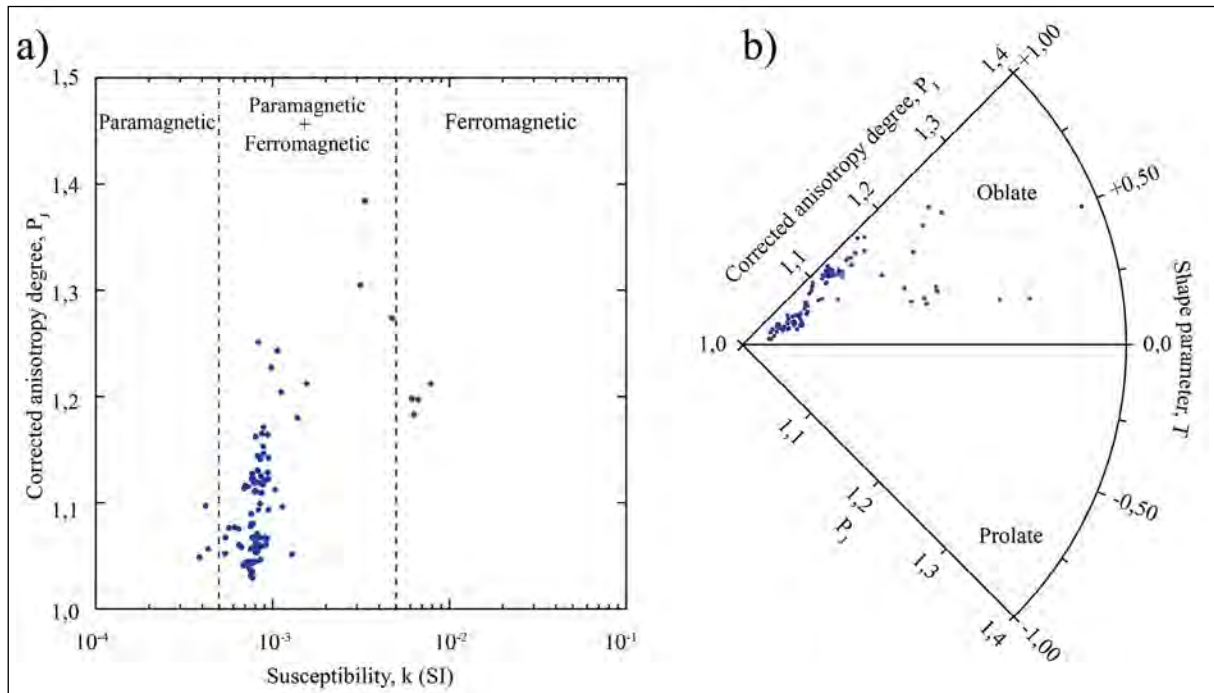
Figure 5- a) Plot of corrected anisotropy degree, P_J, against bulk susceptibility, b) Borradaile-Jackson polar plot of corrected anisotropy degree, P_J, and shape parameter, T (Jelínek, 1981; Borradaile and Jackson, 2004).

BC12. The Pearson product-moment correlation coefficient of 0.702 for this relationship exceeds the critical value of 0.2644 at the 99% confidence level (for n= 92 specimens). This relationship demonstrates that anisotropy in these rocks is controlled by the proportion of ferromagnetic versus paramagnetic contributions to the bulk susceptibility (Rochette et al., 1992), which can be implicated by variations in the relative contributions from ferromagnetic magnetite and paramagnetic amphibole in this case. Specimens from site BC12 fall outside this trend and display the largest susceptibilities encountered in this study ($\sim 7 \times 10^{-3}$ SI), suggesting a dominant contribution from magnetite (Figure 5a) with an estimated maximum concentration of ~0.2 wt % based on bulk susceptibilities (Thompson and Oldfield, 1986).

Specimen-level data indicate the dominance of oblate fabrics, with all specimens displaying positive shape parameters (T) ranging from 0.21 to 0.96 (mean = 0.66), with no correlation between ellipsoid shape and P_J (Figure 5b). At the locality level, k_{max} axes plunge moderately to the SE (Figure 6a). They are parallel to the orientation of the macroscopic mineral lineation observed in the amphibolites in the field (Figure 6b), suggesting that the magnetic lineation represented by the k_{max} axes acts as an accurate proxy for the average orientation of elongate mineral phases in these rocks. This is confirmed by examination of oriented thin sections cut in the k_{max}/k_{min} plane that

demonstrate that k_{max} axes are aligned parallel with the average orientation of the long-axes of amphibole crystals (Figure 7). k_{min} axes, representing the pole to the magnetic foliation, plunge moderately to the NW (Figure 6a) and are oriented parallel to the poles to the macroscopic metamorphic foliation (Figure 6b). The shape of the AMS at locality level may be determined using the bootstrap resampling method of Constable and Tauxe (1990). Bootstrapped eigenvectors derived from pseudo-sampling of the data are shown in Figure 8a and are tightly clustered with well-defined Kent (1982) error ellipses (Figure 8b). Cumulative distributions of the bootstrapped eigenvalues (Figure 8c) are distinct with no overlap of the bounds containing 95% of each eigenvalue, demonstrating an overall triaxial fabric within the metamorphic sole of the ophiolite (Tauxe et al., 2010).

5. Results

Thin section observations of amphibolites from the metamorphic sole of the Mersin ophiolite demonstrate an alignment of the long-axes of amphibole crystals with k_{max} axes of the AMS fabric. This relationship implies that the AMS lineation results from the development of a preferred alignment of amphibole (hornblende) crystal c-axes in these rocks. As such, both fabrics most likely track the finite strain in these rocks that developed at or close to their metamorphic peak. Recent experimental evidence on amphiboles
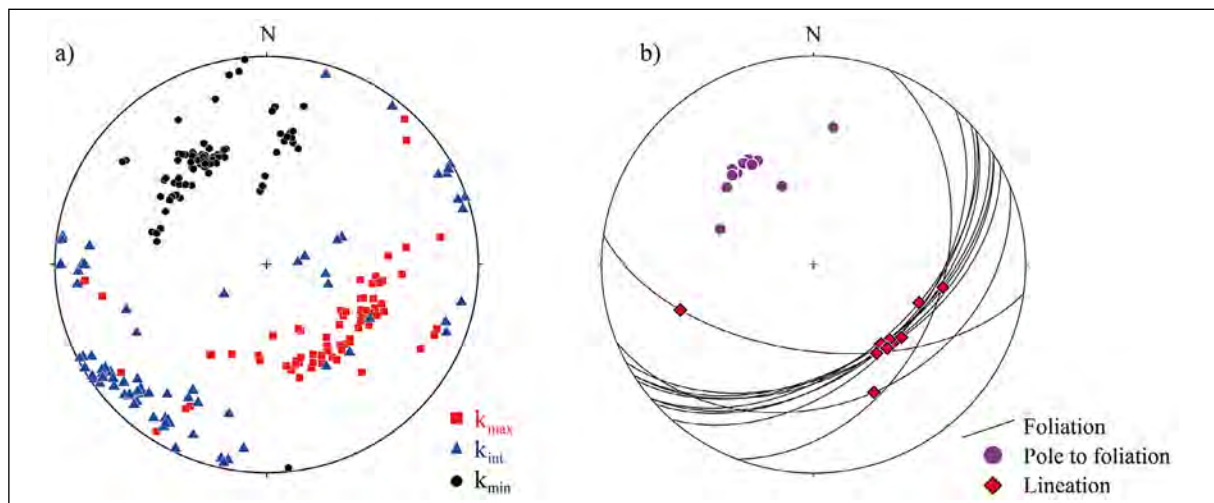
Figure 6- a) Stereographic equal area projections showing the distribution of AMS principal axes for all specimens analysed from the metamorphic sole of the Mersin ophiolite, b) stereographic equal area projections showing the orientation of the macroscopic metamorphic foliation and lineation measured in the field.
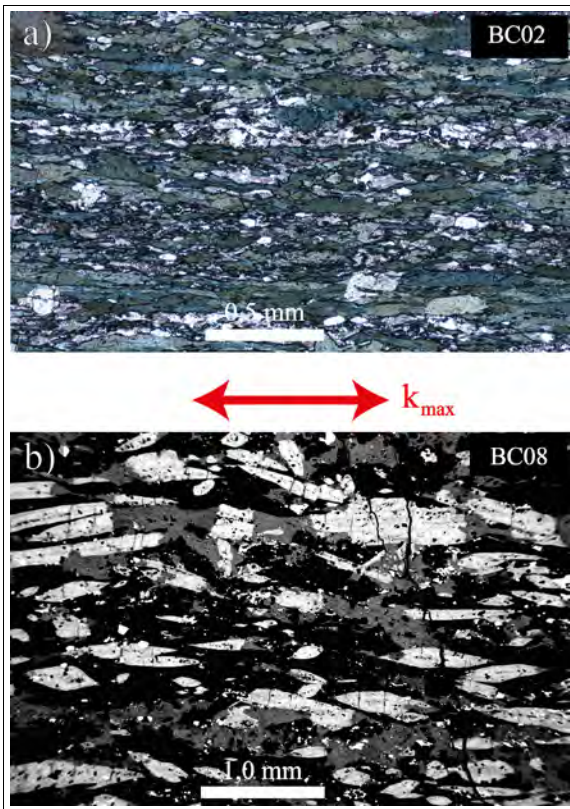
Figure 7- Photomicrograph and back-scattered electron (BSE) images of amphibolite from the metamorphic sole of the Mersin ophiolite. Thin sections are cut in the k_{max}/k_{min} plane with k_{max} parallel to the long dimension as shown; a) Thin section (plane polarised light) showing metamorphic foliation defined by the preferred alignment of blue-green amphibole, plagioclase and epidote, b) BSE image showing detail of amphibole (light shade), plagioclase (dark shade), and epidote/chlorite (intermediate shade) crystals. Note the micro-cracking (micro-boudinage) of amphibole perpendicular to the foliation (crack opening apparently parallel to k_{max}).

has demonstrated that k_{max} axes in single amphibole crystals lie parallel to amphibole crystallographic b-axes, rather than their c-axes (Biedermann et al., 2015), but that preferential alignment of crystal c-axes results in bulk AMS fabrics with k_{max} axes parallel to the mineral lineation in amphibole-rich rocks (Biedermann et al., 2018). Our results suggest that there is also a contribution to the AMS fabric from minor amounts of magnetite present in the specimens. In contrast to amphibole crystals, AMS in single crystals of magnetite results from shape rather than crystallographic anisotropy (Tarling and Hrouda, 1993), with k_{max} axes normally parallel to the long-axes of magnetite crystals. An exception to
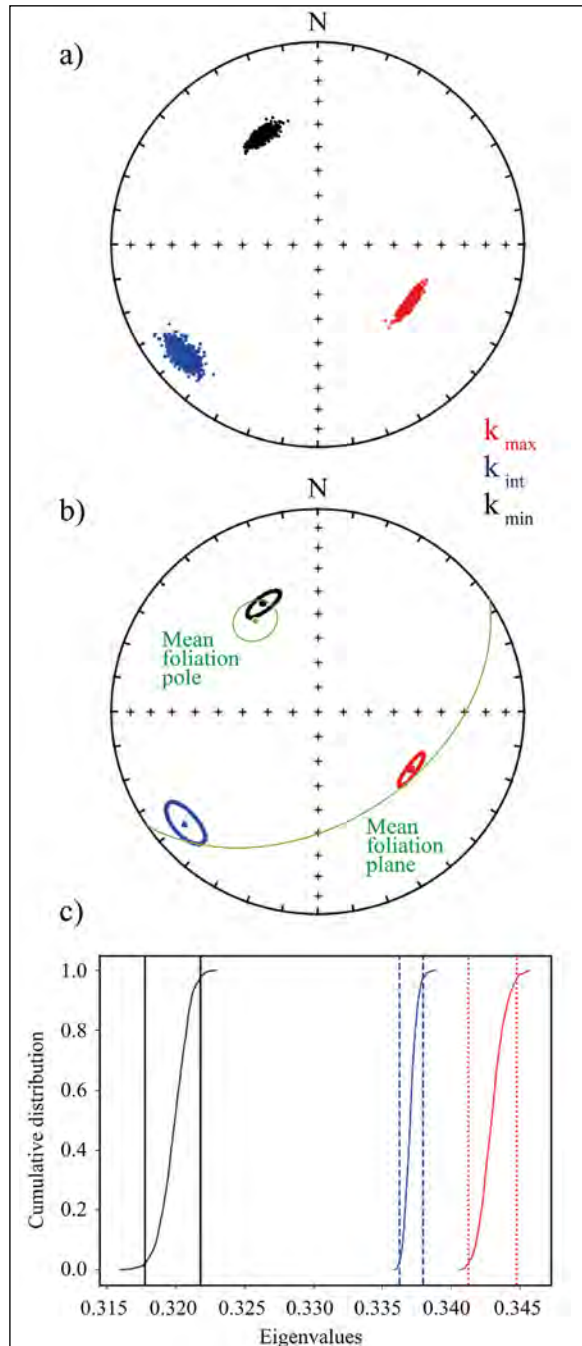
Figure 8- Bootstrap analysis of the shape of the AMS fabric in the metamorphic sole of the Mersin ophiolite, using the technique of Constable and Tauxe (1990); a) Stereographic equal-area projection of bootstrapped eigenvectors at the locality-level (geographic coordinates), b) Kent (1982) error ellipses for each distribution of eigenvectors demonstrating near-perfect alignment with the orientation of the macroscopic metamorphic fabric observed in the field, c) Cumulative distributions of the bootstrapped eigenvalues associated with the eigenvalues plotted in Figure 8a. Solid, dashed, and dotted vertical lines represent bounds containing 95% of each eigenvalue (Tauxe et al., 2010). The lack of overlap of these bounds demonstrated the presence of a triaxial fabric within these rocks.

this is single domain (<1μm) magnetite crystals which have k_{max} axes parallel to their short-axis (Potter and Stephenson, 1988), leading to the development of inverse AMS fabrics. The consistency of AMS fabrics across specimens with different susceptibilities and agreement with the orientation of the metamorphic lineation seen in the field and in thin sections suggests that: i) the preferred orientation of any magnetite crystal present in the Mersin metamorphic sole rocks is coaxial with the preferred orientation of amphibole crystals; and ii) that inverse fabrics associated with single-domain magnetite are absent. Magnetite was not observed as a discrete phase during the petrographic analysis of the amphibolites, and so the inferred alignment of paramagnetic and ferromagnetic contributions to the AMS signal may reflect the presence of magnetite as an exsolution product within amphibole crystals, with their shape-preferred orientations or distribution anisotropy (Stephenson, 1994) controlled crystallographically by the amphibole lattice.

The overall triaxial AMS fabric is seen in the metamorphic sole and dominance of oblate ellipsoids at specimen-level likely reflects finite strain with a strong flattening component (producing clustering of k_{min} axes), combined with the shearing producing preferred alignment of mineral long-axes, resulting in clustering of k_{max} axes. This is consistent with the formation of the metamorphic fabric along with the upper interface of a down-going subducting plate and subsequent exhumation and accretion to the base of the Mersin ophiolite. A new tectonic model for this process, based on tectonic analysis of paleomagnetic data from the cumulate gabbros of the ophiolitic suite, mafic dykes cutting the metamorphic sole and dykes intruding the mantle sequence, was recently proposed by Morris et al. (2017) (Figure 9).

This incorporated key elements of a new mechanism for metamorphic sole formation and exhumation proposed by van Hinsbergen et al. (2015). The paleomagnetic analysis demonstrated that the
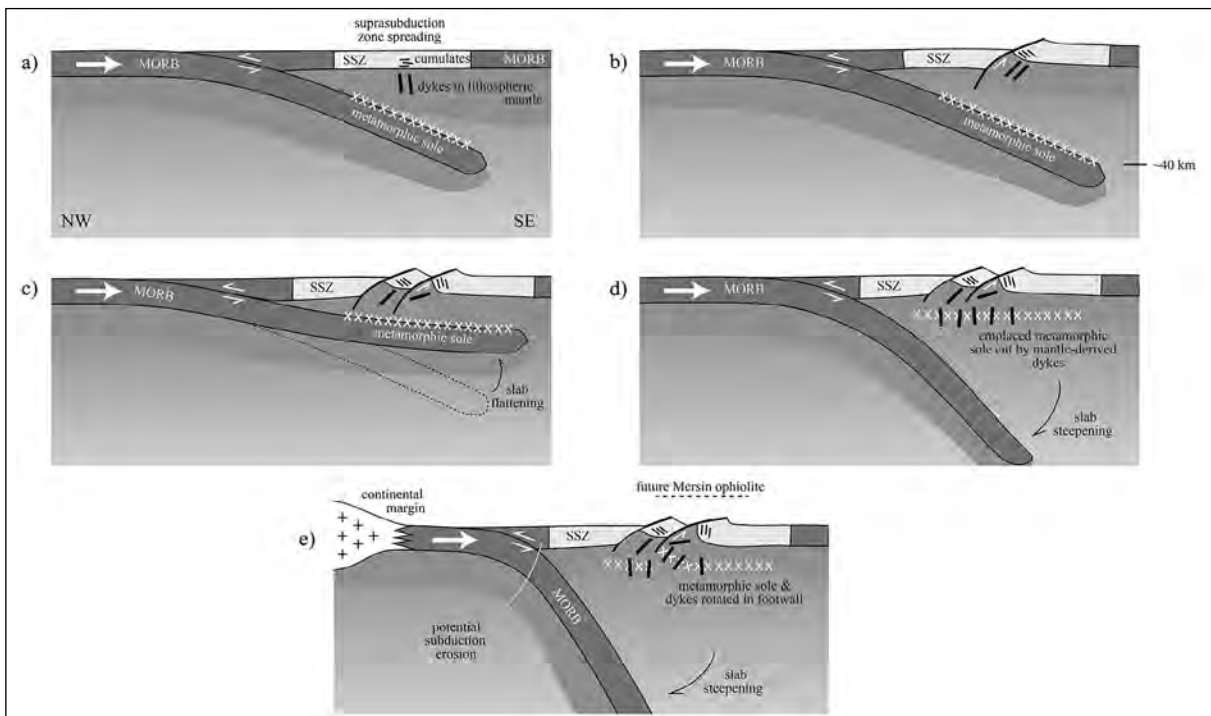
Figure 9- Conceptual model for the evolution of the Mersin ophiolite and its metamorphic sole in a fore-arc environment (modified after Morris et al., 2017); a) formation of the metamorphic sole during incipient subduction leads to the development of shear fabrics in the sole rocks, accompanied by suprasubduction zone spreading to form the Mersin ophiolite, b) tectonic rotation of the ophiolite in the footwall of an oceanic detachment fault during detachment-mode spreading, c) flattening of the down-going slab leads to the exhumation of the metamorphic sole rocks and the development of pure shear, oblate fabrics, d) accretion of the metamorphic sole to the base of the suprasubduction zone ophiolite and intrusion by mafic dykes, e) rotation of the metamorphic sole and associated dykes by capture in the footwall of an oceanic detachment fault.

Mersin ophiolite experienced major rotation around a shallowly-plunging, NE-SW-trending, ridge-parallel axis, inferred to result from rolling-hinge rotation during formation by detachment-mode seafloor spreading (Morris et al., 2017; Escartín and Canales, 2011). Dykes cutting the metamorphic sole also experienced rotation around the same ridge-parallel inclined axis but with a lower magnitude of net rotation (Morris et al., 2017). These constraints on tectonic rotation require exhumation of the metamorphic sole, accretion to the base of the overlying oceanic lithosphere before the intrusion of dykes into the sole, and subsequent capture of the sole rocks by the rotating footwall block of the oceanic detachment fault (Morris et al., 2017). This may be achieved by slab flattening in response to supra-subduction zone spreading, mantle wedge volume decrease, and upper plate extension (Figure 9; Morris et al., 2017; Van Hinsbergen et al., 2015), leading to shallowing and exhumation of the sole rocks and development of its inverted metamorphic gradient (Parlak et al., 1996). This tectonic model based on paleomagnetic tectonic rotation analysis can readily explain the magnetic anisotropy results presented here, with i) shearing along with the upper interface of the down-going slab during subduction initiation producing mineral elongation fabrics, and ii) subsequent development of strongly oblate fabrics by pure shear during flattening and exhumation of the slab and sole rocks before the accretion of the metamorphic sole to the base of the ophiolite. It is also consistent with recent interpretations of the geodynamic evolution of the metamorphic soles of other Turkish Neotethyan ophiolites (e.g. in the Beyşehir-Hoyran Nappes; Parlak et al., 2019), where exhumation is inferred to have occurred during roll-back shortly after subduction initiation.

Acknowledgements

References

Bascou, J., Raposo, M. I. B., Vauchez, A., Egydio-Silva, M. 2002. Titanohematite lattice-preferred orientation and magnetic anisotropy in high-temperature mylonites. Earth and Planetary Science Letters 198 (1-2), 77-92.

Biedermann, A. R., Koch, C. B., Pettke, T., Hirt, A. M. 2015. Magnetic anisotropy in natural amphibole crystals. American Mineralogist 100 (8-9), 1940-1951.

Biedermann, A. R., Kunze, K., Hirt, A. M. 2018. Interpreting magnetic fabrics in amphibole-bearing rocks. Tectonophysics 722, 566-576.

Borradaile, G. J., Hamilton, T. 2004. Magnetic fabrics may proxy as neotectonic stress trajectories, Polis rift, Cyprus. Tectonics 23 (1).

Borradaile, G. J., Jackson, M. 2004. Anisotropy of magnetic susceptibility (AMS): magnetic petrofabrics of deformed rocks. Geological Society of London, Special Publications 238 (1), 299-360.

Bouchez, J. L. 1997. Granite is never isotropic: an introduction to AMS studies of granitic rocks. Granite: From Segregation of Melt to Emplacement Fabrics, Springer, Dordrecht, 95-112.

Cañón Tapia, E. 2004. Anisotropy of magnetic susceptibility of lava flows and dykes: a historical account. Geological Society of London, Special Publications 238 (1), 205-225.

Constable, C., Tauxe, L. 1990. The bootstrap for magnetic susceptibility tensors. Journal of Geophysical Research 95, 8383- 8395.

Di Chiara, A., Morris, A., Anderson, M. W., Menegon. L., Tremblay, T. 2020. Magnetic anisotropy reveals Acadian transpressional fabrics in an Appalachian ophiolite (Thetford Mines, Canada). Geophysical Journal International 222 (2), 1034-1045.

Dilek, Y., Thy, P., Hacker, B., Grundvig, S. 1999. Structure and petrology of Tauride ophiolites and mafic dike intrusions (Turkey): implications for the Neotethyan ocean. Geological Society of America Bulletin 111 (8), 1192-1216.

Escartín, J., Canales, J. P. 2011. Detachments in oceanic lithosphere: deformation, magmatism, fluid flow, and ecosystems. Eos Transactions American Geophysical Union 92 (4).

Ferré, E., Martín-Hernández, F., Teyssier, C., Jackson, M. 2004. Paramagnetic and ferromagnetic anisotropy of magnetic susceptibility in migmatites: measurements in high and low fields and

kinematic implications. Geophysical Journal International 157 (3), 1119-1129.

Ferré, E. C., Teyssier, C., Jackson, M., Thill, J. W., Rainey, E. S. G. 2003. Magnetic susceptibility anisotropy: a new petrofabric tool in migmatites. Journal of Geophysical Research 108 (B2), 2086.

Jelínek, V. 1981. Characterization of the magnetic fabric of rocks. Tektonophysics 79 (3-4), 63-67.

Kent, J. T. 1982. The Fisher-Bingham distribution on the sphere. Journal of the Royal Statistical Society 44 (B), 71–80.

Kruckenberg, S. C., Ferré, E.C., Teyssier, C., Vanderhaeghe, O., Whitney, D. L., Seaton, N. C. A., Skord, J. A. 2010. Viscoplastic flow in migmatites deduced from fabric anisotropy: an example from the Naxos dome, Greece. Journal of Geophysical Research 115, B09401.

Martín Hernández, F., Lüneburg, C. M., Aubourg, C., Jackson, M. 2004. Magnetic fabric: methods and applications. Geological Society of London, Special Publications 238, 551.

Mattei, M., D'Agostino, N., Zananiri, I., Kondopoulou, D., Pavlides, S., Spatharas, V. 2004. Tectonic evolution of fault- bounded continental blocks: comparison of paleomagnetic and GPS data in the Corinth and Megara basins (Greece). Journal of Geophysical Research 109.

Morris, A. 2000. Magnetic fabric and palaeomagnetic analyses of the Plio-Quaternary calc-alkaline series of Aegina Island, South Aegean volcanic arc, Greece. Earth and Planetary Science Letters 176, 91-105.

Morris, A., Anderson, M. W., Omer, A., Maffione, M., Van Hinsbergen, D. J. J. 2017. Rapid fore-arc extension and detachment-mode spreading following subduction initiation. Earth and Planetary Science Letters 478, 76-88.

Morris, A., Meyer, M., Anderson, M. W., MacLeod, C. J. 2019. What do variable magnetic fabrics in gabbros of the Oman ophiolite reveal about lower crustal magmatism at fast-spreading ridges?. Geology 47, 275-278.

Omer, A. H. 2014. Integrated geophysical, geochemical, and structural analysis of the Mersin ophiolite, southern Turkey. PhD Thesis, University of Plymouth, Plymouth, United Kingdom (unpublished).

Parés, J. S. 2015. Sixty years of anisotropy of magnetic susceptibility in deformed sedimentary rocks. Frontiers in Earth Science 3, 1-13.

Parlak, O., Delaloye, M. 1996. Geochemistry and timing of post-metamorphic dyke emplacement in the Mersin Ophiolite (southern Turkey): New age constraints from $^{40}Ar/^{39}Ar$ geochronology. Terra Nova 8, 585-592.

Parlak, O., Delaloye, M. 1999. Precise 40Ar/39Ar ages from the metamorphic sole of the Mersin ophiolite (southern Turkey). Tectonophysics 301, 145-158.

Parlak, O., Robertson A. H. F. 2004. The ophiolite-related Mersin Melange, southern Turkey: its role in the tectonic– sedimentary setting of Tethys in the Eastern Mediterranean region. Geological Magazine 141, 257-286.

Parlak, O., Bozkurt, E., Delaloye, M. 1996. The obduction direction of the Mersin Ophiolite: structural evidence from subophiolitic metamorphics in the Central Tauride Belt, Southern Turkey. International Geology Review 38, 778- 786.

Parlak, O., Delaloye, M., Bingöl, E. 1995. Origin of subophiolitic metamorphic rocks beneath the Mersin ophiolite, southern Turkey. Ofioliti 20, 97-110.

Parlak, O., Dunkl, I., Karaoğlan, F., Kusky, T., Zhang, C., Wang, L., Koepke, J., Billor, Z., Hames, W. E., Şimşek, E., Şimşek, G., Şimşek, T., Öztürk, S. E. 2019. Rapid cooling history of a Neotethyan ophiolite: evidence for contemporaneous subduction initiation and metamorphic sole formation. Geological Society of America Bulletin 131, 2011-2038.

Parlak, O., Karaoğlan, F., Rızaoğlu, T., Klötzli, U., Koller, F., Billor, Z. 2013. U-Pb and ^{40}Ar-^{39}Ar geochronology of the ophiolites and granitoids from the Tauride belt: Implications for the evolution of the Inner Tauride suture. Journal of Geodynamics 65, 22-37.

Potter, D. K., Stephenson, A. 1988. Single domain particles in rocks and magnetic fabric analysis. Geophysical Research Letters 15, 1097-1100.

Rochette, P., Jackson, M., Aubourg, C. 1992. Rock magnetism and the interpretation of anisotropy of magnetic susceptibility. Reviews of Geophysics 30, 209-226.

Staudigel, H., Tauxe, L., Gee, J. S., Bogaard, P., Haspels, J., Kale, G., Leenders, A., Meijer, P., Swaak, B., Tuin, M., Van Soest, M. C., Verdurmen, E. A. Th., Zevenhuizen, A. 1999. Geochemistry and intrusive directions in sheeted dikes in the Troodos ophiolite: implications for mid-ocean ridge spreading centers. Geochemistry Geophysics Geosystems 13, 1.

Stephenson, A. 1994. Distribution anisotropy: two simple models for magnetic lineation and foliation. Physics of the Earth and Planetary Interiors 82, 49-53.

Tarling, D. H., Hrouda, F. 1993. The Magnetic Anisotropy of Rocks, Chapman and Hall, London, 217.

Tauxe, L., Butler, R. F., Banerjee, S. K., Van der Voo, R. 2010. Essentials of Paleomagnetism, University of California Press, Berkeley, California, 500.

Tekin, U. K., Bedi, Y., Okuyucu, C., Göncüoglu, M. C., Sayit, K. 2016. Radiolarian biochronology of upper Anisian to upper Ladinian (Middle Triassic) blocks and tectonic slices of volcano-sedimentary successions in the Mersin Mélange, southern Turkey: new insights for the evolution of Neotethys. Journal of African Earth Sciences 124, 409–426.

Thompson, R., Oldfield, F. 1986. Environmental Magnetism. Allen and Unwin, London, 227.

Van Hinsbergen, D. J., Peters, K., Maffione, M., Spakman, W., Guilmette, C., Thieulot, C., Kaymakcı, N. 2015. Dynamics of intraoceanic subduction initiation: suprasubduction zone ophiolite formation and metamorphic sole exhumation in context of absolute plate motions. Geochemistry, Geophysics, Geosystems 16 (6), 1771-1785.

Bulletin of the Mineral Research and Exploration

Paleoecological investigation of the Miocene (23.03-5.33 mya) rodents (Mammalia: Rodentia) in Anatolia

Hasan VURAL[a][*] and Şakir Önder ÖZKURT[b]

[a]Ahi Evran University, Faculty of Sciences and Literature, Department of Anthropology, Kırşehir, Türkiye
[b]Ahi Evran University, Faculty of Education, Department of Science Education, Kırşehir, Türkiye

Research Article

ABSTRACT

Anatolia's geographical location as a land bridge between Europe, Asia, and Africa, makes it an important passage for mammal migrations, with a rich fossil potential. However, detailed scientific studies on the Neogene paleogeography of Anatolia are scarce. Rodentia is among the major mammal groups generally adapting to different habitat types and rapidly evolving with the changing geography. Investigating this group provides data to increase the accuracy of ecological analyses. We selected Rodentia fossils from the Miocene excavation sites with published papers, and examined specimens of 14 families from 106 localities. Cricetidae, Muridae, Gliridae, and Sciuridae were found to be most dominant rodent families in Anatolia during the Early Miocene, indicating a high humidity, whereas ecological changes towards the end of this epoch led to a complex formation in the biogeography of micromammals. In the Middle Miocene, a 65% decrease in Muridae, the emergence of Eomyidae, and a significant increase in Spalacidae suggest a climate shift, towards tropical or semi-tropical conditions. In the Late Miocene, Muridae regaining its maximum level and becoming the most crowded family may indicate an unexpected rise in humidity, while the stable prevalence of Eomyidae and Castoridae point to the continuity of aquatic environments and humidity.

1. Introduction

Due to their rapid and wide geographic distribution and evolution, fossil groups of small mammals are extensively used in aging sediments belonging to the Neogene-Paleogene. These fossils contribute to the creation of an intra- and intercontinental biochronology of sediments, shedding light on the paleoecology and paleogeography of different regions. Anatolia's geographical position as a land bridge between Asia, Africa, and Europe during the Neogene-Paleogene, as it is today, has provided a passage for the intercontinental migration of mammals. Therefore, terrestrial sediments of the Neogene-Paleogene period are widespread in Anatolia, containing fossils of several members of the mammalian fauna including rodents (Rodentia; mice, squirrels, moles, beavers, hedgehogs, etc.), lagomorphs (Lagomorpha), insectivorous mammals (Soricidae, Scadentia), and bats (Chiroptera). Rodentia constitutes the most crowded order among these small mammal groups. This order first occurred in the Late Paleocene according to paleontological data (Hartenberger, 1998), or in the Early Paleocene according to molecular studies (Wu et al., 2012). With approximately 30 families and an estimated number of more than 2.277 species, they constitute 42% of all extant mammal species (Carleton and Musser, 2005).

Including fossil records to this count may allow for a better understanding of the diversity of micromammals as a group (Chaline and Mein, 1979). In addition to species diversity, and the fact that they can be found on all continents except Antarctica, the extent of the evolutionary success of rodents is directly reflected in how they have adapted to almost all types of habitats including human settlement areas, besides their natural habitats such as trees, underground, deserts, steppes or forests, and even wetlands (Erdal, 2017).

Anatolia is a mainland formed by the merging of different continental parts. The closure of the Tethys Ocean, which was located between the two ancient supercontinents of Gondwana in the south and Laurasia in the north, and the collisions of both the Indian subcontinent and the Arabian Plate with Eurasia were the main critical events during Anatolia's terrestrial formation (Şengör and Yılmaz, 1981; Rögl, 1999). During the Oligocene epoch, Tethys was disconnected from the Mediterranean, and the Paratethys Sea was formed, covering a large portion of southeastern Europe, including the present-day Aral Sea, the Caspian Sea, and the Black Sea (Rögl, 1999). In the beginning of Miocene, land masses increased particularly in the Sub-Paratethyan bioprovince, which corresponds to the region where Anatolia is located. Around the Middle Miocene, connections were established between Paratethys and the Pacific, through the Indian Ocean, later to be closed off again. The connection between Paratethys and the Mediterranean established through the Eastern Anatolia was also closed with the collision of the Arabian Plate with Eurasia at the end of the Middle Miocene (Rögl, 1999). The connections of Paratethys with other oceans affected the intercontinental dispersal of mammals. During the Miocene, Paratethys gradually retreated, leading to an increase in the amount of land masses. Due to this increase, the fossil records of mammalian fauna in Anatolia are mostly known from the terrestrial sediments belonging to the Neogene.

Record of the African and Old World Miocene points to a decrease in humidity, accompanied by the diversification of seasonal open-air plants and animal communities (Bernor, 1984). The Miocene/Pliocene boundary indicates a shift in the environment and fauna, from warmer temperate seasonal climates to cooler temperate environments (Bernor, 1996). Although the global cooling in this period is less significant than the ones in the Middle Miocene and the Pliocene/Pleistocene, the Late Miocene is characterized by very distinctive changes in terrestrial ecosystems. One of the most well-known changes is the strong dispersion of low-biomass plants: woodlands begin to replace forests, while savannas and grasslands spread and settle on a global scale (Van Dam, 1997). Ecological conditions of the Early Miocene indicate humid forest environments, dominated by low seasonality (Fortelius et al., 2014). In addition, paleobotanical findings from the Early Miocene sediments in Anatolia suggest the presence of humid and swamp-like areas in Western Anatolia, along with a sporadic presence of more open environments (Akgün et al., 2007; Akkiraz et al., 2011; Kayseri Özer et al., 2014). During the Middle Miocene, we see an increase of land masses in Anatolia (Rögl, 1999). Global temperatures reached maximum levels during these periods (Kaya, 2017). The ecological and environmental changes characterized by an increase in seasonality and a drought in the Late Miocene may be seen as the results of a parallel evolution in mammal species (Kaya, 2017).

This study aims to interpret the Miocene paleoecology of Anatolia, or to make ecological analyses regarding family groups with higher numbers of species by determining the Rodentia numbers in different localities and to identify the paleoenvironment in accordance with these analyses, based on database records published on Rodentia fossils obtained from several paleontological excavations carried out in Anatolia.

2. Material and Method

The data of our study consists of monographs and the surface investigation results of paleontological excavations carried out in Anatolian Miocene excavation sites, as well as scientific literature published on the paleoecology, paleoclimate, and paleobiology of the Miocene. We used the New and Old World Database of Fossil Mammals (NOW) as our main database (Fortelius et al., 2014). After obtaining the Rodentia order list from the NOW database, we excluded the specimens that were not published in any papers, and created a new data list. This final list contained Rodentia members from 106 localities, representing 14 families and around 130 species.

Among these localities, Rodentia findings were found in the following sites: Balçıklıdere, Akhisar, Altıntaş, Amasya, Ayseki, Bağiçi, Bayırköy, Bayraktepe, Belenyenice, Bostanyeri, Büyükanafartalar, Cumali, Çakıllı, Çandır, Dededağ, Dendil, Develiköy, Dumlupınar, Düzyayla, Eskisubaşı, Gördes, Göstere, Gözetlemederesi, Hancılı, Harta, Hayranlı, Hoşköy, İnkonak, Kalamış, Kaletepe, Kaleköy, Kaplangı, Karaçay, Karaözü, Kargı, Kavurca, Keseköy, Kılçak, Kinik, Kırca, Kumköy, Mahmutköy, Mahmutlar, Mürefte, Pişmanköy, Sabuncubeli, Sandıklı-Koçgazi, Sarıçay, Şemsettin, Sinaptepe, Sofça, Söke, Süleymanlı, Tuğlu, Yapıntı, Yeni Eskihisar, Yurtyenice, and Yukarıkızılca1. In addition to these, ongoing fossil excavations are currently being carried out in Kurutlu, Sofular, Yeni Yaylacık, Paşalar, and Çorakyerler.

We compiled the data for order Rodentia in Microsoft Excel 2007, and created graphics using the same software. We prepared the locality maps on the geological map of Anatolia. The percentages in graphics represent the ratio of the number of species in families relative to the number of species in other families.

3. Findings

3.1. Early Miocene Rodentia from Anatolia and Their Localities

As the tropical regions of the Late Oligocene and the Early Miocene expanded globally, the Early Miocene became dominated by green plants, as well as tropical and subtropical climates (Ataabadi, 2010). The Early Miocene was generally a humid period with high precipitation (Fortelius et al., 2002), and a complicated timeframe with weak seasonality and low temperatures (Utescher et al., 2000). While Muroidea was dominant in Anatolia in the Early Miocene, Gliridae and Eomyidae were dominant in Europe. This indicates a faunal barrier between the Afro-Arabic and the Eurasian plates. In this period, a few Asian mammalian taxa such as the genera *Cricetodon*, *Spanocricetodon*, and *Democricetodon* from the family Cricetidae, alongside *Vasseuroyms* and *Glirulus* from the family Gliridae emerged in Anatolia. These taxa have also migrated to the Balkans and Western Europe (Agusti et al., 2001; Koufos et al., 2005). *Glirulus*, *Democricetodon* and *Cricetodon* are inhabitants of

forest biotopes (Nargolwalla, 2009). This may indicate that the localities where these genera lived had an ecology where subtropical or tropical temperatures prevailed, along with humid conditions. Localities for the genera in question are Belenyenice, Dededağ, Dumlupınar, Gökler 4A, Hancılı 2, Harta, Kargı 1, Kargı 2, Kargı 3, Keseköy, Kılçak 3a, Kılçak 3b, Kılçak 0", Kınık, Kınık 2, Sabuncubeli, Söke, and Yapıntı for *Cricetodon;* Harami, Kargı 1, Kargı 2, Kılçak 3a, Kılçak 3b, Kılçak 0, and Söke for *Spanocricetodon*; Belenyenice, Harami, Harami 4, Kılçak 3a, Kılçak 0, Kılçak 0, and Kınık 1 for *Vasseuroyms*; and Keseköy and Söke for *Glirulus*. Genus *Debruijina* from the family Spalacidae was first seen in Anatolia in MN2. *Megacricetodon*, *Anomalomys* and *Karydomys* first appeared in Anatolia in MN3 (Alçiçek, 2010). The localities where these genera are found are Belenyenice, Dededağ, Dumlupınar, Hancılı 2, Harami, Hoşköy, Keseköy, Kınık 1, Söke, Yapıntı, and Yurtyenice for Megacricetodon; Belenyenice, Dededağ, Hancılı 2, and Söke for Anomalomys; and Dumlupınar, Söke, and Yapıntı for Kardomys. Forests constituted the predominant habitat type in the beginning of the Miocene, and the most common species of large mammals were the brachydont (low-crowned teeth) forest forms, while species adapted to open environments were rare. Among the Rodentia fauna, Cricetidae was the dominant family. Not all species of this family are adapted to closed environments, although species of genera such as *Democricetodon* and *Eumyarion* definitely seem to prefer more closed environments (Van den Hoek Ostende, 2001). The Rodentia records of Anatolia from the Early Miocene are different from those of Europe and Central Asia. Some Rodentia species entered Anatolia in earlier periods. In this period, the scarcity of family Ctenodactylidae is replaced by Muroidea, which is marked by the emergence of *Eumyarion microps* as well as species belonging to *Deperetoyms*, *Democricetodon*, *Enginia*, and *Heterosminthus* (Ünay et al., 2003). The scarcity of Ctenodactylidae is reflected by the presence of only one genus (*Sayims*) found in Harta, Keseköy, and Yapıntı among all localities we investigated in Anatolia. From this period, the genus *Eumyarion* is found in localities Gökler 4A, Gördes, Hancılı 2, Harami, Kargı 2, Keseköy, Kılçak 3a, Kılçak 3b, Kılçak 0, Kınık 1, Kınık 2, Sabuncubeli, and Yapıntı; *Deperetoyms* is found in Gördes, Harami,

Kargı 2, Kargı 3, Kılçak 3a, Kılçak 3b, Kılçak 0, and Kınık; *Democricetodon* in Belenyenice, Gökler 4A, Gördes Hancılı 2, Harami, Harami 4, Harami 5, Harta, Hoşköy, Kargı 3, Keseköy, Kılçak 3a, Kılçak 3b, Kılçak 0, Kılçak 0, Sabuncubeli, Semsettin, Söke, Yapıntı, and Yurtyenice; and *Enginia* only in Yapıntı. The origin of Sciuridae is unknown. The first Anatolia records of it from this period are in Kargı 2 and Kılçak 0-3b (Ünay et al., 2003). Rodentia families identified from the Early Miocene paleontological excavation sites in Anatolia are Cricetidae (36%), Muridae (28%), Gliridae (15%), Sciuridae (10%),

Castoridae (3%), Dipodidae (3%), Anomalomyidae (1%), Ctenodactylidae (1%), Petauristidae (0.77%), and Spalacidae (0.77%) (Figure 1).

In paleontological studies carried out in Anatolia belonging to this epoch, the localities of Belenyenice, Dededağ, Dumlupınar, Gökler, Gördes, Hancılı, Harami, Harta, Hoşköy, Inkonak, Kaplangı, Kargı, Keseköy, Kılçak, Kınık, Sabuncubeli, Şemsettin, Söke, Yapıntı, and Yurtyenice are given on the map (Figure 2). Anatolian localities, where Rodentia families were seen, are also given as a list (Table 1).
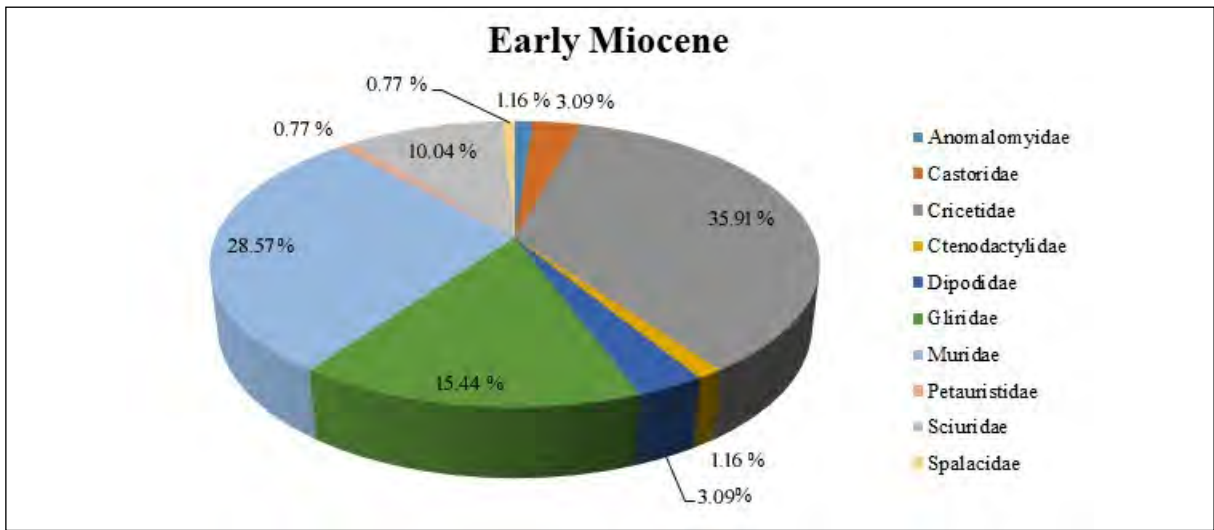
Figure 1- Early Miocene Rodentia findings from Anatolia.
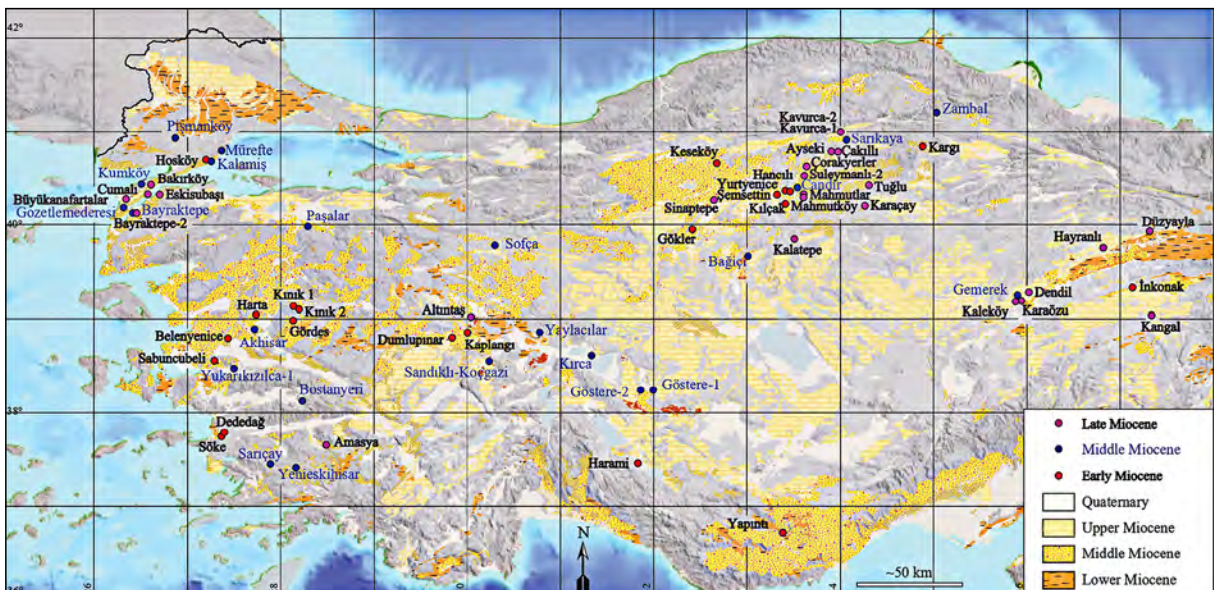
Figure 2- The localities in Anatolia, where Rodentia findings from the Miocene were found.

Table 1- Early Miocene Rodentia families from Anatolia, listed according to their localities.

LOCALITY	MN ZONE	Anomalomyidae	Castoridae	Cricetidae	Ctenodactylidae	Dipodidae	Gliridae	Muridae	Petauristidae	Sciuridae	Spalacidae
Hancılı 2	MN 4			X			X	X			X
Gökler4A	MN 2		X	X			X	X		X	
Keseköy	MN 3			X	X		X	X		X	
Kılçak3a	MN 1		X	X			X	X			
Kılçak 3b	MN 1			X		X		X			
Kılçak 0	MN 1		X	X		X	X	X		X	
Kılçak 0"	MN 1			X		X	X	X		X	
Şemsettin	MN 4			X			X		X	X	
Yurtyenice	MN 4			X			X				
Dededağ	MN 4	X		X			X	X		X	
Söke	MN 3-4	X		X			X	X			
Kargı 1	MN 1			X				X			
Kargı 2	MN 1			X		X		X			
Kargı 3	MN 1			X		X		X		X	
Yapıntı	MN 3-4			X	X		X	X		X	
Harami	MN 2		X	X			X	X		X	
Harami 1	MN 2			X						X	
Harami 3	MN 2									X	
Harami 4	MN 2		X	X			X	X		X	
Harami 5	MN 2		X				X	X			
Dumlupınar	MN 4-5			X			X	X	X		
Belenyenice	MN 4	X		X			X	X			
Gördes	MN 3						X	X		X	
Harta	MN 3			X	X		X	X		X	
Kınık	MN 3							X			
Kınık 1	MN 3			X			X	X		X	
Kınık 2	MN 2		X	X			X	X			
Sabuncubeli	MN 3		X	X			X	X		X	
İnkonak	MP 30			X		X	X	X			
Hoşköy	MN 4			X		X	X			X	
Kaplangı 1	MN 4									X	
Kaplangı 2	MN 4									X	

To make sense of the ecology of extinct mammals, it may be necessary to look at the ecology of their living relatives. It is a widely known fact that the family Castoridae (beavers) lives in or near water. We may say that the fossil relatives of this family also preferred similar environments. Therefore, the presence of Castoridae reflects the presence of wet environments (Daams and Ders Meulen, 1984). Gliridae, which is thought to have originated in Europe, appeared in Anatolia in the Late Oligocene and the number of species belonging to this family also diversified in this period (Ünay, 1994). The family Castoridae is known from the localities of Gökler 4A, Harami, Harami 4, Harami 5, Kılçak 3a, Kılçak 0, Kınık 2, and Sabuncubeli. We can say that these localities match the ecology mentioned above. Cricetidae and Muridae, the families with the highest number of species, were recorded from the Central Anatolian, Western Anatolian, and the Mediterranean Regions, with respect to their current geographic

boundaries. Families Gliridae and Sciuridae, on the other hand, were only recorded from Central Anatolia with provided numbers, although they were seen in both Central and Western Anatolia.

Most members of the family Spalacidae (0.77%) are adapted to open meadowlands. The fact that they were less in number than the other Rodentia members in the Early Miocene may be the result of Anatolia's heavily forested ecology. However, although the members of Muridae (28%) and Cricetidae (35%) may not be reckoned as definite forest dwellers, they appear to be the two most dominant families during this period. Gliridae (15%) species constitute a group that was adapted to a humid and more closed ecology. The above-mentioned families form a complex pattern during this period. According to the analyses, it is possible to say that the ecology was dominated by deciduous trees, moist, and had partially open habitats.

3.2. Middle Miocene Rodentia from Anatolia and Their Localities

Ecological conditions of the Middle Miocene resemble those in the Early Miocene. In this period, the home ranges of numerous mammals that had immigrated from Africa expanded in Eurasia, while the Earth's tropical regions shifted towards the north and the middle latitudes of Eurasia due to an increase in Arctic glaciers and the cooling of polar regions. As a result, possibly a tropical and semi-tropical climate zone dominated the middle latitudes from Eastern Asia to Western Europe, including Anatolia (Kaya, 2017). Regional palynological evidence indicates a subtropical or tropical climate around the Mediterranean during the Middle Miocene (Akgün et al., 2007). In this period, Western Anatolia is generally represented by mixed mesophytic and evergreen forests. Some regions are characterized by broad-leaved deciduous forests (Kayseri-Özer, 2017). This period is characterized by Castoridae and Gliridae (MN6-8). Although *Cricetodon* and *Megacricetodon* of Asian origin were known from before, *Byzantinia*, *Myocricetodon* and *Pliospalax* are seen in this period for the first time (Alçiçek, H., 2010). Localities for these genera are Bağiçi, Bayraktepe, Derekebir, Pişmanköy, Yaylacılar, Yeni Eskihisar, Sandıklı-Koçgazi, Kırca, Gözetlemederesi, Sofça Akhisar, Kalamış for *Byzantinia*; Kalamış,

Sinap 64, Sinap 65, Yeni Eskihisar, and Bağiçi for *Myocricetodon*; Bayraktepe 1, Paşalar, Sarıçay, Sandıklı-Koçgazi, Kırca, Bağiçi, Pişmanköy, Göstere, Sofça, Yeni Eskihisar, and Sarıçay for *Pliospalax*. While *Eomyidae* of North American origin is seen in Central Asia and Europe, it appears in Anatolia during the Middle Miocene, and this may be related to the MN5 entry of *Keremidomys* and *Eomyops* species into Europe (Ünay et al., 2003). While Eomyidae was the dominant family in Europe during the Early Miocene, the first findings from Anatolia is MN5 unearthed in Çandır (Kaymakçı, 2000). The existence of families Castoridae and Eomyidae during this period indicates a paleoecology similar to that of the Early Miocene. While Eomyidae is seen in Europe in MN3, it is seen in Anatolia in MN5. This may indicate an ecology similar to that of Europe in localities where Eomyidae is seen in MN5.

Localities which provided the Middle Miocene Rodentia fossils from Anatolia were Akhisar, Bağiçi, Bayraktepe, Bostanyeri, Çandır, Derekebir, Dumlupınar, Gemerek, Göstere 1, Göstere 2, Gözlemederesi, Kalamış, Kırca, Kumköy, Mürefte, Pasalar, Pişmanköy, Sandıklı-Koçgazi, Sarıçay, Sarıkaya, Sinaptepe, Sofça, Yaylacılar, Yeni Eskihisar, and Zambal (Figure 2). The localities where Rodentia families of this period were seen (Saraç, 2003) are given as a list (Table 2).

The most crowded Rodentia group in the Middle Miocene is the family Cricetidae, with 32.35%; followed by Gliridae, which has the second higher numbers with 19.12%. Sciuridae has a ratio of 16.18%, while Spalacidae has 9.31%. Families with lower numbers are Muridae, with a ratio of 5.39%; Gerbillidae, with 4.41%; Eomyidae, with 3.92%; Dipodidae and Petauristidae, each with 2.94%; Castoridae, with 2.45%; and Ctenodactylidae and Platacanthomyidae, each with 0.49% (Figure 3).

3.3. Late Miocene Rodentia from Anatolia and Their Localities

In the Late Miocene, seasonality is assumed to have increased, while closed forest environments were replaced by more open habitats (Ataabadi, 2010). The Late Miocene is estimated to be a warmer period than today (Pound et al., 2012). Rising drought during the

Table 2- Middle Miocene Rodentia families from Anatolia, listed according to their localities.

LOCALITY	MN ZONE	Castoridae	Cricetidae	Ctenodactylidae	Dipodidae	Eomyidae	Gerbillidae	Gliridae	Muridae	Petauristidae	Platacanthomyidae	Sciuridae	Spalacidae
Yaylacılar	MN 7-8		X										
Sandıklı-Koçgazi	MN 5-7		X		X	X		X				X	X
Kırca	MN 7-8		X					X				X	X
Bağiçi	MN 7-8		X										
Çandır	MN 6		X			X		X	X	X		X	
Sinap 64	MN 8						X						
Sinap 65	MN 8						X						X
Paşalar	MN 6	X	X	X	X			X	X			X	X
Bayraktepe 1	MN 7-8	X	X							X			X
Gözetlemederesi	MN 6-8	X	X									X	
Kumköy	MN 6-8		X					X					
Zambal 1	MN 6											X	
Sarıkaya	MN 5		X						X				
Bostanyeri	MN 6		X						X				
Yenicekent 1	MN 8-9		X										
Yenicekent 2	MN 8-9		X										
Yenicekent 3	MN 8-9		X										
Yenicekent 4	MN 8-9		X										
Pişmanköy	MN 7	X	X			X	X	X				X	X
Yukarıkızılca 1	MN 5-6		X					X	X			X	X
Göstere 1	MN 6-8								X				
Göstere 2	MN 6-8							X	X				X
Sofça	MN 7-8		X		X	X	X	X				X	X
Akhisar	MN 7-8		X					X					
Berdik 1	MN 7-8												X
Sarıçay	MN 7		X			X		X	X	X	X	X	X
Yeni Eskihisar	MN 7-8		X				X						
Gemerek	MN 6-8		X					X	X				
Mürefte	MN 5		X		X			X				X	
Kalamış	MN 7		X				X					X	

Late Miocene is thought to have led to an increase in the amount of open environments in East Asia and East Africa, with hypsodont (high-crowned teeth) mammal species proliferating and becoming adapted to the savanna ecosystem (Eronen et al., 2009). According to studies, the species diversity is known to have increased to maximum levels around 10 mya, during the Vallesian age (Agustí and Anton, 2005). The Vallesian Crisis (9.7-9.6 Mya) was first described by Agustí and Moya-Sola (1990). Increasing seasonality, and low winter temperatures in particular, brought an end to the evergreen subtropical forests of Western Europe (Fostelius et al., 2014). The Late Miocene vegetation was dominated by Asteraceae (the aster family), representing open environments with almost no trees (Yavuz Işık et al., 2011). In addition, the examination of pollen findings from the Mediterranean Basin suggested that the plant diversity gradually decreased
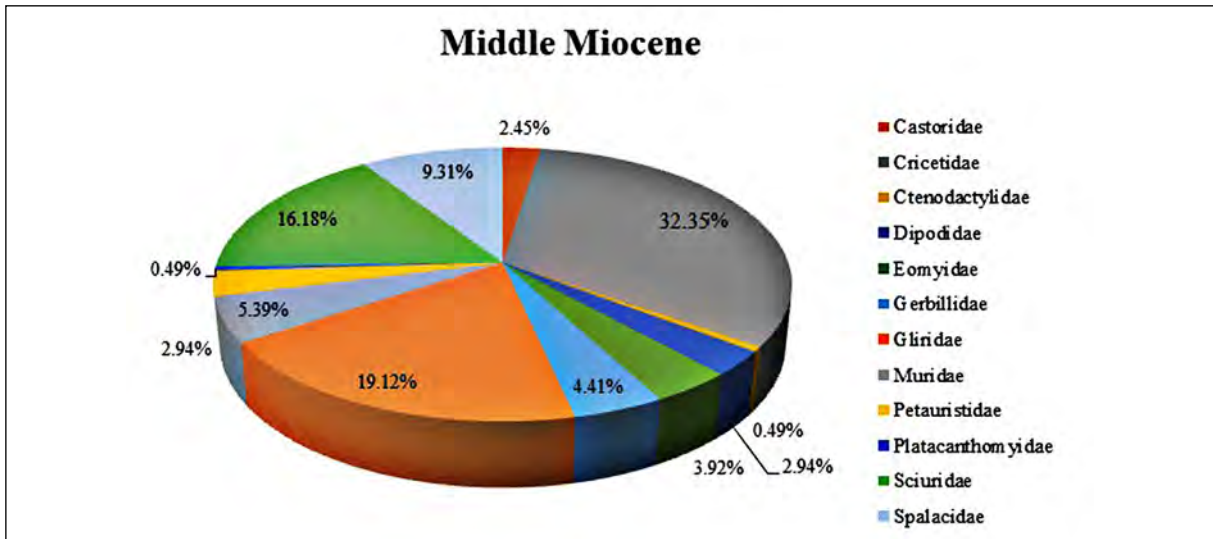
Figure 3- Middle Miocene Rodentia findings from Anatolia.

during the Middle-Late Miocene and Pliocene, and that the majority of these plant groups had very high water demand. It is estimated that the plants adapted to warmer climates proliferated (Jimenez Moreno et al., 2007). The decrease in Sciuridae and Cricetidae during the Late Miocene, as well as the diversification of Muridae species, can be interpreted as indicators of ecological change. The decline in Sciuridae is seen in its tree forms. This analysis shows us that arboraceous environments were replaced by open steppes.

The localities which provided Late Miocene Rodentia fossils from Anatolia were Altıntaş, Amasya, Ayseki, Bayırköy, Bayraktepe, Büyükanafartalar, Cumali, Çakıllı, Çorakyerler, Dendil, Develiköy, Düzyayla, Eskisubaşı, Güney, Admired, Kalamış, Kaletepe, Kaleköy, Kangal, Karaçay, Karaözü, Kavurca, Kütahya, Mahmutlar, Mahmutköy, Süleymanlı, and Tuğlu (Figure 2). For these localities, the frequency of the number of species of Rodentia families compared to other families are shown in a pie-chart (Figure 4), and their localities are given as a list (Table 3).

The most crowded group according to fossil findings is Muridae (24%), which displays a dispersal
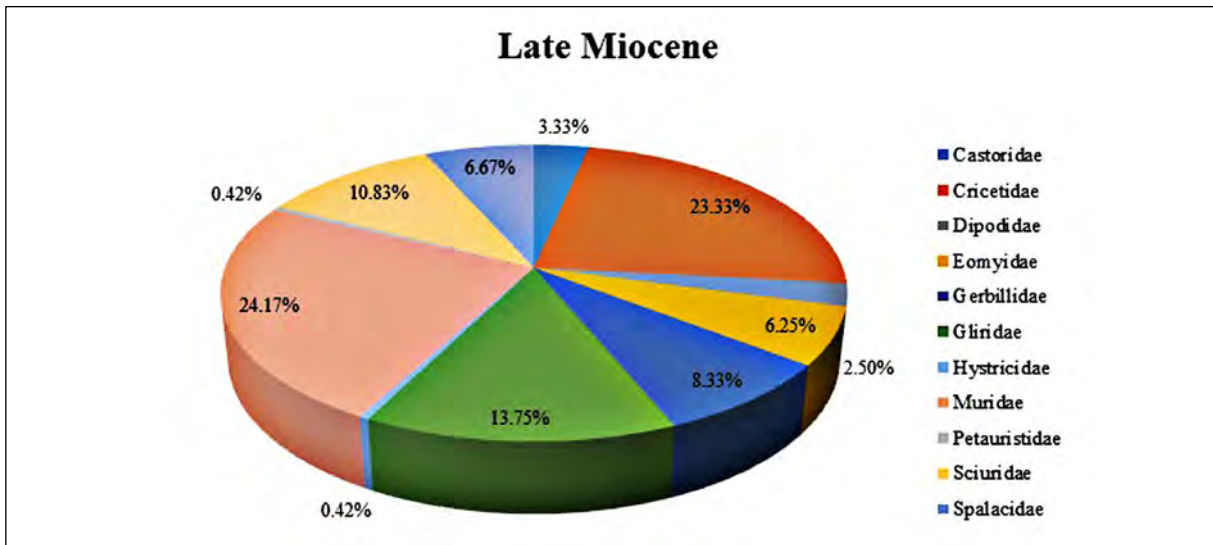
Figure 4- Late Miocene Rodentia findings from Anatolia.

Table 3- Late Miocene Rodentia families from Anatolia, listed according to their localities.

LOCALITY	MN ZONE	Castoridae	Cricetidae	Dipodidae	Eomyidae	Gerbillidae	Gliridae	Hystricidae	Muridae	Petauristidae	Sciuridae	Spalacidae
Sandık-Garkın	MN 11		X									
Kalamış	MN 8-9					X						
Sinap	MN 9								X			X
Sinap4	MN 9					X						X
Sinap12	MN 9					X			X			X
Sinap8A	MN 9					X			X			
Sinap41	MN 9											X
Sinap42	MN 9					X			X			
Sinap49	MN 10					X						
Sinap84	MN 9								X			X
Sinap108	MN 9								X			
Sinap120	MN 9											X
Amasya	MN 13											X
Amasya 2	MN 13					X			X			X
Direcik 1	MN 9											X
Cumali	MN 10-11	X	X				X		X			
Bakırköy	MN 12		X	X	X		X	X			X	
Büyükanafartalar	MN 9-10		X									
Bayraktepe 2	MN 9	X	X						X		X	
Eskisubaşı	MN 9-10	X	X				X					
Çorakyerler	MN 10-11		X	X	X	X	X		X			X
Kalatepe 1	Late Miocene		X		X	X			X			
Kaletepe 2	Late Miocene				X				X			
Mahmutlar	Late Miocene					X			X			
Tuğlu	MN 9		X		X	X	X		X		X	
Çakıllı	MN 12-13								X			
Ayseki	MN 12-13		X				X		X			
Süleymanlı 2	MN 13		X			X	X		X		X	X
Kavurca 1	MN 10-13		X		X	X	X		X		X	X
Kavurca 2	Late Miocene		X				X		X			
Güney	MN 9		X									
Mahmutgazi	MN 11-12								X			
Dereikebir	MN 9		X				X		X			
Mahmutköy	MN 9-10		X			X	X		X			
Aşağıcigil 1	MN 9		X				X		X			
Altıntaş 1	MN 9								X		X	
Kütahya A	MN 9										X	
Develiköy 2	MN 14					X			X		X	
Düzyayla	MN 12	X	X	X	X	X	X		X	X	X	
Hayranlı 1	MN 10-11						X				X	
Kangal 1	MN 13										X	
Kaleköy	MN 10-12		X			X	X		X		X	X
Dendil	MN 10		X			X	X		X		X	
Karaözü	MN 10-12		X	X	X	X	X				X	X

from the western part of Anatolia extending towards central regions. Another dense group, Cricetidae (23%), has a dispersal parallel to this. While the families Gliridae (13%) and Sciuridae (10%) are particularly dispersed in the western and inland parts; Gerbillidae (3%), Spalacidae (6%), and Eomyidae (6%) were dispersed in the central parts. The family Dipodidae (2%) maintained its density in South-Western Anatolia. The genus Dipodidae is seen in Anatolia, and differs from the Euro-Asian genera (Bruijn et al., 2013). Gerbillidae, Spalacidae, and Dipodidae sharing the same ecology is an indicator of the existence of an open meadowland, steppe and a semi-arid habitat in the Late Miocene. The decrease in Gliridae and Sciuridae during this period, compared to their densities in the Middle Miocene, can be ecologically characterized by a decline in forest environments. The dominance of Muridae species taking precedence over the dominance of Cricetidae, and the decrease in Gliridae both indicate a decline in moist and forested areas. However, the increase in Eomyidae was in contrast to the decline in humidity. This is because Eomyidae is a family of micromammals adapted to a moist and more closed ecosystem (Engesser and Kälin, 2017).

If we compare specific families (Figure 5) for a paleoecological evaluation of the Miocene findings from Anatolia; the family Castoridae preserving its density in the Early, Middle, and Late Miocene indicates the continuous existence of partial aquatic environments in Anatolia throughout the entire

Miocene (Table 4). While Castoridae was found in Anatolia until the 1950s, the family is currently unseen. Although the decline in Cricetidae seen in the Early Miocene until the Late Miocene does not provide information about the Anatolian ecology, the diversification of species in this family may indicate that its members had no difficulty in adapting to their habitat. The number of modern species belonging to this family seems to have reached the maximum. The family Gliridae, experiencing a decline in the late periods of the Middle Miocene until the Late Miocene, suggests that the species adapted to moist habitats of the ecology decreased in the Late Miocene, while a more continental climate became dominant. The current density of this family being almost equal to that in the Late Miocene suggests the Miocene ecology was similar to that of today. The fact that Gliridae reached its maximum level in the Middle Miocene, while Muridae dropped to its minimum level during the same period may propose an ecological dominance relationship between these two families. This parallel rise-drop forms the basis of environmental changes. The emergence of Eomyidae in the Middle Miocene and its continued existence through the Late Miocene, on the other hand, gives the impression that the habitat may have preserved its forest density in ecological terms. At the same time, Sciuridae maintaining its maximum level during the Middle Miocene indicates the continued existence of arboraceous environments.

As a general evaluation; families Gliridae and Sciuridae reach their maximum levels in the
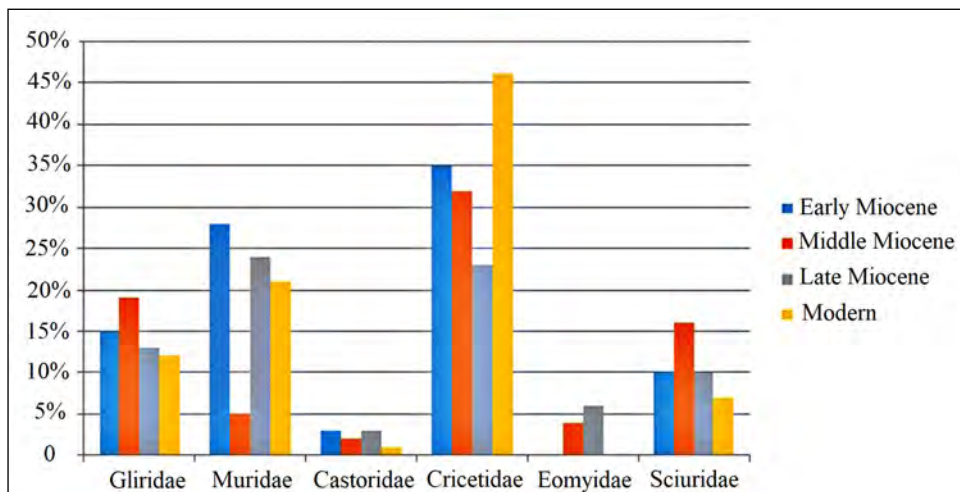
Figure 5- Comparison of the modern and Miocene Rodentia families of Anatolia.

Table 4- Modern and Miocene Rodentia families of Anatolia.

MODERN (Yiğit et al. 2006)	EARLY MIOCENE	MIDDLE MIOCENE	LATE MIOCENE
Castoridae 1.54% Cricetidae 46.15% Dipodidae 4.62% Gliridae 12.31% Hystricidae 1.54% Muridae 21.54% Myocastoridae 1.54% Sciuridae 7.69% Spalacidae 3.08%	Anomalomyidae 1.16% Castoridae 3.09% Cricetidae 35.91% Ctenodactylidae 1.16% Dipodidae 3.09% Gliridae 15.44% Muridae 28.57% Petauristidae 0.7% Sciuridae 10.04% Spalacidae 0.77%	Castoridae 2.45% Cricetidae 32.35% Ctenodactylidae 0.49% Dipodidae 2.94% Eomyidae 3.92% Gerbillidae 4.41% Gliridae 19.12% Muridae 5.32% Petauristidae 2.94% Platacanthomyidae 0.49% Sciuridae 16.18% Spalacidae 9.31%	Castoridae 3.33% Cricetidae 23.33% Dipodidae 2.50% Eomyidae 6.25% Gerbillidae 8.33% Gliridae 13.75% Hystricidae 0.42% Muridae 24.17% Petauristidae 0.42% Sciuridae 10.83% Spalacidae 6.67%

Middle Miocene. Seeing these two families at their maximum during this period, when compared to the rest of Miocene, indicates that Anatolia was a moist and forested habitat in the Middle Miocene ecosystem. The same period, the Middle Miocene, is also when Muridae drops to its minimum. The factor minimizing this family during the Middle Miocene is the ecological structure in moist and forested habitats. The presence of Castoridae during the entire Miocene suggests the ongoing presence of partial aquatic habitats throughout the epoch. The family Cricetidae experienced a linear decrease during Miocene, which may be due to Cricetidae passing on its dominance in different ecological niches to the members of other families. The occurrence of Eomyidae only in the Middle and the Late Miocene may have resulted from the paleoecological environment showing similar characteristics for Eomyidae during the Middle Miocene and the early periods of the Late Miocene.

4. Results

Terrestrial mammal ecosystems are mostly regionally or temporarily discontinuous, and are controlled by a combination of topographic, tectonic, climatic, and vegetational dynamics (Eronen et al., 2009). Anatolian paleogeography during the Miocene can be mainly summarized in three different stages. The first period, the Early Miocene in Anatolia, was dominated by low seasonality and mammal species adapted to moist and forested environments. The first Miocene faunas of Anatolia most likely represented very moist and possibly forested environments

(Fortelius, 2014). Although marshes were well established in some parts of Anatolia during the Early Miocene, we should be careful about overgeneralizing to assume that entire Anatolia was covered with lush forests at that period (Joniak et al., 2019). As this study focuses on Rodentia, the presence of Castoridae in Harami, Harami 4, Harami 5, Kılçak 3a, Kılçak 0, Kınık 2, and Sabuncubeli in the Early Miocene Anatolia indicates that these localities had woodlands and aquatic habitats with low flow rate. The occurrence of Dipodidae in Hoşköy, Kargı 2, and Kargı 3 localities does not show that these regions were much of closed environments as habitats. Rather, this family represents open steppes or semi-arid habitats. Even though the density of Sciuridae being lower than that of the Middle Miocene, and equal to that of the Late Miocene causes a hesitation concerning the forested environments, the diversity seen in Gliridae evens these ratios, suggesting that the woodlands were frequent. In addition, we may say that the Old World mammal faunas generally had homogeneous similarity patterns against the homogeneous environmental conditions in this period, especially towards the end of Early Miocene.

Although the Climatic Optimum period of the Middle Miocene was marked by a predominantly humid climate, regional precipitation data indicates that only some places were moist while others were relatively dry (Fortelius et al., 2002). The presence of Castoridae members in Pasalar, Gözetlemederesi, Bayraktepe 1, and Pişmanköy localities show that these localities had moist habitats. Based on their teeth

models, *Eumyarion* species in particular are thought to be more abundant in moist environments or sediments showing similar environmental conditions (Fortelius et al., 2002). The findings of Eomyidae members in Çandır, Sofça, Sarıçay, Karaçay, Kaletepe 1, Kaletepe 2, Düzyayla, Pişmanköy, Kavurca, and Sandıklı-Koçgazi localities prove that these environments were also moist. As temperatures increased, Gliridae adapted to different habitats and geographically dispersed to a wider variety of locations in Europe and Asia. The dramatic downfall of Gliridae started at the beginning of the Middle Miocene, about 16 million years ago, and was triggered by environmental changes such as the seasonal expansion of open environments. According to Akkiraz et al. (2011), Anatolia was warm and moist in the Middle Miocene. On the other hand, the average hypsodonty measurements of herbivores and other extant large mammals from Greece through Afghanistan point to the existence of open and grassland ecosystems during the Middle Miocene (Fortelius et al., 2014). Anatolian Gliridae during the Middle Miocene consisted of *Microdyromys*, *Myomimus*, *Miodyromys*, *Peridyromys*, *Muscardinus*, *Vasseuromys*, *Glirulus*, and *Paraglis* species. The presence of these species in the family Gliridae represents the existence of deciduous trees and forests.

A tropical or semi-tropical climate prevailed dominated the Middle Miocene. Towards the end of this period, changes in environmental and climatic conditions caused the formation of a mixed pattern in the mammalian biogeography. A decrease in the density of Cricetidae by almost 25%, and in Muridae by about 65%, as well as significant increases in families such as Spalacidae and Eomyidae indicate a climate change in the Middle Miocene. The replacement of moist and forested areas that existed throughout the Miocene by an ecosystem with high seasonality and more open environments led to changes in the mammalian fauna.

In the Late Miocene, the grassland ecosystem became dominant and the number of large mammal species adapted to open habitats increased (Kaya and Kaymakçı, 2013). A significant faunal change was seen, from forest dwellers to ground-dwelling species. This change was characterized by *Myomimus* findings displaying a vegetational shift from forested environments of the Late Miocene to open forests and steppe-like habitats, as well as an increase in their population size. Pollen analysis shows that the Central Anatolia Region was typically dry in the Late Miocene (Akgün et al., 2007). Biotic interactions of Gliridae with other small mammal groups such as Muridae should also be considered. Correspondingly, the biodiversity of Gliridae during the Late Miocene Anatolia is represented by six genera; *Glirulus*, *Microdyromys*, *Miodyromys*, *Myomimus*, *Muscardinus*, and *Ramys* (Kaya and Kaymakçı, 2013). This shows that the Muridae species entering Europe were pre-adapted to the conditions in more open ecosystems. At the very least, they would have to be present everywhere in order for the local fauna to have a chance of better coping with the environmental changes, and thus it seems reasonable to assume that Anatolia already had open environments and that the hamsters had already begun adapting to it (Joniak et al., 2019). While Muridae comprised approximately 24% of the entire Rodentia order in the Late Miocene, Gliridae comprised 13%. We may say that the decline seen in Gliridae during the Late Miocene, when compared to the Middle Miocene, was due to the ecological dominance of a dry environment.

Cricetidae members were the dominant species of Neogene rodent communities in Türkiye and its surroundings. Since they were widespread all over Eurasia, they provide biochronological correlations with the Neogene mammalian chronology of Europe (Erten et al., 2014). According to available Miocene fossil records from Anatolia, the family Cricetidae is represented by 12 genera; *Cricetodon*, *Democricetodon*, *Deperetoyms*, *Enginia*, *Karydomys*, *Lartetomts*, *Latocricetodon*, *Megacricetodon*, *Melissiodon*, *Meteamys*, *Mirabella*, and *Spanocricetodon*. Cricetidae constitutes 35% of the entire Rodentia order in the Early Miocene, 32% of the order in the Middle Miocene, and 23% in the Late Miocene. Cricetidae members are generally more associated with open environments, but this generalization does not seem valid for the first Miocene representatives of the family from Anatolia. The dominance of Cricetidae in Anatolia can be seen both paleoecologically and biogeographically. Smaller species of the genera *Democricetodon* and *Eumyarion* certainly seem to prefer more closed environments (Van den Hoek Ostende, 2001). The localities of Çandır, Düzyayla, Gördes, Harami 4, Harami 5, Sabuncubeli, Şemsettin, Kılçak0, Kılçak3a and Kılçak

3b, Yurtyenice, Söke, Kumköy, Yapıntı, Harami, Sofça, Harta, and Hoşköy, where these species were seen, were possibly located in a deciduous woodland environment. On the other hand, *Megacricetodon* is a species that can cope better with open environments (Van den Hoek Ostende, 2001). The presence of *Palaeosciurus feignouxi*, a species of European origin, suggests a moist environment with dense vegetation. Localities of Gökler, Keseköy, Kılçak 0, Kılçak 3a, and Kılçak 3b, where *P. feignouxi* specimens were found, share the ecology of this squirrel species.

The number of Gliridae species coincides with the continental climatic events of the Cenozoic. The first Gliridae members appeared during Late Eocene through Early Oligocene, and the number of species remained limited. At the end of Late Oligocene and the beginning of Early Miocene, Gliridae experienced an increase in the number of species (Freudenthal, 1997). During this time, Gliridae numbers reached the highest paleobiodiversity peak of the family's history (5 to 60 species). During the Late Oligocene warming, *Microdyromys heissigi*, *Microdyromys praemurinus*, *Microdyromys monspeliensis*, and *Microdyromys legidensis* emerged. The earliest representative of *Peridyromys murine* (Mirambueno 1, MP 27) is known from the Late Oligocene in Spain (Freudenthal, 1997). In Miocene, seven genera of Gliridae lived in Türkiye; *Gliridinus*, *Glis*, *Vasseuromys*, *Microdyromys*, *Paraglirulus*, *Miodyromys*, and *Bransatoglis* (Kaya and Kaymakçı, 2013). Environmental changes in Europe and the Eastern Mediterranean that occurred between the Middle and the Late Miocene caused a serious decrease in the number of Gliridae species that were adapted to a humid climate. While this family constituted 19% of the entire Rodentia order during the Middle Miocene, this ratio decreased to 12% in the Late Miocene. In the late periods of Miocene, forest and wetland ecosystems were replaced by steppes and clearings in forests. This change is characterized by an increase in *Myomimus* numbers during this period (Kaya and Kaymakçı, 2013). While this species was represented with only a few examples in the Early Miocene, the number of findings increases in Middle Miocene, almost reaching its maximum. The members of Gliridae generally have extremities well-adapted for climbing trees. Their diet includes fruits, nuts, insects, eggs, and small invertebrates. *Myomimus* is the only genus of this family that is not specialized

in arboreal life. *Dryomys*, a genus closely related to *Microdyromys*, is semi-arboreal. *Myomimus* lives in clusters of trees, on the ground, or in underground nests in Turkmenistan, Uzbekistan, Afghanistan, Iran, Palestine, Türkiye, and Bulgaria, all of which have open environments. On the other hand, *Dryomys* lives in dense mountain forests and bushes in Switzerland, some regions of Germany, Latvia, Türkiye, Iran, Mongolia, and in mountainous highlands of northern Pakistan (Kurtonur and Özkan, 1991; Nowak, 1999; Holden, 2005).

In the Late Miocene, as the paleoecology transformed into open environments and the drought increased in Anatolia, Rodentia families that were adapted to the moist and forested habitats were replaced by those adapted to steppe and savannah habitats. During the Late Miocene in Anatolia, the family Cricetidae started to decrease in density once again, the family Muridae increased the amount of its distribution areas compared to the Middle Miocene, while the families Sciuridae and Spalacidae experienced a relative decline. The family Gerbillidae was seen, and an increase was observed in the ecological dispersal of the family Eomyidae.

To generalize, the Anatolian paleoecology is thought to be dominated by a humid and temperate climate in the Early Miocene, a temperate and semi-tropical climate in the Middle Miocene, and a climate with more open and dry seasonal transitions towards the end of the Late Miocene. Also in the Late Miocene, meadowlands increased, while savannas and grasslands expanded (Kaya and Mayda, 2011; Demirsoy, 1999). Although a relatively warm period was detected in both Pliocene and Pleistocene, the climate was observed to change gradually and to enter a constant trend of cooling, along with increased cooling and expanding dry environments at higher latitudes (Janis, 1989).

If we compare the modern Rodentia fauna with that of the Miocene; the current density ratio of the family Castoridae to the entire order Rodentia is 1%, while it appears to be 3% in the Early Miocene, 2% in the Middle Miocene, and 3% in the Late Miocene. In the current ecology, this family reflects a sporadic presence of aquatic environments. The abundance in Miocene, on the other hand, indicates a higher amount

of aquatic environments than today. If we consider the family Dipodidae; its current density is about 5%, while this average ratio was 3% in Miocene, which may indicate that the Miocene ecology was more forested than today. The current density of the family Gliridae is 12%, which is close to its ratio in the Late Miocene. This close ratio may have resulted from Anatolia's location showing similar ecologies in both periods. The absence of the family Eomyidae today and its emergence in Middle Miocene may be due to the geographic change, and the family members entering Anatolia along with that change. The family's existence in Middle Miocene indicates that the humidity levels and the amount of forested areas in that period were different from the present. The members of Cricetidae preserved their dominance in the current ecology as they did in Miocene. The high diversity of the modern Rodentia fauna shows that Anatolia has a complex ecology. Likewise, we may say that the diversity of Rodentia fauna during Miocene indicates the presence of different habitats in its paleoecology. Regarding the period between the Early Miocene and the end of Middle Miocene, it may be more accurate to say the ecology was tropical and partially forested, rather than saying that it had an entirely closed and moist ecology. In the Late Miocene, the order Rodentia diversified and increased its biodiversity in Anatolia, which had its faunal peak as the rest of the world. Along with the ecological structure changing since the Late Miocene until the present day, we see an increase in the biodiversity of Rodentia species that became adapted to more arid steppes and open environments.

Acknowledgements

References

Agustí, J., Antón, M. 2005. Mammoths, Sabertooths, and Hominids: 65 Million Years of Mammalian Evolution in Europe. Columbia University Press, New York, 328.

Agustí, J., Cabrera, L., Garcés, M., Krijgsman, W., Oms, O., Parés, J. M. 2001. A calibrated mammal scale for the Neogene of Western Europe: state of the art. Earth-Science Reviews 52, 247-260.

Agustí, J., Moya Sola, S. 1990. Neogene-Quaternary mammalian faunas of the Balearics. Atti dei Convegni Lincei 85, 459-468.

Akgün, F., Kayseri, M. S., Akkiraz, M. S. 2007. Palaeoclimatic evolution and vegetational changes during the Late Oligocene–Miocene period in Western and Central Anatolia (Turkey). Palaeogeography, Palaeoclimatology, Palaeoecology 253(1-2), 56-90.

Akkiraz, M. S., Akgün, F., Utescher, T., Bruch, A. A., Mosbrugger, V. 2011. Precipitation gradients during the Miocene in Western and Central Turkey as quantified from pollen data. Palaeogeography, Palaeoclimatology, Palaeoecology 304(3-4), 276-290.

Alçiçek, H. 2010. Stratigraphic correlation of the Neogene basins in southwestern Anatolia: Regional palaeogeographical, palaeoclimatic and tectonic implications. Palaeogeography, Palaeoclimatology, Palaeoecology 291(3-4), 297-318.

Ataabadi, M. M. 2010. The Miocene of western Asia: fossil mammals at the crossroads of faunal provinces and climate regimes. PhD Thesis, University of Helsinki, Helsinki.

Bernor, R. L. 1984. A zoogeographic theater and biochronology play: the time/biofacies phenomena of Eurasian and African Miocene mammal provinces. Paléobiologie continentale 14(2), 121-142.

Bernor, R. L. 1996. The evolution of Western Eurasian Neogene mammal faunas: the 1992 Schloss Reisensberg Workshop concept. Bernor, R. L., Fahlbusch, V., Mittmann, H. W., Rietschel, S. (Ed.). The Evolution of Western Eurasian Neogene Mammal Faunas, 1-6, Columbia University Press, New York, 487.

Bruijn, H. D., Ünay, E., Hordijk, K. 2013. A Review of the Neogene Succession of the Muridae and Dipodidae from Anatolia, with Special Reference to Taxa Known from Asia and/or Europe Fossil Mammals of Asia. Neogene Biostratigraphy and Chronology, Columbia University Press.

Carleton, M. D., Musser, G. G. 2005. Order Rodentia. Wilson, D. E., Reeder, D. M. (Ed.). Mammal Species of the World: A Taxonomic and

Geographic Reference. John Hopkins University Press, Baltimore, 745-2142.

Chaline, J., Mein, P. 1979. Les Rongeurs et l'évolution. Edition Doin, Paris, 235.

Daams, R., A. J. Van der Meulen. 1984. Palaeoenvironmental and palaeoclimatic interpretation of micromammal faunal successions in the Upper Oligocene and Miocene of north central Spain. Palaeobiology Continentale 14, 241-257.

Demirsoy, A. 1999. Genel Türkiye Zoocoğrafyası. Meteksan, Ankara, 603.

Engesser, B., Kälin, D. 2017. *Eomys helveticus* n. sp. and *Eomys schluneggeri* n. sp., two new small eomyids of the Chattian (MP 25/MP 26) subalpine Lower Freshwater Molasse of Switzerland. Fossil Imprint 73(1-2), 213-224.

Erdal, O. 2017. Küçük memeli paleontolojisinin Türkiye'deki Kuvaterner çalışmalarına katkısı: tanımlar ve uygulamalar. Türkiye Jeoloji Bülteni 60, 637-664.

Eronen, J. T., Ataabadi, M. M., Micheels, A., Karme, A., Bernor, R. L., Fortelius, M. 2009. Distribution history and climatic controls of the Late Miocene Pikermian chronofauna. Proceedings of the national Academy of Sciences 106(29), 11867-11871.

Erten, H., Sen, S., Görmüş, M. 2014. Middle and late Miocene Cricetidae (Rodentia, Mammalia) from Denizli Basin (southwestern Turkey) and a new species of *Megacricetodon*. Journal of Paleontology 88(3), 504- 518.

Fortelius, M., Eronen, J. T., Jernvall, J., Liu, L., Pushkina, D., Rinne, J., Zhou, L. 2002. Fossil mammals resolve regional patterns of Eurasian climate change over 20 million years. Evolutionary Ecology Research 4(7), 1005-1016.

Fortelius, M., Eronen, J. T., Kaya, F., Tang, H., Raia, P., Puolamäki, K. 2014. Evolution of Neogene mammals in Eurasia: environmental forcing and biotic interactions. Annual Review of Earth and Planetary Sciences 42, 579-604.

Freudenthal, M. 1997. Paleogene rodent faunas from the province of Teruel (Spain). In Actes du Congrès BiochroM 97, 397-415.

Hartenberger, J. L. 1998. Description de la radiation des Rodentia (Mammalia) du Paléocène Supérieur au Miocène; incidences phylogénétiques. Comptes Rendus de l'Académie des Sciences - Series IIA - Earth and Planetary Science 326(6), 439-444 (in French).

Holden, M. E. 2005. Family Gliridae. Wilson, D. E., Reeder, D. M. (Ed.). Mammal Species of the World: A Taxonomic and Geographic Reference, Johns Hopkins University Press, Baltimore, 2142.

Janis, C. M. 1989. A climatic explanation for patterns of evolutionary diversity in ungulate mammals. Palaeontology 3(32), 463-481.

Jimenez Moreno, G., Popcscu, S. M., Ivanov, D., Suc, J. P. 2007. Neogene flora, vegetation and climatic dynamics in Southeastern Europe and the Northeastern Mediterranean. Williams, M., Haywood, A. M., Gregory, F. J., Schmidt, D. N. (Ed.). Deep-Time Perspectives on Climate Change: Marrying the Signal From Computer Models and Biological Proxies. The Micropalaeontological Society, Geological Society of London, Special Publications 503-507.

Joniak, P., Peláez-Campomanes, P., Mayda, S., Bilgin, M., Halaçlar, K., Van Den Hoek Ostende, L. W. 2019. New faunas of small mammals from old Harami mine (Early Miocene, Anatolia, Turkey). Palaeobiodiversity and Palaeoenvironments 99(4), 673-700.

Kaya, F. 2017. Anadolu'nun Neojen dönem memeli paleobiyocoğrafyası ve paleoekolojisi, Kebikeç. İnsan Bilimleri İçin Kaynak Araştırmaları Dergisi 43, 156-176.

Kaya, F., Kaymakçı, N. 2013. Systematics and dental microwear of the late Miocene Gliridae (Rodentia, Mammalia) from Hayranlı, Anatolia: implications for paleoecology and paleobiodiversity. Palaeontologia Electronica 16(3), 16-3.

Kaya, T., Mayda, S. 2011. 35 Milyon yıldan günümüze Batı Anadolu. Aktüel Arkeoloji Dergisi 19, 110-118.

Kaymakçı, N. 2000. Tectono-stratigraphical evolution of the Cankiri Basin (Central Anatolia, Turkey). PhD Thesis, Utrecht University, The Netherlands, 190.

Kayseri-Özer, M. S. 2017. Cenozoic vegetation and climate change in Anatolia – a study based on the IPR-vegetation analysis. Palaeogeography, Palaeoclimatology, Palaeoecology 467, 37-68.

Kayseri-Özer, M. S., Sözbilir, H., Akgün, F. 2014. Miocene palynoflora of the Kocaçay and Cumaovası basins: a contribute onto the synthesis of Miocene. Turkish Journal of Earth Sciences 23, 233-259.

Koufos, G. D., Kostopoulos, D. S., Theodora, D. 2005. Neogene/Quaternary mammalian migrations in Eastern Mediterranean. Belgian Journal of Zoology 135, 181-190.

Kurtonur, C., Özkan, B. 1991. New records of *Myomimus roachi* (Bate, 1937) from Turkish Thrace (Mammalia: Gliridae). Senckenbergiana Biologica 71, 239-244.

Nargolwalla, M. C. 2009. Eurasian Middle and Late Miocene Hominoid paleobiogeography and the geographic origins of the Homininae. PhD Thesis, Toronto University, Canada.

Nowak, R. M. 1999. Walker's Mammals of the World. John Hopkins University Press, Baltimore, 1625-1635.

Pound, M. J., Haywood, A. M., Salzmann, U., Riding, J. B. 2012. Global vegetation dynamics and latitudinal temperature gradients during the Mid to Late Miocene (15.97-5.33 Ma). Earth Science Reviews 112(1-2), 1–22.

Rögl, F. 1999. Mediterranean and Paratethys. Facts and hypotheses of an Oligocene to Miocene paleogeography (short overview). Geologica carpathica 50(4), 339-349.

Saraç, G. 2003. Türkiye omurgalı fosil yatakları. Maden Tetkik ve Arama Genel Müdürlüğü, Rapor No:10609, Ankara.

Şengör, A. C., Yılmaz, Y. 1981. Tethyan evolution of Turkey: a plate tectonic approach. Tectonophysics 75(3-4), 181-241.

Ünay, E. 1994. Early Miocene rodent faunas from the eastern Mediterranean area. Part IV. The Gliridae. Proceedings of Koninklijke Nederlandse Akademic Van Wetenschappen B97, 445−490.

Ünay, E., De Bruijn, H., Saraç, G. 2003. A preliminary zonation of the continental Neogene of Anatolia based on rodents. Deinsea, 10(1), 539-548.

Utescher, T., Mosbrugger, V., Ashraf, A. R. 2000. Terrestrial climate evolution in Northwest Germany over the last 25 million years. Palaios 15, 430–49.

Van Dam, J. A. 1997. The small mammals from the Upper Miocene of the Teruel-Alfambra region (Spain): paleobiology and paleoclimatic reconstructions. Geologica ultraiectina 156, 1-204.

Van Den Hoek Ostende, L. W. 2001. Insectivore faunas from the lower Miocene of Anatolia. Part 8: stratigraphy, palaeoecology, palaeobiogeography. Scripta Geologica 122, 101–122.

Wu, S., Wu, W., Zhang, F., Ye, J., Ni, X., Sun, J., Organ, C. L. 2012. Molecular and paleontological evidence for a post-Cretaceous origin of rodents. PLoS ONE 7(10), e46445.

Yavuz Işık, N. Saraç, G., Ünay, E., De Bruijn, H. 2011. Palynological analysis of Neogene mammal sites of Turkey - Vegetational and climatic implications. Yerbilimleri 32, 105-120

Yiğit, N., Çolak, E., Sözen, M., Karataş, A. 2006. Rodents of Turkey, Meteksan, Ankara, 80.

Bulletin of the Mineral Research and Exploration

GIS-based analytical hierarchy process, weight of evidence and logistic regression models for the landslide susceptibility predicting in Echorfa Region (northwestern of Algeria)

Zine El Abidine ROUKH[a][*] and Abdelmansour NADJI[a]

[a]Oran 2 Mohamed Ben Ahmed University, Faculty of Earth Science and the Universe, Laboratory of Georesources, Environments and Natural Risks, El-M'Naouar, Oran, 31000, Algeria

Research Article

ABSTRACT

The main objective of this study is destined to combine the Analytical Hierarchy Process (AHP), Weight of Evidence (WOE), Logistic Regression (LR) methods and geographic information system (GIS) to predict landslide susceptibility of the Echorfa region (northwestern of Algeria). Nine factors such as slope, aspect, lithology, distance to faults, lineaments density, distance to the streams, precipitations, land use and altitude are included in landslide susceptibility evaluation process. A detailed landslide inventory map was established by satellite images and filed surveys. Three landslide susceptibility maps are established using the different statistical models. Five landslide susceptibility categories are generated by the GSI classification nil, low, moderate, high and very high susceptibility. The performance of the different models in landslide susceptibility is calculated based in the area under curve of the Receiver Operating Characteristic (ROC) which give a satisfactory result. The results showed that the WOE is more performance than the two other techniques. The produced landslide susceptibility maps provide important spatial information about landslide prone area, where the constructed map's content will help the decision makers in land use planning.

1. Introduction

Landslides are geodynamic phenomena that occur in many part of the world and often the most severe on the earth surface. They cause changes to the landscape and can destroy building, structures and sometimes it reaches catastrophic levels and cause a death. These slope movements occur during earthquake, and /or during intense rainy periods with prolonged precipitation and the combined action of various geomorphological factors (Roukh, 2020).

This problem is currently one of the major concerns of the scientists responsible for the geological risks management. Nowadays, landslide susceptibility mapping become a consistent method used in landslide prone area zoning. This technique is based in the application of quantitative, semi quantitative and qualitative models to calculate spatial distribution of the landslide susceptibility index (LSI). Several guidelines are developed in the term of landslide susceptibility, hazard and risk zoning for land use planning destined to local, state and national government officials, land use planners, geotechnical professionals and project managers (Flentje et al., 2007; Fell et al., 2008)

In the practice, several models based on geographic information system are used in the

landslide susceptibility mapping. The bivariate statistical methods is largely used for evaluate landslide susceptibility versus authors (Süzen and Doyuran, 2004; Mohammady et al., 2012; Zine El Abidine and Abdelmansour, 2019). The multivariate statistical models are also integrated in several works related to landslide susceptibility zoning, (Baeza and Corominas, 2001; Santacana et al., 2003; Ercanoğlu et al., 2004), machine learning ensemble (Micheletti et al., 2014; Pham et al., 2017; Chen et al., 2018). Artificial neural network (ANN) models are applied in calculation weights for landslide susceptibility (Lee et al., 2004; Yılmaz, 2009; Zare et al., 2013). Others researches are compared several models to selected the adopted landslide susceptibility model (Xu et al., 2012; Bourenane et al., 2016; Chen et al., 2017; Merghadi et al., 2018; Mahdadi et al., 2018; Karim et al., 2019).

The favorable geological, geomorphological and climatic conditions make certain regions located in northern part of Algeria prone to landslides phenomena; these phenomena cause annual few human losses and considerable damage in term of basic infrastructure such as highways, private and state property (Guemache et al., 2011; Djerbal et al., 2017; Achour et al., 2017; Hallal et al., 2019) . Attempts have been made to the landslide susceptibility mapping (Bourenane et al., 2015; Hadji et al., 2017; Dahoua et al., 2017; El Mekki et al., 2017; Mahdadi et al., 2018; Zine El Abidine and Abdelmansour, 2019; Karim et al., 2019; Roukh, 2020). However, these studies are insufficient in relation to the large area of this part of the country.

The objective of this study is to establish a comprehensive methodology based on the exploitation of multi - source data in order to the landslide susceptibility mapping of the Echorfa sector sited in Oran region (north western of Algeria). Therefore, an integrated analytical approach consists of: i) the establishment of database contains the landslide causative factors and landslide inventory, ii) the estimation of the weighting of each parameter by integration of the AHP, WOE and LR methods coupled with GIS functionalities, iii) the evaluation and the mapping of the landslide susceptibility and iv) validation and interpretation of the obtained results.

2. General Characteristic of the Study Area

The study area is part of the Beni Chougrane Mountains sited in northwestern of Algeria (Figure 1a). It's located at the intersection of eight municipalities: Sig, Zahana, Echorfa, El Gaada, Ogaz (Wilaya of Mascara), Makedra (W. Sidi Bel Abbes) and Oued Tlelat and Tafraoui municipality (W. Oran) (Figure 1b). This zone covers an area of 408 km² and a total perimeter of 89.761 km². It is located exactly between the longitude (727595.762, 760285.913) and latitude (3923356.604, 3937796.033 according to (WGS_1984_UTM_Zone 30N) coordinate projection system.

The Bas Chelif basin is part of the western Algerian sublittoral Neogene basins. The significant Neogene sedimentation covers the western part of this intra-mountainous basin, of which the Miocene covers the vast majority of the deposits. It is surrounded by the northern foothills of the Dahra and the Arzew mountains, and by the mountains of Tessala and Beni Chougrane and the secondary-age Ouarsenis massif to the south, which provides it with material through erosion. The study area is part of the Lower Chelif Cenozoic sedimentary complex. According to the geological map (Figure 2), three regions are distinct: i) a mountainous area corresponds to an anterogenic period occupying the southwestern half of the map, ii) a plateau area visible on the northwestern part of the map occupied by the plain of M'Léta. From the litho - stratigraphic point of view: i) The secondary represented by shales and marl of Cretaceous age constitutes the substratum of a Cenozoic cover. This substratum is visible in the valley of Oued Mekedra and in the depression west of the lauriers roses, these are black - grey marly limestones intercalated with hard fine - paste limestone banks, ii) the Cenozoic is mainly located in the southern part of the map, and it is represented by the Neogene formations. The Miocene: it is typically transgressive deposits on secondary terrain such as the following formations; Middle Miocene: a sequence of detritus, siltstones, sandstones and gray argillite conglomerates (200 m thick). The Upper Miocene: the base levels of the Miocene series are generally detrital and represented by silts and red conglomerates resting on a thin lithological formation of cinerite, these formations are particularly well developed in Djebel Touakes,
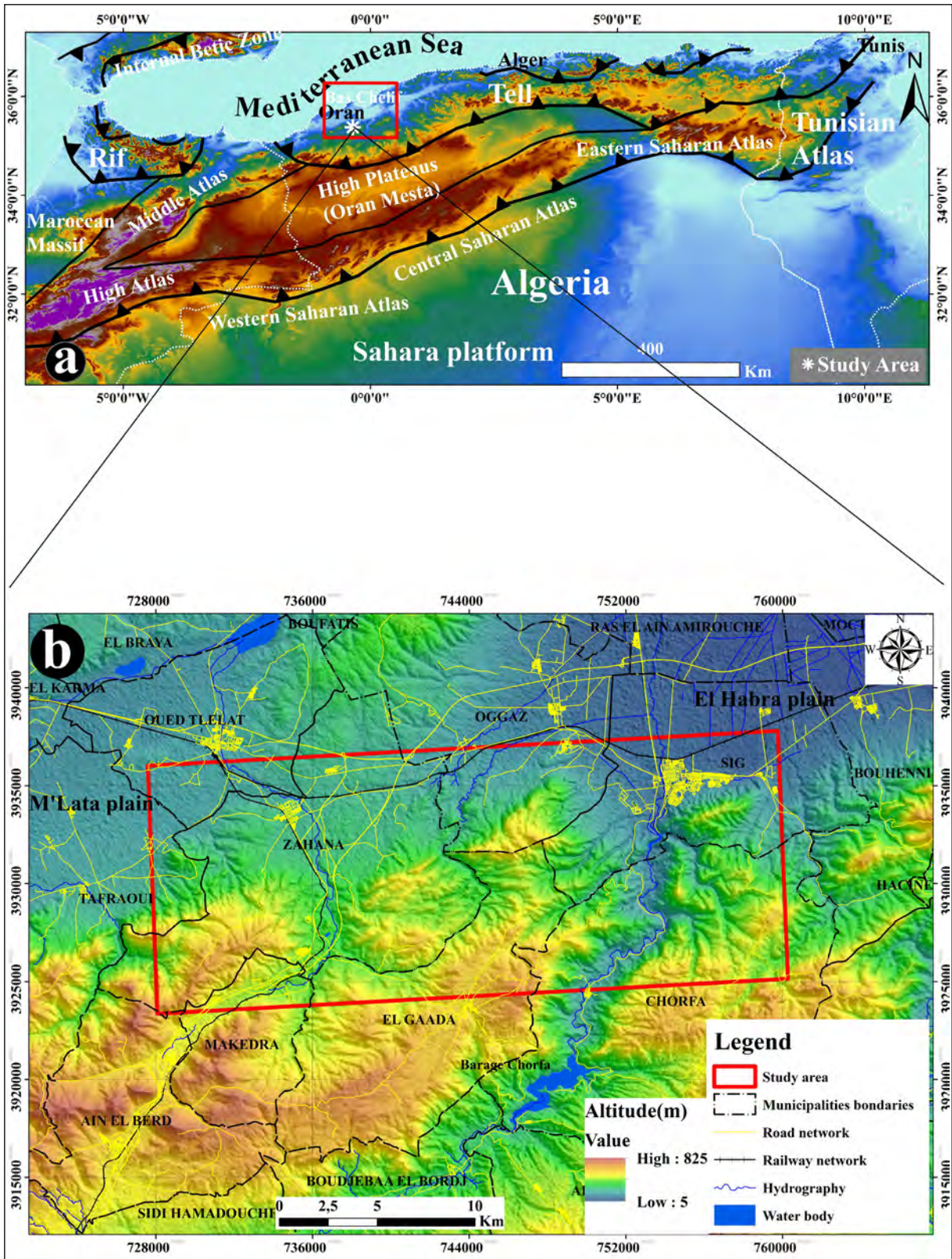
Figure 1- a) Geographic position of the study area versus the Chelif basin northwestern of Algeria, b) geographic location versus municipalities division of the NW of Algeria.
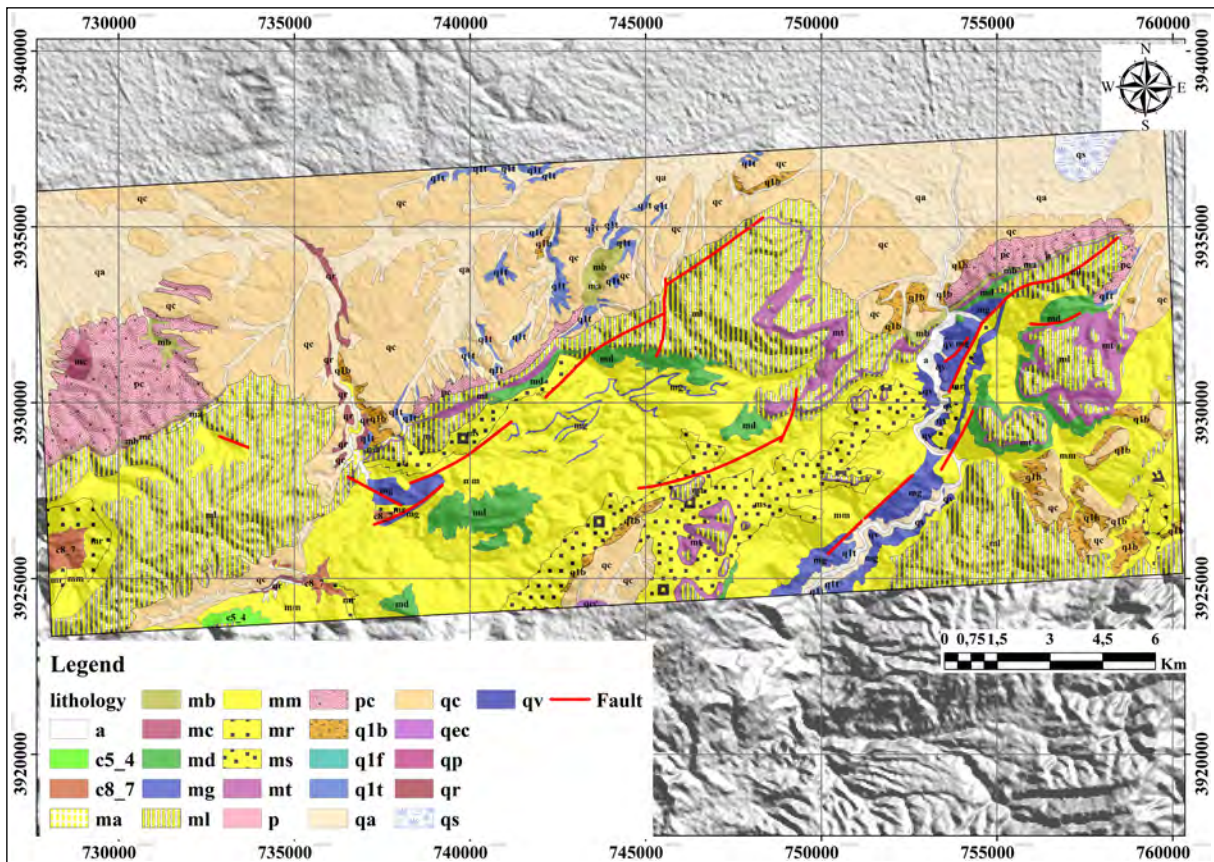
Figure 2- Geological map of the study area (digitized by 1/50000 scale geological map of the St Denis-Du- Sig, Sheet N°182, B10 C7).

above which plastic blue marls have been found containing a microfauna characteristic of the upper Miocene and finally the series ends with gypsum and gypsum - marly, iii) The Pliocene: discordant with previous formations appears: Lower / Middle Pliocene (Calabrien): represented by reddish sandstones well cemented down to tender limestones and sandy marls of which the latter are part of marine formations. Upper Pliocene: it is a heterogeneous alternation of marl, sand silts and conglomerates (continental formations); iv) the Quaternary: the Quaternary formations occupies all northwest and northeast of the map, they are represented by: Early Quaternary corresponding to a calcareous carapace hiding the subjacent terrain. Recent Quaternary represented by non - rudoinous argilo - limoneous alluvial named recent alluvial. The current forms the major bed rivers.

The study area is defined by four morphological units: i) a mountainous area in the south of the plain represented by the Tessala Mountains and those of Beni Chougrane; ii) a depression zone in the northwest represented by the M'Leta plain; iii) another depression zone located in the NE represented by the El Habra Plain, iv) an area of the plateaus located in the center represented by the Zahana and Sig plateaus.

The study area is located in the intersection of three sub-watersheds (Figure 3), the Sebkha of Oran watershed code 04 - 04, El Habra watershed code 11 - 06 and the Echorfa watershed code 11 - 04. The hydrographic network characterized by a high density where the main rivers in this area that of Oued El Mebtouh which feeds the Mactaa swamps and the second river that of Oued Tlelat whose runoff reaches at Dayat Oum Ghezal.

The climate of the study area compared to the country's climate is characterized by a contrasting climate, a Mediterranean climate on the coast and desert climate in the south. The Mascara region is located in the Oran high plains; addressed as intermediate, hot and dry in summer, cold and rainy in winter. The average monthly precipitation during
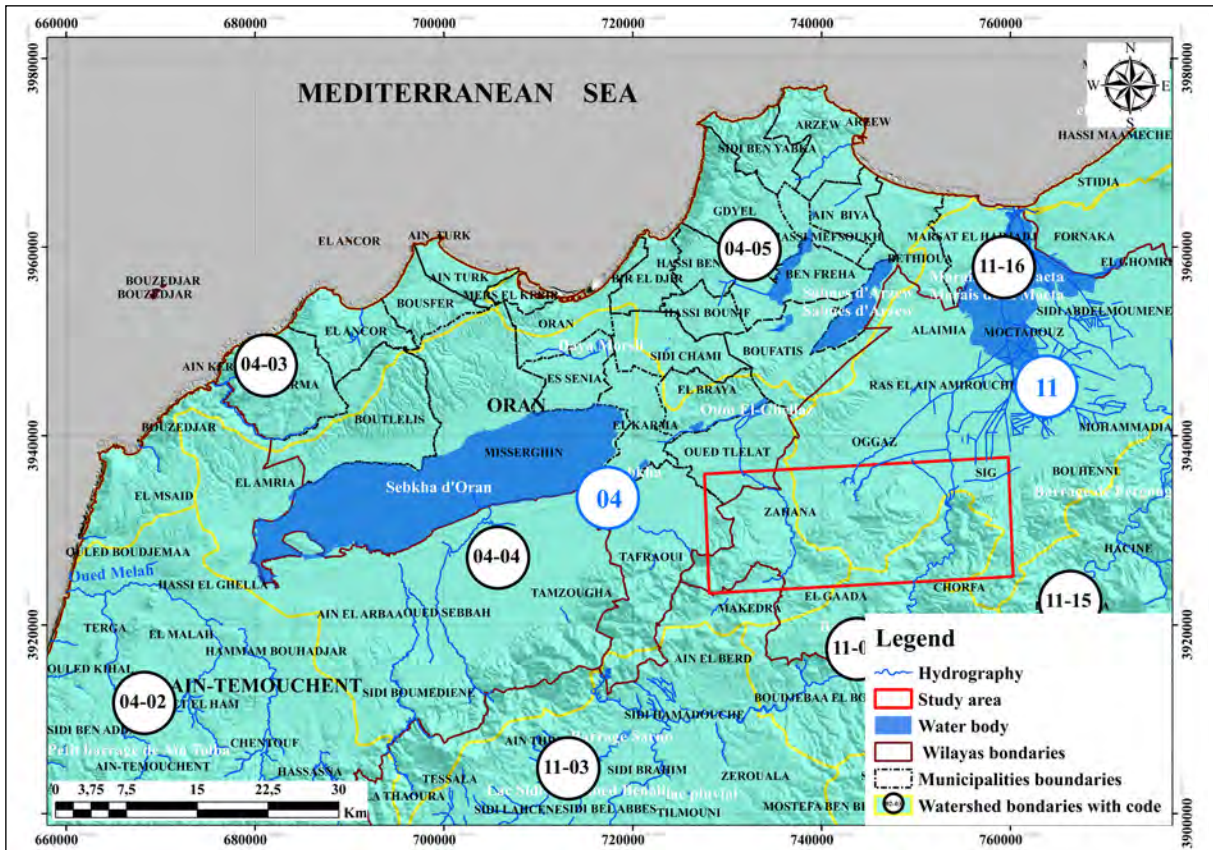
Figure 3- Hydrographic characteristics of the study area (watershed boundaries digitized by the 1/500.000 scale hydro - climatogical network and water quality monitoring of the north Algerian).

the reference period (1982 - 2012) of the Echorfa Dam station (ANRH), was taken as reference. The average monthly precipitation study has shown that the rainy period begins in the October and split ends in April. During this period, it was noted maximum precipitation appears in November (56.0 mm) and for the minimum in July (1.4 mm). The average annual precipitation study allows us to note that: the rainiest year is recorded 514.9 mm; however, the driest year with a rainfall of 153.0 mm. The temperature together with precipitation is a major parameter that defines the climate of region; it is also one of the essential terms in the definition of the flow deficit. For our study area, the Mascara station is the only one where we were able to have a measurements series of this parameter during 2003 and 2012. Maximum temperatures in summer according to the exploitation of the ONM data, a maximum of 27.98 °C in July and the cold winter season with a minimum of 9.04 °C in January. The climatic regime of the study area is semi - arid.

The study area is part of the Algeria's Tellian Atlas belt belonging to the limit of the Africa - Eurasia tectonic plate which forms a deformed plug about 100 km wide. The North western of Algeria has an experienced several earthquakes and is among the 09/10/1790 Oran earthquake with an macro intensity of I = X (Bouhadad and Laouami, 2002; Marinas and Salord, 1991). The 1819 Mascara events with an intensity of I = X and that of 1851 with an macro intensity of I = VIII (Guessoum et al., 2018). Recently, significant earthquakes are recorded at the Echorfa surroundings region, the Hassine (Mascara) earthquake of August 1994 with a magnitude of moment Mw = 5.7 (Benouar et al., 1994; Ayadi et al., 2002) and those of Ain Temouchent (December 1999, Mw = 5.7) and Oran (Juan 2008, Mw = 5.5) (Belayadi et al., 2017). According to Thomas (1985), the study area is located in the Beni Chougrane zone characterized by NE - SW reverse fault, where in the El Habra and M'Lata plains the direction of the reverse faults is NW - SE. Therefore, the study area characterized by significant

seismicity due to several active faults (Figure 4). The spatiotemporal distribution of these events plays a very important role in slope movements triggering or reactivating.

3. Landslide Susceptibility Mapping

In this work, an adopted methodology is established for the purpose of the landslide prone areas zoning. This approach consists firstly to establishing a set of thematic maps (data collection of the landslide causative factors and landslide inventory map). Secondly, an assessment of the landslide susceptibility index using AHP, WOE and LR models and GIS environment. Thirdly, mapping the LS by the classification of the GSI and validating of the obtained results. The following flowchart represents the methodology used in this work (Figure 5).

3.1. Landslide Inventory Mapping

Landslide inventory map present the essential parameter in the landslide susceptibility mapping (Fell et al., 2008; Corominas et al., 2014). In this study, an inventory map is established by the interpretation of the Google Earth satellite images as well as the field surveys and the positioning via Global Positioning System (GPS) area (Figure 6). It is mentioned that no landslide inventory maps are established in the study area. The objective of this inventory is to identify, localized and describe the main slope movements that occurred in the study area as well as to build and to calculate the performance of landslide susceptibility models.

3.1.1. Example of Some Remarkable Landslide

The expertise in - situ present a fundamental step in
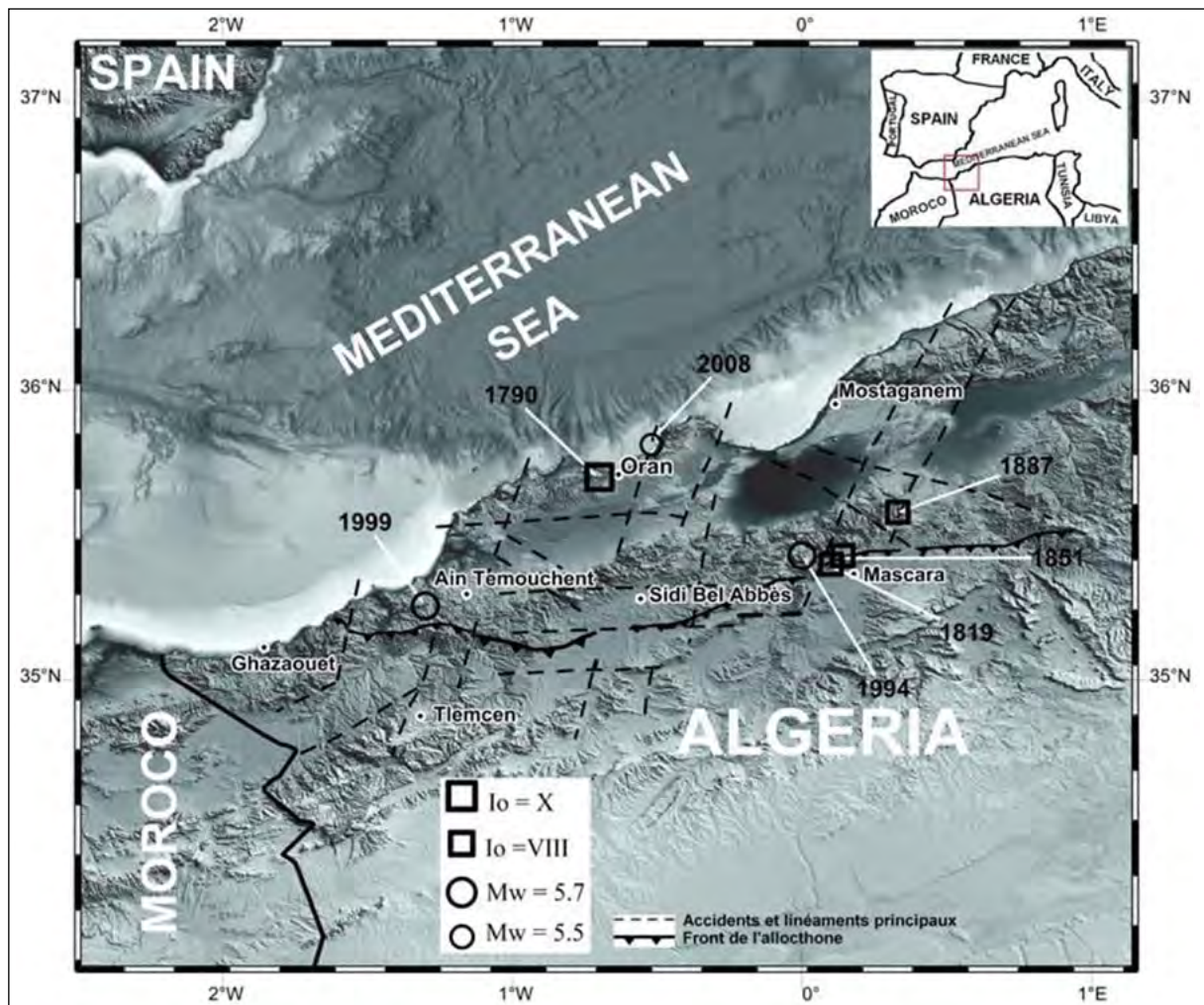
Figure 4- Main tectonic structure (Thomas, 1985) and relevant earthquakes that took place in Norwest Algeria (Belayadi et al., 2017).
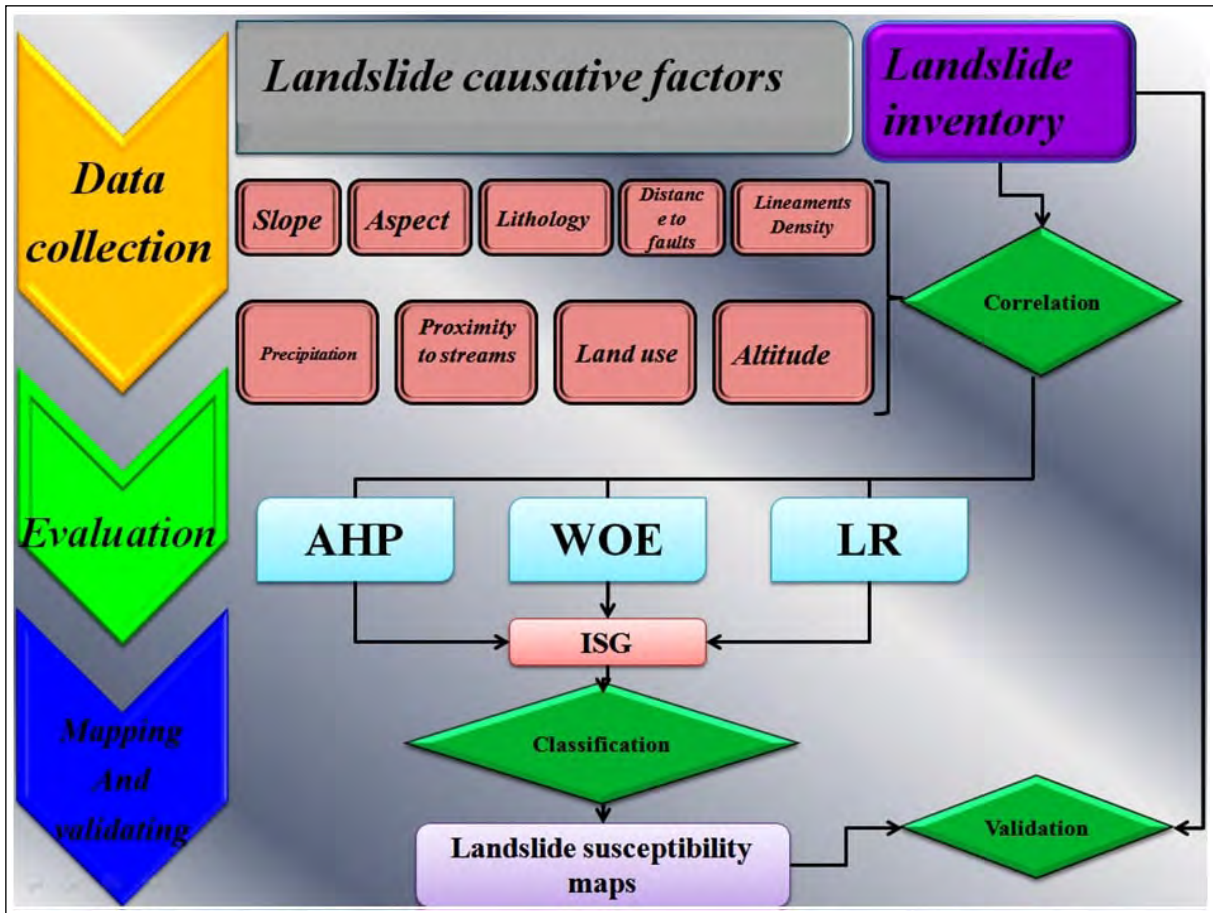
Figure 5- Methodology flowchart for the process work.

the landslide inventory, of which the geologist expert is able to identify, localized measure the affected site and to verify the landslides inventoried by the interpreting of the aerial photos, satellite images, archive, press or the previous documents. In this work, the extensive field surveys allowed us to identify several landslides (Figure 7).

Some examples are discussed in the following paragraph:

A rotational landslide is located using the Google Earth satellite images (Figure 7a) it occupies an area of 8.2 Ha. Among the instability index observed are those deviations of the river trajectory and remarkable degradation in the topography.

A second rotational landside is identified from the Google Earth images (Figure 7b); it's characterized by main and minor scrap, a sliding surface and an ablation zone. The area of this landslide is approximately 9 Ha.

A third translational landslide type is identified via the GPS during the field surveys (Figure 7c).

A rotational landslide is identified near the road (towards the Echorfa town) whose the observed coordinates are (X_UTM = 752259.7, Y_UTM = 3931563.93) (Figure 7d).

A toppling affected the limestone formations are observed near El Gaada town. The coordinates of the site are (X_UTM = 751309.02, Y_UTM = 3930215.64) (Figure 7e).

An old complex landslide affected the marl-limestone formation is identified from the Google Earth images and verified on the field (Figure 7f). The area of the landslide is 6.4 Ha.

A rock fall of limestone formations are observed next to the road leading from Sig to Echorfa town (Figure 7g). The observe coordinats of the slope
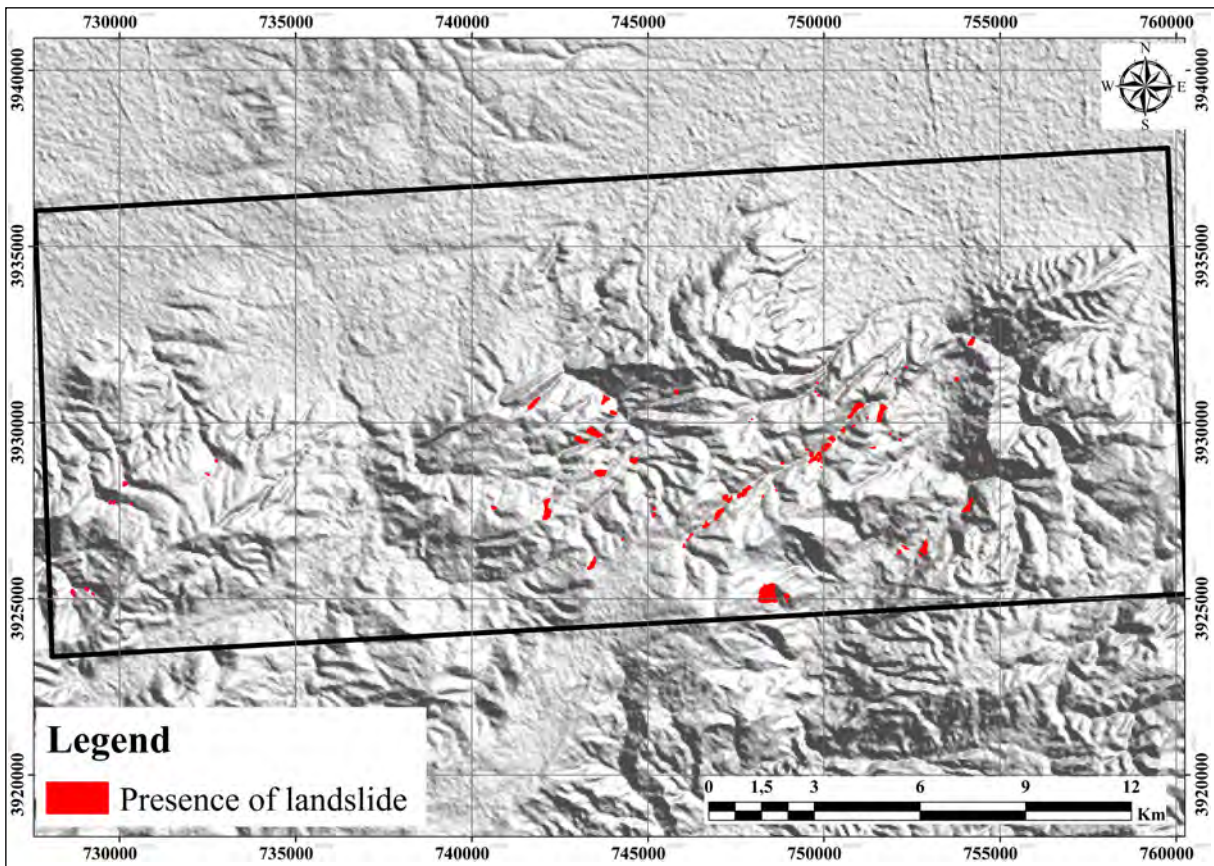
Figure 6- Landslide inventory map.

movement are (X_UTM = 752312.21, Y_UTM = 3931540.77).

According to Cruden and Varne (1996) classification, the slope movements concerned by this inventory are exclusively those which relate to the following phenomena: toppling, landslide (rotational translational and complex) and rock falls. In this research, landslides are used to construct landslide susceptibility maps which sampling in 70% of the total for models building and 30% for validation.

3.2. The Landslide Causative Factors

The processes behind landslides are very complex and diverse; geology, the relief and the slope exposure are more or less constant fundamental parameters over long period. Several factors can have a destabilizing influence on a slope such as slope, slope aspect, stratigraphy, distance to faults, the lineaments density, the altitude levels, and distance from the streams and other triggering factors related to the precipitation and the groundwater circulation as well as earthquakes which trigger or reactivate ground movements.

In this study nine parameters are integrated into a GIS environment such as, slope, aspect, lithology, lineaments density, and distance to faults, precipitation and distance to the streams, land use and altitude in order to assess the landslide susceptibility index.

3.2.1. Slope Degree

Presents a fundamental parameter in the landslide susceptibility evaluation, the variation of the slope directly influence in the landslide process, in this context the slope map (Figure 5a) is derived from the digital elevation model (DEM) of the study area and it reclassified into five classes (0 - 10°), (10 - 20°), (20 - 30°), (30 - 40°) and > 40° using the ArcGIS software modules (Figure 8a).

3.2.2. Slope Aspect

This factors influences in the slope instability by the soil concentration moisture changes according to
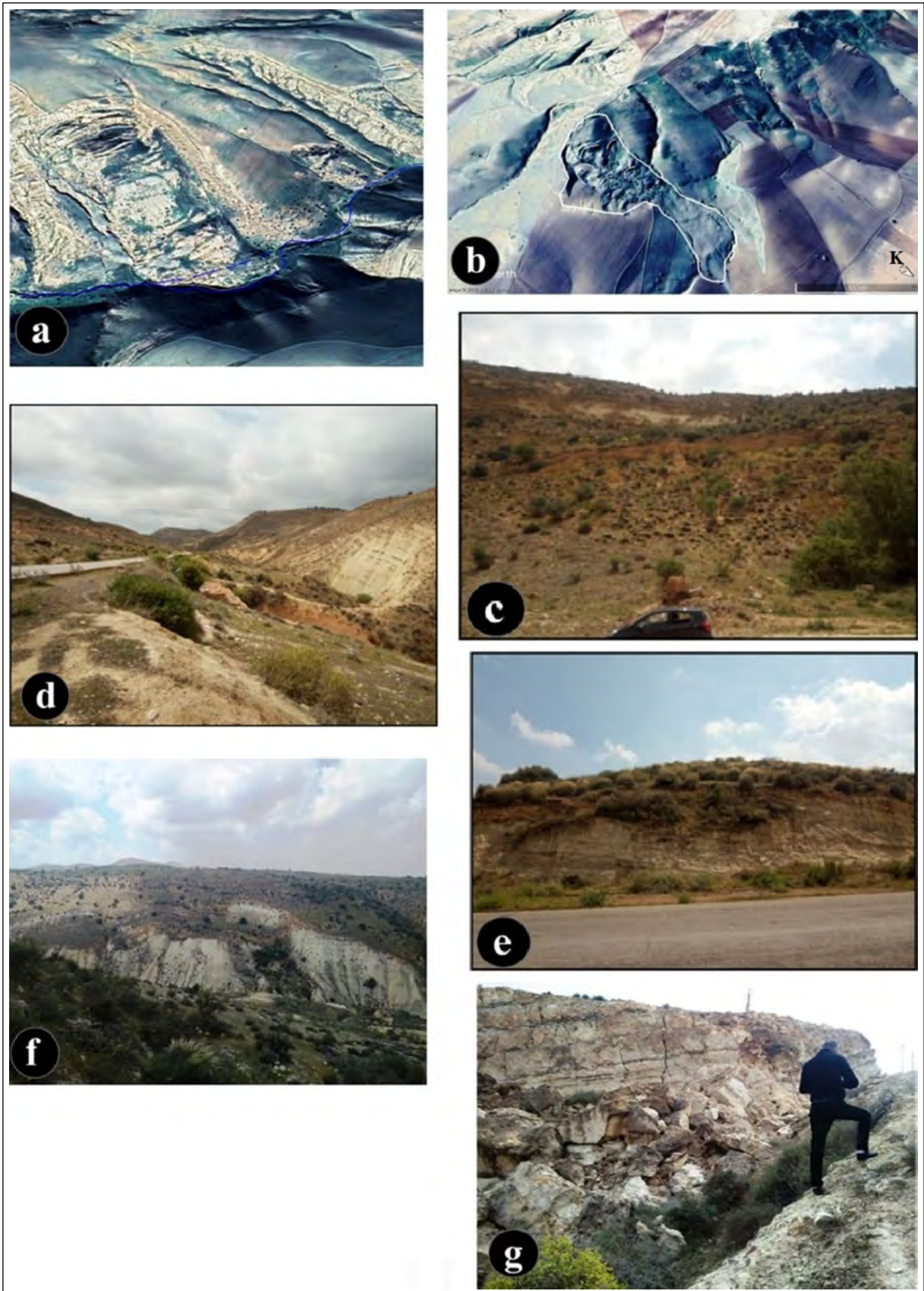
Figure 7- Example of some remarkable landslide inventoried in the study area; a) Active rotational landslide, b) rotational landslide identified by Google Earth, c) translational landslide, d) rotational landslide, e) topples, f) complex landslide and g) rock fall.

the slope exposure in relation to precipitation and wind in one hand, in other hand by the fractures orientation. The slope aspect direction measured from 0 to 360°. Using DEM and GIS allowed extracting the slope direction value, which classified into eight directions (Flat, N, NE, E, SE, S, SW and NW) (Figure 8b).

3.2.3. Lithology

The type of the terrain is one of the most causative parameters for landslide process; the mechanical characteristics of the soil represent the basic data imposed by their type and their history. The significant lithological variation, in the same geological formation can be influenced on the slope movements' distribution. The lithological map of the study area is established by the digitization of the lithological formations of the Saint Denis de sig 1:50,000 scale geological map. According to the lithological characteristics (Table 1), the lithological map is established by the classification of the outcropped lithological formations into five units (Figure 8c).

3.2.4. Distance To Faults

Areas located proximity to faults zones are heavily fractured and present zone of weakness, which provide a geological condition for landslides to occur. In this study, the Euclidian distance was applied to generate the fault buffer zone map and then reclassified into six classes with 500 m of interval < 500, 500-1000, 1000-1500, 1500-2000, 2000-2500 and > 2500 m (Figure 8d).

3.2.5. Lineaments Density

The density map represents the number of lineaments by the area (number / km²). The lineament density indicates the rock fracturing degree. In this study, the lineaments are extracted by the treatment of the Hillshade images produced by the DEM. As a result, the lineament density varies from 0 and 6, their classification into five classes allowed us to produce the lineament density map of the study area (Figure 8e).

3.2.6. Precipitation

Represent all the meteoric water which fall on the earth' surface in liquid or solid form, the precipitation volume participates in the landslides triggering.

Areas with heavy rainfall are more susceptible to the landslides. The average annual precipitation map of the study area is generated from the North Algeria precipitation map (ANRH, 2007). They classified into four zones 250, 300, 350, 400 mm / year (Figure 8f).

3.2.7. Distance to Streams

The proximity to the streams increases the degree of the susceptibility due to erosion caused by the water current in the foot of the talus. The distance to the streams map realized by the buffer zone of the hydrographic network which is classified into five classes (0 - 100, 100 - 200, 200 - 300, 300 - 400, 400 – 500 and >500m) (Figure 8g).

Table 1- Description of the lithological formations outcropped in the study area.

Symbol	Age	Type of formation	Classes
a	Actual	Major rivers bed formation	Class 5
qa		Clay-silt alluvium	Class 1
qec		Limestone	Class 1
qp		Accumulation glacis	Class 4
qr		Level of rivers rebufied terrace	Class 4
qs	Quaternary	El Habra plain halipeds	Class 1
qv		Oued Sig polygenic glacis	Class 5
q1b		Diversifying crusts	Class 5
q1f		Scree slopes	Class 4
q1t		Limestone shell	Class 1
qc		Limestone shell	Class 1
p	Pliocene	Sandstone and marine sandy marl	Class 5
pc		Sandy marl and red conglomerate	Class 5
ma		Gypsum and gypsum marl	Class 4
mb		Fine sand	Class 5
mc		Limestone (gypsum series)	Class 1
md		Marly-limestone	Class 4
mg		Sand, sandstone and conglomerate	Class 4
ml	Miocene	Lithothamniac limestone	Class 2
mm		Blue marl	Class 4
mr		Silt and red conglomerate	Class 4
ms		Sandy marls	Class 5
mt		Tripoli and tripoli marl	Class 4
c5_4	Cretaceous	Marly-limestone	Class 3
c8_7		Marly-limestone	Class 3
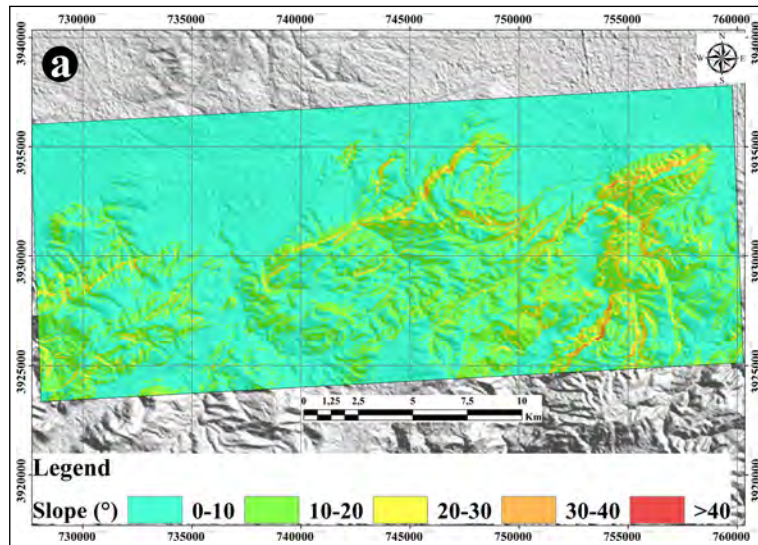
Figure 8- Landslide conditioning factors included in the landslide susceptibility process; a) slope degree, b) aspect, c) lithology, d) distance to faults, e) lineaments density, f) precipitation, g) proximity to the streams, h) land use, i) altitude.
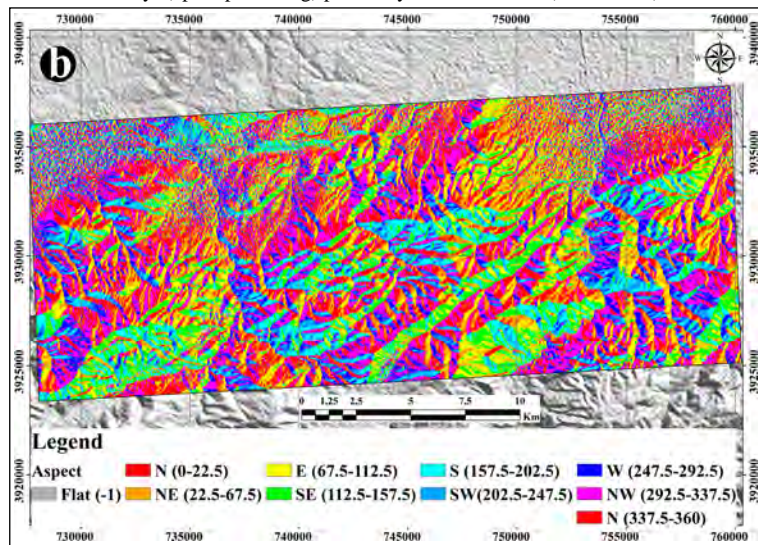
Figure 8- (Continue).
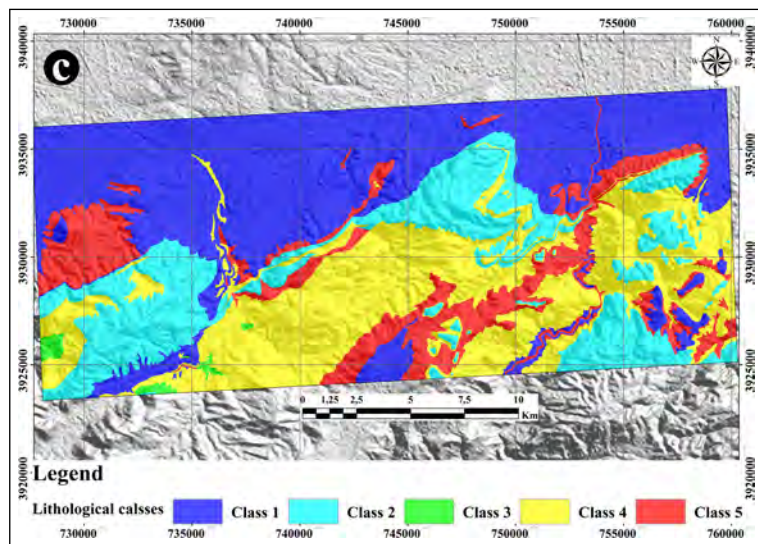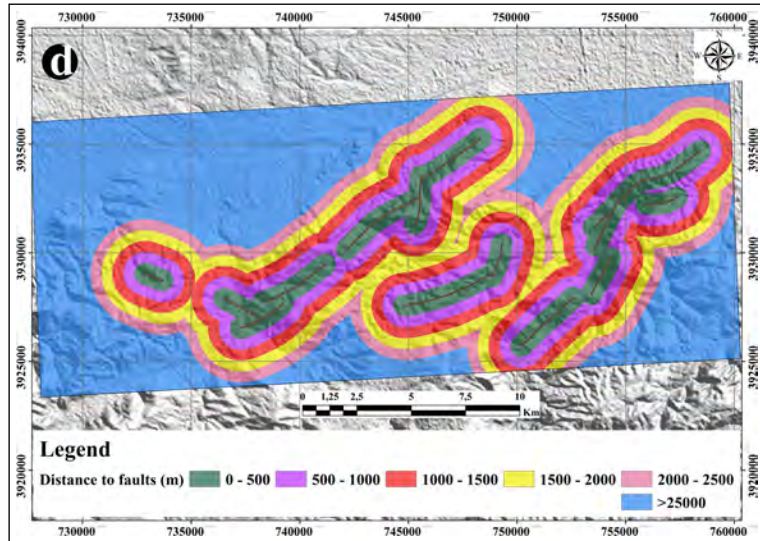
Figure 8- (Continue).
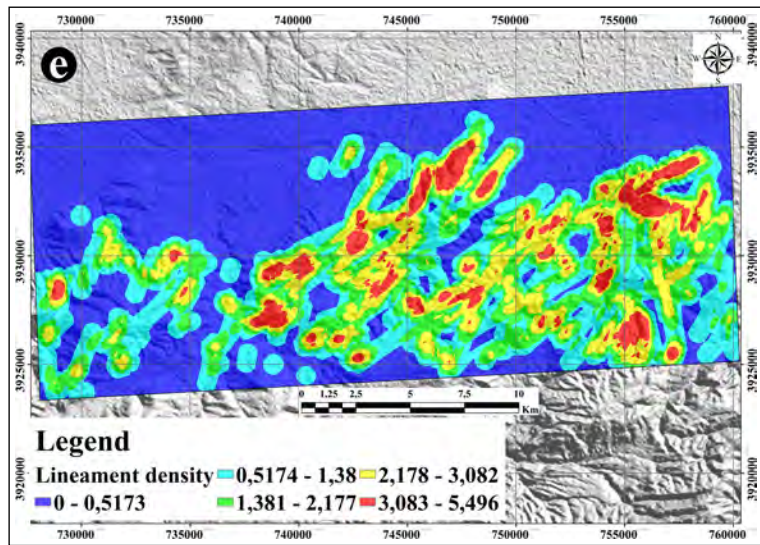
Figure 8- (Continue).
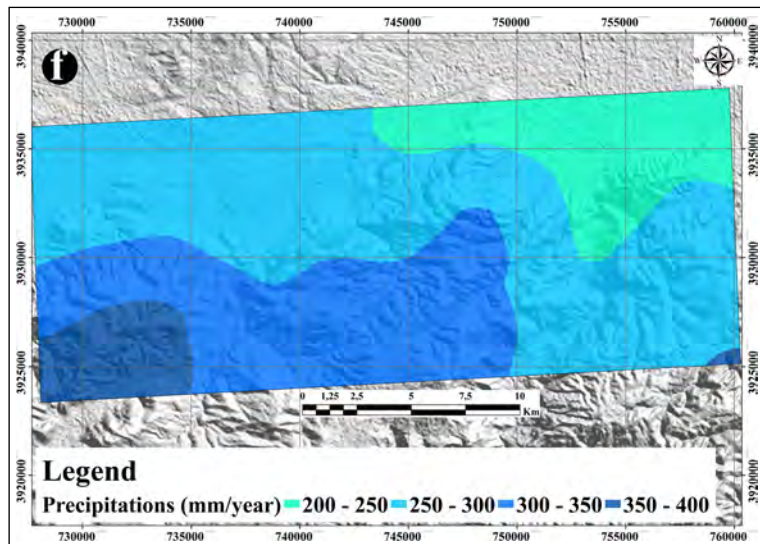
Figure 8- (Continue).
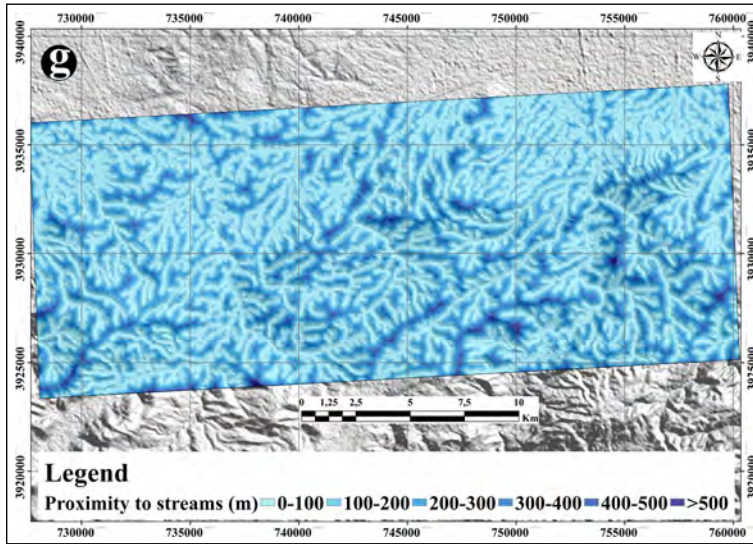
Figure 8- (Continue).
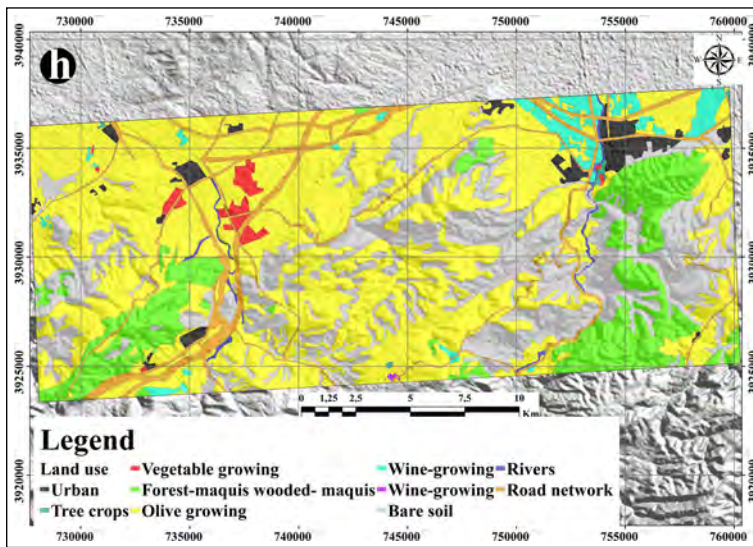
Figure 8- (Continue).
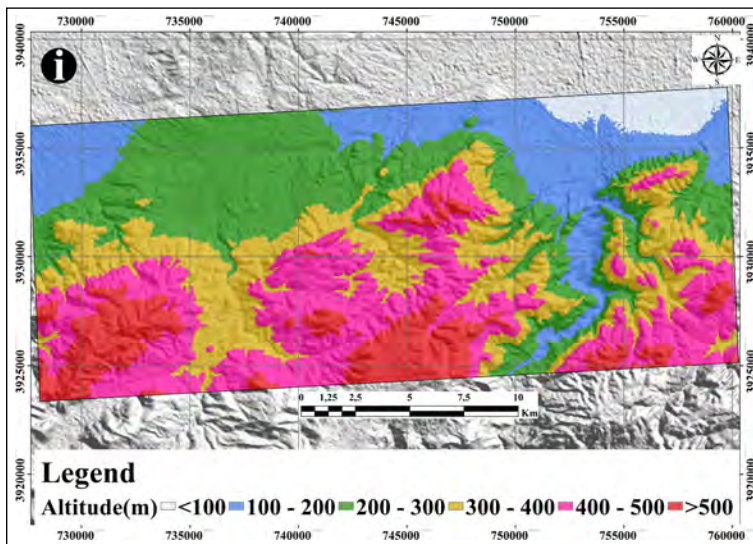
Figure 8- (Continue).

Figure 8- (Continue).

3.2.8. Land Use

The land use type plays a very important role in the slope stability, where the forested area are the least prone to landslide compared to region with no vegetation. In this context, the land use map is established by the digitalization of three 1/25000 scale land use maps (Beneder, 2011), the produced map contain eleven classes (Figure 8h).

3.2.9. Altitude

The altitude is the vertical elevation of a place from the sea level. It is a very important factor which effect land sliding by the fact that difference of several parameters between the different altitude levels as temperature, precipitation and the intensity of the gravity which varies according to the altitude. The altitude map of the study area generated by the classification of the DEM value into six classes: <100, 100-200, 200-300, 300,400, 400-500 and >500 (Figure 8i).

3.3. Analytical Hierarchy Process Method

The AHP method is a multicriteria decision making approach. It is based in complex calculation using matrix algebra formulation. It was developed by Saaty, 1980. This model has been used in several domains, such concerning: The planning of the combined transportations, the rationing of the energy, the risks management, the comparative analysis of the logistic operations, flood hazard and landslide susceptibility.

The AHP model consists to apply the following steps: i) establishment decision making problem into hierarchy, ii) establishment of comparative judgment, iii) synthesis of priorities and estimating of consistency.

In literature, several studies were based on AHP model to evaluate the weight of the landslide conditioning factors but not for the different classes of the landslide conditioning factors such as the of work of (Barredo et al., 2000; Akgün and Türk, 2010; Mondal and Maiti, 2012). Other researchers used AHP model to calculate the weight of landslide conditioning factors and their different classes, (Intarawichian and Dasananda, 2010; Yalcin et al., 2011; Phukon et al., 2012; Chen et al., 2016). In this research, the AHP technique was used to calculate the weights for each landslide conditioning factors.

In AHP model, to compute the weight of each factor a pair - wise comparison matrix should be established; this is done by comparing each factor against others factors using a value between 1 and 9 or 1/2 and 1/9 according to the effectiveness degree (Table 2).

These judgments are confirmed using consistency ratio, is defined as CR (Equation 1) Saaty, 1977.

$$CR = \frac{CI}{RI} \tag{1}$$

Where RI is the average of the resulting consistency index depending on the order of the matrix given by Saaty, 1980 and CI is the consistency index expressed as:

$$CI = \frac{\lambda_{max} - n}{(n-1)} \tag{2}$$

Where λ max is the largest or principal eigenvalue of the matrix and that can be easily calculated from the matrix and n is the order of the matrix. If CR is greater than 0.1, the comparison matrix is inconsistent and should be revised

Table 2- Scale of preference between two parameters in AHP (Saaty, 1977).

Scales	Degree of preferences	Explanation
1	Equally	Two activities contribute equally to the objective.
3	Moderately	Experience and judgment slightly to moderately favor one activity over another.
5	Strongly	Experience and judgment strongly or essentially favor one activity over another.
7	Very strongly	An activity is strongly favored over another and its dominance is showed in practice.
9	Extremely	The evidence of favoring one activity over another is of the highest degree possible of an affirmation.
2, 4, 6, 8	Intermediate values	Used to represent compromises between the preferences in weights 1, 3, 5, 7 and 9.
Reciprocals	Opposites	Used for inverse comparison.

Table 3 indicates that for the present case the CR value is less than 0.1, which demonstrate that the preferences used to elaborate the comparison matrix, are reasonable. The weight values of each the conditioning factors are defined and calculated by the establishment of the AHP model (Table 3).

Finally, the LSM was constructed using AHP model by the following equation:

$$LSI = \sum_{i=1}^{n} W_j wij \quad (3)$$

Where Wj is the weight value of each conditioning factors , (wij) is the weight value of class i of causative factor j, and n is the number of the conditioning factors included in the landslide susceptibility process.

For the weighting value of each class (wij) we attribute of each class a rank varies from 1 to 9 according to the susceptibility degree, Table 4 summarized the calculation results in this study.

3.4. Weight of Evidence Method

The WOE method is one of the most bivariate Bayesian statistical methods used in earth sciences, this method was applied in several domains such as identification of mineral potential (Bonham-Carter, 1989), landslide susceptibility (Regmi et al., 2010) and flood susceptibility (Tehrany et al., 2014; Khosravi et al., 2016). Weight of each landslide conditioning factors can be estimated by combining each conditioning factor with landslide inventory

(presence or absence of landslide, following Equation 4, 5and 6 (Bonham-Carter, 1994)):

$$W^+ = \ln \frac{P(\frac{B}{L})}{P(\frac{B}{\bar{L}})} \quad (4)$$

$$W^- = \ln \frac{P(\frac{\bar{B}}{L})}{P(\frac{\bar{B}}{\bar{L}})} \quad (5)$$

Where, P is the probability, B and B are respectively the presence or absence of potential landslide predictive factor, L and L are respectively the presence or absence of landslide. W^+ and W^- are the weight of presence or absence of landslide.

$$EC = W^+ - W^- \quad (6)$$

Where, WC is the weight contrast; indicate the correlation between landslide occurrence and landslide conditioning factors.

Positive and negative values of the weight contrast WC, which mean that the highest value, indicate a great correlation between predictable variable and landslide and vice versa.

The intersection between different causative factors and landslide inventory map (training data) allowed us to extract a database contain landslide area in each class, stable area in each class, total of landslide area and total of stable area. Their statistical analysis allowed estimates W^+, W^- and WC using Equation 4, 5 and 6, respectively (Table 5). Landslide susceptibility index were assigned by integrate equation in map algebra function in ArcGIS:

Table 3- The pair - wise comparison matrix, factor weights and consistency ratio, slope [1], aspect [2], lithology [3], distance to faults [4], lineaments density [5], precipitation [6], proximity to streams [7], land use [8], altitude [9].

Parameter	[1]	[2]	[3]	[4]	[15	[6]	[7]	[8]	[9]	Weight
[1]	1	4	2	3	5	3	2	6	7	27.662
[2]	1/4	1	1/3	1/2	1	1/2	1/3	2	4	06.574
[3]	1/2	3	1	2	3	2	1	4	3	16.228
[4]	1/3	2	1/2	1	2	1	1/2	2	3	09.532
[5]	0,2	1	1/3	1/2	1	1/2	1/3	2	3	06.104
[6]	1/3	2	1/2	1	2	1	1/2	2	4	09.851
[7]	1/2	3	1	2	3	2	1	4	5	16.867
[8]	1/6	1/2	1/4	1/2	1/2	1/2	1/4	1	2	4.237
[9]	1/7	1/4	1/3	1/3	1/3	1/4	0,2	1/2	1	2.943
CR = 0.018										$\sum$(W) = 100

Table 4- Rank, and normalized Rank of each class, AHP weighting of each parameter and general weighting of each class.

Parameters	Class	Rank	Normalized rank (Wi)	W (AHP)	Weighting
Slope (°)	<10	1	0.040	27.662	1.106
	10-20	3	0.120	27.662	3.319
	20-30	5	0.200	27.662	5.532
	30-40	7	0.280	27.662	7.745
	>40	9	0.360	27.662	9.958
Aspect	Flat	1	0.025	6.574	0.164
	N	5	0.128	6.574	0.841
	NE	3	0.076	6.574	0.500
	E	2	0.051	6.574	0.335
	SE	2	0.051	6.574	0.335
	S	5	0.128	6.574	0.841
	SW	6	0.153	6.574	1.006
	W	7	0.179	6.574	1.177
	NW	8	0.205	6.574	1.348
Lithology	Class 1	2	0.076	16.228	1.233
	Class 2	3	0.115	16.228	1.866
	Class 3	5	0.192	16.228	3.116
	Class 4	7	0.269	16.228	4.365
	Class 5	9	0.346	16.228	5.615
Distance to faults (m)	0-500	9	0.333	9.532	3.177
	500-1000	7	0.259	9.532	2.471
	1000-1500	5	0.185	9.532	1.765
	1500-2000	3	0.111	9.532	1.059
	2000-2500	2	0.074	9.532	0.706
	>2500	1	0.037	9.532	0.353
Lineaments density (n/km²)	0 – 0.51	1	0.047	6.104	0.287
	0.51 – 1.38	2	0.095	6.104	0.580
	1.38 – 2.17	4	0.190	6.104	1.160
	2.17 – 3.08	6	0.285	6.104	1.740
	3.08 –5.49	8	0.380	6.104	2.320
Precipitation (mm/year)	<250	1	0.090	9.851	0.887
	250-300	2	0.181	9.851	1.783
	300-350	3	0.272	9.851	2.679
	>350	5	0.454	9.851	4.472
Distance to streams (m)	<100	8	0.333	16.867	5.617
	100 – 200	6	0.250	16.867	4.217
	200 – 300	4	0.166	16.867	2.800
	300 – 400	3	0.125	16.867	2.108
	400 – 500	2	0.083	16.867	1.400
	>500	1	0.041	16.867	0.692
Land use	Urban	4	0.108	4.237	0.458
	Tree crops	1	0.027	4.237	0.114
	Vegetable growing	3	0.081	4.237	0.343
	Forest-maquis wooded- maquis	1	0.027	4.237	0.114
	Big culture	4	0.108	4.237	0.458
	Olive growing	1	0.027	4.237	0.114
	Wine-growing	2	0.054	4.237	0.229
	Bare soil	8	0.216	4.237	0.915
	Rivers	7	0.189	4.237	0.801
	Road network	6	0.162	4.237	0.686
Altitude (m)	<100	1	0.035	2.943	0.103
	100 – 200	2	0.071	2.943	0.209
	200 – 300	4	0.142	2.943	0.418
	300 – 400	6	0.214	2.943	0.630
	400 – 500	7	0.250	2.943	0.736
	>500	8	0.285	2.943	0.839

Table 5- Statistical analysis of the WOE parameters and weight of each conditioning factor.

Parameter	Class	Pixels in the classes	Landslide pixels classes	W+	W-	C
Slope (°)	0 – 10	1759734	2075	-0.9979085	0.8379506	-1.8358591
	10-20	706082	4877	0.77546774	-0.56545143	1.34091918
	20 – 30	132384	1103	0.96436012	-0.09014597	1.05450609
	30 - 40	13289	245	1.76884112	-0.0248005	1.79364162
	> 40	436	38	3.3948006	-0.00441496	3.39921556
Aspect	Plat	59886	6	-3.46458842	0.02254948	-3.48713791
	N	448266	1468	0.02559732	-0.00538576	0.03098308
	NE	365636	813	-0.36263845	0.04837752	-0.41101597
	E	303316	1153	0.1752127	-0.02546451	0.20067721
	SE	286127	1726	0.63927771	-0.11626756	0.75554527
	S	218225	686	-0.01545604	0.00139737	-0.0168534
	SW	200455	408	-1.50799814	0.06288188	-1.57088002
	W	261235	1936	-0.7164873	0.05538602	-0.77187332
	NW	468779	142	0.25847951	-0.0666118	0.32509131
Lithology	Class 1	998012	0	0	0	0
	Class 2	504972	332	-1.57795563	0.1746274	-1.75258303
	Class 3	15538	0	0	0	0
	Class 4	751227	6541	1.01363738	-1.21505342	2.2286908
	Class 5	342175	1426	0.27223717	-0.04826394	0.32050111
Distance to Fault (m)	0-500	282420	921	-2.3402519	0.51924938	-2.85950130
	500-1000	303698	1967	0.30942590	-0.3997504	0.34940095
	1000-1500	330899	1936	0.70227021	-0.1532889	0.85555911
	1500-2000	320918	2061	0.60850033	-0.1291375	0.73763786
	2000-2500	255011	1108	0.71079527	-0.1458925	0.85668780
	>25000	1118978	345	-0.9965183	-0.0026253	-0.95789279
Lineaments density (km/km²)	0 - 0.51	1185867	223	-2.83480325	0.58057402	-3.41537727
	0.51 - 1.38	514074	2063	0.22963675	-0.06527754	0.29491429
	1.38 - 2.17	427344	2832	0.54645869	-0.23699526	0.78345395
	2.17 - 3.08	340810	2265	0.73673936	-0.1776738	0.91441316
	3.08 - 5.49	143829	955	0.73581456	-0.06520433	0.8010189
Distance to Streams (m)	0 - 100	1187425	5344	0.34476434	-0.42279188	0.76755622
	100 - 200	827835	2281	-0.14761911	-0.14103651	-0.00658259
	200 - 300	426302	521	-0.96210874	0.11404971	-1.07615845
	300 - 400	141918	189	-0.87610342	0.03304562	-0.90914905
	400- 500	25403	3	-3.30007054	0.00944381	-3.30951435
Precipitation (mm/year)	250	409260	255	-1.63639749	0.1398383	-1.77623579
	300	1311790	169	-0.29222467	0.22800147	-0.52022613
	350	711342	4785	0.74890377	-0.5364303	1.28533409
	400	179532	3129	-1.22344662	0.05090179	-1.27434841
Land use	Urban	58744	0	0	0	0
	Tree crops	2891	0	0	0	0
	Vegetable growing	713	0	0	0	0
	Forest-maquis wooded- maquis	309301	441	-0.80650041	0.07176416	-0.87826456
	Big culture	1336674	2122	-0.69965686	0.42439734	-1.1240542
	Olive growing	66130	0	0	0	0
	Wine-growing	25103	0	0	0	0
	Bare soil	632357	5493	1.00684737	-0.80267428	1.80952165
	Rivers	13515	0	0	0	0
	Road network	167799	282	-0.64290247	-0.03440622	-0.60849624
Altitude(m)	< 100	81259	0	0	0	0
	100 - 200	408742	474	-1.01479799	0.11206231	-1.1268603
	200 - 300	687331	1993	-0.0960651	0.41126357	-0.50732867
	300 - 400	544439	2612	0.40886173	-0.0629098	0.4717716
	400 - 500	608334	2924	0.41099391	-0.1672183	0.57821221
	>500	281820	334	-0.99234467	0.0734715	-1.06581618

LSI_{woe}= Wc*Slope + Wc*Aspect + Wc*Lithology + Wc*Distance to faults + Wc* Lineaments density + Wc* Precipitaton + Wc*Distance to streams + Wc*Land use + Wc* Altitude   (7)

3.5. The Logistic Regression Method

Logistic regression is one of the most widely used statistical methods in geosciences. The method is based on the relationships established between the values of certain quantitative or qualitative variables and the presence or absence of a certain phenomenon. For landslides, it allows to determine the relative contributions of the different causes, also benefiting from the graphical expression of the prediction model. One of the most important advantages of this method is that the independent variables can have both continuous and discrete values, occurring in any combination of the two types. Also, compared to other statistical methods, it does not require a normal distribution of values. The probability (P) of landslide occurrence, calculated for each elementary surface unit, can take values between 0 and 1, according to the Equation 8:

$$P(y) = \frac{1}{1+e^{-y}}$$ (8)

Where, P(y) varies from 0 to 1, Y is expressed by the following linear equation

$$Y = b_o + b_1 x_1 + b_2 x_2 + ... + b_n x_n$$ (9)

Where, Y is the dependent variable presented by the absence (0) or presence (1) of a phenomenon, b_0 is the intercept, b_1, b_2, ..., b_n are the partial regression coefficients, x_1, x_2, ..., x_n are the independent variables (predisposing factors).

In this study, a data base contains the raster landslide and the conditioning factors maps created by the combine module in ArcGIS software and converted in dbf format. For the analysis process, the correlation between the landslide distribution and each causative factor are calculated using Xlstat package, in order to produce a LSM. For each conditioning factor class, the ratio between the landslide percentage and the percentage of the same class is used to estimate the

weight of each class (Table 6). A quantitative value from 0 to 1 is given as weight factor for each class.

For this study, the logistic regression model established is given in following equation:

P(y) = 1 / (1 + exp (- (-8,18464 - 0,12674 * Fault + 0,14324 * Precipitation + 0,25625 * Lineament Density -0,69206 * Distance to streams + 0,23182 * Land use + 0,22328 * Slope + 0,52545 * Lithology -0,00363 * Aspect + 0,13794 * Altitude)))   (10)

4. Results and Discution

The obtained pair wise comparison matrix (Table 4) showed the most influenced parameters to the landslide is the slope with a weighting of 0.228 as well as the lithology and the distance to the streams. The least influenced parameters for the landslide occurrence are the land use and the Altitude.

The outcome of this analysis indicates that the LSI increase with the slope degree increasing. Aspect analysis indicates that north, south, western and north western slope directions of the reliefs are the most susceptible by the landslide. The major rivers bed formation, clay-silt alluvium, accumulation glacis, the river Sig polygenic glacis, sandy marls, fine sand, sandy marl and red conglomerate, sandstone and marine sandy marl, screed slopes and diversifying crusts present the most susceptible outcropping formations to landslides. Areas located near faulting zone present the most susceptible zone to the landslides. The outcropped lithological formations characterized by high lineaments density represent the weakness areas which are the most landslide prone areas. The landslides are directly related to the precipitations, in this area the landslide susceptibility increase with the precipitation increasing, the most prone areas that are characterized by heavy rainfall. We mentioned that areas located near the streams characterized by the high and very high susceptibility where the important flow velocity erodes the lower part of the talus. The areas that are characterized by high density of vegetation like forest lands, scrublands provide hydrological and mechanical effects that typically stabilize slopes witch considered as the less landslide susceptible areas, in this area the barren land, the rivers zone and road network areas considered as the most landslide prone areas where the slope stability effects are absents. In

Table 6- Statistical analysis of the LR model and weight of each conditioning factor.

Parameters	Class	Pixels in classes	Landslide pixels classes	% of total area	% of landslide area	Factor weight	LR	LR weighting
Slope (°)	<10	1759734	2075	67.373068	24.886064	0.42546648	0.22383	0.095232161
	10-20	706082	4877	27.033012	58.491245	1		0.22383
	20-30	132384	1103	5.068446	13.228592	0.22616363		0.050622204
	30-40	13289	245	0.508782	02.938355	0.0502358		0.011244279
	>40	436	38	0.016693	0.455745	0.00779168		0.001744011
Aspect	Flat	59886	6	2.292792	0.07196	0.00309917	-0.00363	-0.00001125
	N	448266	1468	17.162285	17.606141	0.75826446		-0.0027525
	NE	365636	813	13.998717	9.75054	0.41993802		-0.00152438
	E	303316	1153	11.612738	13.828256	0.59555785		-0.00216188
	SE	286127	1726	10.954641	20.700408	0.89152893		-0.00323625
	S	218225	686	8.354949	8.227393	0.35433884		-0.00128625
	SW	200455	142	7.674608	1.703046	0.07334711		-0.00026625
	W	261235	408	10.001627	4.89326	0.2107438		-0.000765
	NW	468779	1936	17.947644	23.218997	1		-0.00363
Lithology	Class 1	998012	0	38.209826	0	0	0.52545	0
	Class 2	504972	332	19.333327	3.98177	0.05075677		0.026670142
	Class 3	15538	0	0.594887	0	0		0
	Class 4	751227	6541	28.761431	78.448069	1		0.52545
	Class 5	342175	1460	13.100491	17.510194	0.22320746		0.11728436
Distance to faults (m)	0-500	1118633	921	42.827914	11.045814	0.44687045	-0.12674	-0.05663636
	500-1000	253903	1967	9.720915	23.590789	0.95439107		-0.12095952
	1000-1500	318857	1936	12.20774	23.218997	0.93934983		-0.1190532
	1500-2000	328963	2061	12.594657	24.718158	1		-0.12674
	2000-2500	301731	1108	11.552055	13.288558	0.53760311		-0.06813582
	>25000	281499	345	10.777453	4.137683	0.16739447		-0.02121557
Lineaments density (n/km²)	0 – 0.51	1185867	223	45.402031	2.674502	0.07874294	0.25625	0.020177878
	0.51 – 1.38	514074	2063	19.681806	24.742144	0.72846045		0.186667991
	1.38 – 2.17	427344	2832	16.361266	33.96498	1		0.25625
	2.17 – 3.08	340810	2265	13.048231	27.164788	0.79978814		0.20494571
	3.08 –5.49	143829	955	5.506628	11.453586	0.33721751		0.086411988
Precipitation (mm/year)	<250	409260	255	15.668903	3.058287	0.05329154	0.14324	0.00763348
	250-300	179532	169	6.873551	2.026865	0.0353187		0.005059051
	300-350	711342	4785	27.234396	57.387863	1		0.14324
	>350	1311790	3129	50.223111	37.526985	0.6539185		0.093667285
Distance to streams (m)	<100	1187425	5344	45.461681	64.092108	1	-0.69206	-0.69206
	100 – 200	827835	2281	31.69444	27.35668	0.42683383		-0.29539462
	200 – 300	426302	521	16.321372	6.248501	0.09749251		-0.06747067
	300 – 400	141918	189	5.433464	2.266731	0.03536677		-0.02447592
	400 – 500	25403	3	0.972578	0.03598	0.00056138		-0.00038851
	>500	3041	0	0.116428	0	0		0
Land use	Urban	66130	0	2.531849	0	0	0.23182	0
	Tree crops	25103	0	0.961092	0	0		0
	Vegetable growing	2891	0	0.110685	0	0		0
	Forest-maquis wooded- maquis	309301	441	11.841879	5.289038	0.080284		0.018611436
	Big culture	1336674	2122	51.175819	25.449748	2.58859566		0.600088247
	Olive growing	13515	0	0.517434	0	0		0
	Wine-growing	713	0	0.027298	0	0		0
	Bare soil	632357	5493	24.210381	65.879108	1		0.23182
	Rivers	167799	282	6.424342	3.382106	0.05133807		0.011901191
	Road network	58744	0	2.249069	0	0		0
Altitude (m)	<100	81259	0	3.111077	0	0	0.13794	0
	100 – 200	408742	474	15.649071	5.684817	0.1621067		0.022360999
	200 – 300	687331	1994	26.315112	23.914608	0.68194254		0.094067155
	300 – 400	544439	2612	20.844358	31.326457	0.89329685		0.123221368
	400 – 500	608334	2924	23.290638	35.068362	1		0.13794
	>500	281820	334	10.789743	4.005757	0.11422709		0.015756484

this study, the susceptibility to the landslide is increase with the altitude of the reliefs increasing.

The application of the AHP method shows that the global landslide susceptibility index varies between 5.647 and 31.332, their classification into five landslide susceptibility classes using natural break (jenks) shows that 17.87% of the total area characterized by null susceptibility to the landslide, 29.82% of the study area characterized by low susceptibility, 21.24% of the total area characterized by a moderate susceptibility, 20.69% characterized by high susceptibility, the rest of the study area (10.38%) characterized by very high landslide susceptibility (Figure 9a, b).

According to the obtained LSM (Figure 9), the most landslide susceptibility areas are located in the east and the center part of the study area, whereas the northern part of the map characterized by low and null landslide susceptibility.

For the weight of evidence model, the resulting weight contrast, are shown in (Table 5), the interpretation of this results demonstrate than the more susceptible classes correspond to slope greater than 40°, SE and NW facing slopes, very susceptible lithological formation (class 4), (1000 - 1500) class fault proximity field, rocks characterized by high density of lineament, area with high precipitation (300 - 400), area near streams, barren land, and altitude range between 400 and 500 meters. The values less or equal to zero of C indicate that this class does not affect the distribution of landslide in the Echorfa region.

The final LSI of study area for WOE approach range between -19.1243 and 10.7522. The LSM of the Echorfa region was established by classification of LSI values into five levels (Figure 10a) using natural break method: Null with (27.97%) of total area, Low with 19.08%, Moderate with 20.63%, the High level 20.47%, and 11.85% falls in very high level (Figure 10b).
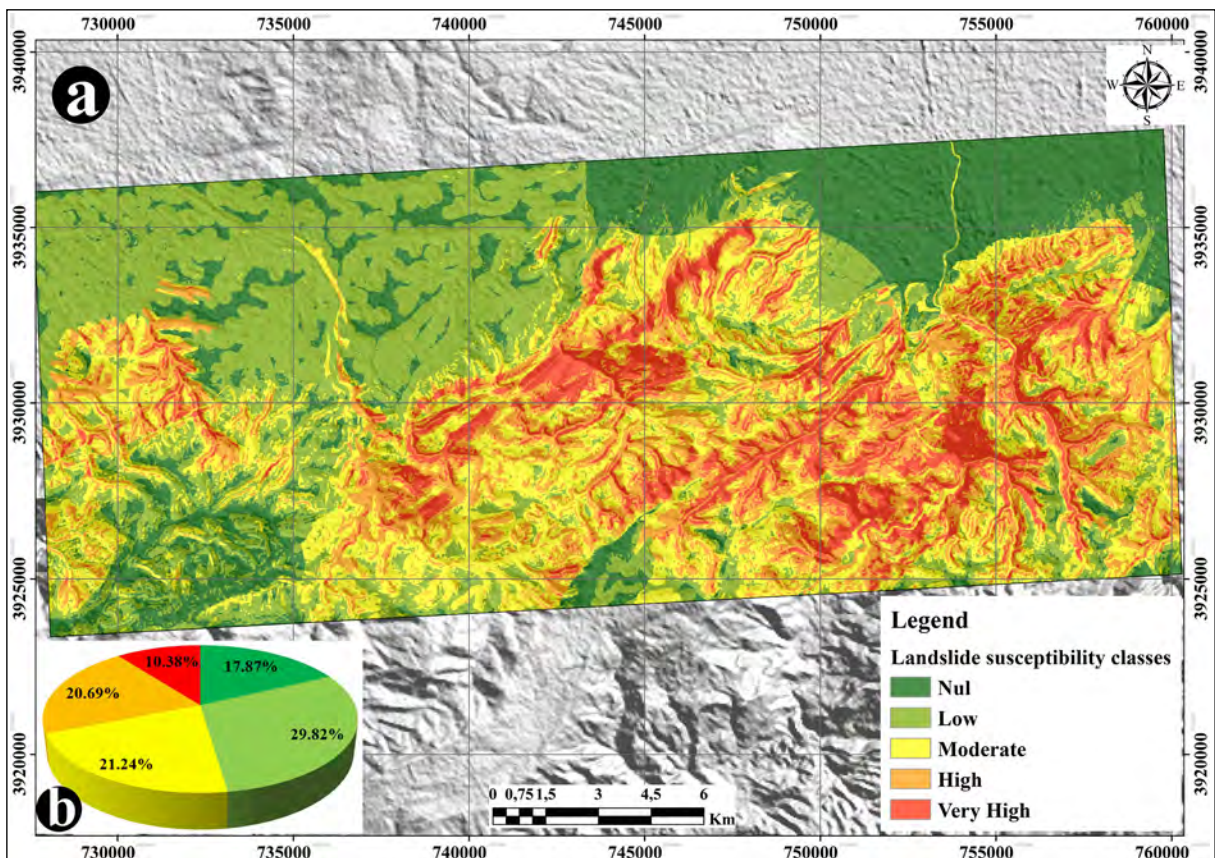
Figure 9- a) The AHP -landslide susceptibility map, b) distribution pie - chart of the landslide susceptibility classes.
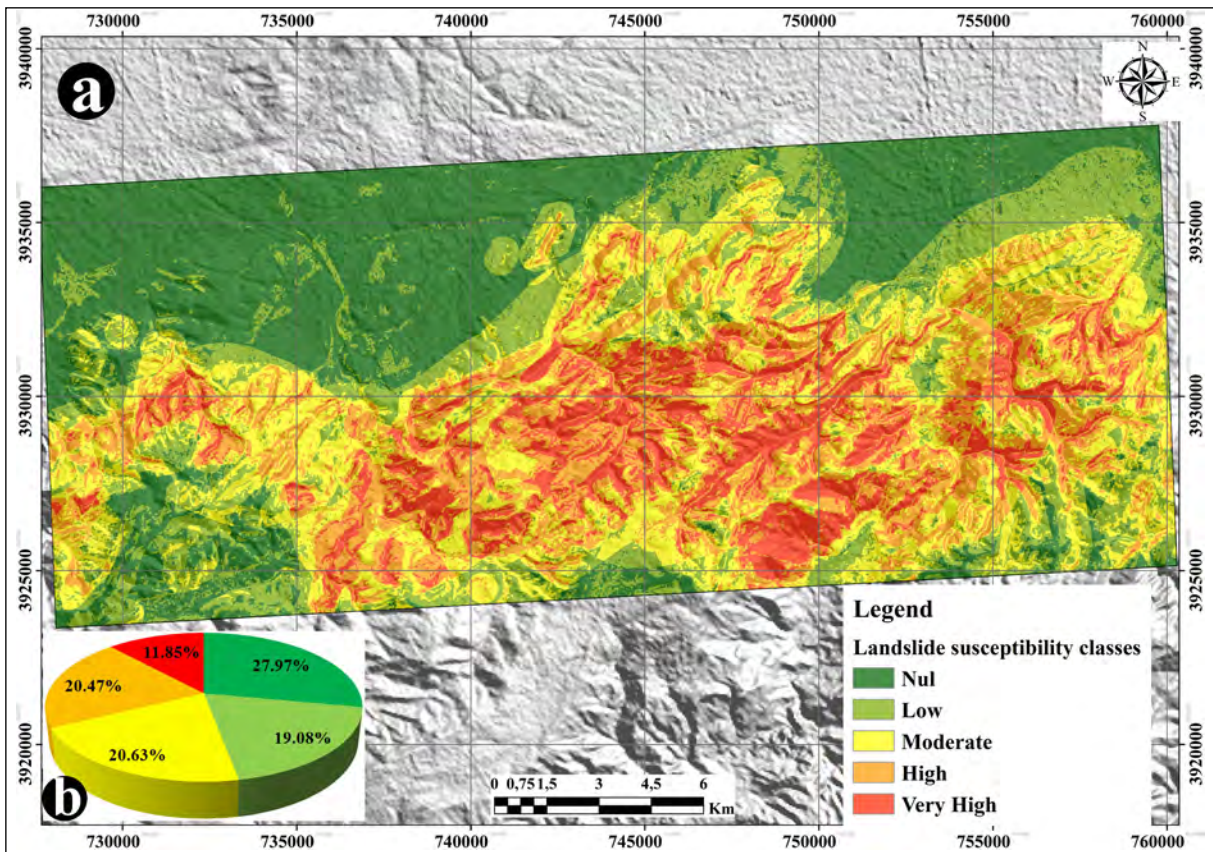
Figure 10–a) The WOE - landslide susceptibility map, b) distribution pie - chart of the landslide susceptibility classes.

For the LR model and according to the Table 6 and Equation 10, slope, lithology, lineaments density, precipitation, land use and altitude give positive values which mean that these factors contribute to occurrence of the landslide. On the other hand, Aspect, distance to fault and proximity to streams has a negative role in landslides occurrence. By using Equation 10, the landslide occurrence probability is estimated. The produced LSM using LR model indicate that 37.64 % of the total area characterized by no susceptibility, 30.52% presented by low susceptibility, 19.15% characterized by moderate susceptibility, 8.75% of the total area falls in high susceptibility and the rest of the study area 3.93% represented by very high susceptibility (Figure 11).

5. Validation

The validation of the obtained LSMs presents an essential step in order to calculate the performance of the used method in landslides prone area zoning. In this context, Roc Curve validation technique is used to calculate the performance of the statistical models integrated in the landslide susceptibility mapping.

ROC curve method is used to validate the obtained LSMs established by the AHP, WOE and LR methods. This statistic method is based in the comparison of the obtained LSM and the produced inventory map (validation data). The realization of the ROC curve consists first in classifying the LSI into 100 classes with an interval of 1%, then, the reclassified map is combined with the landslide events map, and finally, the production of the ROC curve is based in statistical analysis of the converted combination result file into compatible Excel software format.

To calculate the performance of the used methods, it is generally based on the evaluation of the area under curve (AUC) the ROC curve obtained. The AUC result is 95.13% for the WOE model, 91.92% for the AHP method and 83.57% for the LR model (Figure 12).
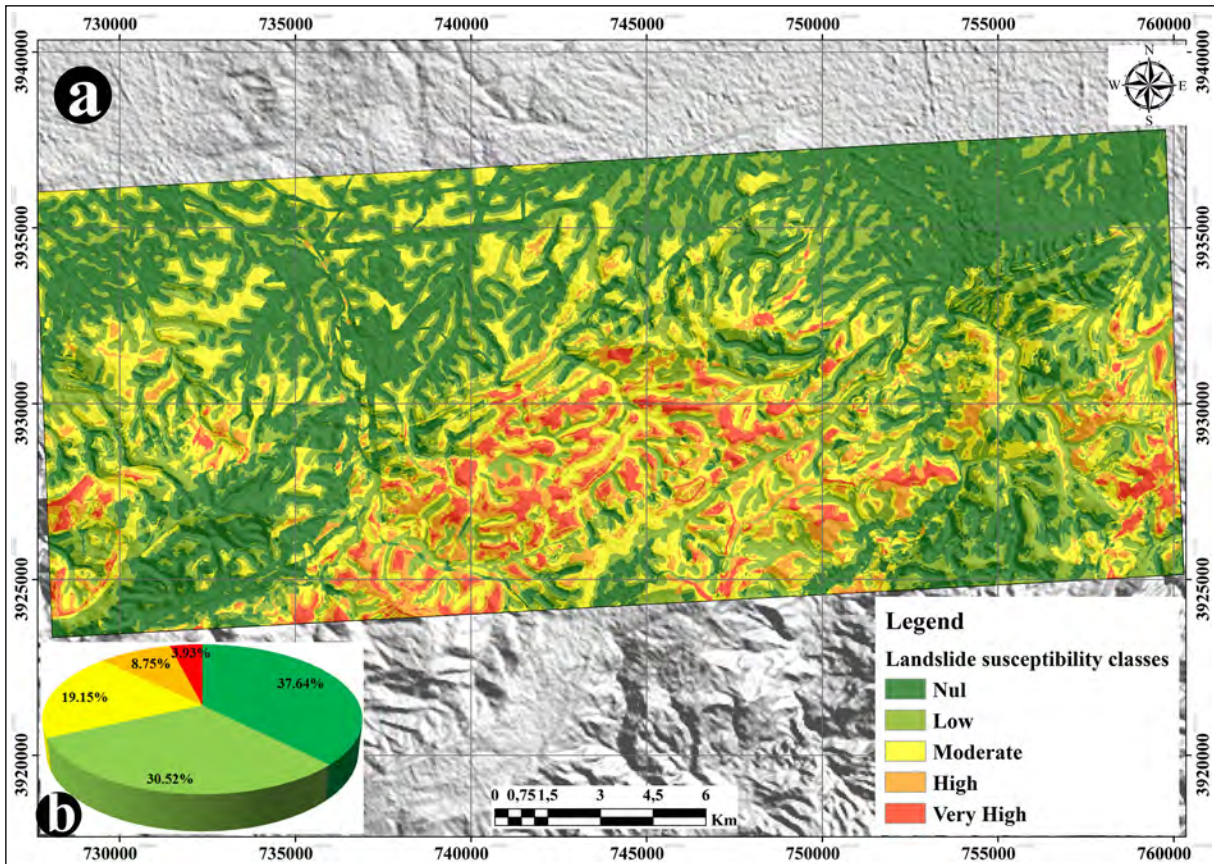
Figure 11– a) The LR - landslide susceptibility map, b) distribution pie - chart of the landslide susceptibility classes.
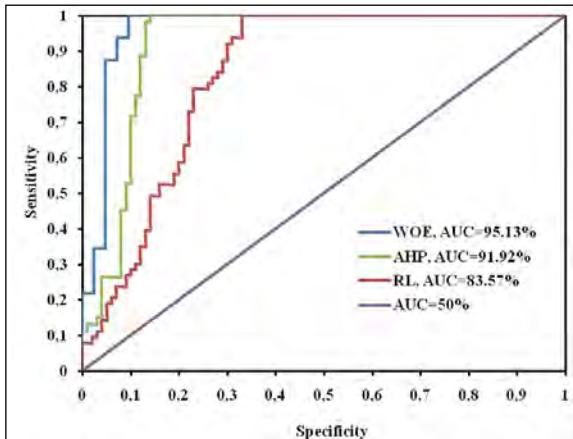
Figure 12- Diagram of ROC curve representing the performance of the statistical models.

ROC curve obtained for WOE, AHP and LR indicate that the used models in this research give good results in LSM. By comparing the ROC curve results we mentioned that the LSM produced by WOE method is the successful one.

6. Conclusion

The landslides presented one of the most common geological hazards in the world; they cause annually a considerable damages and human losses. In Algeria, a few attempts at landslide are applied in the northeastern part of the country. These contributions are generally focused on the application of the geophysical methods for landslide investigations on locale scale and the application of statistical methods based in GIS for the landslide susceptibility zoning on medium scale.

The investigations in the Echorfa region (NW of Algeria) indicate the lake on information about slope movements occurred in this area that involved the production of the landslide prone areas maps.

The LSMs produced by the categories the GSI into five classes according to the susceptibility degree. High and very high susceptibility characterizes the reliefs of the east and central part of the study area. Insignificant and low susceptibility classes

characterizes the northern part of this region (plains and plateaus) constituting the slope movements sheltered zones.

The validation process of the obtained results of the ROC curve model indicates the aptitude of the three models in the landslide susceptibility mapping. Hence, the WOE approach gives reasonable good accuracy in predicting landslide susceptibility of the Echorfa region.

The obtained LMSs can be considered as a basic document for the concerned authorities to take preventive measurements in the high and very high landslide susceptibility zones. In other hand, it provides a useful tool for the land use planner to select suitable fields for the future projects.

References

Achour, Y., Boumezbeur, A., Hadji, R., Chouabbi, A., Cavaleiro, V., Bendaoud, E. A. 2017. Landslide susceptibility mapping using analytic hierarchy process and information value methods along a highway road section in Constantine, Algeria. Arabian Journal of Geosciences 10, 194.

Akgün, A., Türk, N. 2010. Landslide susceptibility mapping for Ayvalık (Western Turkey) and its vicinity by multicriteria decision analysis. Environmental Earth Sciences 61, 595-611.

ANRH. 2007. Agence Nationale des resources hydriques. Carte des pluis moyens annuelles du Nord de l'Algérie, INCT., Alger, Algerie.

Ayadi, A., Ousadou-Ayadi, F., Bourouis, S., Benhallou, H. 2002. Seismotectonics and seismic quietness of the Oranie region (Western Algeria): The Mascara earthquake of August 18 th 1994, M w= 5.7, M s= 6.0. Journal of Seismology 6, 13-23.

Baeza, C., Corominas, J. 2001. Assessment of shallow landslide susceptibility by means of multivariate statistical techniques. Earth Surface Processes and Landforms: The Journal of the British Geomorphological Research Group 26, 1251-1263.

Barredo, J., Benavides, A., Hervás, J., van Westen, C. J. 2000. Comparing heuristic landslide hazard assessment techniques using GIS in the Tirajana basin, Gran Canaria Island, Spain. International Journal of Applied Earth Observation and Geoinformation 2, 9-23.

Belayadi, I., Bezzeghoud, M., Nadji, A., Fontiela, J. 2017. Sismicité de l'Algérie Nord Occidentale entre 1790 et 2016: catalogue sismique. Comunicaçõe Geológicas 104.

Beneder, 2011. Carte d'occupation du sol wilaya d'Oran, Mascar et Sidi Belabess notice explicative. Bureau national d'études pour le développement rural, Rapport inédite.

Benouar, D., Aoudia, A., Maouche, S., Meghraoui, M. 1994. The 18 August 1994 Mascara (Algeria) earthquake-a quick-look report. Terra Nova 6, 634-638.

Bonham-Carter, G. F. 1989. Weights of evidence modeling: a new approach to mapping mineral potential Statistical applications in the Earth Sciences 171-183.

Bonham-Carter, G. F. 1994. Geographic Information Systems for Geoscientists Modeling with GIS. Elsevier, 398.

Bouhadad, Y., Laouami, N. 2002. Earthquake hazard assessment in the Oran region (Northwest Algeria). Natural Hazards 26, 227-243.

Bourenane, H., Bouhadad, Y., Guettouche, M. S., Braham, M. 2015. GIS-based landslide susceptibility zonation using bivariate statistical and expert approaches in the city of Constantine (Northeast Algeria). Bulletin of Engineering Geology and the Environment 74, 337-355.

Bourenane, H., Guettouche, M. S, Bouhadad, Y., Braham, M. 2016. Landslide hazard mapping in the Constantine city, Northeast Algeria using frequency ratio, weighting factor, logistic regression, weights of evidence, and analytical hierarchy process methods. Arabian Journal of Geosciences 9, 154.

Chen, W., Li W., Chai, H., Hou, E., Li, X., Ding, X. 2016. GIS-based landslide susceptibility mapping using analytical hierarchy process (AHP) and certainty factor (CF) models for the Baozhong region of Baoji City, China .Environmental Earth Sciences 75, 63.

Chen, W., Peng, J., Hong, H., Shahabi, H., Pradhan, B., Liu, J., Zhu, A. X., Pei, X., Duan, Z. l. 2018. Landslide susceptibility modelling using GIS-based machine learning techniques for Chongren County, Jiangxi Province, China. Science of the Total Environment 626, 1121-1135.

Chen, W., Pourghasemi, H. R., Zhao, Z. 2017. A GIS-based comparative study of Dempster-Shafer, logistic regression and artificial neural network models

for landslide susceptibility mapping. Geocarto International 32, 367-385.

Corominas, J., Van Westen, C., Frattini, P., Cascini, L., Malet, J-P., Fotopoulou, S., Catani, F., Van Den Eeckhaut, M., Mavrouli, O., Agliardi, F., Pitilakis, K., Winter, M-G., Pastor, M., Ferlisi, S., Tofani, V., Herva´s, J., Smith, J-T. 2014. Recommendations for the quantitative analysis of landslide risk. Bulletin of Engineering Geology and the Environment 73, 209-263.

Cruden, D. M., Varnes, D. J. 1996. Landslide Types and Processes, Special Report, Transportation Research Board, National Academy of Sciences 247, 36-75.

Dahoua, L., Yakovitch, S., Hadji, R H. 2017. GIS-based technic for roadside-slope stability assessment: an bivariate approach for A1 East-west highway, North Algeria. Mining Science 24.

Djerbal, L., Khoudi, I., Alimrina, N., Melbouci, B., Bahar, R. 2017. Assessment and mapping of earthquake-induced landslides in Tigzirt City, Algeria. Natural Hazards 87, 1859-1879.

El Mekki, A., Hadji, R., Chemseddine, F. 2017 Use of slope failures inventory and climatic data for landslide susceptibility, vulnerability, and risk mapping in souk Ahras region. Mining Science 24.

Ercanoğlu, M., Gökçeoğlu, C., Van Asch, T. W. 2004. Landslide susceptibility zoning north of Yenice (NW Turkey) by multivariate statistical techniques. Natural Hazards 32, 1-23.

Fell, R., Corominas, J., Bonnard, C., Cascini, L., Leroi, E., Savage, W. Z. 2008. Guidelines for landslide susceptibility, hazard and risk zoning for land-use planning. Engineering Geology 102, 99-111.

Flentje, P. N., Miner, A., Whitt, G., Fell, R. 2007. Guideline for landslide susceptibility, hazard and risk zoning for land use planning. Australian Geomechanics 42, 13-36.

Guemache, M. A., Chatelain, J. L., Machane, D., Benahmed, S., Djadia, L. 2011. Failure of landslide stabilization measures: The Sidi Rached viaduct case (Constantine, Algeria). Journal of African Earth Sciences 59, 349-358.

Guessoum, N., Benhamouche, A. A., Bouhadad, Y., Bourenane, H., Abbouda, M. 2018. Field evidence of Quaternary seismites in the Mostaganem-Relizane (western Algeria) region: Seismotectonic implication. Arabian Journal of Geosciences 11, 641.

Hadji, R., Rais, K., Gadri, L., Chouabi, A., Hamed, Y. 2017. Slope failure characteristics and slope movement susceptibility assessment using GIS in a medium scale: a case study from Ouled Driss and Machroha municipalities, Northeast Algeria. Arabian Journal for Science and Engineering 42, 281-300.

Hallal, N., Yelles Chaouche, A., Hamai, L., Lamali, A., Dubois, L., Mohammedi, Y., Hamidatou, M., Djadia, L., Abtout, A. 2019. Spatiotemporal evolution of the El Biar landslide (Algiers): new field observation data constrained by ground-penetrating radar investigations. Bulletin of Engineering Geology and the Environment 78(3).

Intarawichian, N., Dasananda, S. 2010. Analytical hierarchy process for landslide susceptibility mapping in lower Mae Chaem watershed, Northern Thailand. Suranaree Journal of Science and Technology 17.

Karim, Z., Hadji, R., Hamed, Y. 2019. GIS-based approaches for the landslide susceptibility prediction in Setif Region (NE Algeria). Geotechnical and Geological Engineering 37, 359-374

Khosravi, K., Nohani, E., Maroufinia, E., Pourghasemi, H. R. 2016. A GIS-based flood susceptibility assessment and its mapping in Iran: a comparison between frequency ratio and weights-of-evidence bivariate statistical models with multi-criteria decision-making technique. Natural Hazards 83, 947-987.

Lee, S,. Ryu, J. H., Won, J. S., Park, H. J. 2004. Determination and application of the weights for landslide susceptibility mapping using an artificial neural network. Engineering Geology 71, 289-302.

Mahdadi, F., Boumezbeur, A., Hadji, R., Kanungo, D. P., Zahri, F. 2018. GIS-based landslide susceptibility assessment using statistical models: a case study from Souk Ahras province, NE Algeria. Arabian Journal of Geosciences 11, 476.

Marinas, J. L., Salord, R. 1991. Problems regarding the investigation of the 1790 oran seismic period. Tectonophysics 193, 237-239.

Merghadi, A., Abderrahmane, B., Tien Bui, D. 2018. Landslide susceptibility assessment at Mila Basin (Algeria): a comparative assessment of prediction capability of advanced machine learning methods. ISPRS International Journal of Geo-Information 7, 268.

Micheletti, N., Foresti, L., Robert, S., Leuenberger, M., Pedrazzini, A., Jaboyedoff, M., Kanevski, M. 2014. Machine learning feature selection

methods for landslide susceptibility mapping. Mathematical Geosciences 46, 33-57

Mohammady, M., Pourghasemi, H. R., Pradhan, B. 2012. Landslide susceptibility mapping at Golestan Province, Iran: a comparison between frequency ratio, Dempster–Shafer, and weights-of-evidence models. Journal of Asian Earth Sciences 61, 221-236.

Mondal, S., Maiti, R. 2012. Landslide susceptibility analysis of Shiv-Khola watershed, Darjiling: a remote sensing and GIS based Analytical Hierarchy Process (AHP). Journal of the Indian Society of Remote Sensing 40, 483-496.

Pham, B. T., Bui, D. T., Prakash, I., Dholakia, M. 2017. Hybrid integration of Multilayer Perceptron Neural Networks and machine learning ensembles for landslide susceptibility assessment at Himalayan area (India) using GIS. Catena 149, 52-63.

Phukon, P., Chetia, D., Das, P. 2012. Landslide susceptibility assessment in the Guwahati city, Assam using analytic hierarchy process (AHP) and geographic information system (GIS). International Journal of Computer Applications in Engineering Sciences 2, 1-6.

Regmi, N. R., Giardino, J. R., Vitek, J. D. 2010. Modeling susceptibility to landslides using the weight of evidence approach: Western Colorado, USA. Geomorphology 115, 172-187.

Roukh, Z. 2020. Cartographie algébrique d'aléa multirisque du littoral Oranie, Nord Ouest de l'Algérie, (risque sismique, glissement de terrain, inondation). Thèse de doctorat, Université d'Oran 2, 289.

Saaty, T. L. 1977. A scaling method for priorities in hierarchical structures. Journal of Mathematical Psychology 15, 234-281

Saaty, T. L. 1980. The Analytic Hierarchy Process: Planning. Priority Setting. Resource Allocation, MacGraw-Hill, New York, International Book Company, 287.

Santacana, N., Baeza, B., Corominas, J., De Paz, A., Marturiá, J. 2003. A GIS-based multivariate statistical analysis for shallow landslide susceptibility mapping in La Pobla de Lillet area (Eastern Pyrenees, Spain). Natural Hazards 30, 281-295.

Süzen, M. L., Doyuran, V. 2004. Data driven bivariate landslide susceptibility assessment using geographical information systems: a method and application to Asarsuyu catchment, Turkey. Engineering Geology 71, 303-321.

Tehrany, M. S., Pradhan, B., Jebur, M. N. 2014. Flood susceptibility mapping using a novel ensemble weights-of-evidence and support vector machine models in GIS. Journal of Hydrology 512, 332-343.

Thomas, G. 1985. Géodynamique d'un bassin intramontagneux Le bassin du Bas Chélif occidental (Algérie) durant le Mio-Plio-Quaternaire. Thèse de doctorat, Université de Pau, 594.

Xu, C., Xu, X., Dai, F., Saraf, A. K. 2012. Comparison of different models for susceptibility mapping of earthquake triggered landslides related with the 2008 Wenchuan earthquake in China. Computers and Geosciences 46, 317-329.

Yalçın, A., Reis, S., Aydınoğlu, A., Yomralıoğlu, T. 2011. A GIS-based comparative study of frequency ratio, analytical hierarchy process, bivariate statistics and logistics regression methods for landslide susceptibility mapping in Trabzon, NE Turkey. Catena 85, 274-287.

Yılmaz, I. 2009. Landslide susceptibility mapping using frequency ratio, logistic regression, artificial neural networks and their comparison: a case study from Kat landslides (Tokat—Turkey). Computers and Geosciences 35, 1125-1138.

Zare, M,. Pourghasemi, H. R., Vafakhah, M., Pradhan, B. 2013. Landslide susceptibility mapping at Vaz Watershed (Iran) using an artificial neural network model: a comparison between multilayer perceptron (MLP) and radial basic function (RBF) algorithms. Arabian Journal of Geosciences 6, 2873-2888.

Zine El Abidine, R., Abdelmansour, N. 2019. Landslide susceptibility mapping using information value and frequency ratio for the Arzew sector (North-Western of Algeria). Bulletin of the Mineral Research and Exploration 160, 197-211.

Bulletin of the Mineral Research and Exploration

http://bulletin.mta.gov.tr

Stratigraphy of the metamorphic rocks of Niğde Massif and new evidence of Triassic rifting of the Inner Tauride Ocean (Central Anatolia, Türkiye)

Mustafa Kemal ÖZKAN[a*], Metin BEYAZPİRİNÇ[b], Ali Ekber AKÇAY[b], Muhamed ÇOBAN[c], Osman CANDAN[d], Osman Ersin KORALAY[d], Meftun Kerem SÖNMEZ[b] and Halil YUSUFOĞLU[b]

[a]General Directorate of Mineral Research and Exploration, Eastern Black Sea Regional Directorate, Trabzon, Türkiye
[b]General Directorate of Mineral Research and Exploration, Depoartment of Geological Researches, Ankara, Türkiye
[c]General Directorate of Mineral Research and Exploration, Southeastern Anatolia Regional Directorate, Diyarbakır, Türkiye
[d]Dokuz Eylül University, Geological Engineering Department, İzmir, Türkiye

ABSTRACT

Metamorphites of Niğde Massif, which form the basis of study area covering the Niğde vicinity in Central Anatolia, are composed of Late Devonian Gümüşler, Carboniferous-early Permian Kaleboynu late Permian Kızıldağ formation and unconformable Triassic-Late Cretaceous cover units from bottom to the top, which are separated from each other with unconformities. The Triassic succession (Söğütlüdere formation) of phyllite-marble-schist alternations with common amphibolite levels is first distinguished in this study, unconformably overlies the Paleozoic succession. Thick homogeneous marbles of Jurassic-Cretaceous period, is defined by quartzite at the bottom representing the unconformity at the base, is defined as the Kırtepe formation. The succession probably ends with the Late Cretaceous metaflysch (Kırkpınar formation) constituting metaophiolite blocks with unconformable contact relationships. Amphibolite sample of the Söğütlüdere formation gives 239 Ma (Middle Triassic) age, which is interpreted as the crystallization age of the primary basic magmatism. The youngest detrital zircon ages (223-224 Ma) obtained from the metaclastics of the same formation shows that the primary deposition age of the formation is probably Late Triassic, which is consistent with this data. Geochemical data indicate an extensional environment of the alkaline composition and anorogenic originated basic volcanism developed on the continental crust. When these results evaluated together with the regional data, the metabasites of the Söğütlüdere formation can be interpreted as the first phase products of rifting, which commenced with the rifting process of the Tauride-Anatolide Platform in the Triassic period and resulted in the opening of the Inner Tauride Ocean and the break off the Kırşehir Block.

1. Introduction

The study area located on the Kırşehir Block in Central Anatolia (Şengör and Yılmaz, 1981; Okay and Tüysüz, 1999) covers the Niğde vicinity. The area bounded by the İzmir-Ankara-Erzincan Suture Zone (North Anatolian Ophiolite Belt) in the north and the Inner Tauride Suture in the south form the Kırşehir Block, one of the main tectonic units of Türkiye. Tuz Gölü and Central Anatolian faults predominantly follow these suture zones (Figure 1). Kırşehir Block generally consists of ophiolites and nappes of oceanic origin emplaced on high grade metamorphic rocks and
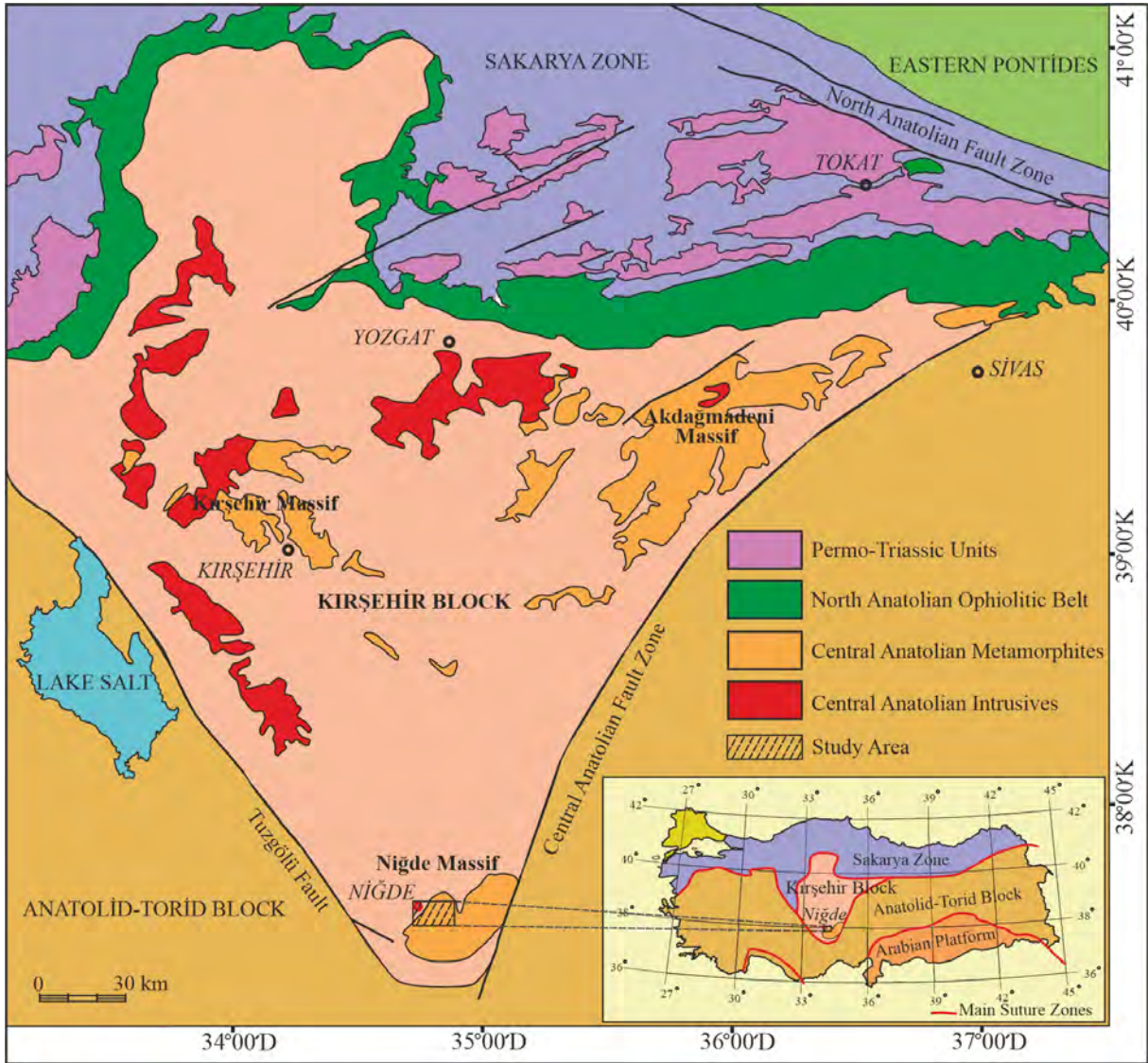
Figure 1- Location map of the study area.

granitic plutons together with their surface equivalents cutting cross those. All these units are covered by Paleogene and Neogene sedimentary rocks. The Niğde Massif has been the subject of detailed research for many years, but the ages and stratigraphies of the rocks that make up the massif remain debated. In this study, the main aim is to reveal the lithofacies features and contact relationships of the above-mentioned rocks with a regional research, to determine their age with paleontological-radiometric data, and to discuss the evolution of the massif using the results.

Detailed studies on the stratigraphy of the Niğde Massif were made by Göncüoğlu (1977, 1981). It was

stated that Gümüşler formation, Kaleboynu formation and Aşıgediği formation, from bottom to top, is grouped under Niğde group and they are in cutting-cross relationship with Üçkapılı granodiorite. In addition, it was argued that the metamorphism evolved from medium pressure-high temperature type to low pressure-high temperature type and PT conditions reached partial melting occassionally, and the main metamorphism phase and ophiolite emplacement in the massif took place before the Cenomanian. Yalınız and Göncüoğlu (1998) stated that the ophiolites on the Central Anatolian metamorphic rocks, despite being disturbed, preserved their primary ophiolitic sequence and they were cut-cross by granitoids. They argued

that the ophiolites developed in the fore-arc basin due to an intraoceanic subduction in the İzmir-Ankara Ocean during the middle Turonian-early Santonian, and were emplaced onto the Central Anatolian metamorphic rocks following the early Santonian and prior to the Maastrichtian. Aydın et al. (1998) studied the Uppermost Late Cretaceous magmatism in the Central Anatolian Crystalline Complex. Whitney et al. (2001) suggested that the Central Anatolian Crystalline Complex can be divided into at least four tectonic blocks (Kırşehir, Akdağ, Niğde and Aksaray massifs) indicating different temperature-pressure-time evolutions. They stated that the massifs were exposed to thrust and folding processes due to the collision in the north, and they slowly exhumed with following erosion. Whitney et al. (2007) studied the Yo-yo tectonics during the strike-slip faulting of the Niğde Massif. They stated that two complete burial/exhumation cycles were present through the Massif in an oblique-slip deformation zone over a period longer than ~80 Ma, one observed at a regional scale and the other at a more local scale from the Cretaceous (burial) to Miocene (cooling and exhumation). Boztuğ et al. (2009) argued that Central Anatolian granitoid melts emerged after the collision, an oceanic arc emplaced on the Tauride-Anatolide platform during Campanian-Maastrichtian and rapidly uplifting in the early-middle Paleocene resulted. Advokaat et al. (2014) mentioned block rotations in Paleocene. Cengiz Çinku et al. (2016) concluded that the Niğde-Kırşehir Massif rotated counterclockwise up to 25.5°±7.3° during the Middle Eocene in their paleomagnetism study. Demircioğlu and Eren (2003, 2017) determined that both the Niğde Massif and Paleocene-Eocene cover rocks were deformed together, based on mesoscopic tectonic analyses. They stated that the metamorphics forming the Niğde Massif underwent ductile deformation with at least four phases (D_1, D_2, D_3 and D_4). Çoban (2019) stated that the rocks of the Niğde Massif underwent multi-phase deformation and high-grade metamorphism and acquired a foliated structure before the Late Cretaceous. Due to closure of the Inner Tauride Ocean, Ulukışla group and rocks of the massif were together exposed before the Oligocene and they stated strike-slip and normal faults developed in the region during the neotectonic period. Demircioğlu and Coşkuner (2021) argued that type-3 fold interference structures, especially branching to the northeast and

southwest, developed in the rocks as a result of multi-stage deformation of high-grade metamorphic rocks of the Niğde Massif.

In this study, the stratigraphic characteristics of the metamorphic masses of the Niğde Massif were revealed in detail using the new stratigraphic, sedimentological, petrographic, geochemical and geochronological data obtained within the scope of the project as well as the previous studies. Additionally, the meaning and importance of the Triassic succession, which is distinguished for the first time in this study, including the first phase products of the Inner Tauride Ocean rifting are discussed in terms of the regional geology.

2. Regional Geology

The metamorphic, magmatic and ophiolitic rock assemblages in Central Anatolia were named as Central Anatolian Crystalline Complex (CACC) (Göncüoğlu et al., 1991, 1993). Considering the geographical areas where the metamorphic masses outcrop in the CACC were defined with different names; Akdağ Massif (Baykal, 1947), Kırşehir Crystalline Massif (Bailey and McCallien, 1950; Egeran and Lahn, 1951), Central Anatolia Massif, Kızılırmak Massif (Ketin, 1955, 1963; Erkan and Ataman, 1981), Niğde group/Niğde Massif (Göncüoğlu, 1977, 1981), Kaman group (Seymen, 1981a, b) and Central Anatolian Crystalline Complex (Erler and Bayhan, 1995).

The rocks of İzmir-Ankara-Erzincan Zone (North Anatolian Ophiolite Belt) and Sakarya Zone (Permo-Triassic units) outcrop in the north of the Kırşehir Block whereas Inner Tauride Suture Belt and Anatolide-Tauride Block rocks in the westerly-southerly and easterly (Figure 1). Sakarya Zone, İzmir-Ankara-Erzincan Zone, Kırşehir Massif, Inner Tauride Suture Belt and Anatolide-Tauride Block units are observed in tectonic relationship (nappe) with each other from north to south. The Niğde Massif units in Kırşehir Block, which will be explained in detail in this study, consitute the basement. Salt Lake Basin units represented by deep sea sediments consisting of the remains of the Inner Tauride Ocean are observed in the western part of the Kırşehir Block whereas the presence of the basin and post-collisional basin

sediments of the Inner Tauride Ocean is observed in the southern part. Görür et al. (1998) suggested that Ulukışla Basin developed as a fore-arc basin due to subduction of the Inner Tauride Ocean between Bolkar carbonate platform and Kırşehir-Niğde microplates towards northerly direction. On the other hand, some researchers argued that this basin developed resulting with the extensional (Göncüoğlu et al., 1991; Çemen et al., 1999) or transtensional tectonic regime (Alpaslan et al., 2006) due to collision within Anatolide-Tauride platform following the closure of the Neotethys Ocean. Clark and Robertson (2002) stated that Ulukışla Basin is a basin that developed under the effect of extensional tectonics on the Inner Tauride Suture Zone. In the south of the Inner Tauride Suture Belt separating the Kırşehir Block and the Tauride-Anatolide Block, the Tavşanlı Zone and Afyon Zone units of the Tauride-Anatolide Block crop out with tectonic contacts. The units of the Kırşehir Block and the Anatolide-Tauride Block are bounded by the Tuzgölü Fault towards west and by the Central Anatolian Fault Zone (Ecemiş Fault Zone) towards easterly direction. In the study area covering the Niğde Massif, metamorphic rocks, ophiolitic rocks, granitoid and cover units of the Ulukışla Basin and Ürgüp Basin crop out in the most general sense (Figure 2).

3. Material and Methods

Detailed geologial mapping was conducted in the study area between Niğde and Çamardı (1/100000 in scale, Adana-M33 sheet) and correlations together with observations were also made out of the study area if needed. Thin sections of the samples collected from the study area were prepared and examined in detail under the polarizing microscope and their petrographic properties were defined. Chemical analyzes (major, trace and rare earth element) of selected 12 samples using field observations and petrographic examinations were carried out at Department of Mineral Analysis and Technology Laboratories of General Directorate of Mineral Research and Exploration (MTA). The samples were first grounded into powders in the laboratory. The powdered sample (0.2 g) was mixed with 1.5 g of Li-BO_2 and dried at 105°C, and major oxide analyzes were performed in a Thermo-ARL brand XRF device. The samples were solved according to TS ISO 14869-

1 and TS ISO 14869-2 and analyzed in ICP-OES and ICP-MS devices. Zircon U/Pb dating of two samples from the metabasite member of the Söğütlüdere formation was conducted at the University of Arizona, Department of Geosciences Laboratory (USA). After the rock samples had gone through standard mineral separation processes, the zircons were hand-picked in alcohol and placed in epoxy with reference materials. The discs containing the grains were then wet abraded with sandpaper of various thicknesses and polished with diamond paste. Followingly, cathodoluminescence (CL) images were captured on a Philips XL-30 scanning electron microscope (SEM) equipped with the Bruker Quanta 200 energy dispersion X-ray microanalysis system at the Electron Microbeam/X-Ray Diffraction Laboratory (EMXDF), University of British Columbia. An operating voltage of 15 kV with a spot diameter of 6 μm and a peak count time of 30 seconds was used. After removal of the carbon coating, the grain holding surface was washed with mild soap and rinsed with high purity water. Prior to analysis, the disc surface was cleaned with 3 N HNO_3 acid and rinsed again with high-purity water to remove any superficial Pb contamination that might interfere with the early part of spot analyses.

4. Stratigraphy of the Metamorphic Rocks of Niğde Massif

The metamorphic rocks of the Niğde Massif, which form the basis of the study area and can be correlated with the Yahyalı nappe (Blumenthal, 1952) located in the Taurus Mountains in terms of stratigraphic characteristics, constitute conformable and transitional contacts of the Late Devonian Gümüşler, Carboniferous-early Permian Kaleboynu, late Permian Kızıldağ formation unconformably overlying the Triassic Söğütlüdere formation which is first distinguished and defined, Jurassic-Cretaceous Kırtepe and Late Cretaceous Kırkpınar formations from the bottom to the top. The Late Devonian-Early Cretaceous sequence has undergone metamorphism under amphibolite and above facies progradely and occasionally greenschist facies retrogradely. The metamorphics of the Niğde Massif, from bottom to top, consist of quartzite, quartz schist, mica schist, calc schist, occasionally plaque-like marble, dolomitic marble, metabasite, talc schist, metasiltstone, metamudstone, cherty marble and schist, marble and
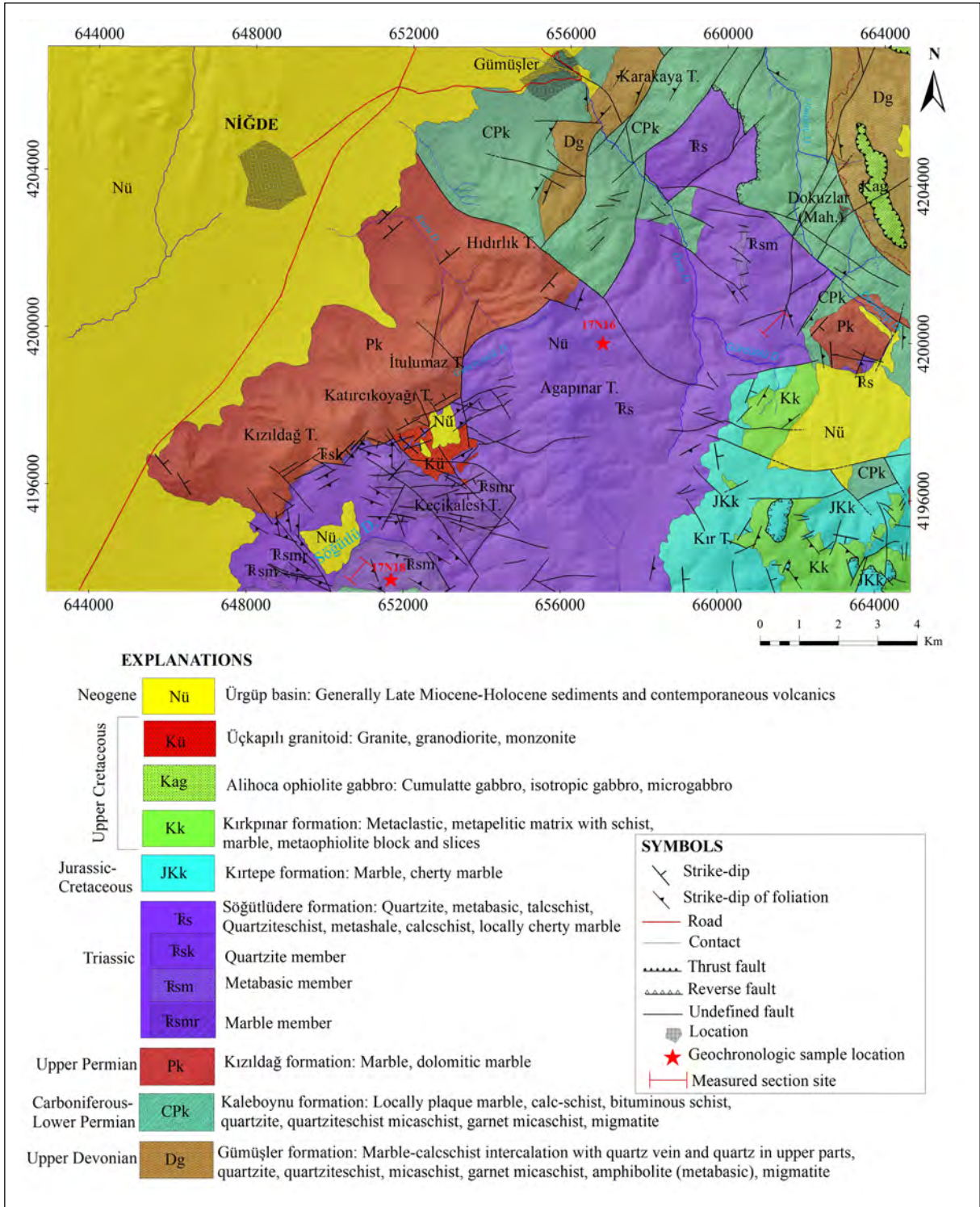
Figure 2- Geological map of the study area.

metaophiolite blocks in a metaclastic-metapelitic matrix (Figure 3).

The Gümüşler formation, located at the base of the Niğde Massif and named by Göncüoğlu (1981),

is generally greenish, gray in color, with partially migmatized sillimanite-garnet mica schist at lower sections, paragneiss, amphibolite, quartz schist, quartzite, and amphibolite intercalations in the upper

Age	Formation	Member	Thickness (m)	Lithology	Explanations
U. Cretaceous	Kırkpınar Fm. Üçkapılı Gr.	Metaoph.. Blocks and slices	~370		Metaclastic, metapellitic, matrix with schist, marble, metaophiolite blocks and slices
					Unconformity
Jurassic-Cretaceous	Kırtepe Formation		~420		Cherty marble; yellowish grey, yellow, cream, whit colored massive, very thick bedded calcite filled faulted-fractured metachert nodule and bands
		Quartzite			Quartzite
					Unconformity
Triassic	Söğütlüdere Fm.	Quartzite|Metabasic|Mb	~550		Quartzite micaschist ⬟ *U-Pb 223-224 Ma* Metabasic ⬟ *U-Pb 239 Ma* Quartzite, metabasic, talcschist, quartzschist, phyllite. calcschist, locally cherty marble
					Unconformity
Upper Permian	Kızıldağ Formation		~300		Marble; grey, blackish grey colored, medium-thick-very thick and bedded, calcite filled, faulted fractured
Carboniferous-Lower Permian	Kaleboynu Formation	Marble	~430		locally plaque black, grey colored thin-thicked bedded and locally fossiliferous (Fusulinid molds, Brachiopod shells, algae crinoid) marble, calcschist, bituminous schist,quartzite, quartz schist micaschist, garnet micaschist, migmatite
Upper Devonian	Gümüşler Formation		~350		Quartz schist, micaschist, garnet micaschist, amphibolite (metabasic) and migmatite in upper levels quartzite with marble-calcschist alternation locally bituminous schist intercalation (10-15 cm) and quartz vein

Figure 3- Generalized columnar section of the Niğde Massif.

parts within the calcschist-marble levels (Figure 4). Considering its stratigraphic position and correlating it with similar facies in the Taurus Mountains (Late Devonian successions in the Geyikdağı unit and Aladağ nappe and their metamorphic equivalents in the Bolkardağı Nappe and Yahyalı Nappe), age of the unit was determined as Late Devonian. The unit can be correlated with Yahyasaray formation located at the base of the Akdağmadeni Massif (Beyazpirinç and Akçay, 2017), metapelites in the Akdağmadeni metasedimentary group (Şahin, 1991), a part of Köklüdere formation (Dökmeci, 1980) in the Akdağ metamorphic group and Kalkanlıdağ formation (Seymen, 1982) at the base of Kırşehir Massif.

The Kaleboynu formation, named by Göncüoğlu (1981), is generally yellowish gray in color and consists of calcschist, plaque marble-dolomitic marble, quartzite, quartz schist, mica schist, sericite-schist, with occasionally marble lenses and bituminous schist intercalations (Figure 5). Hornfels and calc-silicate fels rocks were occasionally developed depending on the granite intrusions. The Kızıldağ formation conformably overlies the Kaleboynu formation, which overlies the Gümüşler formation conformably and transitionally, and the Söğütlüdere formation unconformably. Fusulinid molds, brachiopoda and macrofossil shell fragments were observed in the unit, and Carboniferous-early Permian age has been suggested considering their correlation with similar facies in the Taurus Mountains (Carboniferous-early Permian successions in the Geyikdağı unit and Carboniferous-early Permian sequences in the Aladağ nappe and their metamorphic equivalents in the Bolkardağı nappe and Yahyalı nappe) for the Kaleboynu formation. The unit can be correlated with Akçakışla formation (Beyazpirinç and Akçay, 2017) in Akdağmadeni Massif, semimetapelites (Şahin, 1991) in Akdağmadeni metasedimentery group, parts of the Köklüdere and Özerözü formations (Dökmeci, 1980), Tamadağ formation (Seymen, 1981b) defined around Kaman district (Kırşehir province) and Kervansaray formation (Kara and Dönmez, 1990) in Kırşehir Massif.

Figure 4- a) Schist-calcschist-marble alternation in the upper levels of the Gümüşler formation, b) metabasites cutting-cross quartz mica schists and c) migmatized metapelites.

Figure 5- a) Schist-calcschist-marble intercalation containing bituminous schist intercalations in the Kaleboynu formation, b) brachiopodas and c) marbles containing fusulinid molds.

The Kızıldağ formation, which is equivalent of a part of the Aşıgediği formation (Göncüoğlu, 1981) and was distinguished for the first time in this study, is gray, blackish gray in color, thin-thick bedded, medium-coarse crystalline and joint systems have commonly developed. Dissolution voids are observable. It consists of marble levels occasionally intercalated with bituminous schist and dolomitic marble. Considering its stratigraphic position and correlating with similar facies in the Taurus Mountains, late Permian age has been suggested for the unit, which conformably overlies the Kaleboynu formation. The unit can be correlated with Topaktaş formation in Akdağmadeni Massif (Beyazpirinç and Akçay, 2017), metacarbonates in Akdağmadeni metasedimentary group (Şahin, 1991) and Bozçaldağ formation in Kırşehir Massif (Seymen, 1982). Triassic Söğütlüdere, Jurassic-Cretaceous Kırtepe and Late Cretaceous Kırkpınar formations, which overlie all these Paleozoic successions and are unconformably separated from each other, were distinguished for the first time in this study. Kırtepe formation, with quartzite units reaching up to 50 m in thickness and defining the unconformable contact relation at the base, is composed of occasionally dolomitized homogenous marble. General characteristics of the formation are that weathering colour is gray and fresh surface is in different colours i.e. yellow, cream, gray and white. It is thick-bedded and massive in texture, and joint-fracture systems are also present. Jurassic-Cretaceous age was suggested considering the stratigraphic position of the unit, which unconformably overlies the Gümüşler formation, Kervansaray formation and Söğütlüdere formation, and correlations with similar facies in the Taurus Mountains. The unit can be correlated with a part of the Saytepe formation in the Kırşehir Massif (Beyazpirinç et al., 2020), the Hisarbey formation in the Akdağmadeni Massif (Beyazpirinç and Akçay,

2017) and the Aşıgediği formation in the Niğde Massif (Göncüoğlu, 1981).

Kırkpınar formation, which is the upper-most part of the Niğde Massif and is distinguished for the first time in this study, generally presents the Late Cretaceous blocky metaflysch characteristics consisting of quartzite, quartz schist, mica schist and metabasite with metaophiolite, marble, schist blocks and rarely observed metaconglomerate (channel fillings) (Figure 6). The unit can be considered as the metamorphic equivalent of the Cenomanian Karaböğürtlen formation in the Western Taurus Mountains, which is first named by Philippson (1915) and it can be correlated with Davulbaz formation in Akdağmadeni Massif (Beyazpirinç and Akçay, 2017) and partly correlated with blocky levels of Özerözü formation (Dökmeci, 1980) in Akdağ metamorphic group.

Triassic metamorphics in the study area constituting the main subject of this study is distinguished for the first time in this study and named as Söğütlüdere formation. Quartzite, quartz-schist and sericite-schists at the base of the Söğütlüdere formation is distinguished as Quartzite member. Amphibolite/ metabasites with marble intercalations are defined as Metabasite member. Thick marble levels as interbeds and lenses are defined as Marble member. The unit generally starts with a quartzite unconformity and is represented by quartz mica schist, mottled coloured phyllite, amphibolite (metabasite), talc schist, mica schist, calc schist intercalated with chert and red coloured, brecciated-like, occassionally fossiliferous (Ammonite-like forms, gastropoda, pelecypoda and macrofossil molds) marble, cherty marble in the upper sections (Figure 7). One of the distinguishing characteristics of the Söğütlüdere formation is that

Figure 6- a) Unconformable contact between Kırkpınar formation (Kk) and Kırtepe formation (JKk), b) metaconglomerate within Kırkpınar formation, c) metaophiolite and marble blocks.
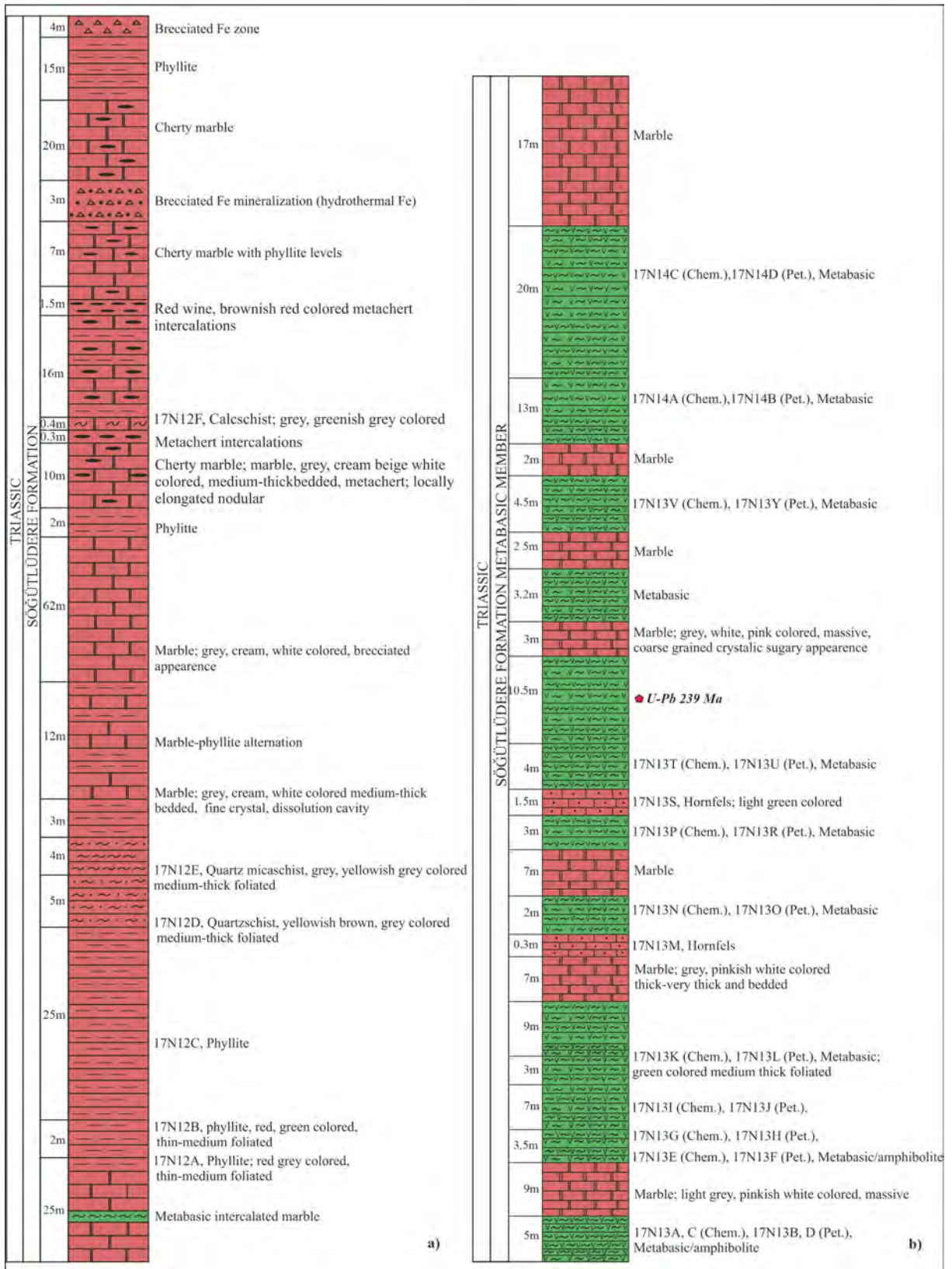
Figure 7- a) Measured section of Söğütlüdere formation (SW of the Özyurt Village; Adana-M33b1 sheet; UTM ED50 Zone 36 661558, 4200722), b) measured section of the metabasite member (East of Sazlıca, Söğütlüdere; Adana-M33a2 sheet; UTM ED50 Zone 36 4193697, 650638).

claret red-mottled coloured, thin to medium foliated, marble intercalated phyllites are most likely Early Triassic in age and predominantly forms the base of the unit. Cherty marble is gray, cream, beige in color, medium-thick bedded, fractured and contains chert in the form of nodules, staining and occasionally intercalations (Figure 8).

In the measured section of Söğütlüdere, which is the key site for the metabasite member, amphibolite/ metabasites with light gray, pinkish white colored, thick-very thick bedded marble interlayers were observed (Figure 9). It was determined that the samples collected from the metabasite member are mostly composed of hornblende-plagioclase composition and weakly oriented amphibolites. These minerals are accompanied by clinopyroxenes in the hornfels-like, fine-grained granoblastic texture and non-oriented sections of metabasites, where they are more massive in texture and fine-grained.

Figure 8- a) General view from the Söğütlüdere formation, b) Mottled phyllites with marble intercalations derived from metamudstone-metasiltstone-metaclaystone, representing the Lower Triassic sections of the unit, c) Red colored, brecciated-like, occassionally fossiliferous (Ammonite-like forms, gastropoda, pelecypoda and macrofossil shell fragments) marble and d) cherty marbles.

Figure 9- General view from the metabasite member of the Söğütlüdere formation.

The metabasites in the unit consist of oriented, relatively coarse crystalline common amphibolites with fels appearance and fine grained massive texture. Diopsidefels detected in petrographic analysis shows nematogranoblastic texture and consists of clinopyroxene, plagioclase, epidote and small amounts of quartz and calcite minerals as main components. Clinopyroxene minerals are medium-grained, anhedral, commonly fissured, and they display green pleochroism. Plagioclase minerals are typical with polysynthetic twinning and are highly sericitized. Epidote minerals are typical with medium to fine grained, in anhedral forms with yellowish pleochroism. Small amounts of quartz and calcite minerals are medium grained and anhedral. Titanite minerals (sphene/leucoxene) are observed as accessory components in the rock. In addition, there are secondary calcite minerals as fillings in vein-shaped cracks in the rock. Amphibolite has nematogranoblastic texture and consists of medium-grained, prismatic, green pleochroic hornblendes and plagioclase feldspars with medium-grained, subhedral, occasionally sericitized, displaying polysynthetic twin lamellae. Quartz minerals are rarely observed and they are fine-grained and anhedral. Anhedral epidotes are medium-grained and rarely fine-grained. Titanites (sphene) are mostly common as accessory minerals in the rock and secondary calcite minerals are also present. The well-oriented rock was probably metamorphosed under the conditions of lower amphibolite facies. Clinoamphibole minerals in hornblende composition are medium-grained, subhedral, in prismatic forms and they display green pleochroism. Clinopyroxene minerals are medium-grained, anhedral, and heavily fissured. Plagioclase minerals are medium grained and highly sericitized. Quartzs are medium grained and anhedral. Calcite minerals are medium-grained and observed in anhedral forms. In addition, titanite minerals as accessory minerals are highly abundant and opaque minerals in the rocks are also highly observable. Calc-silicate fels have nematogranoblastic texture and consist of clinopyroxene, quartz and calcite minerals as the major components. Clinopyroxene minerals are medium-grained, anhedral, and heavily fissured. Quartz is medium grained and anhedral. Calcite minerals are medium and locally fine-grained, and they are in anhedral forms. Plagioclase minerals are common

with their polysynthetic twinning. Clinozoisite minerals, which are rarely observed, are fine-grained and anhedral. Titanite minerals are found in the rock as an accessory component. The rock was probably metamorphosed under the lower amphibolite facies conditions. Tremolite actinolite schist has fibroblastic texture and consists of medium-grained, prismatic structure, light green pleochroism actinolite and colorless tremolite minerals as the major component. Plagioclase mineral has polysynthetic twin lamellae. The muscovite minerals, which are observed in small amounts, are fine-grained and flaky. Titanite minerals are observable in the rock as an accessory component. Minerals show parallel arrangement in the rocks with well-developed orientation. The rock was probably formed as a result of retrograde metamorphism of a basic rock under greenschist facies conditions. The Jurassic-Cretaceous Kırtepe formation with highly folded and fractured structure unconformably overlying the Kaleboynu formation and the Kızıldağ formation unconformably overlies the unit (Figure 10). The unit, which partially corresponds to a part of the Aşıgediği formation (Göncüoğlu, 1981) in the Niğde Massif, can be correlated with the Demirtepe formation (Beyazpirinç et al., 2020) in the Kırşehir Massif.

5. Geochemistry

Major, trace and rare earth element analyzes of a total of nine samples were carried out in Department of Mineral Analysis and Technology (MTA) to determine the geochemical and petrological properties of marble intercalated amphibolite/metabasites, which are distinguished at the member level within the Söğütlüdere formation. The graphs used in geochemical interpretations were generated using Excel and the GCDkit program, and the analysis results are given in Table 1.

5.1. Classification

In order to determine whether the amphibolite/ metabasites separated at a member level in the Söğütlüdere formation, which might display sedimentary (para-amphibolite) or magmatic (ortho-amphibolite) origin, the results of the analyses were presented by the $Ni-TiO_2$ and $Ni-Zr/TiO_2$ graphs developed by Winchester et al. (1980) and Winchester

Figure 10- a) Unconformable contact relationship with the Jurassic-Cretaceous Kırtepe formation (JKk) overlying the Söğütlüdere formation (Trs) and quartzites derived from pure quartz arenite in the basement of quartzite along the contact, and b) Unconformable contact relationship with the late Permian Kızıldağ formation (Pk) located at the base of the Söğütlüdere formation.

and Max (1982). The results shown that the Ni contents of metabasites are between 91.00 and 377.60 ppm, the Zr contents are between 15.20 and 43.50 ppm, and the Zr/TiO_2 ratios vary between 0.0006 and 0.0016. As a result, the metabasites are originated from magmatic rocks following the plots into that can be seen in the trends which are created by the plots in the $Ni-TiO_2$ and $Ni-Zr/TiO_2$ graphs (Figure 11).

The samples of the Metabasite member samples of the Söğütlüdere formation (magmatic in origin) are classified by using the the total alkali versus silica

(TAS) (Le Bas et al., 1986) diagram (Figure 12a), the origin rock of the metabasites is alkaline and basaltic in composition. In addition to this, the samples are classified as basalt and trachybasalt. Moreover, the loss on ignition (LOI) values of the analyzed samples vary between 0.85-5.05. Since it is possible to have some changes through major element oxide values of the rocks (especially SiO_2, CaO, K_2O and Na_2O) during hydrothermal alteration processes, metabasites are also classified in the Zr/Ti-Nb/Y diagram modified by Pearce (1996), in which elements that cannot be mobilized easily under low alteration and
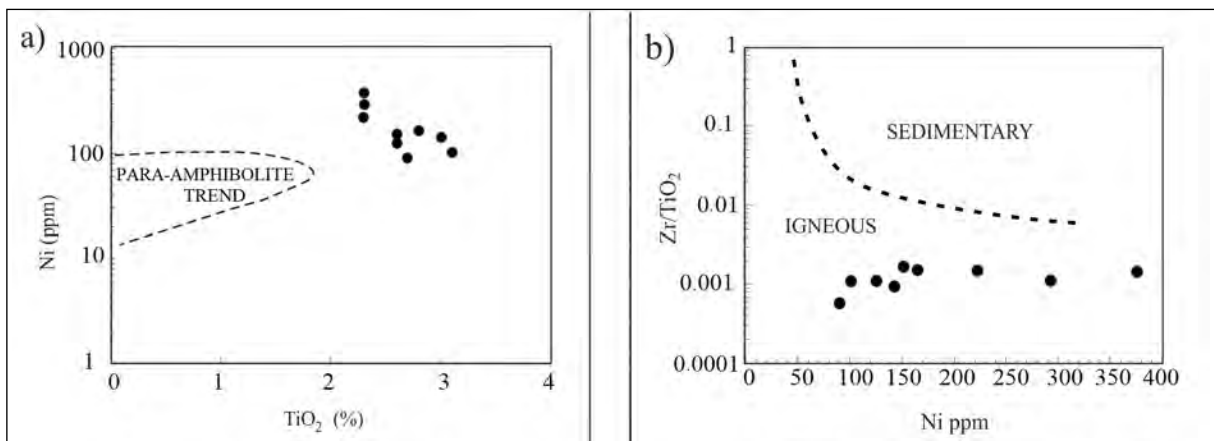
Figure 11- The rock samples of the Metabasite member of the Söğütlüdere formation; a) Winchester and Max (1982), b) Winchester et al. (1980) diagrams.

Table 1- Whole rock (major, trace and rare earth elements) chemical analysis results of the rock samples from the Metabasite member of the Söğütlüdere formation.

SAMPLE	17N13A	17N13C	17N13E	17N13G	17N13K	17N13N	17N13T	17N14A	17N14C
Major Oxides Wt. %									
SiO2	46.30	44.20	43.60	48.10	44.80	43.10	46.60	45.00	46.80
Al_2O_3	13.40	13.60	13.00	14.40	10.70	12.30	12.60	13.10	13.00
Fe_2O_3	11.30	13.30	11.90	11.50	12.10	11.00	12.90	12.30	13.00
CaO	12.40	12.60	14.00	9.40	13.90	15.40	12.00	13.50	11.50
MgO	3.90	5.70	5.40	5.30	8.30	4.90	7.00	5.90	6.30
Na2O	3.70	3.20	3.40	4.40	2.90	3.10	3.30	3.20	3.30
K2O	1.60	1.00	1.10	1.10	0.50	1.80	0.40	1.00	0.90
TiO2	2.30	3.10	2.60	2.70	2.30	2.30	3.00	2.80	2.60
MnO	0.10	0.20	0.20	0.10	0.20	0.10	0.20	0.20	0.20
P_2O_5	0.60	0.90	0.60	1.00	0.60	0.70	0.70	0.80	0.50
SrO	0.05	0.06	0.05	0.03	0.03	0.03	0.06	0.08	0.06
BaO	0.02	0.02	0.01	0.02	<0.01	0.03	0.01	0.03	0.03
Loss on ignition	4.20	2.05	4.00	1.80	3.30	5.05	0.85	1.90	1.55
Total	99.87	99.93	99.86	99.85	99.63	99.81	99.62	99.81	99.74
Trace Elements ppm									
Ba	160.00	164.60	118.00	133.90	60.80	162.90	76.80	211.00	165.10
Nb	35.90	58.40	60.40	70.70	45.50	41.30	60.30	62.10	40.80
Zr	25.40	34.70	43.50	15.20	31.80	34.90	28.80	42.70	28.70
Cs	1.10	0.30	0.40	0.20	0.20	0.30	<0.1	0.30	0.20
Ga	16.80	17.40	18.40	16.70	13.40	16.50	16.30	17.30	16.80
Hf	1.00	1.20	1.40	0.70	1.10	1.10	1.20	1.40	1.00
Rb	41.80	22.00	27.00	16.00	<10	24.00	<10	30.40	15.00
Sn	<10	<10	<10	<10	<10	<10	<10	<10	<10
Sr	463.00	428.50	415.00	247.30	249.60	256.90	470.80	665.00	485.40
Ta	1.90	3.00	2.70	3.50	2.20	1.90	2.90	2.60	2.10
Th	2.60	3.00	3.20	3.90	2.30	1.10	2.50	2.10	0.60
Tl	0.20	0.10	0.10	<0.1	<0.1	<0.1	<0.1	0.10	<0.1
U	<0.1	<0.1	<0.1	<0.1	<0.1	<0.1	<0.1	<0.1	<0.1
V	48.40	57.10	56.50	54.90	49.60	43.40	52.60	53.00	54.80
W	<10	<10	<10	<10	<10	<10	<10	<10	<10
Y	19.10	19.30	21.60	22.10	16.10	18.80	22.80	20.90	20.20
As	13.60	12.00	11.50	9.80	10.20	9.90	9.90	12.00	10.10
Be	1.80	1.50	2.20	1.50	2.10	1.60	2.30	1.30	2.30
Cd	0.10	0.10	<0.1	0.10	<0.1	0.10	0.10	<0.1	<0.1
Co	49.00	48.10	53.30	43.80	59.90	47.70	52.20	49.80	48.40
Cr	399.40	298	395.10	155	669	283	402	451.00	279
Cu	69.20	94.30	120.40	53.10	97.20	89.60	96.30	71.70	78.50
Ge	3.30	3.20	3.10	3.10	3.00	2.90	3.00	3.10	3.00
Mo	<0.1	<0.1	<0.1	<0.1	<0.1	<0.1	<0.1	<0.1	<0.1
Ni	293.10	100.80	151.50	91.00	377.60	222.80	143.20	164.90	125.60
Pb	<0.1	1.70	<0.1	<0.1	<0.1	<0.1	0.10	<0.1	<0.1
Sb	<0.1	<0.1	<0.1	<0.1	<0.1	<0.1	<0.1	<0.1	<0.1
Sc	29.10	32.80	35.90	24.10	31.20	23.00	35.00	32.40	40.00
Zn	127.50	129.10	125.80	129.80	123.70	132.10	132.80	136.60	121.00
La	16.90	27.00	27.60	31.10	19.70	19.50	27.80	28.80	17.80
Ce	38.90	56.40	57.20	64.40	42.70	40.40	60.40	57.30	37.70
Pr	4.10	5.60	5.70	6.60	4.40	4.30	6.30	5.70	4.20
Nd	17.30	22.30	22.30	25.90	17.00	17.80	24.40	22.10	16.30
Sm	3.80	4.30	4.50	5.00	3.60	3.70	4.90	4.40	3.50
Eu	1.40	1.40	1.70	1.60	1.20	1.40	1.60	1.60	1.40
Gd	4.70	4.50	5.10	5.20	3.80	3.90	5.70	4.50	4.30
Tb	0.70	0.60	0.70	0.70	0.50	0.60	0.80	0.60	0.60
Dy	3.60	3.40	4.10	4.20	3.00	3.30	4.30	3.40	3.70
Ho	0.60	0.60	0.70	0.90	0.60	0.60	0.80	0.60	0.70
Er	1.70	1.70	1.90	2.00	1.50	1.50	1.90	1.80	1.70
Tm	0.20	0.20	0.20	0.20	0.20	0.20	0.30	0.20	0.20
Yb	1.10	1.00	1.20	1.50	0.90	0.90	1.30	1.00	1.20
Lu	0.10	0.10	0.20	0.20	0.10	0.10	0.20	0.10	0.20

metamorphism conditions are used, indicating that the origin rock is determined as alkali basalt (Figure 12b).

5.2. Tectonic Environment

Tectonic discrimination diagrams are used in order to analyze the Metabasite member of the Söğütlüdere formation (Figure 13). The tectonic discrimination diagram proposed by Agrawal et al. (2008) (Figure 13a) that used trace elements (La, Sm, Yb, Nb and Th) which tend to not behave mobile in low grade alteration and metamorphism, and the tectonic discrimination diagram proposed by Cabanis and Lecolle (1989) diagram that used La/10-Y/15-Nb/8 ternary diagram (Figure 13b) for basic and ultrabasic rocks indicate that the Söğütlüdere formation is assosiated with the. Moreover, the Nb/Yb-TiO$_2$/Yb diagram (Pearce, 2008) was also used to determine tectonic environment that indicates the island arc basalts field with alkali composition are the tectonic environment (Figure 13c).

5.3. Distribution of Trace and Rare Earth Elements (REE)

The multi-element spider diagrams normalized to MORB and chondrite (Figure 14) were used to determine the magma source and nature of the Metabasite members of the Söğütlüdere formation. The main pattern shown that is formed by the samples in the MORB normalized multi-element spider diagram indicate the enrichment of large ion radius lithophile elements (Sr, K, Rb, Ba and Th) and the depletion of Zr, Hf, Y and Yb elements. Since crustal assimilation causes positive Zr and Hf anomalies during magma emplacement (Zhou et al., 2004), the negative Zr-Hf anomalies in the trace element diagram normalized according to MORB can be interpreted as the main magma might not have exposed to crustal contamination. The depletion of Y and Yb indicates the presence of amphibole and/or some garnet in the source (Figure 14a). It is also observed that the light rare earth elements (LREE) are enriched compared to heavy rare earth elements (HREE) in the multi-element distribution diagram normalized to chondrite (Figure 14b).

When the relations between the regional-geological location and the results of the chemical analyses chemical analysis results are examined, the rocks of the metabasite member of the Söğütlüdere formation can be interpreted as the first phase products of rifting that started with the breaking-away of the Tauride-Anatolide Platform in the Triassic period.

6. Geochronology

Two samples were used in order to determine the age of schist and amphibole of the Söğütlüdere formation, using the U/Pb zircon method. Zircons obtained from quartz-rich micaschist (17 N 16 sample) were used
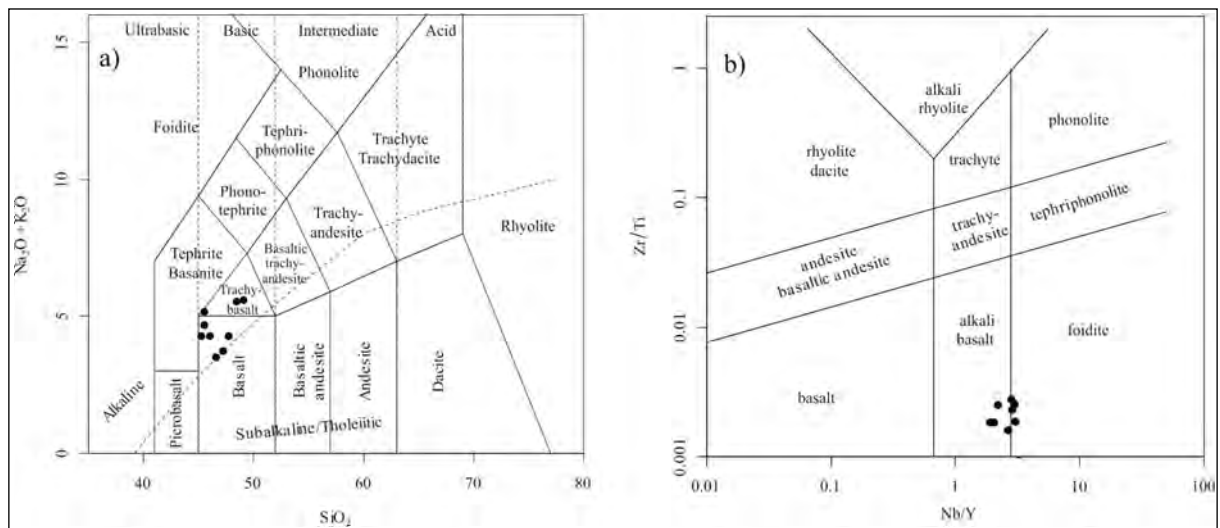
Figure 12- The rock samples of the metabasite member of the Söğütlüdere formation; a) Le Bas et al. (1986), b) Pearce (1996) classification diagrams.
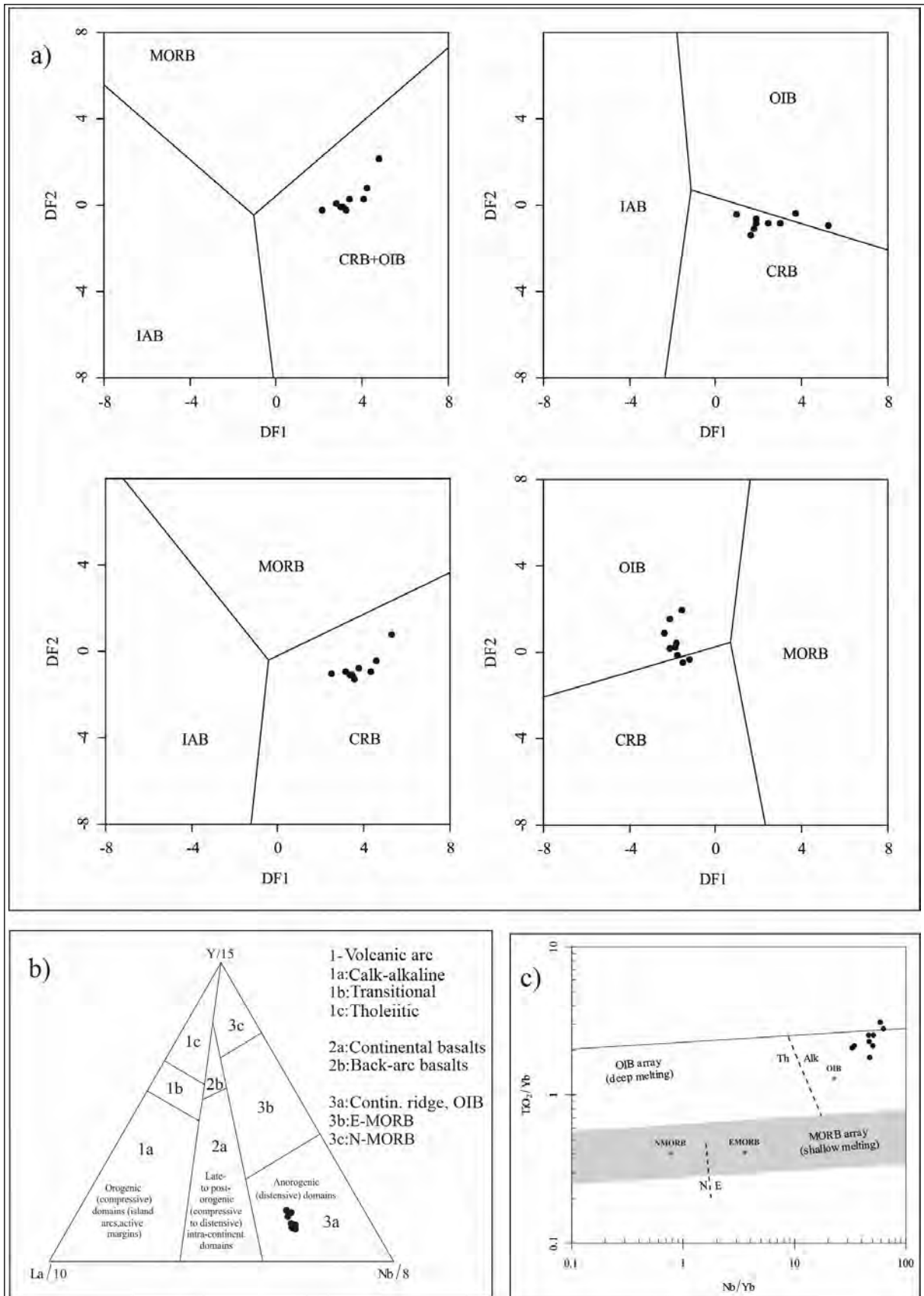
Figure 13- Rock samples of the Metabasite member of the Söğütlüdere formation in the tectonic environment discrimination diagrams; a) Agrawal et al. (2008), b) Cabanis and Lecolle (1989), c) Pearce (2008).
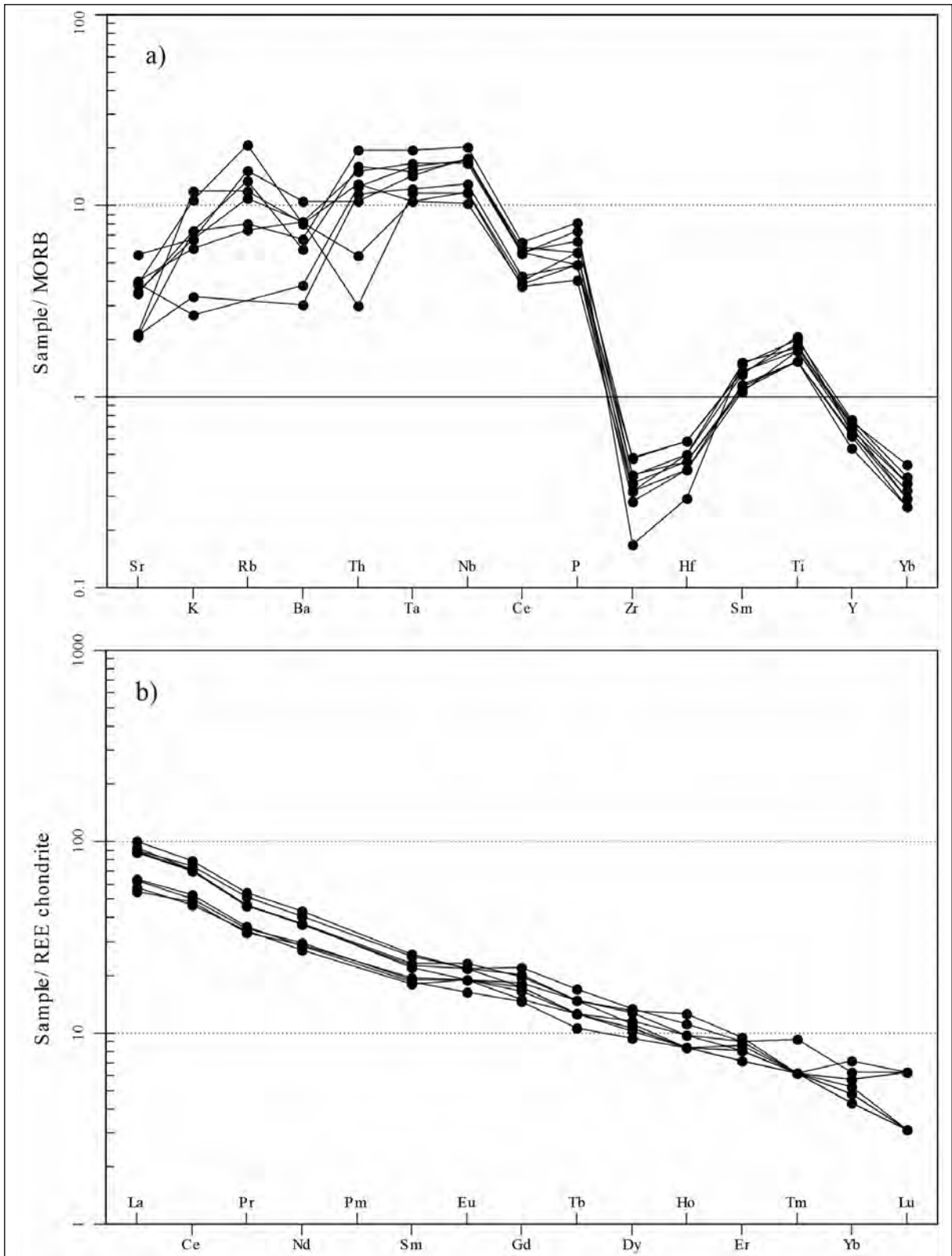
Figure 14- The rock samples of the Metabasite member of the Söğütlüdere formation; a) Multi-element spider diagram of trace elements normalized to MORB (Pearce, 1983), b) Multi-element spider diagram of rare earth elements normalized to chondrite (Boynton, 1984).

for the determine the U-Pb age with the help of LA-ICP-MS technique. The samples were collected from approximately 1 km north of Agapınar Hill and south of Gümüşler village (Adana M33 sheet; UTM ED50 Zone 36 0656960; 4199853). The sample is composed of biotite-muscovite-quartz-plagioclase-rutile-apatite-zircon and shows characteristic lepidoblastic texture. The zircons are acicular-like and not corroded much in the cathodoluminescence images of the examined sample (Figure 15). Grains with slightly rounded edges (gr 35) are also observed in the sample. Most of the grains have oscillating zoning reflecting the magmatic origin. Some grains (i.e gr 25 and 40) contain residual cores.

Analysis results of the samples are given in Table 2. From the analysis of 68 zircons selected from the sample, it was observed that 67 of them gave ages compatible between 90-110% (^{206}Pb/^{238}U age/^{207}Pb/^{235}U age *100) (Figure 16). Carboniferous zircons (301-342 Ma) (37%) (25 grains) and Neoproterozoic zircons (542-979 Ma) (28%) (19 grains) constitute the most abundant age group (Figure 17). Following those, 9% (6 grains) of Permian (253-292 Ma), 6% (4 grains) of Paleoproterozoic (1904-2100 Ma) and Ordovician of (453-473 Ma), 5% (3 grains) of Cambrian (512-532 Ma), 3% (2 grains) of Silurian (423-442 Ma) and Triassic (223-224 Ma)

grains are present. Mesoproterozoic (1012 Ma) and Devonian (402 Ma) ages were obtained from only one zircon grain. Considering the two grains that yield the youngest age (223-224 Ma), the deposition age of the primary rock can be interpreted as Norian or earlier.

The amphibolite (metabasite) sample 17 N 18 was collected from 2 km SW of Keçikalesi Hill, located on the southern border of the study area (Adana M33 sheet; UTM ED50 Zone 36 0651685; 4193730). The rock is predominantly composed of hornblende. It also contains biotite, sphene apatite and opaque minerals. Nematoblastic texture resulting from the parallel orientation of the acicular-like amphiboles is observed in the sample. In order to find the crystallization age of the basaltic rock that forms the primary rock of amphibolite, zircon grains was tried to be enriched, but only two zircons were obtained from the sample. In the cathodoluminescence images of these two zircons (Figure 18), it is observed that the gr 2 zircon has acicular-like texture and oscillating zoning reflecting the magmatic origin. In the second grain (gr 1), only a small section reflecting magmatic zoning remains, while the other sections are zoneless and bright. This shows that this grain has been affected by metamorphism and its textural properties have disturbed. The age obtained based on these textural data was interpreted as the age of metamorphism.
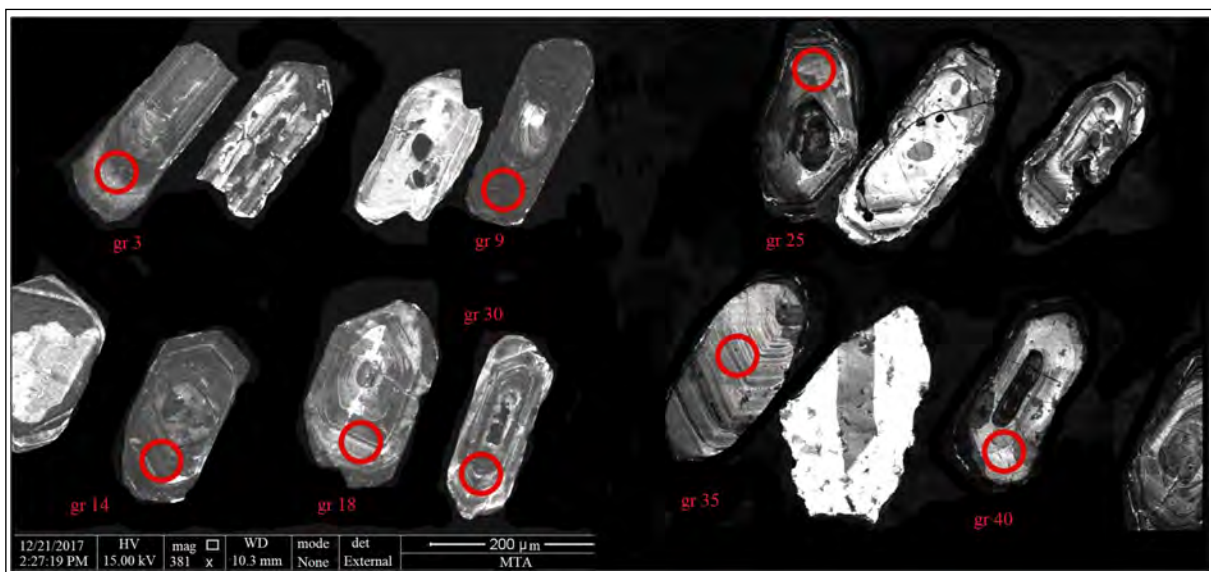
Figure 15- Cathodoluminescence photographs of zircons of quartzschist sample (17 N 16) and analysis spots in selected zircon grains for age determination.

Table 2- Isotope ratios of sample 17 N 16.

	17 N 16 number isotope ratios								Ages (Ma)						
SAMPLE	206Pb•/207Pb•	± (%)	207Pb•/235U•	± (%)	206Pb•/238U	± (%)	Error correlation	206Pb•/238U	± (Ma)	207Pb•/235U•	± (Ma)	206Pb•/207Pb•	± (Ma)	% Concordia 6/8-7/5
gr 1	18.0312	1.2796	0.2684	1.7869	0.0351	1.2473	0.6980	222.5	2.7	241.5	3.8	429 .8	28.5	92
gr 2	18.3990	0.7063	0.2654	1.2802	0.0354	1.0678	0.8341	224.4	2.4	239.0	2.7	384.6	15.9	94
gr 3	18.8394	0.7398	0.2931	1.3880	0.0401	1.1744	0.8461	253.2	2.9	261.0	3.2	331.2	16.8	97
gr 4	14.2255	2.2493	0.4007	2.6097	0.0414	1.3235	0.5071	261.3	3.4	342.2	7.6	936.1	46 .1	76
gr 5	18.0575	1.2200	0.3445	1.5557	0.0451	0.9653	0.6205	284.6	2.7	300.6	4.0	426 .6	27.2	95
gr 6	17.8689	1.1290	0.3569	1.7548	0.0463	1.3435	0.7656	291.6	3.8	309.9	4.7	449 .9	25.1	94
gr 7	18.7095	0.6860	0.3518	1.1575	0.0478	0.9323	0.8055	300.7	2.7	306.1	3.1	346.9	15.5	98
gr 8	18.5659	0.9941	0.3562	1.5904	0.0480	1.2415	0.7806	302.1	3.7	309.4	4.2	364.3	22.4	98
gr 9	18.7384	0.7106	0.3588	1.2253	0.0488	0.9982	0.8147	307.0	3.0	311.3	3.3	343.4	16.1	99
gr 10	18.6591	0.5217	0.3641	1.0264	0.0493	0.8839	0.8612	310.2	2.7	315.3	2.8	353.0	11.8	98
gr 11	18.6286	0.6831	0.3663	1.2864	0.0495	1.0900	0.8473	311.5	3.3	316.9	3.5	356.7	15.4	98
gr 12	18.7706	0.8230	0.3643	1.3765	0.0496	1.1613	0.8437	312.2	3.5	315.4	3.7	339.5	16.7	99
gr 13	18.7375	0.6931	0.3676	1.225 1	0.0500	1.0101	0.8246	314.3	3.1	317.8	3.3	343.5	15.7	99
gr 14	19.0143	0.7577	0.3698	1.3580	0.0510	1.1270	0.8299	320.8	3.5	319.5	3.7	310.3	17.2	100
gr 15	19.0768	0.9015	0.3687	1.5717	0.0510	1.2874	0.8191	320.9	4.0	318.7	4.3	302.8	20.5	101
gr 16	18.9931	1.1023	0.3730	1.3177	0.0514	0.7220	0.5479	323.1	2.3	321.9	3.6	312.8	25.1	100
gr 17	18.9882	0.7490	0.3735	1.4990	0.0515	1.2985	0.8662	323.5	4.1	322.2	4.1	313.4	17.0	100
gr 18	19.0954	0.6534	0.3726	1.3736	0.0516	1.2083	0.8796	324.5	3.8	321.6	3.8	300.6	14.9	101
gr 19	18.8406	0.8230	0.3789	1.3972	0.0518	1.1290	0.8081	326.0	3.6	326.2	3.9	331.1	18.7	100
gr 20	18.6996	0.7232	0.3823	1.2943	0.0519	1.0734	0.8293	325.5	3.4	328.7	3.6	348.1	16.3	99
gr 21	18.5120	0.8065	0.3868	1.5797	0.0519	1.3583	0.8599	326.5	4.3	332.0	4.5	370.8	18.1	98
gr 22	18.7850	0.8483	0.3816	1.2948	0.0520	0.9782	0.7555	326.9	3.1	328.2	3.6	337.8	19.2	100
gr 23	18.2897	0.8611	0.3944	1.4118	0.0523	1.1188	0.7925	328.8	3.6	337.5	4.1	398.0	19.3	97
gr 24	18.3783	1.4207	0.5327	1.6956	0.0710	0.9256	0.5459	442 .4	4.0	433 .6	6.0	387.1	31.9	102
gr 25	17.2123	0.6596	0.6102	1.2637	0.0762	1.0779	0.8530	473 .4	4.9	483 .7	4.9	532.5	14.4	98
gr 26	17.3014	1.9686	0.6588	2.3061	0.0827	1.2012	0.5209	512.2	5.9	513.9	9.3	521.2	43.2	100
gr 27	16.5881	1.4880	0.7034	1.7386	0.0847	0.8992	0.5172	523.9	4.5	540.8	7.3	612.8	32.1	97
gr 28	17.0671	1.0978	0.6940	1.5104	0.0859	1.0374	0.6868	531.5	5.3	535.2	6.3	551.0	24.0	99
gr 29	17.5189	0.8791	0.6893	1.3120	0.0876	0.9739	0.7423	541.5	5.1	532.4	5.4	493 .7	19.4	102
gr 30	16.6802	0.4470	0.7683	0.9069	0.0930	0.7892	0.8701	573.2	4.3	578.8	4.0	600.9	9.7	99
gr 31	15.9337	0.8860	0.8126	1.6329	0.0940	1.3717	0.8400	578.9	7.6	603.9	7.4	699.2	18.9	96
gr 32	16.4480	0.7987	0.8472	1.4905	0.1011	1.2584	0.8443	620.9	7.4	623.1	6.9	631.2	17.2	100
gr 33	15.7785	1.0693	1.0599	1.3738	0.1213	0.8625	0.6278	738.3	6.0	733.8	7.2	720.0	22.7	101
gr 34	8.143 1	0.6641	5.6289	1.3298	0.3326	1.1521	0.8664	1850.9	18.5	1920.5	11.5	1996.6	11.8	96
gr 35	18.8049	1.3748	0.3032	2.3747	0.0414	1.9362	0.8154	261.3	5.0	268.9	5.6	335.4	31.1	97
gr 36	18.5560	0.4013	0.3076	1.1608	0.0414	1.0892	0.9383	261.6	2.8	272.3	2.8	365.5	9.0	96
gr 37	18.6095	0.6384	0.3235	1.1626	0.0437	0.9717	0.8358	275 .6	2.6	284.6	2.9	359.0	14.4	97
gr 38	18.7040	0.5981	0.3649	1.2222	0.0495	1.0659	0.8721	311.6	3.2	315.9	3.3	347.6	13.5	99
gr 39	18.5132	0.7191	0.3729	1.1979	0.0501	0.9580	0.7998	315.1	2.9	321.8	3.3	370.7	16.2	98
gr 40	19.0286	0.6519	0.3648	1.2612	0.0504	1.0796	0.8561	316.8	3.3	315.8	3.4	308.6	14.8	100
gr 41	18.7707	0.5561	0.3702	1.0185	0.0504	0.8532	0.8378	317.1	2.6	319.8	2.8	339.5	12.6	99
gr 42	18.9276	0.6718	0.3674	1.3087	0.0505	1.1231	0.8582	317.3	3.5	317.7	3.6	320.7	15.3	100
gr 43	18.9005	0.6472	0.3764	1.0706	0.0516	0.8528	0.7966	324.5	2.7	324.4	3.0	323.9	14.7	100
gr 44	18.7608	0.7296	0.3826	1.2919	0.0521	1.0662	0.8253	327.3	3.4	328.9	3.6	340.7	16.5	99
gr 45	19.0557	0.7013	0.3931	1.1803	0.0543	0.9493	0.8043	341.2	3.2	336.6	3.4	305.3	16.0	101
gr 46	16.8281	0.7336	0.5272	1.2282	0.0644	0.9851	0.8020	402 .2	3.8	430.0	4.3	581.8	15.9	94
gr 47	16.8797	0.9412	0.5543	1.3166	0.0679	0.9207	0.6993	423 .4	3.8	447 .8	4.8	575.1	20.5	95
gr 48	17.3661	0.9232	0.5771	1.3556	0.0727	0.9926	0.7322	452 .5	4.3	462 .6	5.0	513.0	20.3	98
gr 49	17.5598	0.6366	0.5753	1.3201	0.0733	1.1564	0.8760	456 .0	5.1	461.4	4.9	488.6	14.1	99
gr 50	17.5902	0.7147	0.5930	1.1788	0.0757	0.9374	0.7952	470.3	4.3	472 .8	4.5	484 .8	15.8	99
gr 51	17.1681	0.6047	0.7050	1.1999	0.0878	1.0364	0.8637	542.6	5.4	541.8	5.0	538.1	13.2	100
gr 52	17.5675	1.2434	0.7126	1.8607	0.0908	1.3842	0.7439	560.4	7.4	546.3	7.9	487 .6	27.4	103
gr 53	16.8581	0.6371	0.7523	1.1544	0.0920	0.9627	0.8339	567.5	5.2	569.6	5.0	577.8	13.8	100
gr 54	17.3496	0.9455	0.7312	1.3545	0.0920	0.9699	0.7161	567.6	5.3	557.3	5.8	515.1	20.8	102
gr 55	16.8241	0.7006	0.7587	1.2697	0.0926	1.0588	0.8340	571.0	5.8	573.2	5.6	582.2	15.2	100
gr 56	16.5935	0.6732	0.7853	1.2257	0.0945	1.0243	0.8357	582.4	5.7	588.5	5.5	612.1	14.5	99
gr 57	16.8288	0.7002	0.7990	1.1253	0.0976	0.8810	0.7828	600.1	5.0	596.3	5.1	581.6	15.2	101
gr 58	17.4206	2.2674	0.8180	2.6551	0.1034	1.3815	0.5203	634.3	8.3	606.9	12.1	506.1	49.9	105
gr 59	15.8591	0.7981	1.0076	1.1225	0.1159	0.7894	0.7032	707.2	5.3	707.7	5.7	709.2	17.0	100
gr 60	15.7177	0.6148	1.0294	1.0855	0.1174	0.8946	0.8241	715.6	6.1	718.6	5.6	728.2	13.0	100
gr 61	14.9947	0.8572	1.1786	1.2408	0.1282	0.8971	0.7230	777.8	6.6	790.7	6.8	827.2	17.9	98
gr 62	13.9566	0.8013	1.6199	1.3584	0.1640	1.0969	0.8075	979.2	10.0	978.0	8.5	975.1	16.3	100
gr 63	13.9518	0.7371	1.4430	1.6049	0.146 1	1.4256	0.8883	878.9	11.7	907.0	9.6	975.9	15.0	97
gr 64	13.8720	0.7699	1.6899	1.1580	0.1701	0.8650	0.7470	1012.6	8.1	1004.7	7.4	987.5	15.7	101
gr 65	13.8123	0.6730	1.6290	0.9840	0.1633	0.7179	0.7295	974.8	6.5	981.5	6.2	996.3	13.7	99
gr 66	8.5774	0.6563	5.3987	1.0497	0.3360	0.8192	0.7804	1867.4	13.3	1884.7	9.0	1903.7	11.8	99
gr 67	8.3839	0.7987	5.2208	1.4162	0.3176	1.1695	0.8258	1778.0	18.2	1856.0	12.1	1944.6	14.3	96
gr 68	7.6819	0.6584	6.7624	1.1874	0.3769	0.9882	0.8322	2061.9	17.4	2080.8	10.5	2099 .6	11.6	99
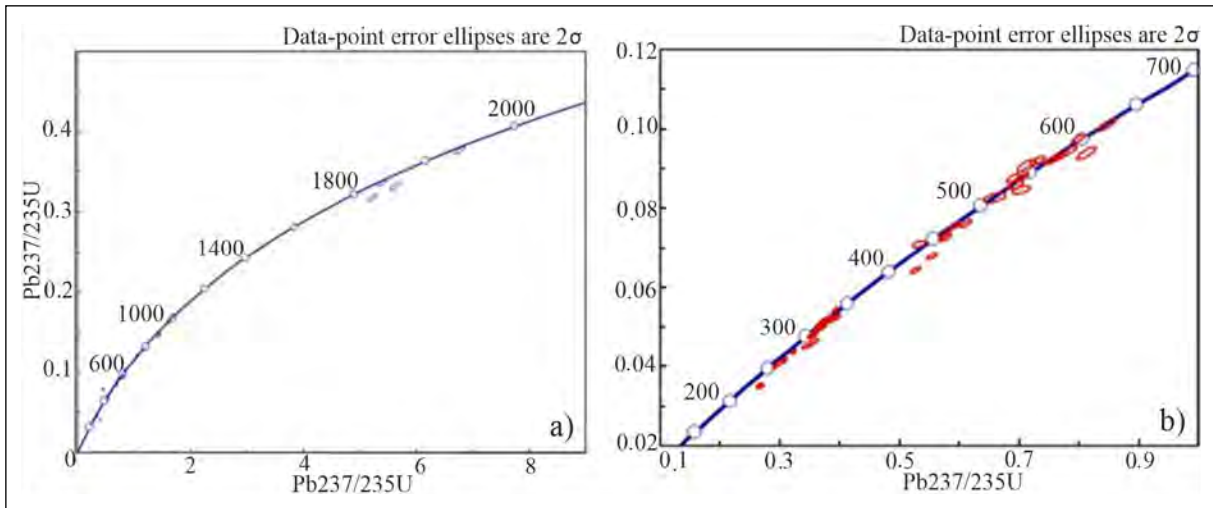
Figure 16- a) All zircons of the sample 17 N 16 on the concordia diagram, and b) the grains younger than 600 Ma on the concordia diagram.
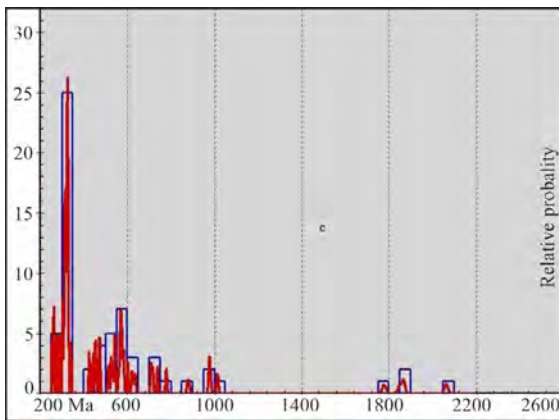
Figure 17- Histogram of sample 17 N 16 showing the age distribution.

An age of 238.5±2.8 Ma (Middle Triassic) was obtained from a zircon grain (gr 2) with a magmatic texture with 99% compatibility (Table 3; Figure 19). The other zircon grain (gr 1) yields an age of 82.7±0.8 Ma (Campanian). It is observed that the first age is compatible with the Triassic depositional age obtained from the previous sample. Campanian can interpreted as metamorphic age considering the tectono-metamorphic evolution of the region.
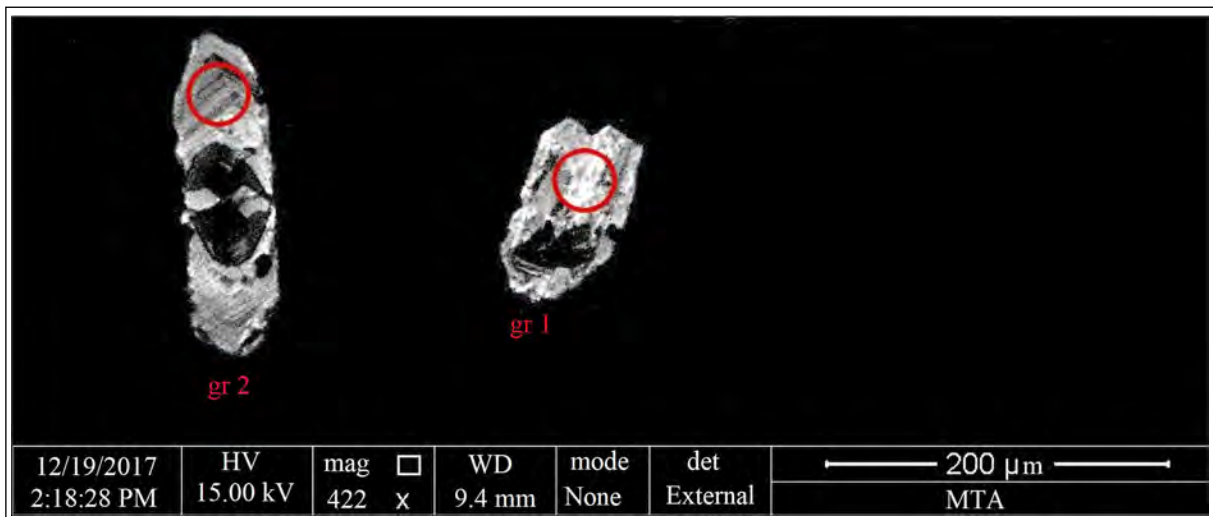
Figure 18- The cathodoluminescence photographs of the zircons of the 17 N 18 amphibolite sample and the analysis spots through the age determination.

Table 3- Isotope ratios of sample 17 N 18.

Isotope Ratios							Apparent Ages (Ma)							
206Pb*	±	207Pb*	±	206Pb*	±	error	206Pb*	±	207Pb*	±	206Pb*	:!:	Best age	±
207Pb*	(%)	235U*	(%)	238U	(%)	corr_	238U*	(Ma)	235U	(Ma)	207Pb*	(Ma)	(Ma)	(Ma)
19.0356	6.0	0.0935	6.1	0.0129	1.0	0.16	82.7	0.8	90.8	5.3	307.7	137.5	82.7	0.8
19.4177	0.7	0.2676	1.3	0.0377	1.2	0.87	238.5	2.8	240.7	2.9	262.3	15.0	238.5	2.8
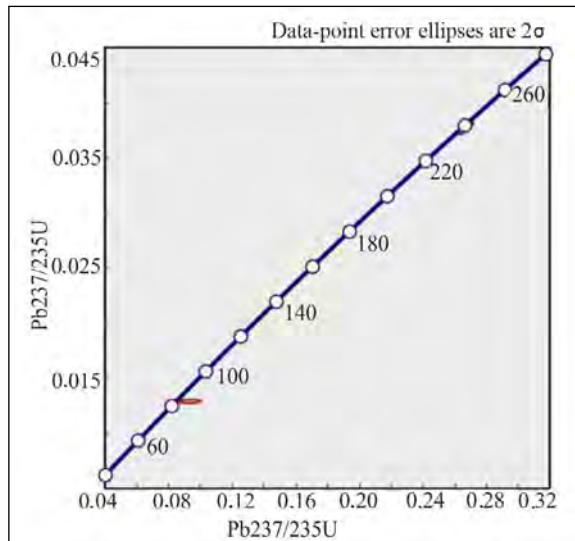
Figure 19- Two zircons aged in sample 17 N 18 on the concordia diagram.

7. Results

The findings obtained from this study and their meaning in terms of regional tectonics can be grouped under four headings:

7.1. Stratigraphy of the Niğde Massif

Paleozoic-Mesozoic was given for the age of the metamorphics of the Niğde Massif which displays very wide range, and it was accepted that it consists of three formations with a conformable contact relationship with each other in previous studies. In this study, the Late Devonian, Carboniferous-early Permian and late Permian deposits representing a conformable and transitional succession and a total of six Triassic, Jurassic-Cretaceous and Late Cretaceous formations overlying and unconformably separated from each other were distinguished. Niğde group by Göncüoğlu (1981) and the Kaleboynu and Gümüşler formations defined by Atabey et al.

(1990) under Niğde metamorphic sequence were generally distinguished in the same way in this study, although there are minor differences in the definition. However, a significant part of the marbles, which is included in the Gümüşler formation by Atabey et al. (1990), was distinguished as the Jura-Cretaceous Kırtepe formation, which unconformably overlies the older units in the metamorphic succession. On the other hand, previous researchers have defined the Aşıgediği formation considering very different lithofacies together; however, four formations within this unit have been defined in this study as the Triassic Söğütlüdere, Jurassic-Cretaceous Kırtepe, Late Cretaceous Kırkpınar formation and late Permian Kızıldağı formation seperated with unconformable contacts (Figure 20). Thus, the stratigraphy of the Niğde Massif is completely renewed and the Late Devonian-Late Cretaceous formation partly separated from each other by unconformities that have been distinguished.

7.2. Age and Tectonic Environment of Basic Volcanism

The unit (Söğütlüdere formation) of the amphibolite sample used for radiometric dating. This unit is unconformably underlain by the marbles of late Permian Bozçaldağ formation and is unconformably overlain by the Jurassic-Cretaceous marbles. Furthermore, it displays characteristics that can be correlated with similar Lower-Middle Triassic successions in the Taurus Mountains (Geyikdağı unit, Aladağ nappe, also Bodrum nappe, Bolkardağı nappe). The 239 Ma (Middle Triassic) zircon U/Pb age obtained from the amphibolite sample is consistent with these stratigraphic data and shows that the common basic magmatism in the Niğde Massif is Triassic in broad sense. The geochemical results of the amphibolites indicate that the basic magmatism is associated with alkaline composition and displays anorogenic character. Geochemical, geochronological
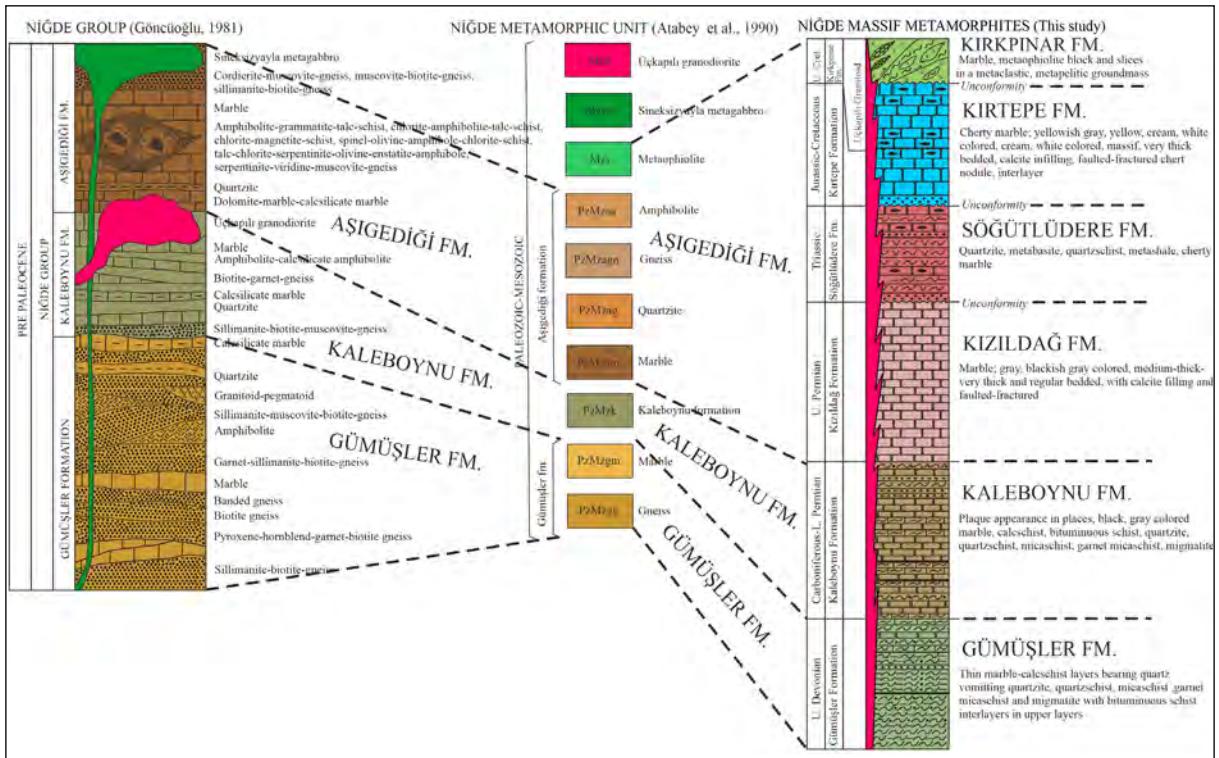
Figure 20- Correlation sections of the Niğde Massif metamorphics.

data and stratigraphic observations show that volcanism during the Triassic indicates an extensional tectonic environment that developed in a continental crust.

7.3. Source Rock Problem of the Triassic Metaclastics

In recent years, studies on the determination of source rocks of clastic rocks have become very popular and many articles have been published on this subject. Detritic zircon geochronology has been widely used for these type of further provenance studies (Fedo et al., 2003), which helps to approach paleogeographic position of a tectonic unit in a given period of time. The Istanbul Zone (Okay et al., 2011), Sakarya Zone (Akdoğan et al., 2019; Ustaömer et al., 2016), Taurus (Ustaömer et al., 2019), Menderes (Zlatkin et al., 2013) and Bitlis (Ustaömer et al., 2012) massifs and Karaburun-Chios (Meinhold et al., 2008; Löwen et al., 2017) have been especially studied using this technique. For this purpose, clastic zircon dating was carried out using the U/Pb method from a schist sample of the Middle-Late Triassic Söğütlüdere formation in the Niğde Massif. Results of 67 analysis spots with 90-110% concordance are as they are given;

4 grains of (6%) Paleoproterozoic (1904-2100 Ma), 1 grain of Mesoproterozoic (1012 Ma), 19 grains of (29%) Neoproterozoic (542-979 Ma), 3 grains of (5%) Cambrian (512-532 Ma), 4 grains of (6%) Ordovician (453-473 Ma), 2 grains of (3%) Silurian (423-442 Ma), 1 grains of Devonian (1%) (402 Ma), 25 grains of (38%) Carboniferous (301- 342 Ma), 6 grains of (9%) Permian (253-292 Ma) and 2 grains of (3%) Triassic (223-224 Ma) (Figure 17). Neoproterozoic (29%) and Carboniferous (38%) zircons constitute the two dominant populations in the rock. Some zircons of the Paleozoic period are also present apart from those. Among the Precambrian zircons in the sample, Neoproterozoic ones constitute the dominant group, while 4 Paleoproterozoic zircons accompany them. The sample clearly contains voids in terms of Mesoproterozoic zircon (1 unit) (Figure 17). It is commonly accepted that the Gondwana completed its amalgamatiom process in the early Cambrian (Torsvik and Cock, 2013). Magmatic and metamorphic processes along the northern margin of supercontinent has critical importance to understand the positions of primary paleogeographic positions of the microplates, which was broken away from that margin and drifted

towards northerly. The region around the Amazon Craton to the west is characterized by the widespread presence of Mesoproterozoic (1600-1000 Ma) zircons associated with the Greenville Orogeny (1250-980 Ma). The West African Craton is defined by the presence of approximately 2000 Ma of magmatic activity (Altumi et al., 2013). The Arabian-Nubian Shield and the Saharan Metacraton are characterized by the presence of extensive Neoproterozoic (Cryogenic-Ediacaran) magmatism (Johnson and Kattan, 2007; Johnson et al., 2011; Robinson et al., 2014; references therein) towards east especially throughout the Northeast Africa. Considering the zircon population in the sample used for geochronological studies, 2000 Ma and 1250-980 Ma (Mesoproterozoic) grains are extremely poor in terms of zircon (2 in total), on the contrary, Neoproterozoic zircons constitute the second dominant peak with a rate of 29%. These data point to the Saharan Metacraton and the Arabian-Nubian Shield in Northeast Africa as the source rock of the Precambrian zircons for the sample of the Söğütlüdere formation. This possibility is also compatible with the modern idea of the north of Arabia, which was proposed for the pre-Triassic paleogeographic location of the Taurus Mountains based on various geological data (Şengör and Yılmaz, 1981; Şengör et al., 1984; Stern, 1994; Stampli and Borel, 2002; Monod et al., 2003; Gessner et al., 2004; Linnemann et al., 2007; Ustaömer et al., 2009). The most dominant zircon assemblage in the sample is Carboniferous with a rate of 38%.

As well documented (Okay and Topuz, 2017, references therein), the southern margin of Laurussia is characterized by the Pelagonian Zone in Greece (315-275 Ma; Anders et al., 2007) and the Cyclades (317 Ma; Engel and Reischmann, 1998) (Central European crystalline basements in the West), Caucasus in the east (331-325 Ma; Gamkrelidze et al., 2011), the Carboniferous high temperature metamorphism of the Variscan basement of the Sakarya Zone (345-310 Ma; Topuz et al., 2007; Ustaömer et al., 2013) and existence of accompanying widespread syn-post metamorphic plutons (325-310 Ma; Topuz et al., 2010, 2020; Ustaömer et al., 2013). In recent years, Carboniferous zircons form an extremely dominant assemblage, especially in the zircon dating of the Taurus (Ustaömer et al., 2019), Konya mélange (Löwen et al., 2018, 2019) and Karaburun-Chios mélange (Löwen et al.,

2017) clastics and the Variscan crystalline basement was predicted as the source rock and the southern edge of Laurussia as the paleogeographic location based on the data obtained. However, new findings obtained in recent years indicate the presence of Carboniferous magmatism, which is generally associated with a short-term subduction or extensional regime in the northern margin of the Gondwana (Teke Dere; Robertson and Ustaömer, 2009; Feke unit/Saimbeyli; Dalkılıç, 2009; Çataloturan/Eastern Taurus; Göncüoğlu et al., 2007; Afyon Zone; Candan et al., 2016; Binboğa metamorphics; Robertson et al., 2021). Ustaömer et al. (2019) revealed that these zircons do not match with the Laurussian magmatic activity based on the Hf isotope values of the zircons selected in Triassic sandstones of the Taurus Mountains. When the stratigraphic similarities of the Niğde Massif metamorphites with the Taurus units and the data that the Anatolide-Tauride Block remained connected to Gondwana until the Triassic are evaluated together, Carboniferous magmatism development on the northern margin of the Gondwana can be predicted as the source rock of the zircons in the Söğütlüdere formation clastics. In the aged sample, the presence of Ordovician, Silurian and Devonian zircons was also detected in addition to these zircons. Until recently, problems have been experienced in the source rock interpretations of these aged detrital zircons in the Taurus units. However, radiometric data in recent years have revealed the presence of magmatism at these ages on the northern margin of the Gondwana. Topuz et al. (2021) suggested the 430-440 Ma (Late Ordovician-Silurian) aged anorogenic metagranites associated with the opening process of the Paleotethys Ocean in Ağrı/Taşlıçay. The presence of the Ordovician metagranites (467 Ma) is also known in the Tavşanlı Zone (Okay et al., 2008). In addition to these, two Triassic zircon grains were dated in the sample. Widespread presence of Triassic magmatic activity in the north of Gondwana (Karaburun 247 Ma, Akal et al., 2011; Menderes Massif 246-235 My, Koralay et al., 2001; Afyon Zone 250-229 Ma, Akal et al., 2012; Özdamar et al., 2013).) has been documented in many studies.

The Northeast African/Saharan Metacraton and the Arabian-Nubian Shield can be interpreted as the source area of the Precambrian zircons from the sample dated based on the data and results presented above.

For the Paleozoic-Triassic zircons in the sample, the periodic extensional regimes and magmatic activities associated with short-term subduction on the northern margin of Gondwana can be suggested as the source rocks.

7.4. The Position of Basic Volcanism in Regional Tectonics

The similarities of the Paleozoic succession of the Niğde Massif within the Kırşehir Block, which was defined as the continental block in previous studies, to the Arabian Plate (Perinçek, 1990) and Taurus units (Özgül, 1976; Özgül and Kozlu, 2002) indicate that this continental block remained attached to north of the Gondwana during the Paleozoic. The findings until nowadays show that the northern margin of the Gondwana has been affected by periodic extensional regime since the Early Paleozoic and short-term subduction in the Carboniferous (Candan et al., 2016; Robertson et al., 2021). As a result of these extension processes, it is widely accepted that continental fragments broke away from the north of the Gondwana during the Early Paleozoic-Early Mesozoic interval and were drifted northward and amalgamated to the continental fragments in the north (the fragments constituing the Laurussia in broad sense) (Von Raumer and Stampfli, 2008; Stampfli et al., 2013; Torsvik and Cocks, 2013 and references therein). It is suggested that Avalonia was the first continental fragment broken away from the north of the Gondwana (the part of Amazonia and West African cratons) associated with the opening of the Reich Ocean in the Middle Ordovician (~470 Ma), which is resulted in Caledonian Orogeny, and amalgamated with Laurentia and Baltica to form Laurussia in the north during late Silurian (~420 Ma) (Stampfli and Borel, 2002; references in Von Raumer and Stampfli, 2008). The second continental fragment broke away from the northern part of Gondwana is called the Armorica Continent, especially in Central Europe, although it is defined by different names in many studies (Stampfli and Borel, 2002; Stampfli et al., 2013 and references therein). It is generally accepted this continental fragment was broken away from the North Africa and breaking-away processes resulted in the opening of the Paleotethys Ocean. However, the timing of the opening of the Paleotethys Ocean and whether this opening occurred at the same

time along the North Africa is still controversial today. New geochemical and geochronological findings indicate that this opening took place in the Balkans and Türkiye around 440 Ma (Late Ordovician-early Silurian) (Topuz et al., 2020, 2021). This continental fragment collided with Laurussia in the north and Pangea was formed during the Late Carboniferous in the following stage (Muttoni et al., 2003; Stampfli et al., 2013). High-grade metamorphism and accompanying widespread magmatism (Variscan Orogeny) commonly observed in Central Europe and its eastern extension, Balkan countries, Sakarya Zone and Caucasus (Okay and Topuz, 2017) are associated with this collision and supercontinent formation. The extension process that was present along the northern margin of the Gondwana in the Early Triassic is associated with the opening of the Neotethys oceans, which largely shaped the present geological structure of the Eastern Mediterranean, and the breaking-away of the Anatolide-Tauride Block from the Gondwana. It is suggested that the Neotethys Ocean system was formed by the formation of two new oceans as the northern and southern branches in the previous studies (Şengör and Yılmaz, 1981; Okay et al., 2006). However, the new findings especially from the Sakarya Zone in recent years indicate Paleotethys Ocean subducted beneath southern margin of the Laurassia during the late Carboniferous or late Permian (Topuz et al., 2004) towards north and commenced to closure and it is suggested that this oceanic area existed until the continental collision in the Eocene (Okay, 2000; Okay and Nikishin, 2015; Okay et al., 2020). In summary, the current dominant suggestion is that the northern branch of the Neotethys Ocean did not open and the Anatolide-Tauride Block was broken away from the Gondwana as a result of the Southern Branch of the Neotethys Ocean opening in the Triassic (Göncüoğlu et al., 2003; Okay et al., 2006). The Kırşehir Block is interpreted as an isolated continental fragment within the Tethys Ocean in almost all of the paleogeographic maps within this general tectonic framework (Barrier et al., 2018). The boundary between the Kırşehir Block and the Anatolide-Tauride Block is defined as a suture zone in the tectonic map of Türkiye (Okay and Tüysüz, 1999). This boundary corresponds a former subduction zone considering the suggestions of the Late Cretaceous high-pressure metamorphism belt (Afyon Zone) along this boundary (Candan et al.,

2005; Pourteau et al., 2010) and the ophiolitic rocks in Mersin region derived from the same area (Parlak ve Robertson, 2004) and it indicates existence of an oceanic area between the Anatolide-Tauride Block and the Kırşehir Block in Mesozoic period. Only limited data is available for the opening of this oceanic area, which is called the Inner Tauride Ocean and Görür et al. (1984) suggests Early Jurassic.

Field observations and geochemical/geochronological data on the studied amphibolites indicate that initiation of the rifting in Anatolide-Tauride block, opening of the Inner Tauride Ocean and breaking-away processes of the Kırşehir Block occured during Middle-Late Triassic period in terms of long-term periodic extensional processes along the northern margin of the Gondwana. These new findings reveal that the Anatolide-Tauride Block and the Kırşehir Block were contemporaneously broken-away from the northern part of Gondwana.

Acknowledgements

References

Advokaat, E. L., Van Hinsbergen, D. J. J., Kaymakçı, N., Vissers, R. L. M., Hendriks, B. W. 2014. Late Cretaceous extension and Palaeogene rotation-related contraction in Central Anatolia recorded in the Ayhan-Büyükkışla basin. International Geology Review 56(15), 1813-1836.

Agrawal, S., Guevara, M., Verma, S. 2008. Tectonic discrimination of basic and ultrabasic volcanic rocks throughlog-transformed ratios of immobile trace elements. International Geology Review 50, 1057-1079.

Akal, C., Koralay, E., Candan, O., Oberhansli, R., Chen, F. 2011. Geodynamic Significance of the Early Triassic Karaburun Granitoid (Western Turkey) for the Opening History of Neo-Tethys. Turkish Journal of Earth Science 20, 255-271.

Akal, C., Candan O., Koralay E., Oberhansli R., Chen, F., Prelevic, D. 2012. Early Triassic potassic volcanism in the Afyon Zone of the Anatolides/Turkey: implications for the rifting of the Neo-Tethys. International Journal of Earth Sciences 101, 177-194.

Akdoğan, R., Okay, A. I., Dunkl, I. 2019. Striking variation in the provenance of the Lower and Upper Cretaceous turbidites in the central Pontides (northern Turkey) related to the opening of the Black Sea. Tectonics 38, 1050-1069.

Altumi, M., Elicki, O., Linnemann, U., Hofmann, M., Sagawe, A. 2013. A U-Pb LA-ICP-MS detrital zircon ages from the Cambrian of Al Qarqaf Arch, central-western Libya: Provenance of the West Gondwanan sand sea at the dawn of the early Palaeozoic. Journal of African Earth Sciences 79 (2013) 74-97.

Alpaslan, M., Frei, R., Kurt, M. A., Boztuğ D., Temel, A., Göncüoğlu, G., Gül, M., Uçurum, A. 2006. Ulukışla havzasının evrimine petrolojik bir yaklaşım. 59. Türkiye Jeoloji Kurultayı, 20-24 Nisan 2006, Ankara, 46-47.

Anders, B., Reischmann, T., Kostopoulos, D., Lehnert, O., Matukov, D., Sergeev, S. 2007. Zircon geochronology of basement rocks from the Pelagonian Zone, Greece: constraints on the pre Alpine evolution of the western most Internal Hellenides. International Journal Earth Science 96, 639-661.

Atabey, E., Göncüoğlu, M. C., Turhan, N. 1990. 1/100000 ölçekli Açınsama Nitelikli Türkiye Jeoloji Haritaları Serisi, Kozan-J19 Paftası, No: 33. Maden Tetkik ve Arama Genel Müdürlüğü, Ankara.

Aydın, N. S., Göncüoğlu, M. C., Erler, A. 1998. Latest Cretaceous magmatism in the Central Anatolian crystalline complex: review of field, petrographic and geochemical features. Turkish Journal of Earth Sciences 7, 259-268.

Bailey, E. B., Mc Callien, W. J. 1950. Ankara melanjı ve Anadolu şariyajı. Bulletin of the Mineral Research and Exploration 15(40).

Barrier, E., Vrielynck, B., Brouillet, J. F., Brunet, M. F. 2018. Paleotectonic reconstruction of the Central Tethyan realm. tectonono-sedimentary-palinspastic maps from Late Permian to Pliocene. DARIUS project maps.

Baykal, E. 1947. Zile-Tokat-Yıldızeli bölgesinin jeolojisi. İstanbul Üniversitesi Fen Fakültesi Dergisi 12(3), B, 191-209.

Beyazpirinç, M., Akçay, A. E. 2017. Akdağmadeni Masifi'nin jeolojisi ve jeodinamik evrimi. Maden Tetkik ve Arama Genel Müdürlüğü, Rapor No: 13569, 166, Ankara (unpublished).

Beyazpirinç, M., Akçay, A. E., Özkan, M. K., Sönmez, M. K., Dönmez, M. 2020. Kırşehir Masifi'nin tektono-stratigrafik özellikleri. Maden Tetkik ve Arama Genel Müdürlüğü, Rapor No: 13934, 200, Ankara (unpublished).

Blumenthal, M. M. 1952. Das taurische hochgebirge des Aladağ, neuere forschungen zur seiner geographie, stratigraphie und tektonik. Maden Tetkik ve Arama Enstitüsü Yayın serisi 6, 136.

Boztuğ, D., Jonckheere, R. C., Heizler , M., Ratschbacher, L., Harlavan, Y., Tichomirova, M. 2009. Timing of post-obduction granitoids from intrusion through cooling to exhumation in central Anatolia, Turkey. Tectonophysics 473(1-2), 20, 223-233.

Boynton, W. V. 1984. Cosmochemistry of the rare earth elements; meteorite studies. Rare earth element geochemistry. Henderson, P. (Ed.). Elsevier, Amsterdam, 63-114.

Cabanis, B., Lecolle, M. 1989. Le diagramme La/10-Y/15-Nb/8: un outilpour la discrimination desséries volcaniques et la mise en évidencedes processus de mélange et/ou de contamination crustale. Comptesrendus de l'Académiedes sciences. Série 2, Mécanique, Physique, Chimie, Sciences de l'univers. Sciences de la Terre 309, 2023-2029.

Candan, O., Çetinkaplan, M., Oberhansli, R., Rimmele, G., Akal, C. 2005. Alpine high-pressure/low temperature metamorphism of Afyon Zone and implication for metamorphic evolution of western Anatolia, Turkey. Lithos 84, 102-124.

Candan, O., Akal, C., Koralay, O. E., Okay, A. I., Oberhänsli, R., Prelević, D., Mertz-Kraus, R. 2016. Carboniferous granites on the northern margin of Gondwana, Anatolide-Tauride Block, Turkey-Evidence for southward subduction of Paleotethys. Tectonophysics 683, 349-366.

Cengiz Çinku, M., Hisarli, Z. M., Yılmaz, Y., Ülker, B., Kaya, N., Öksüm, E., Orbay, N., Özbey, Z. Ü. 2016. The tectonic history of the Niğde-Kırşehir Massif and the Taurides since the Late Mesozoic: Paleomagnetic evidence for two-phase orogenic curvature in Central Anatolia. Tectonics 35, 772-811.

Clark, M., Robertson, A. H. F. 2002. The role of the Early Tertiary Ulukısla basin, Southern Turkey, in suturing of the Mesozoic Tethys Ocean. Journal of the Geological Society of London 159, 673-690.

Çemen, I., Göncüoğlu, M. C., Dirik, K. 1999. Structural evolution of the Tuzgölü basin in central Anatolia, Turkey. Journal of Geology 107, 693-706.

Çoban, M. 2019. Niğde Masifi'nin doğu kesiminin (Eynelli-Bademdere-Dikilitaş) jeolojisi ve yapısal özellikleri. Yüksek Lisans Tezi, Konya Teknik Üniversitesi, 133 (unpublished).

Dalkılıç, H. 2009. 1/100.000 ölçekli Türkiye Jeoloji Haritaları, No: 124. Maden Tetkik ve Arama Genel Müdürlüğü, Ankara.

Demircioğlu, R., Eren, Y. 2003. Niğde Masifi (Çamardı-Niğde) Tersiyer yaşlı örtü kayaçlarındaki Oligosen öncesi paleo-gerilme konumu. Süleyman Demirel Üniversitesi Mühendislik ve Mimarlık Fakültesi, 20. Yıl Jeoloji Sempozyumu, 37.

Demircioğlu, R., Eren, Y. 2017. Çamardı (Niğde) yöresinde Niğde Masifi'nin yapısal özellikleri. Bulletin of the Mineral Research and Exploration 154, 15-26.

Demircioğlu, R., Coşkuner, B. 2021. Gümüşler-Özyurt (Niğde) arasının yapısal özellikleri. Alanya Alattin Keykubat Üniversitesi Fen Bilimleri Dergisi 2(3), 120-12.

Dökmeci, İ. 1980. Akdağmadeni yöresinin jeolojisi. Maden Tetkik ve Arama Genel Müdürlüğü, Rapor No: 6953, Ankara (unpublished).

Egeran, E. N., Lahn, E. 1951. Kuzey ve Orta Anadolu'nun tektonik durumu hakkında not. Maden Tetkik ve Arama Dergisi 41, 23-27.

Engel, M., Reischmann, T. 1998. Single zircon geochronology of orthogneisses from Paros, Greece. Bulletin of the Geological Society of Greece 32 (3), 91-99.

Erkan, Y., Ataman, G. 1981. Orta Anadolu Masifi (Kırşehir yöresi) metamorfizma yaşı üzerine K-Ar yöntemi ile bir inceleme. Yerbilimleri Dergisi 8, 27-30.

Erler, A., Bayhan, H. 1995. Orta Anadolu granitoyitlerinin genel değerlendirilmesi ve sorunları. Yerbilimleri 17, 49-67.

Fedo, C. M., Sircombe, K. N., Rainbird, R. H. 2003. Detrital zircon analyses of the sedimentary record.

Hanchar, J. M., Hoskin, P. W. O. (Ed.). Zircon. Reviews in Mineralogy and Geochemistry 53, 277-303.

Gamkrelidze, I., Shengelia, D., Tsutsunava, T., Chung, S. L., Yichiu, H., Chikhelidze, K. 2011. New data on the U-Pb zircon age of the pre-alpine crystalline basement of the Black-Sea-Central Transcaucasian terrane and their geological significance. Bulletin of Georgian National Academy Science 5, 64-76.

Gessner, K., Collins, A. S., Ring, U., Güngör, T. 2004. Structural and thermal history of poly-orogenic basement: U-Pb geochronology of granitoid rocks in the southern Menderes Massif, Western Turkey. Journal of Geological Society 161, 93-101.

Göncüoğlu, M. C. 1977. Geologie des westlichen Niğde Massivs. Doktora Tezi, Bonn Tjniv University, 181 (unpublished).

Göncüoğlu, M. C. 1981. Niğde masifinin jeolojisi. İç Anadolu'nun Jeoloji Simpozyumu, Türkiye Jeoloji Kurumu Yayınları, 16-19.

Göncüoğlu, M. C., Toprak, V., Kuşcu, I., Erler, A., Olgun, E. 1991. Geology of the western part of the Central Anatolian Massif, part 1: southern section. Turkish Petroleum Corporation (TPAO), Report No: 2909, 1-140 (In Turkish).

Göncüoğlu, M. C., Erler, A., Toprak, V., Yalınız, K. M., Kuscu, I., Köksal, S., Dirik, K. 1993. Orta Anadolu Masifinin batı bölümünün jeolojisi. Bölüm 3: Orta Kızılırmak Tersiyer baseninin jeolojik evrimi. Turkish Petroleum Corporation (TPAO), Report No: 3313.

Göncüoğlu, M. C., Turhan, N., Tekin, U. K. 2003. Evidence for theTriassic rift ing and opening of the Neotethyan İzmir-Ankara Ocean, northern edge of the Tauride-Anatolide Platform, Turkey. Bulletin of Geological Society Italy 2, 203-212.

Göncüoğlu, M. C., Çapkınoğlu, Ş., Gürsu, S., Noble, P., Turhan, N., Tekin, U. K., Okuyucu, C., Göncüoğlu, Y. 2007. The Mississippian in the Central and Eastern Taurides (Turkey): constraints on the tectonic setting of the Tauride-Anatolide Platform. Geologica Carpathica 58, 427-442.

Görür, N., Oktay, F. Y., Seymen, İ., Şengör, A. M. C. 1984. Palaeotectonic evolution of the Tuzgölü basin complex, Central Turkey: sedimentary record of a Neo-Tethyan closure. Geological Society of London, Special Publications 17(1), 467-482.

Görür, N., Tüysüz, O., Şengör, A. M. C. 1998. Tectonic evolution of the Central Anatolian basins. International Geology Review 40, 831-850.

Johnson, P., Kattan F. 2007. Geochronologic dataset for precambrian rocks in the Arabian peninsula a catalogue of U-Pb, Rb-Sr, Ar-Ar, and Sm-Nd ages. Open-file Report No: SGS-OF-2007-3 1428 H 2007 G.

Johnson, P. R., Andresen, A., Collins, A. S., Fowler, A. R., Fritz, H., Ghebreab, W., Kusky, T., Stern, R. J. 2011. Late Cryogenian-Ediacaran history of the Arabian-Nubian Shield. A review of depositional, plutonic, structural, and tectonic events in the closing stages of the northern East African orogen. Journal of African Earth Sciences 61, 167-232.

Kara, H., Dönmez, M. 1990. 1/100000 ölçekli Açınsama Nitelikli Türkiye Jeoloji Haritaları Serisi, Kırşehir-G17 Paftası, No:34. Maden Tetkik ve Arama Genel Müdürlüğü, Ankara.

Ketin, İ. 1955. Yozgat bölgesinin jeolojisi ve Orta Anadolu masifinin tektonik durumu. Türkiye Jeoloji Kurumu Bülteni 6, 1-40.

Ketin, İ. 1963. 1/500 000 ölçekli Türkiye Jeoloji Haritası (Kayseri). Maden Tetkik ve Arama Genel Müdürlüğü Yayını, 82, Ankara.

Koralay, O. E., Satır, M., Dora, O. O. 2001. Geochemical and geochronological evidence for Early Triassic calc-alkaline magmatism in the Menderes Massif, western Turkey. International Journal of Earth Sciences 89, 822-835.

Le Bas, M. J., Le Maitre, R. W., Streckeisen, A., Zanettin, B. 1986. A chemical classification of volcanic rocks based on the total alkali-silica diagram. Journal of Petrology 27, 745-750.

Linnemann, U., Gerdes, A., Drost, K., Buschmann, B. 2007. The continuum between Cadomian orogenesis and opening of the Rheic Ocean: constraints from LA-ICP-MS U-Pb zircon dating and analysis of plate-tectonic setting (Saxo-Thuringian zone, northeastern Bohemian Massif, Germany). Geological Society of America, Special Paper 423, 61-96.

Löwen, K., Meinhold, G., Güngör, T., Berndt, J. 2017. Palaeotethys-related sediments of the Karaburun Peninsula, western Turkey: Constraints on provenance and stratigraphy from detrital zircon geochronology: International Journal of Earth Sciences 106(8), 2771-2796.

Löwen, K., Meinhold, G., Arslan, A., Güngör, T., Berndt, J. 2018. Evolution of the Palaeotethys in the Eastern Mediterranean: Age, provenance and tectonic setting of the Upper Palaeozoic Konya Complex and its Mesozoic cover sequence (south-central

Turkey), Geo Bonn 2018, Bonn, Germany, 2-6 September 2018, Abstracts, 61.

Löwen, K., Meinhold, G., Arslan, A., Güngör, T., Berndt, J. 2019. Evolution of the Paleotethys in the Eastern Mediterranean: a multi-method approach to unravel the age, provenance and tectonic setting of the Upper Paleozoic Konya Complex and its Mesozoic cover sequence (south-central Turkey). International Geology Review 62(4), 389-414.

Meinhold, G., Reischmann, T., Kostopoulos, D., Lehnert, O., Matukov, D., Sergeev, S. 2008. Provenance of sediments during subduction of Palaeotethys: Detrital zircon ages and olistolith analysis in Palaeozoic sediments from Chios Island, Greece. Palaeogeography, Palaeoclimatology, Palaeoecology 263, 71-1.

Monod, O., Kozlu, H., Ghienne, W., Dean, W.T., Günay, Y., Herisse, A., Paris, F. 2003. Late Ordovician glaciations in southern Turkey. Terra Nova 15(4), 249-257.

Muttoni, G., Kent, D. V., Garzanti, E., Brack, P., Abrahamsen, N., Gaetani, M. 2003. Early Permian Pangea B to Late Permian Pangea A. Earth and Planetary Science Letters 215, 379-394.

Okay, A. I., Tüysüz, O. 1999. Tethyan sutures of northern Turkey. Geological Society of London, Special Publications 156(1), 475-515.

Okay, A. I. 2000. Was the Late Triassic orogeny in Turkey caused by the collision of an oceanic plateau? Bozkurt, E., Winchester, J. A., Piper, J. A. D. (Ed.). Tectonics and magmatism in Turkey and surrounding area, Geological Society of London, Special Publication 173, 25-41.

Okay, A. I., Satır, M., Siebel, M. 2006. Pre-Alpide Palaeozoic and Mesozoic orogenic events in the Eastern Mediterranean region. Gee, D. G., Stephenson, R. A. (Ed.). European Lithosphere Dynamics. Geological Society of London, Memoirs 32, 389-405.

Okay, A. I., Satır, M., Shang, C. 2008. Ordovician metagranitoid from the Anatolide-Tauride Block, northwest Turkey: geodynamic implications. Terra Nova 20, 280-288.

Okay, N., Zack. T., Okay, A. I., Barth, M. 2011. Sinistral transport along the Trans-European Suture Zone: detrital zircon-rutile geochronology and sandstone petrography from the Carboniferous flysch of the Pontides. Geological Magazine 148(3), 380-403.

Okay, A. I., Nikishin, A. M. 2015. Tectonic evolution of the southern margin of Laurasia in the Black Sea region. International Geology Review 57(5-8).

Okay, A. I., Topuz, G. 2017. Variscan Orogeny in the Black Sea region. International Journal of Earth Sciences 106, 569-592.

Okay, A. I., Zattin, M., Özcan, E., Sunal, G. 2020. Uplift of Anatolia. Turkish Journal of Earth Sciences 29, 696-713.

Özdamar, Ş., Billor, M., Sunal, G., Esenli, F., Roden, M. 2013. First U-Pb SHRIMP zircon and 40Ar/39Ar ages of metarhyolites from the Afyon-Bolkardag Zone, SW Turkey: implications for the rifting and closure of the Neo-Tethys. Gondwana Research 24, 377-391.

Özgül, N. 1976. Torosların bazı temel jeolojik özellikleri. Türkiye Jeoloji Kurumu Bülteni 19, 65-78.

Özgül, N., Kozlu, H. 2002. Kozan-Feke (Doğu Toroslar) yöresinin stratigrafisi ve yapısal konumu ile ilgili bulgular. TPJD Bülteni 14(1), 1-36.

Parlak, O., Robertson, A. 2004. The ophiolite-related Mersin Melange, southern Turkey: its role in the tectonic-sedimentary setting of Tethys in the Eastern Mediterranean region. Geological Magazine 141 (3), 257-286.

Pearce, J. A. 1983. Role of the sub-continental lithosphere in magma genesis at destructive plate margins. Hawkesweoth, C. J., Norry, M. J. (Ed.). Continental basalts and Mantle Xenolithes. Nantwich, Shiva, 230-249.

Pearce, J. A. 1996. A user's guide to basalt discrimination diagrams. Wyman, D. A. (Ed.) Trace Element geochemistry of volcanic rocks: applications for massive sulphide exploration. Geological Association of Canada, Short Course Notes 12, 79-113.

Pearce, J. A. 2008. Geochemical fingerprinting of oceanic basalts with applications to ophiolite classification and the search for Archean oceanic crust. Lithos 100, 14-48.

Perinçek, D. 1990. Hakkari ili ve dolayının stratigrafisi, GDA Türkiye. Türkiye Petrol Jeologları Derneği Bülteni 2, 21-68.

Phillipson, 1915. Reisen und forschungen im westlichen kleinasien. Pett, Mitt., H., 167.

Pourteau, A., Candan, O., Oberhänsli, R. 2010. High-pressure metasediments in central Turkey: constraints on the Neotethyan closure history. Tectonics 29.

Robertson, A. H. F., Ustaömer, T. 2009. Role of Upper Palaeozoic subduction/accretion processes in the closure of Palaeotethys: evidence from the Chios

Melange (E Greece), the Karaburun Melange (W Turkey) and the Teke Dere Unit, SW Turkey. Sedimentary Geology 220, 29-59.

Robertson, A., Parlak, O., Ustaömer, Y. 2021. Late Palaeozoic extensional volcanism along the northern margin of Gondwana in southern Turkey: implications for Palaeotethyan development. International Journal of Earth Sciences 110, 1961-1994.

Robinson, F., Foden, J. D., Collins Payne, A. S. J. L. 2014. Arabian Shield magmatic cycles and their relationship with Gondwana assembly: Insights from zircon U-Pb and Hf isotopes. Earth and Planetary Science Letters 408, 207-225.

Seymen, İ. 1981a. Kaman (Kırşehir) dolayında Kırşehir masifinin stratigrafisi ve metamorfizması. İç Anadolu'nun Jeoloji Simpozyumu, Türkiye Jeoloji Kurumu Bülteni 24(2), 7-14.

Seymen, İ. 1981b. Kaman (Kırşehir) dolayında Kırşehir masifinin metamorfizması. İç Anadolu'nun Jeoloji Simpozyumu, Türkiye Jeoloji Kurumu Bülteni, 24 (2), 101-108.

Seymen, İ. 1982. Kaman dolayında Kırşehir masifinin jeolojisi. Doçentlik Tezi, İstanbul Teknik Üniversitesi Maden Fakültesi, 164, İstanbul (unpublished).

Stampfli, G. M., Borel, G. D. 2002. A plate tectonic model for the Paleozoic and Mesozoic constrained by dynamic plate boundaries and restored synthetic oceanic isochrones. Earth and Planetary Science Letters 196, 17-33.

Stampfli, G. M., Hochard, C., Verard, C., Vilhem, C., Von Raumer, J. 2013. Formation of Pangea. Tectonophysics 593, 1-19.

Stern, R. J. 1994. Arc assembly and continental collusion in the Proterozoic east African orogen: implications for the consolidation of Gondwanaland. Annual Review of Earth Planet Sciences 22, 319-351.

Şahin, M. B. 1991. Başçatak köyü (Akdağmadeni-Yozgat) doğusunun jeolojik ve petrografik özelliklerinin incelenmesi. Yüksek Lisans Tezi, Hacettepe Üniversitesi Fen Bilimleri Enstitüsü, 68, Ankara (unpublished).

Şengör, A. M. C., Yılmaz, Y. 1981. Tethyan evolution of Turkey. A Plate Tectonic Approach. Tectonophysics 75, 181-241.

Şengör, A. M. C., Satır, M., Akkök, R. 1984. Timing of tectonic events in the Menderes Massif, western Turkey: implications for tectonic evolution and evidence for Pan-African basement in Turkey. Tectonics 3, 693-707.

Topuz, G., Altherr, R., Satır, M., Schwarz, M. 2004. Lowgrade metamorphic rocks from the Pulur complex, NE Turkey: implications for pre-Liassic evolution of the Eastern Pontides. International Journal of Earth Sciences 93, 72-91.

Topuz, G., Altherr, R., Schwartz, W.H., Dokuz, A., Meyer, H-P. 2007. Variscan amphibolites-facies rocks from the Kurtoğlu metamorphic complex (Gümüşhane area, Eastern Pontides, Turkey). International Journal of Earth Science 96, 861-873.

Topuz, G., Altherr, R., Siebel, W., Schwarz, W. H., Zack, T., Hasözbek, A., Barth, M., Satır, M., Cüneyt, Ş. 2010. Carboniferous highpotassium I-type granitoid magmatism in the Eastern Pontides: the Gümüşhane pluton (NE Turkey). Lithos 116, 92-110.

Topuz, G., Candan, O., Okay, A.I., Quadt, A., Othman, M., Zack, T., Wang, J. 2020. Silurian anorogenic basic and acidic magmatism in Northwest Turkey: implications for the opening of the Paleo-Tethys. Lithos 356-357, 105302.

Topuz, G., Candan, O., Wang, J., Li, Q., Wuc, F., Yılmaz, A. 2021. Silurian A-type metaquartz-syenite to-granite in the Eastern Anatolia: implications for Late Ordovician-Silurian rifting at the northern margin of Gondwana. Gondwana Research 911-17.

Torsvik, T. H., Cocks, L. R. M. 2013. Gondwana from top to basein space and time. Gondwana Research 24, 999-1030.

Ustaömer, P. A., Ustaömer, T., Collins, A. S., Robertson, A. H. F. 2009. Cadomian (Ediacaran-Cambrian) arc magmatism in the Bitlis Massif, SE Turkey: magmatism along the developing northern margin of Gondwana. Tectonophysics 473, 99-112.

Ustaömer, P. A., Ustaömer, T., Gerdes, A., Robertson, A. H. F., Collins, A. S. 2012. Evidence of Precambrian sedimentation/ magmatism and Cambrian metamorphism in the Bitlis Massif, SE Turkey utilising whole-rock geochemistry and U-Pb LA-ICP-MS zircon dating: Gondwana Research 21, 1001-1018.

Ustaömer, T., Robertson, A.H., Ustaömer, P.A., Gerdes, A., Peytcheva, I. 2013. Constraints on Variscan and Cimmerian magmatism and metamorphism in the Pontides (Yusufeli-Artvin area), NE Turkey from U-Pb dating and granite geochemistry. Geological Society of London, Special Publications 372 (1), 49-74.

Ustaömer, T., Ustaömer, P. A., Robertson, A. H., Gerdes, A. 2016. Implications of U-Pb and Lu-Hf isotopic analysis of detrital zircons for the depositional age, provenance and tectonic setting of the Permian-Triassic Palaeotethyan Karakaya complex, NW Turkey. International Journal of Earth Sciences 105(1), 7-38.

Ustaömer, T., Ustaömer, P., Robertson, A., Gerdes, A. 2019. U-Pb-Hf isotopic data from detrital zircons in late Carboniferous and Mid-Late Triassic sandstones, and also Carboniferous granites from the Tauride and Anatolide continental units in S Turkey: implications for Tethyan Palaeogeography. International Geology Review 62 (9).

Von Raumer J. F., Stampfli, G. M. 2008. The birth of the Rheic Ocean-Early Palaeozoic subsidence patterns and subsequenttectonic plate scenarios. Tectonophysics 461, 9-20.

Winchester, J. A., Park, R. G., Holland, J. G. 1980. The geochemistry of Lewisian semipelitic schists from the Gairloch District, Wester Ross. Scottish Journal of Geology 16, 165-79.

Winchester, J. A., Max, M. D. 1982. The geochemistry andorigins of the Precambrian rocks of the Rosslare Complex, S. E. Ireland. Journal of Geological Society of London 139, 309-19.

Whitney, D. L., Teyssier, C., Dilek, Y., Fayon, A. K. 2001. Metamorphism of the central anatolian crystalline complex, Turkey: influence of orogen-normal collision vs wrench-dominated tectonics on P-T-t paths. Journal of Metamorphic Geology 19, 411-432.

Whitney, D. L., Teyssier, C., Heizler, M. T. 2007. Gneiss domes, metamorphic core complexes, and wrench zones: thermal and structural evolution of the Niğde massif central Anatolia. Tectonics 26, 1-23.

Yalınız, K. M., Göncüoglu, M. C. 1998. General geological characteristics and distribution of the Central Anatolian Ophiolites. Yerbilimleri 20, 19-30.

Zhou, M. F., Lesher, C. M., Yang, Z., Li, J. W., Sun, M. 2004. Geochemistry and petrogenesis of 270 Ma Ni-Cu-(PGE) sulfidebearing mafic intrusions in the Huangshan district, Eastern Xinjiang, Northwest China: implications for the tectonic evolution of the Central Asian orogenic belt. Chemical Geology 209(3-4), 233-257.

Zlatkin, O., Avigad, D., Gerdes, A. 2013. Evolution and provenance of Neoproterozoic basement and lower Paleozoic siliciclastic cover of the Menderes Massif (western Taurides): coupled U-Pb-Hf zircon isotope geochemistry: Gondwana Research 23, 682-700.

Bulletin of the Mineral Research and Exploration

http://bulletin.mta.gov.tr

Production of rare-earth oxides from Eskişehir-Beylikova complex ores

Haydar GÜNEŞ[a], Hüseyin Eren OBUZ[a], Hasan AKÇAY[a], Çiğdem KARA[a] and Ayşe ERDEM[a*]

[a]*Maden Tetkik ve Arama Genel Müdürlüğü Maden Analizleri ve Teknoloji Dairesi, 06800 Ankara, Türkiye*

Research Article

ABSTRACT

In this study, the production technology of barite, fluorite, rare-earth elements, and thorium-bearing rare-earth oxides from the Eskişehir-Beylikova were investigated, and the processes that can be used in the production of thorium-free mixed rare earth oxides were tested. The applied processes are roasting, leaching, solvent extraction and precipitation methods, respectively. After all studies, the optimum roasting temperature and roasting duration are determined as 600 °C and 1 hour. In the extraction stage, the highest leaching efficiency is achieved with 5 M HCl, 1-hour leaching duration, 1/3 solid/liquid ratio and 35 °C leaching temperature. While methyl tri C8-C10 ammonium chloride (Adogen 464) is used for the removal of iron from produced solution, di-(2-ethylhexyl) phosphoric acid (D2EHPA) is used for the removal of thorium. As a result of solvent extraction studies, the solution containing rare earth elements is precipitated under optimum conditions. After precipitation, the product contains 99.65% rare earth oxides.

1. Introduction

Today, engineering studies in the fields of geology, mining, metallurgy and materials have accelerated to balance the supply and demand of rare earth elements (REE), which is one of the main sources of technological developments. Especially the development and usage of permanent magnets made of an alloy of neodymium, iron and boron NdFeB, providing better magnetic properties than the ones before them have had a big impact on improving this field. Due to the usage of these magnets in fields such as electric vehicles and wind turbines, the demand for REEs is constantly increasing. Today, the biggest supplier is China (Cheisson and Schelter, 2019). Considering the increasing worldwide demand and environmental problems caused by REE mines in China, in recent years, the trends towards recycling and alternative mineral resource has started (Sprecher et al., 2014;

Swain and Mishra, 2019). These trends also arise because of strategic reasons. For example, according to the European Commission and other studies, REE is classified as a critical raw material since the price fluctuations in 2011 (European Commission, 2020). The 11th Development Plan, set Türkiye's development vision, and used it as a basic roadmap, aims to develop projects for REEs to meet the raw material needs of the industry, and studies were started for this purpose. The primary REE resources are bastnaesite, monazite and xenotime. Although parisite mineral [Ca(Ce, La)$_2$(CO$_3$)3F], contains lanthanum and cerium and is similar in structure to bastnaesite, cannot be used to produce REE (Obuz et al., 2018). In previous studies, the ore mineral observed in the Eskişehir-Beylikova area were mentioned as barite, fluorite and bastnaesite (Altaş et al., 2018). However, as a result of the recent mineral liberation analysis on the Eskişehir-Beylikova ore, it was determined that the REE-bearing main

Corresponding author: Ayşe ERDEM, ayse.erdem@mta.gov.tr

mineral is Th-parisite (Yeşilören Görmüş et al., 2021). For the evaluation and separation of REE-bearing ores, hydrometallurgy is one of the main methods (Erdem et al., 2021). For the separation and purifications to be carried out in the further stages, the REEs must be transferred to the solution. The process is solving of ores in different solvents such as acids and bases and getting the valuable elements into a solution is called leaching (Krishnamurthy and Gupta, 2015).

In the literature for REE extraction from solids, the soluble forms of REE-bearing minerals are formed by applying a roasting process at first. These processes can be classified as oxidising roasting (Zhao et al., 2018), heating with sulfuric acid (Kul et al., 2008) and chlorination roasting (Chi et al., 2004). In this step in the solution extracted from solid, other elements in the ore structure are also observed depending on ore type and extraction conditions. The solvent extraction technique is used in the separation and purification of the REEs by utilizing some characteristic chemical properties of them (Qi, 2018). This technique is carried out to ensure dispersion of the intended amounts of the required elements by creating two immiscible liquid phases. While one of the phases that are used, includes REE ions the other is the organic components that dissolved in an apolar solvent.

The mentioned organic components are structures that form complexes with metal ions, also called ligands. In this technique, the metal-ligand complexes that are produced by coordination bonds transfer to the organic phase and the desired separation are achieved (Choppin and Morgenstern, 2000; Rydberg et al., 2004; Lawrence, 2010). Sadri et al. (2017) obtained rare earth oxalates by roasting with sulfuric acid at 200 °C, taking to the solution with water, and precipitating with oxalic acid from monazite collected from Marvasat (Iran) placer deposit. Walawalkar et al. (2016), on the other hand, studied REE enrichments from phosphogypsum which is the main by-product of phosphoric acid the leaching by three different acids.

Although the best efficiency is with nitric acid, they argued that hydrochloric acid is more suitable due to the cost of extraction (Walawalkar et al., 2016).

Kursunoglu et al. (2021) used the sulfuric acid roasting technique on bastnaesite-bearing ore instead

of the direct acid leaching method. Then, they obtained rare earth oxalates by taking the obtained solid into a solution with water and precipitating it with oxalic acid directly. After the calcination of these oxalates, the obtained rare earth oxide (REO) product contains 6 % thorium (Th). It is known that this high thorium content will be a problem the matter such as operation and waste management, and so dangerous for human health (Judge and Azimi, 2020). The elements like Fe and Th that come from the mineral after the solution will affect the purity of the solution and may cause problems in the process and must be taken away. For thorium components to be by-products, iron which can display co-execution is emphasized. El Afifi et al. (2019) achieved the elimination of the Th and Fe from chloride solutions containing REE by applying direct precipitation with potassium sulfate and sodium sulfide. However, this technique was not able to provide enough explanation of the output of Th as a by-product. In the study done by Erdem et al. (2020), after the removal of Fe, U and Th from the solution by solvent extraction, the Th recovery process is started. REE solutions which are purified from impurities, can be evaluated by both direct solvent extraction and precipitation-dissolving. In this study, solving and precipitation steps are examined for the next studies in which REE separation will be made. After eliminating the Fe, U and Th impurities from the solution, using the solubility product values, a precipitation method is applied in which impurities that have high concentrations such as Al, Ca, Mn are not present.

2. Raw Material and Technique

2.1 Raw Material and Equipment

The raw ores taken from the Eskişehir-Beylikova area are first subjected to a beneficiation process in General Directorate of Mineral Research and Exploration laboratories. Because of the differences in the grain sizes of the minerals and abrasion resistance, the pre-concentrate production scrubbing method is used primarily. The -10 μm sample obtained as a result of abrasion was subjected to barite flotation and the samples to be used in metallurgical studies were prepared. The pre-concentrate produced as a result of these processes was used in roasting. After the processes, the concentration of fluorite-REE produced from raw minerals is determined

with the X-Ray Fluorescence Spectrometer (XRF) and Inductively Coupled Plasma Atomic Emission Spectroscopy (ICPAES). The roasting temperatures of ore are determined by Differential Thermal Analysis-Thermal Gravity (DTA-TG). All of the acids and chemicals used and di-2-Ethylhexyl phosphoric acid (D2EHPA), tri octyl amine (Alamine 336), and decyl alcohol (1-Decanol) are of analytic quality. Kerosene is acquired from local sources. All of the solvents are directly used without any purification process.

Metal concentration in the solution is determined with the Agilent 725 Series ICP-OES. Concentrations in the solid material were determined with the Thermo Scientific ARL Perform'x 388 XRF. Energy and weight changes with the temperature were determined by SETARAM brand labSys evo model TG-DTA-DSC device.

2.2. Hydrometallurgical Processes

Before solving the solid sample, the roasting experiments are done by a rotary furnace at different temperatures, based on the data obtained from DTA analysis. In these experiments, 700g of sample for each temperature is fed into the preheated oven. By rotating the oven at 30 rpm, the sample was mixed homogeneously at the specified temperature. The sample is placed in a homogeneous temperature area inside the oven and does not overflow. The temperature in the homogeneous temperature area inside the furnace was measured by a thermocouple. After the roasting temperature was determined, experiments were carried out to determine the roasting time at the same temperature. To examine the effect of roasting temperature and time, the extraction time was kept constant for one hour with 5 M HCl with a 1/3 solid/liquid ratio. As a result of the experiments with sulphuric acid (H_2SO_4), hydrochloric acid (HCL) and nitric acid (HNO_3) at different concentrations, the most suitable acid and solid/liquid ratio (1/3,1/4,1/5), extraction time and temperature parameters are determined. The solids prepared at the determined roasting temperature and time were weighed in the required quantities. Then, the solids were slowly added to the acids prepared in the glass beaker placed on the magnetic mixer. After the addition of all the solids, the extraction process is commenced. During the extraction, a Teflon-coated magnetic mixer

was used to ensure that the suspension between the solid-liquid particles was homogeneous. The same diameter beakers and the same mixer were used for all experiments. All experiments were carried out in the same type of magnetic mixer and the mixing speed was kept constant at 550 rpm. When extraction was completed, samples were taken and filtered by using Whatman No: 3 filter paper, a Bühner funnel and Nuce flask. The solid remaining on the filter paper was washed with pure water. The volume of the solution produced from solid-liquid separation is determined and analysed in the ICP-OES device. The remaining solid was dried at 105 °C for 24 hours. The remaining solid was weighed and analysed by XRF. Solvent extraction experiments were carried out in a glass beaker and mixed with a Teflon propeller in a two-phase mechanical mixer. As a result of solvent extraction experiments performed with determined parameters (Erdem et al., 2020), inlet and outlet solutions were analysed and loading rates were determined.

For REE precipitation from the solution, 0,8 mole/l oxalic acid solution was used. REE/oxalate mole ratio, precipitation temperature and time parameters were investigated. As a result of the examination, the parameters with the most REE and the least impurity precipitated were determined. To determine the mixing time, the sample was taken and filtered by calculating the time elapsed since the oxalic acid was added. The filtrate was concentrated with nitric acid to prevent further precipitation.

2.3. Evaluation of the Data

The weight loss values observed in the roasting step are calculated by the formula in Equation 1. In this formula the m_{input} represents the mass entering the roasting and the m_{output} represents the mass of the final product.

$$\% \, weight \, loss = \frac{m_{input} - m_{output}}{m_{input}} \tag{1}$$

The solving rate calculated over the metal concentration at the extraction stage is presented in Equation 2. In equation 2 C_{sol} represents the metal concentration as mg/l in the solution detected by ICP-OES, $_{Vstock}$ represents the volume of solution after washing as litre, C_{solid} represents the concentration of

the metal as mg/kg in the input solid which wishes to take into to solution, and m_{input} is the weight of input solid as kg.

$$Solving\ rate\ (from\ liquid) = \frac{C_{sol} - V_{stock}}{c_{solid} x m_{input}} \qquad (2)$$

The data obtained from the measurement XRF was evaluated in Equation 3.

In Equation 3, C_{input} represents the percent concentration of metal wished to calculate to solving rate in the input solid material, m_{input} weight of the input solid, C_{output} percent concentration of the metal wish to calculate to solving rate in the output solid material, m_{output} weight of the output solid.

$$Solving\ rate\ ion\ (from\ solid) = 1 - \frac{C_{output} - m_{output}}{C_{input} x m_{input}} \qquad (3)$$

The precipitation rate is calculated by Equation 4.

In Equation 4, $Coutput$ represents the metal concentration value in mg/l of remain in solution after precipitation, $Cinput$ metal concentration value in mg/l of solution before precipitation, $Voutput$ is the measured volume after precipitation, $Vinput$ is the volume of precipitated solution in litre.

$$Precipitation\ rate = 1 - \frac{C_{output} - V_{output}}{C_{input} x V_{input}} \qquad (4)$$

3. Experimental Results

3.1. Raw Material Categorization

The contents of the fluorite-REE pre-concentrate obtained from the Eskişehir-Beylikova complex ore determined by the XRF are presented in Table 1. The pre-concentrated ore contains a total of 8.55% rare earth oxide (TREO). DTA-TG analysis was carried out to determine the roasting temperature before the extraction experiments. The DTA-TG analysis result is presented in Figure 1.

Table 1- Composition of Fluorite-REE pre-concentrate obtained from Eskişehir - Beylikova region.

Oxide	CeO_2	La_2O_3	Nd_2O_3	Pr_6O_{11}	Y_2O_3	Er_2O_3	ThO_2	U_3O_8
Composition (%)	4.52	2.92	0.75	0.26	0.09	0.01	0.38	0.03
Oxide	BaO	Fe_2O_3	CaF_2	SiO_2	Al_2O_3	MnO	MgO	LOI
Composition (%)	5.81	9.84	31.8	14.2	6.6	1.66	1.08	12.6
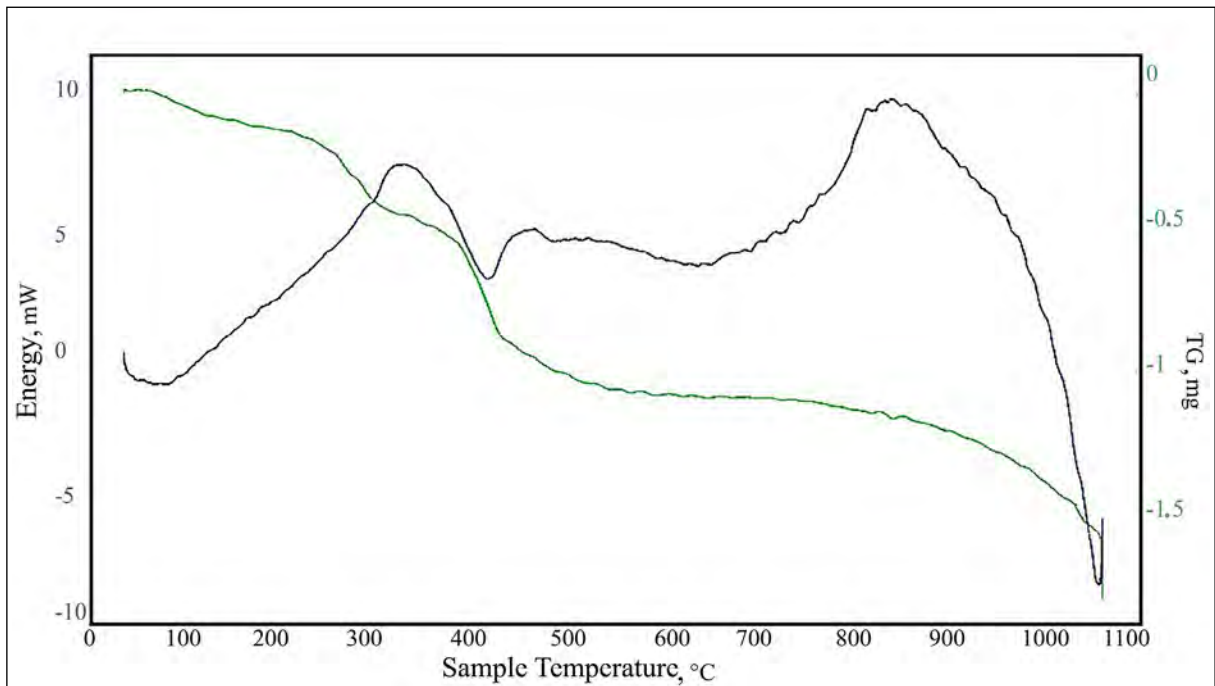
Figure 1- DTA-TG analysis of the Fluorite-REE pre-concentrate obtained from the Eskişehir - Beylikova region.

As a result of the DTA analysis, it was observed that an endothermic reaction happens at a temperature of 414°C. This reaction was compared with later X-Ray diffraction analysis (XRD) analyses and it was determined that the roasting process should be started at 400 °C. The weight loss data obtained in TG analysis is determined as 1.3% in the 210 - 330°C and 2% in the 365 - 470°C range.

3.2. Roasting and Extraction Optimisation

The ore samples were roasted for 1 hour at 400, 500 and 600°C, respectively, and then extracted with HCl. The results obtained with Equation 3 are presented in Figure 2.

As seen in Figure 2, the solving rate increases between the temperatures of 400-600°C, and the rate decreases when the temperature is increased further. The solving rate of total rare earth element (T-REE) increased to 89%, at 600 °C which is the maximum temperature in the roasting process. After, the roasting temperature is determined as 600 °C, at this temperature, with the same extraction parameters, the effect of roasting duration on solving rate was investigated. The results are presented in Figure 3.

While examining the effect of roasting time on taking REEs into solution, while an increase in the solving amount between no roasted 0 points with the 1-hour roasting point in the roasting duration axis, after this, solving rate remained stable at the continued

Figure 3- The effect of roasting time on REE dissolution (600 °C roasting temperature, 5 M HCL, 1/3 solid to liquid ratio, room temperature).

roasting after 1 hour. In this process, the weight loss is calculated as %6 on average.

Direct leaching and post-roasting leaching experiments were carried out to take REEs into solution. In these experiments, the most suitable roasting parameters are used that were determined in the previous steps. The obtained solving rates by extraction with three different acids are given in Figure 4.

In the leaching experiments performed with HCl (Figure 4a), a 40% difference is observed in the solving rate between the non-roasted and roasted samples. It wasn't observed any differences in solving rate after 5 mole/l in the extraction experiments with roasting. In the experiments performed with HNO_3 (Figure 4b), the difference is less between the non-roasted and roasted samples. The solving rate obtained from HNO_3 leaching on the roasted sample is not at the same level as HCl leaching even if used at 8 mole/l. The solving rate in the leaching experiments performed with H_2SO_4 (Figure 4c) sharply decreased after 4 mol/l concentration. The reason for this is the high calcium (Ca) ratio contained in the concentrate. Because of the Ca ratio, calcium sulphate (gypsum) is formed in sulphuric acid extraction.

The 5 M HCl concentration, which was determined as the most suitable parameter, negatively affects the hydrodynamic interactions between the acid and the concentrate during the extraction. As a result, a sharp

Figure 2- The effect of roasting at different temperatures on the solving rate (1-hour roasting time, 5M HCL, 1/3 solid/liquid ratio, 1-hour extraction time).
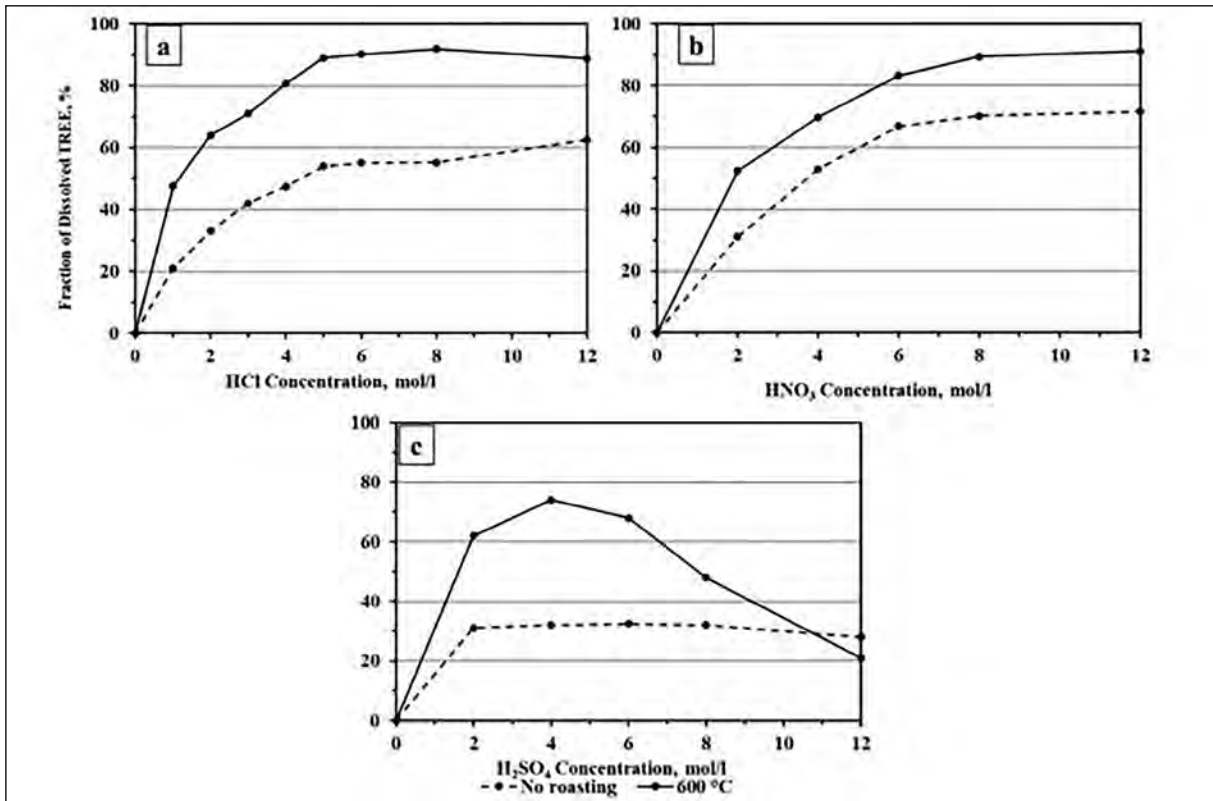
Figure 4- Extraction of unroasted (dashed line) and roasted samples with a) HCl, b) HNO$_3$, c) H$_2$SO$_4$ acids.

decrease is observed in the REE dissolution. According to the differences between these three acids, a higher solving rate with HCl at a lower concentration was determined. The parameters where the effect of 5 M HCl with solid/liquid is observed are tested. The results are presented in Figure 5.

When the effect of the solid/liquid ratio was examined, only a 0.2% increase was observed after the 1/4 ratio. For this reason, 1/4 of the solid/liquid ratio is used for the following steps. Then, the experiments were carried out to examine the effect of leaching temperature on solving rate and the results given in Figure 6.
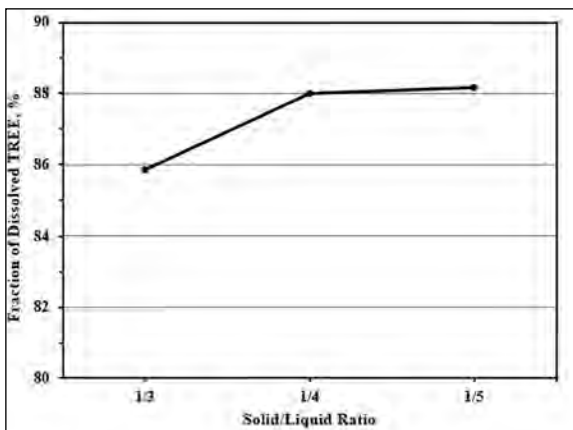
Figure 5- The effect of solid/liquid ratio on the solving ratio in the pre-concentrate sample that was roasted at 600 °C for 1 hour and extracted with 5 M HCl acid for one hour at room temperature.
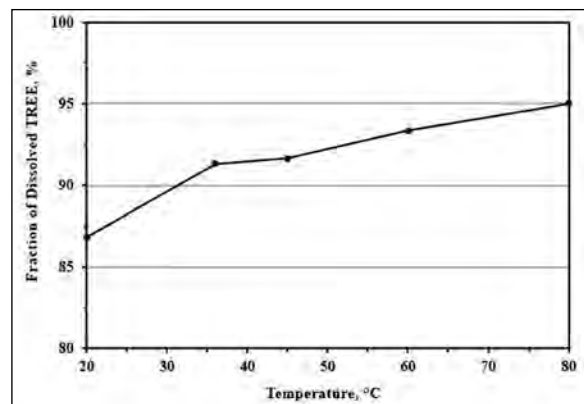
Figure 6- The effect of leaching temperature on solving rate on the pre-concentrate sample which is 1 hour roasting at 600 °C and, one hour leached with 5 M HCl acid and ¼ solid/liquid ratio.

When the extraction temperature was increased from room temperature to 35 °C, 6% increase was observed in solving rate. Subsequently, as the extraction temperature was increased lower increases were observed in the solving rate. Even though the solving rate was increased in the extraction at 80 °C, because of heating costs for keeping extraction at high temperatures, it is evaluated as disadvantageous. For this reason, it was concluded that the optimum extraction temperature is 35 °C. To examine the effect of the extraction time on the determined optimum parameters, the solving rates obtained in the experiments carried out between 15-120 minutes are presented in Figure 7.

When the extraction time was increased from 15 minutes to 60 minutes, an increase of 10% was observed in the solving rate, while an additional 2% increase in the solving rate was observed when the extraction time was increased from 60 minutes to 120

minutes. Considering these data, it was determined that the extraction time of 60 minutes was sufficient for the rate of taking REEs into solution. The concentrations of waste products of input, roasted and extraction solids are presented in Table 2.

The extraction was done in three repetitions under optimum conditions which are 1 hour roasting at 600 °C temperature, and then 1/4 solid/liquid ratio, 35 °C temperature for 60 minutes with 5 M HCl. During these repetitive extractions, different stock volumes are acquired. Concentrations varying according to stock volumes were determined with the ICP-OES. The mean and standard deviations of these values were calculated. The results are presented in Table 3.

Table 3- The content of the solution obtained as a result of roasting and extraction under optimum conditions, determined by ICP-OES.

Element	Average concentration (g/l)	Standard deviation (g/l)
TREE	22.00	0.68
Al	5.30	0.46
Ba	0.67	0.10
Ca	5.09	0.35
Fe	10.58	1.60
Mn	3.91	0.09
Si	0.16	0.01
Th	0.63	0.01

3.3 Solvent Extraction Studies

For REO production from the solution obtained by roasting and extraction of the above-mentioned pre-concentrate, the oxalic acid was added until precipitated all REEs, at first. The precipitation rate of

Figure 7- The effect of extraction time to take REE into solution from pre-concentrate under the determined optimum parameters (1 hour roasting at 600 °C, 5 M HCl, 1/4 solid/ liquid ratio, 35 °C extraction temperature).

Table 2- XRF results of concentrate, roasted concentrate and residue samples.

Sample	CeO_2	La_2O_3	Nd_2O_3	Pr_6O_{11}	Y_2O_3	Er_2O_3	ThO_2	U_3O_8
Concentrate (%)	4.52	2.92	0.75	0.26	0.09	0.01	0.38	0.03
Roasted (%)	4.82	3.18	0.80	0.26	0.10	0.02	0.40	0.03
Waste(%)	0.78	0.44	0.05	<0.01	0.04	0.02	0.14	0.01
Sample	BaO	Fe_2O_3	CaF_2	SiO_2	Al_2O_3	MnO	MgO	LOI
Concentrate (%)	5.80	9.80	31.80	14.20	6.60	1.70	1.10	12.60
Roasted(%)	5.90	10.50	32.60	15.50	7.30	1.80	1.20	7.70
Waste(%)	6.10	10.60	44.00	18.30	4.20	0.60	1.20	5.30

REE oxalates is much higher than that of impurities. The reason of this, the differences solubility product among metal-oxalate salts. Therefore, the solubility of the formed REE oxalates in water is much lower than the oxalates of other elements. For this reason, when the pH value of the solution was 0, the oxalate product obtained from the precipitation with the addition of 30% oxalic acid was calcined until it was completely oxidized and XRF analysis was carried out. The results of the XRF analysis are shown in Table 4.

Table 4- XRF analysis of the final REO concentrate obtained when the pH value is 0, with the addition of 30% oxalic acid direct precipitation from the pre-concentrate obtained by roasting and extraction, under determined optimum conditions.

Element	Composition (%)
TREO	96.20
CeO_2	53.04
La_2O_3	28.9
Nd_2O_3	9.02
Pr_6O_{11}	3.69
Sm_2O_3	0.52
Y_2O_3	0.53
Al_2O_3	0.15
CaO	0.79
Fe_2O_3	0.40
MnO	0.06
SiO_2	0.24
ThO_2	1.85
Minor Oxides	0.80

The solubility product values of the compounds formed by the oxalate ions of Fe, Ca, Al, Th and Mn elements, which have high concentrations in the solution content, cause precipitation, albeit to some extent. When Fe and Th elements are removed from the solution, the REO contents of the obtained solid material will increase. During the Fe and Th removal process, applied optimum parameters determined by Erdem et al. (2020). While 20% in volume Adogen 464 in kerosene with 1/1 organic/aqueous ratio at the -0,58 pH was used for Fe removal, for Th removal was used 30% D2EHPA, solved in kerosene, with the 1/3 organic/aqueous ratio. The contents of the Fe and Th removed solution are given in Table 5.

Table 5- Contents of the Fe and Th removed solution which used the parameters determined by Erdem et al. (2020), from the final concentrate mentioned in Table 4.

Element	Average concentration (g/l)
TREE	22.50
Al	4.91
Ba	0.74
Ca	4.38
Fe	<0.001
Mn	4.24
Si	0.14
Th	0.01

3.4 Precipitation Studies

After oxalate precipitation, directly from the extraction solution, the major impurity was determined to be Th, followed by Ca and Fe. Fe and Th removal provide obtaining valuable by-products, and higher purity REO concentrate. For this reason, from the Fe and Th free solution, oxalic acid precipitation studies were carried out. The effects of different initial pH values and different oxalic acid adding ratio are presented in Figure 8.

The acquired data shows that oxalic acid mol ratios cause precipitation in all pH values. In these parameters, where fixed 30 minutes mixing time, and at -0.3 pH and 0 pH values, it is observed that as the oxalic acid mol ratio increases T-REE precipitation ratio also increases rapidly.
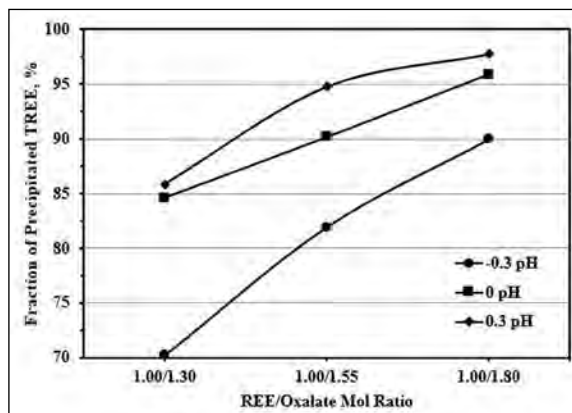
Figure 8- The effect of REE/oxalate mol ratio in different pH values on precipitation ratio of REE in the final REO concentrate (30 minutes of mixing time, 20 °C precipitation temperature).

If at the 0.3 pH, between 1.00/1.55 and 1.00/1.80 REE/oxalate mole ratios, the precipitation ratio increasing speed is decreased. The effect of time parameters, which was getting the maximum precipitation ratio when adding 1.00/1.80 REE/oxalate mole ratio at 0.3 pH value, are observed and presented in Figure 9.
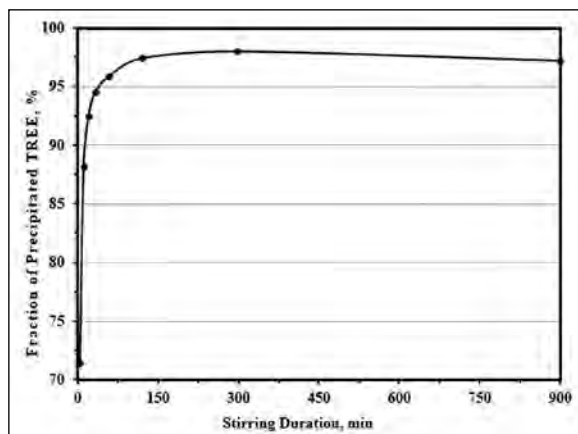
Figure 9- The effect of mixing time of the obtained solution on the REE precipitation ratio (1.00/1.80 REE/oxalate mol ratio, 20 °C precipitation temperature).

When the effect of mixing duration is observed, it is revealed that there is an increment until the 120th second. Between 120-300 seconds there is a 2% increase in the REE precipitation ratio but there is not increasing in the further times. For this reason, 300 seconds is determined as the most suitable for mixing time for precipitation. Then, the parameters were tested to examine the effect of temperature on precipitation, and the results are presented in Figure 10.

The increase of less than 1% was observed between 40-60 °C. After that, precipitation rate is decreased. Since the temperature changes have not been significantly different in the REE precipitation rate, it is decided that the room temperature is the optimum parameter for the experiment. Rare earth oxides were obtained by calcining the rare earth oxalates obtained from the precipitation process using these parameters. The obtained REO was analysed by the XRF and presented the results in Table 6.
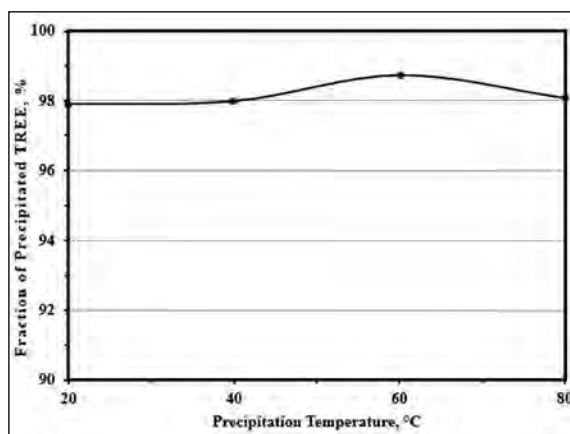
Figure 10- The effect of temperature on REE precipitation ratio (1,00/1,80 REE/oxalate mol ratio, 300 seconds mixing duration). The study of the effect of precipitation temperature revealed a change between 20-40 °C.

Table 6- XRF analysis of REO solid obtained by precipitation after solvent extraction

REOs	Composition (%)
TREO	99.65
CeO_2	53.91
La_2O_3	29.09
Nd_2O_3	11.59
Pr_6O_{11}	4.31
Sm_2O_3	0.44
Y_2O_3	0.31
Minor Oxides	0.35

4. Discussion

As a result of the DTA analyses on the concentration obtained from the Eskişehir-Beylikova complex mineralization in the ore dressing laboratory of MTA, the reaction at 400 °C was taken as a basis and the roasting temperatures were studied at 400-700 °C. After roasting, extraction was done with 5 M HCl at 1/3 solid/liquid ratio for 1 hour. According to the test results, the highest solubility rate was determined at 600 °C. In the roasting time tests carried out at 600 °C, it was determined that sufficient solubility rate was achieved in 1 hour roasting time. In the experiments performed with HCl, H_2SO_4 and HNO_3 at the determined roasting temperatures, it was understood that roasting was necessary to increase the solubility rate. Compared to other acids, it has been observed that a higher solubility rate is achieved at lower concentrations in studies with HCl acid. As a

result of increasing in the concentration by studies with H_2SO_4, the free sulphate ions in the environment combine with the Ca^{+2} ions to form gypsum. Thus, it causes insufficient dissolution of REEs in the environment. Cost and high concentrations are disadvantages of the solution to be made with HNO_3. 5 M is preferred as the HCl concentration, and in the experiments performed with this constant parameter, it is determined that the most effective parameter is temperature. After the solution experiments, the optimum parameters are determined as 5 M HCl, 1/4 solid/liquid ratio and 35 °C extraction temperature. The solubility rate for the whole REE is calculated as %91.55. As a result of the serial experiments, solution contains 22 g/l REE, 10 g/l Fe^{+n} and 0.63 g/l Th^{+4}. When oxalate precipitation and calcination are made directly from the solution, it is determined that only Th, Ca and Fe elements among the impurities in the solution caused large impurities in the final product. From these impurities, Fe and Th are removed from the solution because of they may affect the price and marketability of the final product.

Kursunoglu et al. (2021) used the roasting technique with sulfuric acid on the ore-bearing bastnaesite, which they obtained from this region. Then, this solid material is dissolved in water, precipitated with oxalic acid directly, and obtained rare earth oxalates. Rare earth oxide (REO) product obtained as a result of the calcination of these oxalates contain 6% Th (thorium). It is known that high Th contents will be problem for operation and waste management, and very dangerous for human health (Judge and Azimi, 2020).

A purified solution was obtained by applying the optimum parameters used in previous studies for Th and Fe removal (Erdem et al. 2020). The precipitation parameters from the purified solution were tested. After the appropriate REE/oxalate mole ratio was determined, it is understood that the precipitation took place in a quick time. When precipitation was made with the determined optimum parameters, just 0.35% non-REE oxides were determined in the final product. In this study, parisite has been detected in addition to bastnaesite in complex mineralization (Yeşilören Görmüş et al., 2021). Contrary to known,

REO recovery from parasite-bearing complex ore has been demonstrated in the laboratory application.

5. Conclusion

This study examined the production of REO from fluorite concentration obtained from barite, fluorite, and REE-bearing Eskişehir-Beylikova complex ore. The concentration is firstly roasted and the optimal roasting temperature is determined as 600 °C for extraction. In this temperature, the extraction tests with three different acids showed that most suitable acid for extraction is HCl. The optimal HCl concentration is determined as 5 M mol/l.

After this stage, the optimum conditions obtained with 5 M HCl are 1/3 solid/liquid ratio, 35°C extraction temperature and 60 minutes extraction time. With these parameters, the solubility rate of TREE is determined as 91.55%. T-REE concentration in the solution is measured at 22 g/l. At these stages, obtained REO purity after direct oxalate precipitation and calcination is determined as 96.20%. In this step, ThO_2 is a greatest impurity.

For the minimize ThO_2 and other impurities, the solvent extraction technique is applied. After the extraction with the optimum parameters determined in the previous studies, the precipitation parameters are optimized. To that, optimisation of the precipitation experiments is done. After this optimization, the most suitable precipitation parameters are determined as 1.00/1.80 REE/oxalate mol ratio with a mixing time of 300 seconds at room temperature. REE oxalates obtained with these parameters are calcined and REO concentration is produced. The TREO content of the concentration is determined as 99.65%.

References

Altaş, Y., Tel, H., İnan, S., Sert, Çetinkaya, B., Sengül, S., Özkan, B. 2018. An experimental design approach for the separation of thorium from rare earth elements. Hydrometallurgy 178, 97–105.

Cheisson, T., Schelter, E. J. 2019. Rare earth elements: Mendeleev's bane, modern marvels. American Association for the Advancement of Science 363 (6426), 489–493.

Chi, R., Zhang, X., Zhu, G., Zhou, Z. A., Wu, Y., Wang, C., Yu, F. 2004. Recovery of rare earth from bastnaesite by ammonium chloride roasting with fluorine deactivation. Minerals Engineering 17(9–10), 1037–1043.

Choppin, G. R., Morgenstern, A. 2000. Thermodynamics of solvent extraction. Solvent Extraction and Ion Exchange 18(6), 1029–1049.

El Afifi, E. M., Borai, E. H., Shahr El-Din, A. M. 2019. New approaches for efficient removal of some radionuclides and iron from rare earth liquor of monazite processing. International Journal of Environmental Science and Technology 16(12), 7735–7746.

Erdem, A., Babuçcuoğlu, Y., Güneş, H., Obuz, H. E., Özdemir, E., Kara, Ç., Diktepe, Ş., Akgül, M. B., Özen İlik, B., Akçay, H. 2021. Nadir Toprak Minerallerinin Fiziksel Ayrılması ve Flotasyonu. Derleme. International Journal of Pure and Applied Sciences 7(2), 321-345.

Erdem, A., Güneş, H., Kara, Ç., Akçay, H., Gülmez, A., Alkan, Z. 2020. Production of high purity thorium oxide from complex ores leach liquor. Bulletin of the Mineral Research and Exploration 164, 1–7.

European Commission. 2020. Communication from the commission to the European parlıament, the council, the European economic and social committee and the committee of the regions.

Judge, W. D., Azimi, G. 2020. Recent progress in impurity removal during rare earth element processing: A review. Hydrometallurgy 196, 105435.

Krishnamurthy, N., Gupta, C. K. 2015. Extractive Metallurgy of Rare Earths. CRC Press, United State of America.

Kul, M., Topkaya, Y., Karakaya, I. 2008. Rare earth double sulfates from pre-concentrated bastnaesite. Hydrometallurgy 93(3–4), 129–135.

Kursunoglu, S., Hussaini, S., Top, S., Ichlas, Z. T., Gokcen, H. S., Ozsarac, S., Kaya, M. 2021. Production of mixed rare earth oxide powder from a thorium containing complex Bastnaesite ore. Powder Technology 379, 641–654.

Lawrance, G. A. 2010. Introduction to Coordination Chemistry. John Wiley and Sons Ltd., United Kingdom.

Obuz, H. E., Günes, H., Kara, A., Ugurluer, D., Babuccuoglu, Y., Alkan, M. 2018. Leaching Kinetics of Rare-Earth Elements from Complex Ores by Acidic Solutions. Extraction 2391–2398.

Qi, D. 2018. Hydrometallurgy of Rare Earths: Extraction and Separation. Elsevier, 1-797.

Rydberg, J., Choppin, G. R., Musikas, C., Sekine, T. 2004. Solvent Extraction Equilibria. Solvent Extraction Principles and Practice, Revised and Expanded. CRC Press 121–217.

Sadri, F., Rashchi, F., Amini, A. 2017. Hydrometallurgical digestion and leaching of Iranian monazite concentrate containing rare earth elements Th, Ce, La and Nd. International Journal of Mineral Processing 159, 7–15.

Sprecher, B., Xiao, Y., Walton, A., Speight, J., Harris, R., Kleijn, R., Visser, G., Kramer, G. J. 2014. Life cycle inventory of the production of rare earths and the subsequent production of NdFeB rare earth permanent magnets. Environmental Science and Technology 48(7), 3951–3958.

Swain, N., Mishra, S. 2019. A review on the recovery and separation of rare earths and transition metals from secondary resources. International Journal of Cleaner Production 220, 884–898.

Walawalkar, M., Nichol, C. K., Azimi, G. 2016. Process investigation of the acid leaching of rare earth elements from phosphogypsum using HCl, HNO$_3$, and H$_2$SO$_4$. Hydrometallurgy 166, 195–204.

Yeşilören Görmüş, N., Gürtekin, G., Erdem, A., Gülmez, A. 2021. Kızılcaören (Sivrihisar) bölgesi nadir toprak element (NTE) içeren minerallerin mineral serbestleşme analiz (MLA) yöntemi kullanılarak tayini. International Journal of Pure and Applied Sciences 7(2), 251-264.

Zhao, L., Wang, L., Shuai, G., Long, Z., Cui, D., Huang, X. 2018. Thermal decomposition and oxidation of bastnaesite concentrate in inert and oxidative atmosphere. Journal of Rare Earths 36(7), 758–764.

Bulletin of the Mineral Research and Exploration

http://bulletin.mta.gov.tr

Evaluation of current earthquake activity on the Ganos Fault: MONGAN network test analysis

Eşref YALÇINKAYA[a*] , Marco BOHNHOFF[b,c] , Ethem GÖRGÜN[a] , Hakan ALP[a] , Stephan BENTZ[b] , Ali PINAR[d] , Fatih ALVER[e] , Ömer KILIÇARSLAN[e] , Burçin Didem TAMTAŞ[a] and Burçak GÖRGÜN[a]

[a]İstanbul University-Cerrahpaşa, Faculty of Engineering, Department of Geophysical Engineering, İstanbul, Türkiye
[b]GFZ German Research Center for Geosciences, Potsdam, Germany
[c]Free University of Berlin, Institute of Geological Sciences, Berlin, Germany
[d]Boğaziçi University, Kandilli Observatory and Earthquake Research Institute, İstanbul, Türkiye
[e]Ministry of Interior Disaster and Emergency Management Precidency, Ankara, Türkiye

Research Article

ABSTRACT

The Monitoring of the Ganos Fault data presents significant opportunities and challenges for earthquake detection, location and magnitude calculations, source mechanism solutions, and discovery of fault zone waves. This study indicates mostly of preliminary data analysis and seismological evaluations. While narrow distance aperture installation has an opportunity to detect microearthquakes, it also causes significant difficulties in determining the source parameters of micro-earthquakes. Extracting microearthquakes from continuous data shows that special strategies need to be used. MONGAN data revealed the presence of many earthquakes with magnitude M<1.0 in the study region. These earthquakes are mostly out of network earthquakes and it is very difficult to obtain reliable solutions due to the insufficient azimuthal distribution of the stations. It is obvious that different network techniques and wave particle motion analyzes are contributed to the location and source parameters. Although the fault zone structure consists of two different lithologies that make significant differences in seismic wave phase arrival times and wave amplitudes, we observe fault zone head waves on both sides along the Ganos fault. Moment tensor analyzes depict that reliable source mechanism solutions can be obtained using a small number of station records.

1. Introduction

The segment of the North Anatolian Fault Zone (NAFZ) within Marmara Sea (the section between the 1999 İzmit and 1912 Mürefte earthquake ruptures) is one of the best-known seismic gaps in the world (Figure 1). The westward migration of earthquakes along the NAFZ in the last century arrived in the Marmara Sea after the 1999 İzmit and Düzce earthquakes (Stein et al., 1997). Further west of the

fault, the Ganos Fault segment was broken by the 1912 Mw=7.4 Şarköy/Mürefte earthquake (Aksoy et al., 2010). The last known major earthquake along the Marmara Fault is the 1766 earthquake (Mw7.2) and it has been characterized as an expired seismic cycle since approximately 250 years have passed (Bohnhoff et al., 2016; Bulut et al., 2019). In fact, the main Marmara fault is not a single segment consisting of several parts with different dynamic characteristics. It is claimed that the Tekirdağ segment in the west was
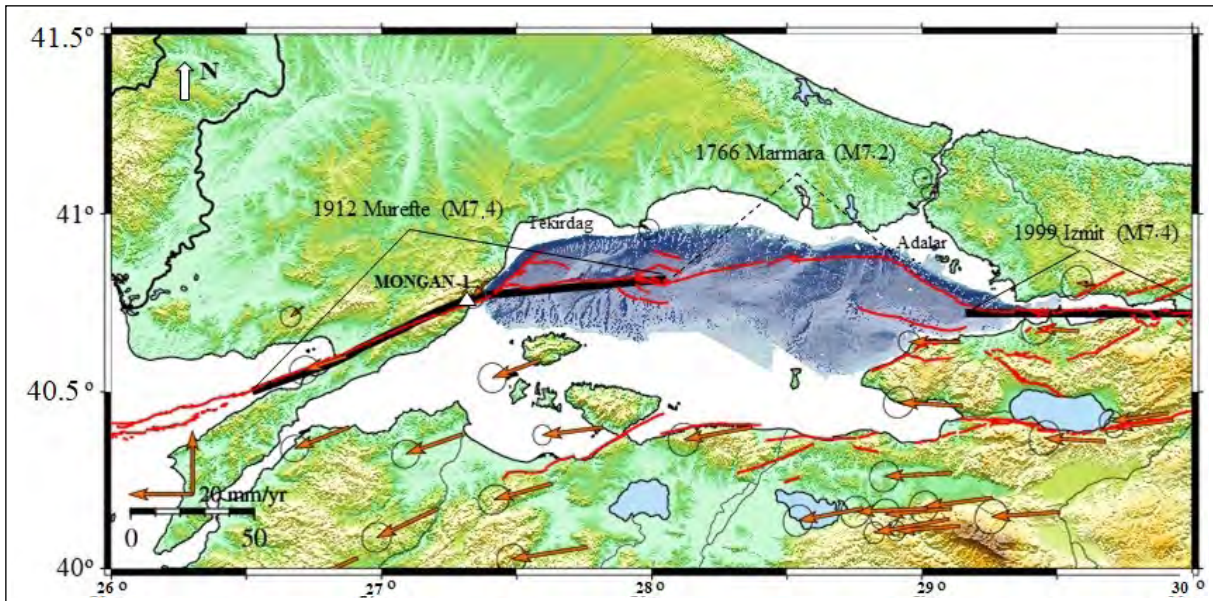
Figure 1- Main structural features of the study region and its surroundings. Red lines represent fault map (Armijo et al., 2005), arrows represent GPS vectors (McClusky et al., 2000), and thick black lines represent 1912 Mw7.4 Şarköy/Mürefte and 1999 İzmit earthquake ruptures. The MONGAN seismic network stations (MONGAN-1, white triangle) are enlarged in Figure 2.

broken by the 1912 earthquake (Armijo et al., 2005; Uçarkuş et al., 2011). The parts of Central Marmara and Princes Islands are the segments that are expected to be ruptured (Bohnhoff et al., 2013; Ergintav et al., 2014). While the Tekirdağ segment has intense seismicity and shows partly creep (Schmittbuhl et al., 2016; Bohnhoff et al., 2017; Uchida et al., 2019), the on-shore segment of the Ganos Fault together with the Saros Bay extension is an aseismic (non-earthquake-producing) and fully locked (Aksoy, 2021). Similarly, the Central Marmara segment exhibits an aseismic-locked feature (Bohnhoff et al., 2013; Lange et al., 2019), while the Princes Islands segment has high seismicity (Wollin et al., 2018). It is extremely important to investigate these multi-part and dissimilar seismic features of the main Marmara Fault in order to predict the real seismic hazard in the region.

One of the most important data in understanding the behavior of fault segments is to reveal different stress states by following the detailed geodetic and seismological features on the fault. However, this kind of detailed analyzes of the segments in the Marmara Sea is only possible with the sea floor observations close to the fault. In recent years, prominent studies focused on this subject are ocean bottom seismometer (OBS) (Özalaybey, 2010; Yamamoto et al., 2017)

and seafloor geodetic measurement networks (Sakic et al., 2016; Yamamoto et al., 2019). The number of microearthquakes recorded with OBS observation stations is approximately 5 times than obtained from conventional land observation networks (Yamamoto et al., 2022).

Revealing the velocity distribution of the opposite blocks and the crushed zone in a fault structure is crucial for many seismological analyzes and fracture mechanics. The velocity contrast between the fault blocks affects the progression and velocity of a rupture during an earthquake (Andrews and Ben-Zion, 1997). In addition, it is effective in terms of the estimation of earthquake location and rupture mechanisms (McGuire and Ben-Zion, 2005). In recent years, dense seismic networks along fault zones have allowed seismologists to verify the presence of fault zone head waves (FZHW) and fault zone trapped waves (FZTW) (Li and Leary, 1990; Ben-Zion and Malin, 1991).

An earthquake monitoring network consisting of 40 stations was established on-shore segment of the Ganos Fault (MONGAN- MONitoring of the GANos Network) in 2018 (Figure 2). The project was supported by the bilateral cooperation of the Scientific and Technological Research Council of Türkiye
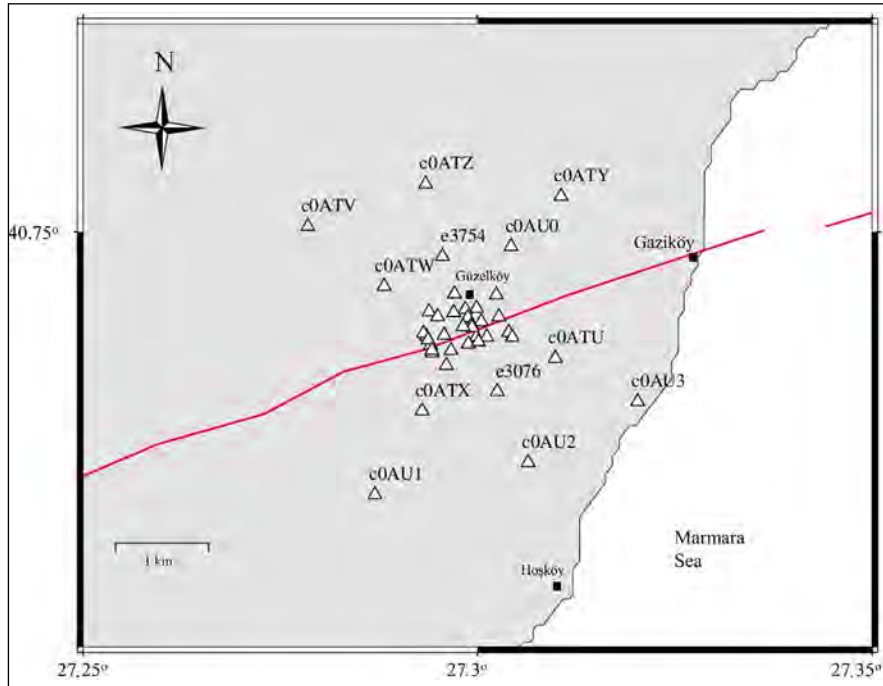
Figure 2- Station locations of MONGAN seismic network (MONGAN-1, triangles) along the Ganos Fault (red line). In order to avoid confusion, only the codes of external stations are given.

(TÜBİTAK) and the German Ministry of Education and Research (BMBF). The aim of the network is to observe a possible micro-seismic activity along the Ganos Fault where exhibits aseismic-locked behavior according to the data obtained from the national seismic networks (Kandilli Observatory and Earthquake Research Institute (KOERI) and the Disaster and Emergency Management Presidency (AFAD) and to image the bimaterial fault structure by analyzing fault zone waves. The seismic network is operated in two stages, in the first stage the stations are operated at the eastern end of the fault (MONGAN-1), in a narrow area for 2 years (Figure 2). In the second stage, the stations are shifted to the western part of the fault (MONGAN-2) and expanded to a wider area for approximately one year (Yalçınkaya et al., 2022). Two different types of sensors (Mark 1Hz L4C and Geophone 4.5Hz) and two different types of recorders (EarthData EDL PR6-24 and DATA-CUBE3) are used at the stations. In the first conjugate article, the characteristics of the seismic network, data collection and data quality were discussed (Yalçınkaya et al., 2022). In this second article, our primary aim is to compose initial tests of seismological analyzes using MONGAN-1 network data. We can list the

general characteristics of earthquakes recorded by the network as follows: They consist of mostly small or microearthquakes, they are also recorded at the stations located on the opposite fault blocks and directly fault zone which have different velocity structures. Lastly, they have mostly not good azimuthal station coverage for reliable location estimation. This study includes preliminary analyzes on the detection of earthquakes recorded by the network, magnitude and location estimation, the discovery of FZHW, and source mechanism solutions for small earthquakes.

2. Earthquake Detection

The process of detecting possible earthquakes from the continuous data recorded within the MONGAN network can be done in two ways, automatic and manual. Manual scanning of data is a very tedious and time-consuming process. Effective use of automatic detection is a priority in order to reduce the workload as much as possible and to use time efficiently. For this purpose, the first 3 months of the collected data were used to test the effectiveness of automatic detection. First, the continuous data were scanned with automatic detection, and then it was manually controlled for the

events missed or incorrectly detected. In the automatic process, the Short Term Average/Long Term Average (STA/LTA) method, which is one of the most basic applications, is used (Allen, 1978).

The parameters used in the STA/LTA method are tested many times in this study and the parameters that are decided to be the most successful ones are presented in Table 1. Generally, the STA is selected 1-2 seconds for regional events, while it can be reduced to 0.3-0.5 seconds for local events. The LTA can be tried starting from 60 seconds up to 30 seconds for local events. The STA/LTA triggering ratio, on the other hand, can be used around 3-4s for small earthquakes at stations with low-noise levels. As seen in Table 1, the automatic detection process starts with a band-pass filter in the range of 2-20 Hz. STA, LTA, and triggering ratio were determined as 0.3 s, 30 s, and 5, respectively. If triggering is provided at least 7 stations in the entire network, it is listed as an event. An event is cut from the continuous data for 180 seconds and stored as a separate file. These parameters may vary depending on the noise levels in the recordings and the number of operating stations at that time. In the second stage, an operator visually scans the data in 30-60 minute windows, using filters in different frequency bands, to delete the incorrectly determined events from the list and add the missed events to the list.

Table 1- Parameter values used in the STA/LTA method within condet subroutine used in the SEISAN (Havskov and Ottemoller, 1999) software.

Parameters	Values
Filter	2-20 Hz
STA time length	0.3 s
LTA time length	30 s
Triggering ratio (STA/LTA)	5
Triggering length (at least)	1 s
Triggering length (at least)	10 s
Number of triggered stations (at least)	7
Time length before triggering	30 s
Cut-off window length	180 s

Table 2 shows the comparison of automatic detection and manual control results for the first three months of the data. In general, it is seen that there are 40-50% of differences between automatic detection and manual control. Some of them are in the form of adding events that the automatic method could not detect, while the other part is in the form of deleting events due to false triggering. The high difference between automatic and manual detection indicates that the automatic method is not succeeded adequately. One of the main reasons for this is that the target earthquakes are too small. Microearthquakes generally remain in environmental noise and STA/LTA ratios are not successful enough to determine them. Testing different filters and viewing many station records simultaneously on the screen during manual control only made it possible to detect these earthquakes. Figure 3 displays two earthquakes discovered by automatic detection and manual control by using different filters, respectively. It may be possible to design the STA/LTA operator with the appropriate parameters for both earthquakes, but this time the number of false detection is highly increased. For more successful detection, it is aimed to use different automatic detection methods such as cross-correlation of waveforms in the next future of this study (Gibbons and Ringdal, 2006; Yoon et al., 2015; Bentz et al., 2019).

3. Phase and Amplitude Readings

In order to make the location and magnitude calculations of the selected earthquakes, the arrival times and amplitude values of the P and S wave phases are needed from the seismograms. While these readings can be made with high precision in data with a high signal-to-noise ratio, the error in the readings increases as signal-to-noise ratio decreases. Although automatic phase reading methods developed in recent years have produced very successful results, manual readings remain valid in terms of precision, especially

Table 2- The number of events obtained as a result of automatic detection and manual control of the data collected in the first three months of the seismic network.

Dates of Event	Automatic detection	Manuel deleted	Manuel added	Ratio of difference	Exact number of events
01-31 October 2017	592	203	69	46%	458
01-30 November 2017	403	22	172	48%	575
01-31December 2017	477	131	84	45%	417

Figure 3- a) Discovered by automatic detection at the c0ATU station vertical component seismogram and b) manually detected a second event using a 5-10 Hz range filter within the red marked area of the same recording.

in cases where the signal-to-noise ratio is low and the waveforms between stations do not show many similarities.

In this study, phase and amplitude readings are done manually on unfiltered-raw data as much as possible. However, some readings can be made using different bandpass filters (e.g. 2-20 Hz, 5-30 Hz), especially in small earthquakes with the low signal-to-noise ratio. It should be noted that each filtering process creates some shifts in phase times and decreases in wave amplitudes. For these reasons, the selected filters are not distorted the general structure of the signal as much as possible. Very small apertures between seismic stations in the MONGAN-1 network require very high precision phase readings. Considering that the longest distance between stations is approximately 4 km, for a planar wave with a velocity of 6 km/s, the time difference occurs at these stations only 0.7 s. It should not be forgotten that this difference is much less at the near-vertical upcoming angles to the stations in close earthquakes.

Another important point in seismic phase reading is to distinguish different wave phases. The availability of different phases, as long as they are determined correctly, increases the accuracy of earthquake locations. These phases are the marking of the arrival times as Pn and Sn phases refracted from Moho, PS, SP phases transformed at the sediment-bedrock boundary, and the crustal Pg and Sg phases come directly to the receiver. Depending on the source-receiver geometry, it is not always possible to observe these phases in the seismograms. In some cases, these phases can be mixed with each other and may cause incorrect location solutions. Figure 4 shows sample phase markings for a three-component seismogram.

The local magnitude (M_L) scale is preferred in the magnitude calculation since local and small earthquakes are generally targeted in this study. First, the seismograms are simulated to a Wood-Anderson-type instrument using response functions and then displacement waveforms are calculated. As mentioned in Yalçınkaya et al. (2022), wave amplitudes clearly
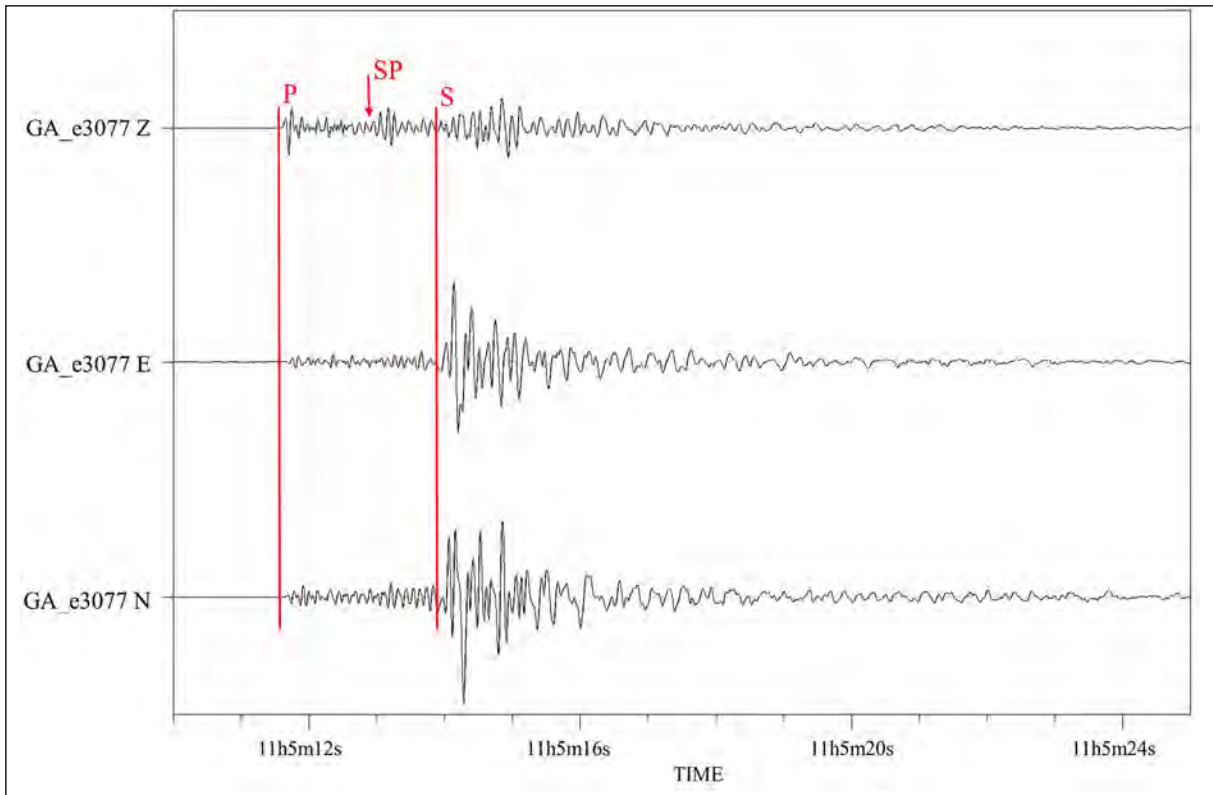
Figure 4- Three component earthquake seismogram and marking of P, S, and SP phases.

have near-surface soil effects, since the stations have different site properties. In order to minimize these effects, it is preferred to read the S wave amplitudes from the vertical component records in the M_L magnitude calculation (Equation 1) (Havskov and Ottemoller, 2010).

4. Location and Magnitude Calculations

The hypocenter algorithm (Lienert and Havskov, 1995) included in the SEISAN software (Havskov and Ottemoller, 1999) is used for location and magnitude calculations. In the first stage, 344 earthquakes that occurred between October 1 and November 30, 2017 are used as a test study. Different velocity models are tested in the analyses. In order to compare with KOERI solutions, which have a denser network in the region, Kalafat et al. (1987) velocity model is preferred.

The used equation for M_L;

$$M_L = \log A + 1.0 * \log R + 0.00167 * R - 1.58 \qquad (1)$$

In this equation, A: amplitude of S wave (mm) and R: distance of source (km). Regression coefficients defined in Equation 1 are taken from Kılıç et al. (2016) which are obtained for earthquakes in Türkiye.

The earthquakes recorded by the MONGAN network and made solutions in this study are evaluated under three groups:

i.   Earthquakes detected and located by the national network

ii. Earthquakes not located by the national network, but detected in both MONGAN and national network records

iii. Earthquakes were detected only by the MONGAN network

The epicenter distribution of the located events (within the first 100 km radius) is shown in Figure 5. The minimum number of stations used in the locations is 19. Root mean error (RMS) values are generally below 0.3, but azimuthal gaps can reach up to 350 degrees, especially in the third group earthquakes. Calculated M_L magnitudes range from -0.7 to 4.3.

The first group of data contains earthquakes recorded by MONGAN, AFAD and/or KOERI stations, and also location-magnitude calculations done by these national agencies. The magnitudes for the first group of earthquakes are generally $M_L>0.5$. The inclusion of MONGAN and national network stations together in the solution gives more reliable locations since they have a less azimuthal gap and more phase readings (Figure 5 yellow circles). The second group of earthquakes consists of events first discovered in the MONGAN network records and then included a limited number of national network station recordings (usually 1-5 stations) in the vicinity. These locations are shown in Figure 5 as red circles.

Their magnitudes are mostly $M_L<1.0$ and their location accuracy which varies depending on the used station distribution is less reliable. Our third group of earthquakes represents events recorded only by MONGAN network stations (Figure 5 blue circles). These seismograms have relatively low signal-to-noise ratios. We use a different type of filters for their phase readings. Moreover, generally, they have very high azimuthal gaps. It is difficult to distinguish seismic phases due to the effects of the bimaterial fault zone properties. The magnitudes of these earthquakes are mostly below $M_L<0.5$ and even negative values.

The epicenter and magnitude comparisons of the earthquakes for the first group of data, which are listed
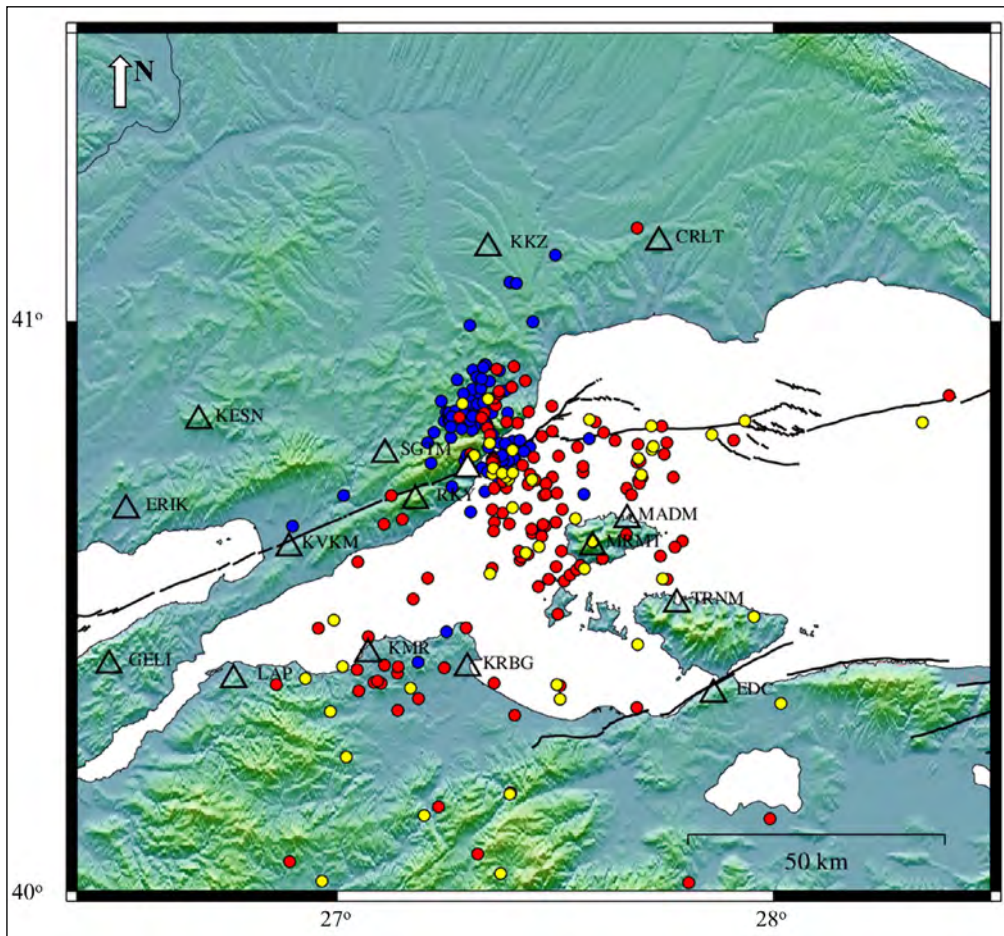
Figure 5- Location map of earthquakes analyzed in this study. The blank and white-filled triangles show the national network and the Ganos Fault monitoring network (MONGAN-1) stations used in the locations, respectively. Yellow circles represent earthquakes that are relocated by using the national network and MONGAN-1 network stations together. Red circles display earthquakes that are located by using the national network and MONGAN-1 network stations together in this study. These locations are not included in the national catalogs. Blue circles represent earthquakes located only by MONGAN-1 network. These events are also not listed in the national catalogs.

in the national catalog as well, are shown in Figures 6a and 6b, respectively. As can be seen, the epicenter solutions obtained in this study and listed in the KOERI catalog are very close to each other except for a few earthquakes. The magnitudes obtained in this study are slightly smaller than the KOERI catalog. Especially, these differences are obvious in small-magnitude earthquakes. The main factor causing this difference may be using the vertical seismogram amplitudes in the magnitude calculation. Amplitude readings are used from vertical components due to local site effects, especially at stations located on soft soils.

The magnitude-distance comparison of the earthquakes for the three groups is given in Figure 7. As seen in the figure, the main contribution of the MONGAN-1 network to the determination of the seismicity in the region occurs at distances of less than about 100 km and in events with magnitude $M_L < 1.0$ (Figure 7 red and blue circles). The earthquakes located by the national networks (excluding OBS) can detect in the region are generally observed as $M_L > 1.0$ earthquakes (Figure 7 black circles).

The third group of earthquakes based only on MONGAN-1 network recordings have high location errors. The biggest factor for this case is that MONGAN-1 stations do not provide good azimuthal coverage for most events, furthermore, azimuthal gaps are so high. The short distances between stations mean that in most earthquakes that occur outside the network, the network acts as a point receiver.

Another finding that is thought to cause errors in the locations is that the wave phases arrive at the stations located in the north of the fault systematically earlier than the stations located in the south. It is known that the Ganos Fault separates two different geological units in the region (Okay et al., 2010). The block in the north of the fault consists of Eocene-aged harder rocks, while the block in the south consists of Miocene-aged softer units. Therefore, it is normal for these units to have different seismic velocities, and for the northern block to have a higher wave propagation velocity than the southern block. In the sample seismogram examined, early wave phase arrivals to the stations in the northern block are clearly seen, although the source distance is the same at both station
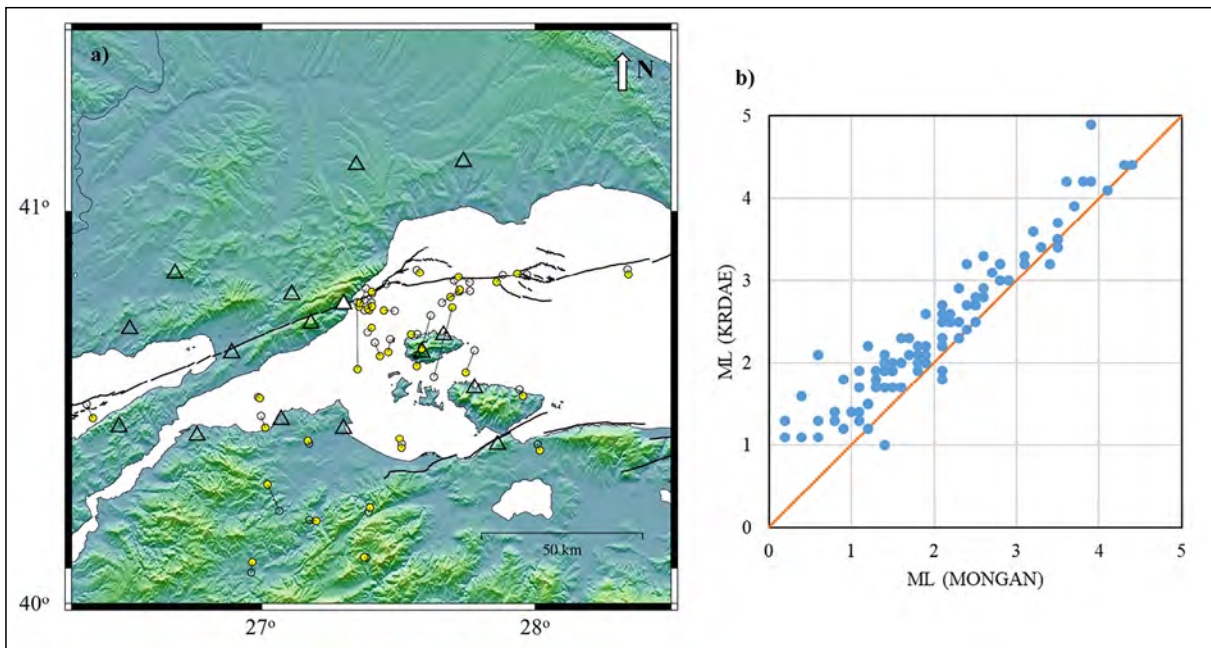
Figure 6- a) Comparison of earthquake locations (blank circles) in the KOERI catalog with the solutions obtained for this study (yellow circles) by including MONGAN-1 network. Thin lines represent differences in the solutions for the same earthquakes. The blank and white filled triangles show the national network and the Ganos Fault monitoring network (MONGAN-1) stations used in the locations, respectively and b) a comparison of earthquake magnitudes (M_L) in the KOERI catalog with the magnitudes obtained in this study by including MONGAN-1 network. The orange line represents 1:1 harmony.
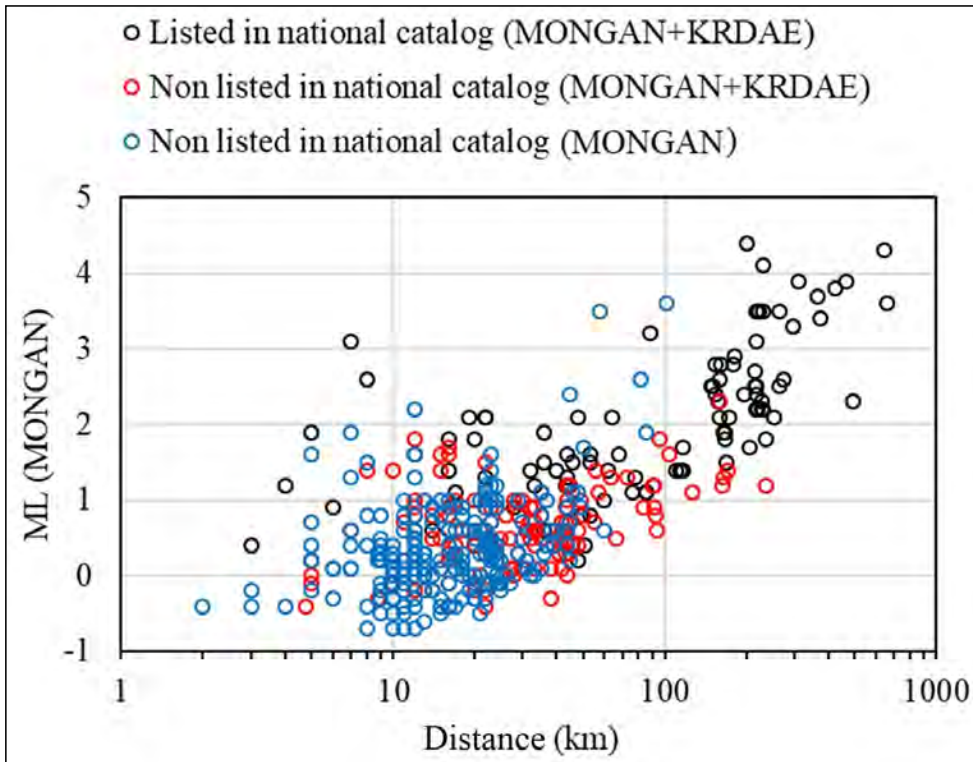
Figure 7- Magnitude-distance relationship of earthquakes obtained in this study for the three different groups.

groups. In Figure 8, the P wave delays at the stations for two examples of earthquakes occurring outside the network are shown with reference to the ATY station where the waves first arrived. As can be seen from the figure, the arrivals of P waves to the stations located in the north of the fault are significantly earlier than those in the south.

These early arrivals at the stations on the northern block cause a significant northward shift of the epicenters, especially when only MONGAN-1 seismograms are used. This is the reason why the epicenters represented by blue circles and partially red circles in Figure 5, unexpectedly emerge north of the main fault where no fault structure and no seismic activity in the national catalogs.

5. Analysis of Fault Zone Head Waves

In bimaterial fault blocks, FZHWs are observed at stations on the slow block, in addition to the early phase arrivals observed at stations on the fast block as exemplified above. These waves propagate along the interface using the fast block and reach the stations on the slow block (Figure 9). FZHW carries important information about the fault zone to seismic stations (Ben-Zion and Aki, 1990). While the P wave directly reaching the station on the slow block from the source has a sharp initial (impulsive) form in the records, the FZHW reaching the station by refracting along the fault zone has a soft onset (emergent) form. FZHW spending a part of its journey in the fast block reaches before the direct P wave to the station located on the slow block of the fault and had a perpendicular distance to the fault $x < x_c$ (Figure 9);

$$x_c = r * tan\left[cos^{-1}\left(\frac{\alpha_2}{\alpha_1}\right)\right] \qquad (2)$$

where x_c: critical distance from the fault, r: wave propagation distance along the fault, α_1 and α_2 represent fast and slow block velocities, respectively. The time difference (Δt) between the FZHW and the direct incident wave depends on the travel distance of the FZHW in the fault zone and the velocity difference between the blocks.

$$\Delta t \sim r\left[\left(\frac{1}{\alpha_2}\right) - \left(\frac{1}{\alpha_1}\right)\right] \qquad (3)$$

FZHW and direct P waves have opposite polarities in earthquakes occurring close to the fault zone
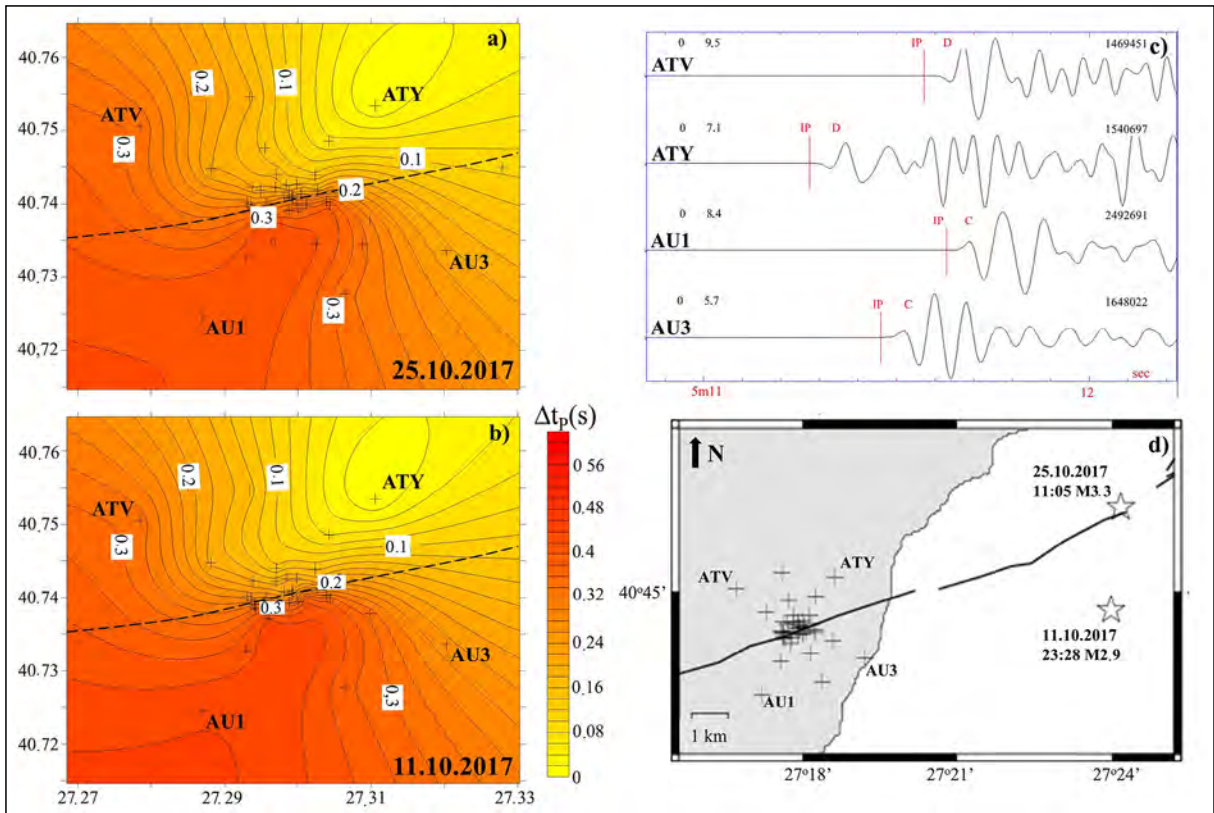
Figure 8- a), b) Contour maps of P wave delay times at network stations for two sample earthquakes (25.10.2017 and 11.10.2017) located in the east of MONGAN-1 network. Cross symbols and dashed lines indicate network station locations and the Ganos Fault, respectively. The delay times are normalized according to the arrival time of the first station (for both earthquakes at ATY station), c) P wave arrivals at sample stations for the 25 October 2017 earthquake marked with red lines and d) locations of the earthquakes (stars) and network stations (crosses).
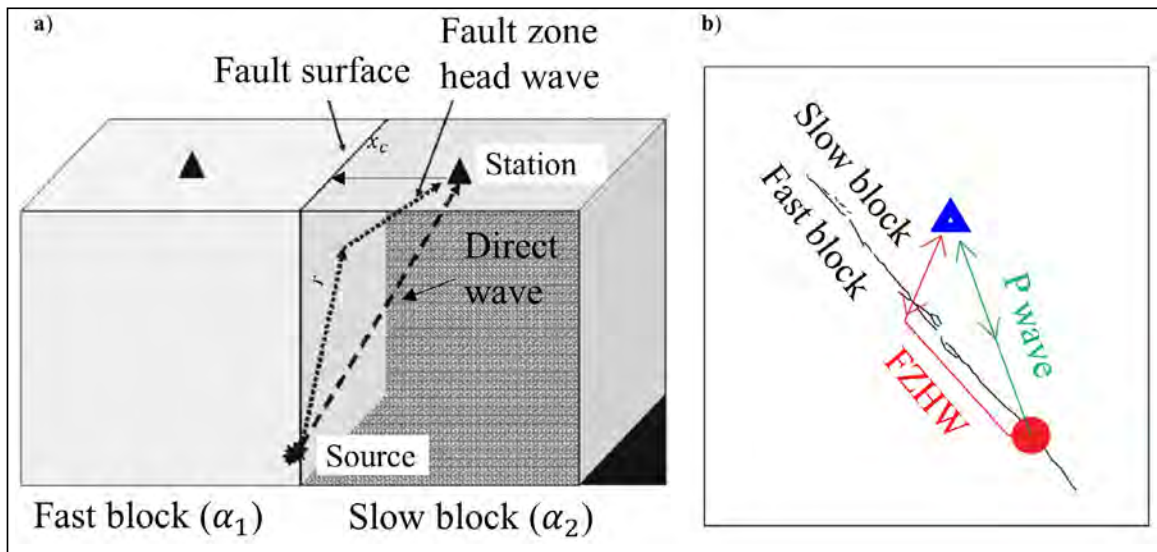
Figure 9- Schematic representation of the wave paths of fault zone head wave (FZHW) and direct P waves; a) Bennington et al. (2013) and b) Allam et al. (2014) have been modified.

(Ben-Zion, 1989, 1990). Another difference between these waves is the particle motion direction in the horizontal medium. While the particle motion is in the direction of the source in the direct incoming wave, this orientation is towards the fault zone in the FZHW (Bulut et al., 2012).

FZHW and direct P wave discrimination on the waveforms at stations close to the fault zone are generated by controlling for these differences. Software developed by Ross and Ben-Zion (2014) was used in the analysis, and the process flow chart is shown in Figure 10a. The program determines the first arrival time of the seismic motion in the vertical component using the STA/LTA ratios. Then, the arrival of a second wave phase is checked by using the Kurtosis and Skewness functions (Saragiotis et al., 2002). After determining these wave arrivals, their polarity is checked by looking at the particle motion of the waves. If the polarity direction of both waves is the same, no FZBD separation is made and the first arrival is directly marked as P wave. If these waves have opposite polarity with respect to each other, the first phase is marked as FZHW, and the following phase is marked as a direct P wave. Figure 10b indicates

the discrimination of FZHW and direct P waves in a sample earthquake seismogram. While the STA/LTA ratio marks the first wave phase, the second wave phase arrival in the Kurtosis function is very sharp. In the skewness function, the polarity transformation between the first and second wave phases occurs.

In this study, 68 earthquakes between October 2017 and May 2018 recorded by MONGAN-1 network stations were analyzed. As a result of this analysis, FZHW was found in 25 earthquake records. In Figure 11, analyzed and FZHW-detected earthquakes are shown in different colors.

As can be seen, the locations of the analyzed earthquakes are generally distributed in the extension of the fault in the Marmara Sea. FZHW detected earthquakes scattered among the others. While some of them are directly along the fault zone, the others are located in south of the fault zone. A distinctive feature related to the locations, magnitudes, and depths of earthquakes with and without FZHW could not be found for the analyzed dataset. In the continuation of the study, it was investigated which stations had more FZHW and which ones were not (Figure 12).
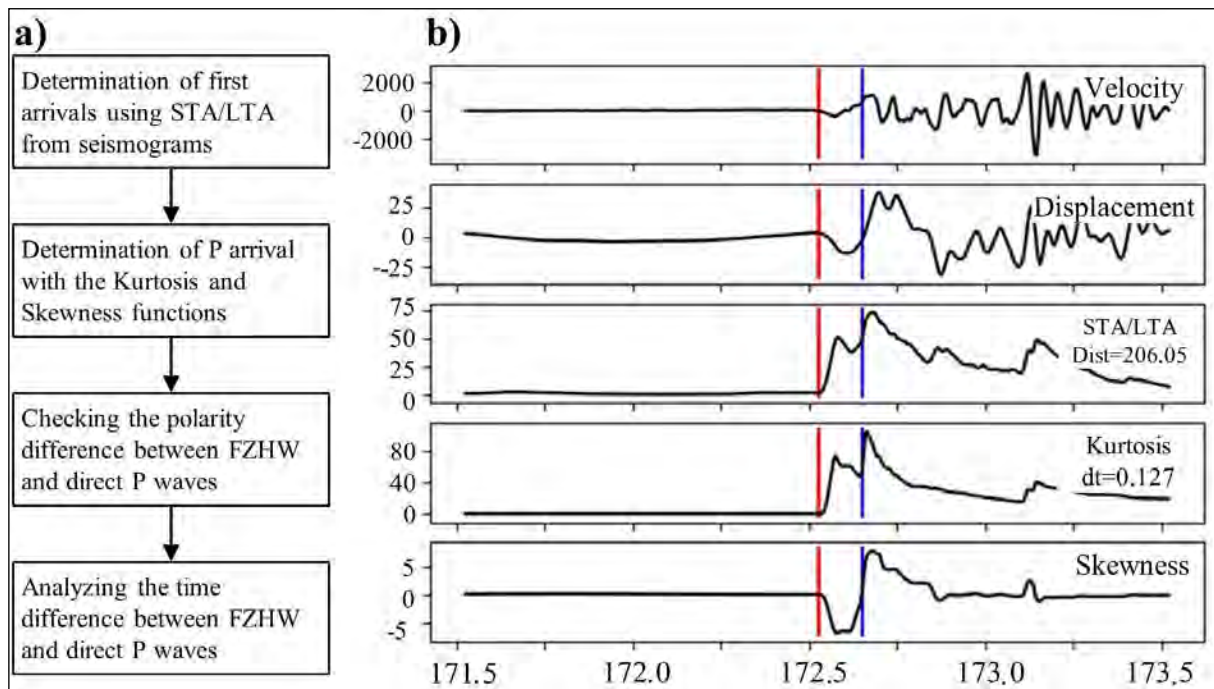
Figure 10- a) Processing steps in determining the fault zone head wave (FZHW) and b) markings of the P wave (blue line) and FZHW (red line) arrivals directly on a sample earthquake seismogram with the help of short time average/long time average (STA/LTA), Kurtosis and Skewness functions.
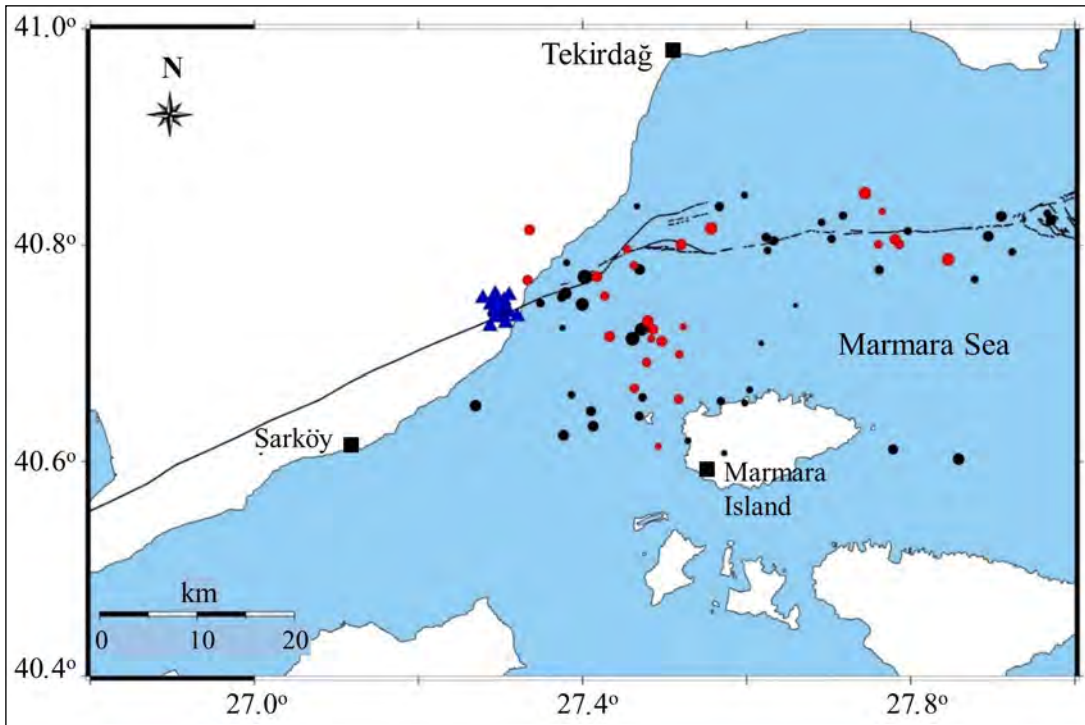
Figure 11- Locations of the analyzed earthquakes. Earthquakes with a fault zone head wave (FZHW) are shown by a red circle and earthquakes without an FZHW are represented by a black circle. The recording stations are indicated by blue triangles.
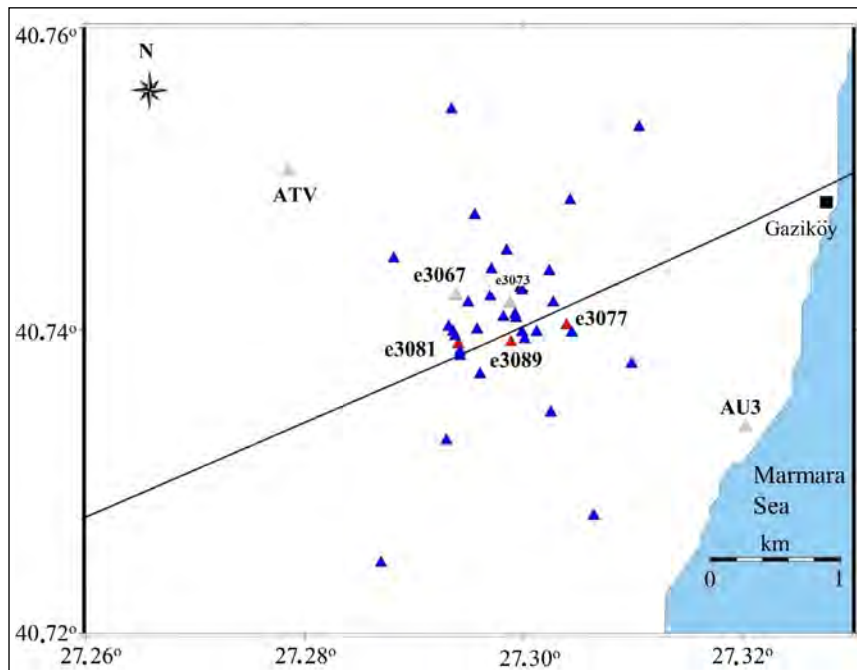
Figure 12- Distribution of stations for 25 earthquakes with fault zone head waves (FZHW). Seismic stations indicated by the red triangle recorded the highest number of FZHW. Seismic stations shown by gray triangles display none of FZHW.

As a result of this research, 36% of 25 earthquakes are observed at e3077, e3081 and e3089 stations. No FZHW could be obtained at ATW, AU3, e3067, and e3073 stations. Theoretically, FZHWs should be recorded at stations on the slow block. However, the analysis shows that FZHWs can be seen on both sides of the fault. Moreover, FZHW is observed in one of the two stations located on the slow side of the fault and very close to each other. According to our analysis, this case is common in stations with low signal-to-noise ratios.

6. Source Mechanism Solutions

The general feature of MONGAN network is that it detects small-magnitude earthquakes with large azimuthal gaps. In contrast, the signal-to-noise ratios are relatively high. In order to understand the stress conditions in the region, it is important obtaining reliable source mechanism solutions of these earthquakes. Since the moment tensor analysis method uses the entire waveform, it enables source mechanism solutions of small earthquakes with a small number of records (Fojtíková et al., 2010).

In this study, the ISOLA program developed by Sokos and Zahradnik (2008) was used for moment tensor analysis. ISOLA seismic moment tensor analysis is similar to Kikuchi and Kanamori (1991)'s multi-point source and iterative deconvolution method, but it uses the entire waveform differently. The inversion process starts with the calculation of Green's functions using the discrete wavenumber method defined by Bouchon (1981) for the displacement seismogram at each station, and the process is performed using the iterative deconvolution method. In the inversion process, synthetic seismograms are created in accordance with the initial parameters. Synthetic and observational seismograms are approximated to each other and the source mechanisms of earthquakes are tried to be determined. Since the method is based on a multi-source definition, a separate solution is generated for each source. Solutions with the smallest difference and the highest correlation between observational and synthetic seismograms are preferred. The agreement between the observational and synthetic seismograms is measured by variance reduction (VR). In selecting the two most accurate double couple (DC) models representing the source mechanism, the variance values as well as the DC component ratio are taken into account.

As input parameters to the program; three components of each station's earthquake record in SAC (Seismic Analysis Code) format, crustal model information, earthquake occurrence time, magnitude and latitude, longitude information, and the duration of the earthquake are entered. In this study, different crustal models were tested and Yamamoto et al. (2015)'s crustal model was used. Figure 13 shows the moment tensor analysis of the Mw=1.8 earthquake that occurred on October 3, 2017, at 04:38 (GMT). In the analysis, recordings of at least 3 stations with a high signal-to-noise ratio are used. The analyzes are repeated in different frequency ranges from 0.5 Hz to 4 Hz, and the obtained values are compared. The time forms of the 1.6-3.3 Hz frequency range, where the best fit is achieved, are shown in Figure 13. As can be seen, synthetic observational fit (VR) > 0.40, Condition Number (CN) <10, Source Mechanism Variation Index (FMVAR) < 30, and Spatial-Time Variation Index (STVAR) < 0.3 values indicate the success of the solution.

In Figure 14, the moment tensor solutions of 5 earthquakes with moment magnitudes 2.9≤Mw≤3.7 are compared with the source mechanism solutions obtained with the zSacWin program (Yılmazer, 2003) using the first P wave polarities. While moment tensor solutions are calculated using MONGAN network seismograms with stations at a very narrow azimuth, first motion P wave polarities are calculated using national network station recordings surrounding the source. As can be seen, the solutions of both methods are quite similar. This result indicates that the moment tensor solutions obtained using a limited number of station coverage are reliable.
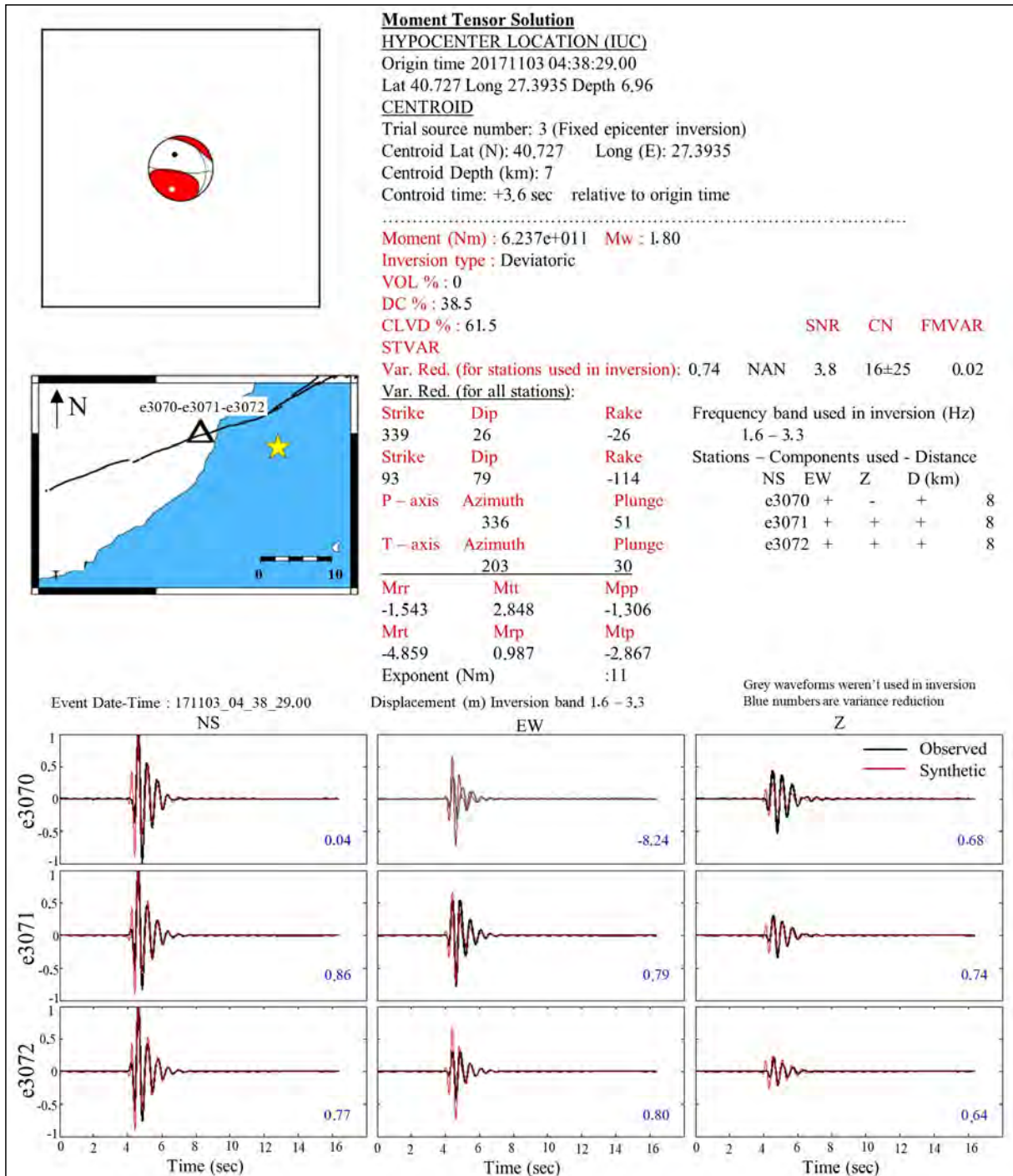
Figure 13- Moment tensor solution obtained by three station seismograms for the M_w=1.8 earthquake that occurred on 03.11.2017 at 04:38 (GMT). While the upper figure shows the solution parameters, the lower figure indicates the synthetic-observed waveform fitting.
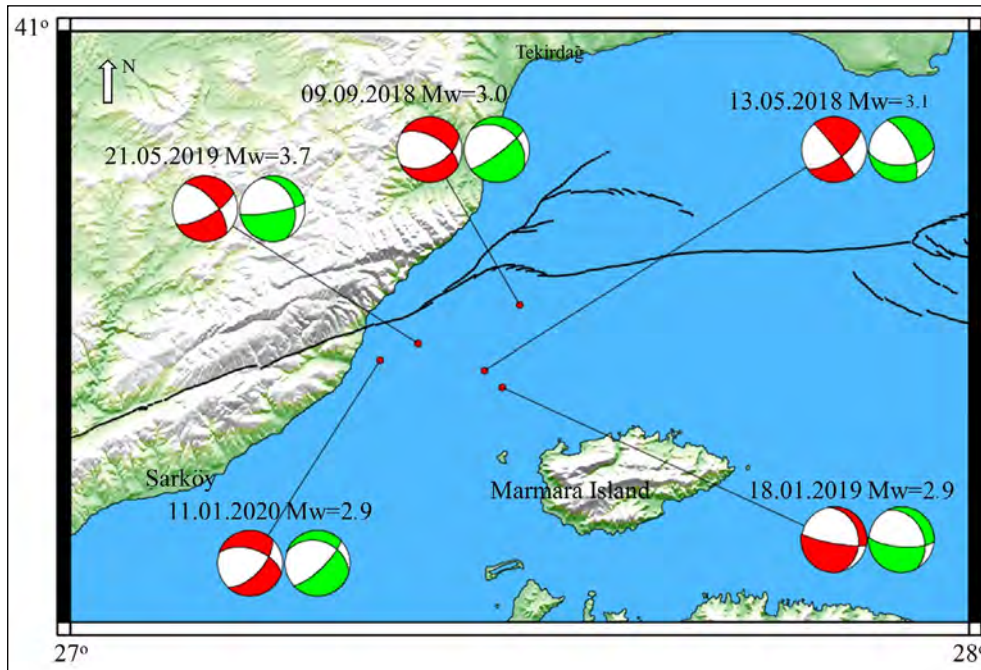
Figure 14- Comparison of source mechanisms obtained from first motion P wave polarity (green) with moment tensor analysis (red).

7. Results

MONGAN network data presents significant challenges and opportunities for earthquake detection, location and magnitude calculations, source mechanism solutions, and fault zone head wave detections. Reliable analyzes from the obtained data can make important contributions to the determination of the current seismicity of the Ganos Fault, the investigation of the fault zone structure, and the understanding of the local stress conditions. This study, which can be considered as a test analysis, has provided the opportunity to see the success limits of the applied analyzes and the necessity of alternative applications.

In the earthquake detection process from continuous data, there were 40%-50% differences between the STA/LTA method and manual check. The method is not achieved in sufficient success, especially in the detection of micro-earthquakes, due to low signal-to-noise ratios. By using different filters during the manual check, the simultaneous view of multiple station records is allowed us to observe microearthquakes. Since the manual check is a very laborious and time-consuming way, it is aimed to use

cross-correlation methods in the future stages of the study, especially in the detection of microearthquakes.

The presence of a sufficient number of stations surrounding the source region in earthquake analyses is very important in terms of increasing the quality of the location. Since MONGAN-1 network data is established in a very small area, it has large azimuthal gaps and produces high vertical/horizontal errors. At the same time, as a result of the very small distances between the stations, there is no difference between the observed wave arrivals in sufficient sensitivity. In addition, the fact that the stations are located on two different fault blocks, fast and slow, cause the waves to reach the stations on the fast block earlier than the stations on the slow block. All these reasons reduce the quality of earthquake solutions. On the other hand, there are many earthquakes that are not included in the national earthquake catalog and are recorded only by the MONGAN-1 network. These earthquakes are generally with M<1 magnitude and are very local earthquakes. In order to increase the solution quality of these earthquakes, it seems essential to use different network techniques, such as beamforming, F-K, or including the source-azimuth directions to be obtained from the P wave first motion polarities (Havskov and

Ottemoller, 2010). In addition, it is expected that the calculation of the regional 3D velocity model and its inclusion in the event locations will increase the quality of the solution.

The effects of the bimaterial structure of the Ganos Fault zone are clearly observed in the seismic wave phases. While early phase arrivals are observed on the fast block in the north of the fault, FZHW arrivals are observed at the stations on the southern block. A systematic distinction regarding FZHW has not been revealed yet. When the number of discovering FZHW increases, the relationship between FZHW arrivals and structural elements can be established.

The results obtained regarding the moment tensor solutions of small earthquakes are remarkably promising. A comparison of different methods in the sample solutions shows that reliable source mechanism solutions can be obtained even with limited data which have a high signal-to-noise ratio. Using high-resolution crustal velocity models and high-frequency intervals are extremely important in testing microearthquakes by using small number of station recordings.

References

Aksoy, M. E., Meghraoui, M., Vallée, M., Çakır, Z. 2010. Rupture characteristics of the AD 1912 Mürefte (Ganos) earthquake segment of the North Anatolian Fault (western Turkey). Geology 38(11), 991-994.

Aksoy, M. E. 2021. The 9 August 1912 Mürefte-Şarköy earthquake of the North Anatolian fault. Mediterranean Geoscience Reviews 3, 95–114.

Allam, A. A., Ben-Zion, Y., Peng, Z. 2014. Seismic imaging of a bimaterial interface along the Hayward Fault, CA, with fault zone head waves and direct P arrivals. Pure and Applied Geophysics 171, 2993-3011.

Allen, R. 1978. Automatic earthquake recognition and timing from single traces. Bulletin of the Seismological Society of America 68, 1521-1532.

Andrews, D. J., Ben-Zion, Y. 1997. Wrinkle-like slip pulse on a fault between different materials. Journal of Geophysical Research 102, 553–571.

Armijo, R., Pondard, N., Meyer, B., Uçarkus, G., Mercier de Lépinay, B., Malavieille, J., Dominguez, S., Gutscher, M-A., Schmidt, S., Beck, C., Cagatay, N., Cakir, Z., Imren, C., Eris, K., Natalin, B., Özalaybey, S., Tolun, L., Lefèvre, I., Seeber, L., Gasperini, L., Rangin, C., Emre, O., Sarikavak, K. 2005. Submarine fault scarps in the Sea of Marmara pull-apart (North Anatolian Fault): implications for seismic hazard in Istanbul. Geochemistry, Geophysics, Geosystems, AGU and the Geochemical Society 6, Q06009.

Ben-Zion, Y. 1989. The response of two joined quarter spaces to SH line sources located at the material discontinuity interface. Geophysical Journal International 98, 213–222.

Ben-Zion, Y. 1990. The response of two half spaces to point dislocations at the material interface. Geophysical Journal International 101, 507–528.

Ben-Zion, Y., Aki, K. 1990. Seismic radiation from an SH line source in a laterally heterogeneous planar fault zone. Bulletin of the Seismological Society of America 80(4), 971-994.

Ben-Zion, Y., Malin, P. 1991. San Andreas fault zone head waves near Parkfield, California. Science 251, 1592–1594.

Bennington, N. L., Thurber, C., Peng, Z., Zhang H., Zhao P. 2013. Incorporating fault zone head wave and direct wave secondary arrival times into seismic tomography: Application at Parkfield, California. Journal of Geophysical Research: Solid Earth 118, 1008-1014.

Bentz, S., Martínez-Garzón, P., Kwiatek, G., Dresen, G., Bohnhoff, M. 2019. Analysis of microseismicity framing $M_L > 2.5$ earthquakes at the Geysers geothermal field, California. Journal of Geophysical Research: Solid Earth 124, 8823–8843.

Bohnhoff, M., Bulut, F., Dresen, G., Malin, P. E., Eken, T., Aktar, M. 2013. An earthquake gap south of İstanbul. Nature Communication 4, 1999.

Bohnhoff, M., Martínez-Garzón, P., Bulut, F., Stierle, E., Ben-Zion, Y. 2016. Maximum earthquake magnitudes along different sections of the North Anatolian fault zone. Tectonophysics 674, 147–165.

Bohnhoff, M., Wollin, C., Domigall, D., Küperkoch, L., Martínez-Garzón, P., Kwiatek, G., Dresen, G., Malin, P. E. 2017. Repeating Marmara Sea earthquakes: indication for fault creep. Geophysical Journal International 210(1), 332–339.

Bouchon, M. 1981. A simple method to calculate Green's functions for elastic layered media. Bulletin of the Seismological Society of America 71(4), 959–971.

Bulut, F., Ben-Zion, Y., Bohnhoff, M. 2012. Evidence for a bimaterial interface along the Mudurnu segment of the North Anatolian fault zone from polarization analysis of P waves. Earth and Planetary Science Letters 327, 17–22.

Bulut, F., Aktuğ, B., Yaltırak, C., Doğru, A., Özener, H. 2019. Magnitudes of future large earthquakes near İstanbul quantified from 1500 years of historical earthquakes, present-day microseismicity and GPS slip rates. Tectonophysics 764, 77-87.

Ergintav, S., Reilinger, R. E., Çakmak, R., Floyd, M., Cakir, Z., Doğan, U., King, R. W., McClusky, S., Özener, H. 2014. Istanbul's earthquake hot spots: Geodetic constraints on strain accumulation along faults in the Marmara seismic gap. Geophysical Research Letters 41, 5783– 5788.

Fojtíková, L., Vavryáuk, V., Cipciar, A., Madarás, J. 2010. Focal mechanisms of micro-earthquakes in the Dobrá Voda seismoactive area in the Malé Karpaty Mts. (Little Carpathians), Slovakia. Tectonophysics 492(1-4), 213-229.

Gibbons, S. J., Ringdal, F. 2006. The detection of low magnitude seismic events using array-based waveform correlation. Geophysical Journal International 165, 149–166.

Havskov, J., Ottemoller, L. 1999. SeisAn Earthquake Analysis Software. Seismological Research Letters 70, 532–534.

Havskov, J., Ottemoller L. 2010. Routine Data Processing in Earthquake Seismology. Springer, 347.

Kalafat, D., Gürbüz, C., Üçer, S. B. 1987. Batı Türkiye'de kabuk ve üst manto yapısının araştırılması. Deprem Araştırma Bülteni 59, 43-64.

Kikuchi, M., Kanamori, H. 1991. Inversion of complex body waves. III. Bulletin of the Seismological Society of America 81, 2335–2350.

Lange, D., Kopp, H., Royer, J.Y., Henry, P., Çakir, Z., Petersen, F., Sakic, P., Ballu, V., Bialas, J., Özeren, M. S., Ergintav, S., Géli, L. 2019. Interseismic strain build-up on the submarine North Anatolian Fault offshore İstanbul. Nature Communications 10(1), 3006.

Li, Y. G., Leary, P. C. 1990. Fault zone trapped seismic waves. Bulletin of the Seismological Society of America 80(5), 1245-1271.

Lienert, B. R., Havskov, J. 1995. A computer program for locating earthquakes both locally and globally. Seismological Research Letters 66(5), 26-36.

Mcclusky, S., Balassanian, S., Barka, A., Demir, C., Ergintav, S., Georgiev, I., Gurkan, O., Hamburger, M., Hurst, K., Kahle, H.G., Kastens, K., Kekelidze, G., King, R., Kotzev, V., Lenk, O., Mahmoud, S., Mishin, A., Nadariya, M., Ouzounis, A., Veis, G. 2000. Global positioning system constraints on plate kinematics and dynamics in the eastern Mediterranean and Caucasus. Journal of Geophysical Research 105, 5695-5719.

McGuire, J., Ben-Zion, Y. 2005. High-resolution imaging of the bear valley section of the San Andreas fault at seismogenic depths with fault zone head waves and relocated seismicity. Geophysical Journal International 163, 152–164.

Okay, A., Özcan, E., Cavazza, W., Okay, N., Less, G. 2010. Basement types, Lower Eocene aeries, Upper Eocene Olistostromes and the initiation of the Southern Thrace Basin, NW Turkey. Turkish Journal of Earth Sciences 19, 1–25.

Özalaybey, S. 2010. Marmara Denizi'nde depremsellik gözlem altyapı kapasitesinin güncellenmesi sonuç raporu. TÜBİTAK, Proje No: CAYDAG-105Y369.

Ross, Z. E., Ben-Zion, Y. 2014. Automatic picking of direct P, S seismic phases and fault zone head waves. Geophysical Journal International 199(1), 268-381.

Sakic, P., Piété, H., Ballu, V., Royer, J. Y., Kopp, H., Lange, D., Petersen, F., Özeren, M. S., Ergintav, S., Geli, L., Henry, P., Deschamps, A. 2016. No significant

steady state surface creep along the North Anatolian Fault offshore İstanbul: results of 6 months of seafloor acoustic ranging. Geophysical Research Letters 43(13), 6817–6825.

Saragiotis, C., Hadjileontiadis, L., Panas, S. 2002. PAI-S/K: a robust automatic seismic P phase arrival identification scheme. IEEE Transactions on Geoscience and Remote Sensing 40, 1395–1404.

Schmittbuhl, J., Karabulut, H., Lengliné, O., Bouchon, M. 2016. Seismicity distribution and locking depth along the main Marmara Fault. Turkish Geochemistry, Geophysics, Geosystems 17, 954–965.

Sokos, E., Zahradník, J. 2008. ISOLA- A Fortran code and Matlab GUI to perform multiple point source inversion of seismic data. Computers and Geosciences 34, 967–977.

Stein, R. S., Barka, A. A., Dieterich, J. H. 1997. Progressive failure on the North Anatolian fault since 1939 by earthquake stress triggering. Geophysical Journal International 128, 594–604.

Uchida, N., Kalafat, D., Pınar, A., Yamamoto, Y. 2019. Repeating earthquakes and interplate coupling along the western part of the North Anatolian Fault. Tectonophysics 769, 228185.

Uçarkuş, G., Çakır, Z., Armijo, R. 2011. Western termination of the Mw 7.4, 1999 İzmit earthquake rupture: Implications for the expected large earthquake in the Sea of Marmara. Turkish Journal of Earth Sciences 20, 379–394.

Wollin, C., Bohnhoff, M., Martínez-Garzón, P., Küperkoch, L., Raub, C. 2018. A unified earthquake catalogue for the Sea of Marmara Region, Turkey, based on automatized phase picking and travel-time inversion: seismotectonic implications. Tectonophysics 747-748, 416-444.

Yalçınkaya, E., Bohnhoff, M., Görgün, E., Alp, H., Bentz, S., Pınar, A., Alver, F., Kılıçarslan, Ö., Tamtaş, B.D., Görgün, B. 2022. Ganos fayı güncel deprem etkinliğinin değerlendirilmesi: MONGAN sismik ağ yapısı ve veri kalitesi. Hacettepe Yerilimleri Dergisi 43(1), 37-60.

Yılmazer, M. 2003. Deprem kaynak parametrelerinin online belirlenmesi, Yüksek Lisans Tezi, İstanbul Üniversitesi, Fen Bilimleri Enstitüsü, Jeofizik Mühendisliği Ana Bilim Dalı, İstanbul, 57.

Yamamoto, Y., Takahashi, N., Çıtak, S., Kalafat, D., Pınar, A., Gürbüz, C., Kaneda, Y. 2015. Offshore seismicity in the western Marmara Sea, Turkey, revealed by ocean bottom observation. Earth Planets Space 67, 147.

Yamamoto, Y., Takahashi, N., Pınar, A., Kalafat, A., Çıtak, S., Comoğlu, M., Polat, R., Kaneda, Y. 2017. Geometry and segmentation of the North Anatolian Fault beneath the Marmara Sea, Turkey, deduced from long-term ocean bottom seismographic observations. Journal of Geophysical Research: Solid Earth 122.

Yamamoto, R., Kido, M., Ohta, Y., Takahashi, N., Yamamoto, Y., Pınar, A., Kalafat, D., Özener, H., Kaneda, Y. 2019. Seafloor geodesy revealed partial creep of the North Anatolian Fault submerged in the sea of Marmara. Geophysical Research Letters 46(3), 1268–1275.

Yamamoto, Y., Kalafat, D., Pınar, A., Takahashi, N., Polat, R., Kaneda, Y., Özener, H. 2022. Seismic velocity structure along the North Anatolian Fault beneath the Central Marmara Sea and its implication for seismogenesis. Geophysical Journal International 228(1), 396–411.

Yoon, C. E., O'Reilly, O., Bergen, K. J., Beroza, G. C. 2015. Earthquake detection through computationally efficient similarity search. Science Advances 1, e1501057.

Bulletin of the Mineral Research and Exploration

A new look at the origin of N-S trending young basins of western Anatolia

Ömer Feyzi GÜRER[a*]

[a]*Kocaeli University, Engineering Faculty, Department of Geological Engineering, Kocaeli, Türkiye*

Research Article

ABSTRACT

In the western Anatolia, the tectonic regime transitioned from crustal shortening to extension during Late Cenozoic time and evidence of this event was imprinted on basement lithologies and N-S and E-W oriented two distinct basin sub-types. Here, we examined the exhumation mechanism of the Menderes massif that forms the basement of these basins from a different perspective. The N-S oriented basins overlying different basement rock types were re-evaluated based on new evidence that has potential to put new constrains for interpreting the tectonic evolution of the area. Unroofing of the Menderes Massif must have developed due to compressional core complex. Per the model generated from our observations, we propose that the western Anatolia underwent a N-S contraction during the Early-Middle Miocene time. In this period from Marmara Sea at north to Mediterranean Sea at south, numerous basins, as in Gördes and Demirci, were bound by N-S oriented oblique faults. Evidence of contraction in the region during Early Middle Miocene time is understood by N-S oriented obique, strike-slip faults, folds, and reverse faults. Starting from the Plio-Quaternary time, the contractional regime was shifted to extension and ensuing E-W oriented grabens were formed in Gediz, Büyük Menderes, and Gökova. The structural deformation associated with these E-W oriented grabens are normal faults and related open folds. Geological evidence of multi-generation extension is recognized in the basins and basin-filling deposits throughout the Neogene to Quaternary time.

---

1. Introduction

Western Anatolia was exposed to the mutual interaction of contraction and extension systems during the Late Cenozoic. According to their position, two groups of basins are mainly present in the region as E-W and N-S trending, and there are several discussions on them. The most important of the major issues is to reveal the main data of the compressional and extensional tectonics and their relations and, accordingly, dating the initial ages of compressional and extensional tectonics. There is no consensus has yet been reached on these issues (Şengör, 1979; Seyitoğlu and Scott, 1991; Yılmaz et

The 11th Development Plan, set Türkiye's development 2014; Sözbilir et al., 2011; Özburan and Gürer, 2012; Gürbüz et al., 2012; Sangu et al., 2020). Three main problems have not been fully reconciled regarding the Neogene-Quaternary geology and structural elements of the region. These are;

1) What is the origin of extension?

Six different models have been proposed to answer this question: a) the southward rollback of the African plate or the back-arc spreading model (McKenzie 1978; Jackson and McKenzie 1988), b) orogenic collapse model (Dewey 1988; Seyitoğlu

---

Corresponding author: Ömer Feyzi GÜRER, ofgurer@kocaeli.edu.tr

and Scott 1991; McClusky et al., 2000), c) tectonic escape model (Dewey and Şengör 1979; Şengör 1987), southward retreat of the northward subducting African slab due to post-orogenic collapse (Gautier et al., 1999; Jolivet, 2001), e) two-phased extension model (orogenic collapse/rollback of the subducting slab and tectonic escape) (Koçyiğit et al., 1999; Yılmaz et al., 2000; Bozkurt 2000, 2001*b*, 2003, 2004; Purvis and Robertson 2004; Bozkurt and Rojay 2005), f) extension in the Aegean Region due to different convergence rates towards the northeast between African slab and the Eurasian lithosphere. The faster southwestward motion of Greece than that in Cyprus and Anatolia resulted in the Aegean-West Anatolian Rift (Doglioni et al., 2002).

2) What is the origin of the N-S basins?

For the origin of N-S trending basins, one of the following six models has been suggested: a) the basins developed as paleotectonic Tibetan type cross-grabens under N-S compression, then changed into neotectonic Aegean type cross-grabens under N-S extensional regime (Şengör et al., 1985; Şengör, 1987; Görür et al., 1995). b) the basins developed as Aegean-type cross-grabens, similar to the strike-slip basins associated with syn-sedimentary volcanism (Bozkurt, 2003). c) the third model suggests that the N-S basins are related to the strike-slip faults developed under N-S compression and E-W extension (Yılmaz et al., 2000; Gürer et al., 2009, 2013; Özburan and Gürer, 2012). d) The basins in N-S and E-W directions developed simultaneously during the N-S extensional regime since the late Oligocene-Early Miocene. The extension was attributed to late orogenic collapse, which occurred just after the Paleogene compression had been ended (Seyitoğlu and Scott, 1991, 1994). e) N-S trending basins are not extension-related, they are intermountain basins (İnci, 1998, 2002). f) the basins are either supradetachment basins or depositions occurred in transtensional basins (Purvis and Roberston, 2004; Seyitoğlu et al., 2004; Ersoy et al., 2011; Sözbilir et al., 2011; Sümer et al., 2020).

3) Is the extension in the region continuous or discontinuous?

a) According to some researchers, the extensional system was continuously active from the Late Oligocene to the Quaternary (Seyitoğlu and Scott,

1991; Işık et al., 2003). Seyitoğlu and Işık (2015) claimed that there was no compressional regime in the region that continued until the Late Pliocene or between Miocene-Pliocene, even for a short period. b) Some other authors have proposed a multistage extensional history with two different suggestions. The first group suggested that the Late Oligocene-Early Miocene stretching could not be responsible for all extensional tectonic history and that continental extension in the region was not a continuous event (Purvis and Robertson, 2004; Bozkurt and Sözbilir, 2004; Bozkurt and Rojay, 2005). According to this model, the stretching direction in Western Anatolia has always been N-S. The second group suggested multiple stretching phases in different directions (Koçyiğit et al., 1999; Yılmaz et al., 2000; Genç et al., 2001; Gürer and Yılmaz 2002; Ring et al., 2003; Gürer et al., 2001, 2003, 2006, 2009, 2021; Koçyiğit, 2005; Kaymakçı, 2006; Çemen et al., 2006; Koçyiğit and Deveci, 2007; Alçiçek and Ten Veen, 2008; Gürbüz et al., 2012; Özburan and Gürer, 2012; Gürboğa et al., 2013).

The largest E-W trending grabens are Bakırçay, Kütahya, Simav, Gediz, Küçük Menderes, Büyük Menderes and Gökova grabens. These grabens and the normal faults restricting them are the most seismically active structures of western Anatolia. There is no consensus on the onset of the formation of E-W trending grabens. However, some researchers, based on paleontological and geochronological data, suggested that grabens began to develop in the Early Miocene (Seyitoğlu and Scott, 1991, 1996), in the Late Miocene (Şengör and Yılmaz, 1981; Şengör et al., 1985; Şengör 1987; Kaymakçı, 2006), or in the Plio-Quaternary (Dewey, 1988; Yılmaz et al., 2000; Sarıca, 2000; Bozkurt, 2000, 2001*b*; Gürer et al., 2009; 2013; Özburan and Gürer, 2012; Yılmaz, 2017*a, b*). Other structural elements of Western Anatolia are the N-S trending basins and uplifts. These basins, mainly Urla, Çubukludağ, Seyitömer, Sabuncupınar, Gördes, Demirci, Selendi-Uşak, Ören, Eskihisar and Tınaz, join-up with the E-W grabens at high angles.

This article aims to give brief information about the basins in Western Anatolia and reevaluate the debates, particularly on the formation of N-S trending basins. These evaluations will be discussed within the scope of the author's studies in the region and other

publications from the literature. Although the origin of the crustal extension is controversial, it is possible to examine the hypotheses about the continuity of the extension with detailed geological studies, especially in the basins.

2. Regional Geological Setting

There are two main types of rock groups in Western Anatolia as the pre-Neogene basement and the Neogene-Quaternary sequences (Figure 1). From north to south, the main tectonic units are a) Sakarya Continent, b) İzmir-Ankara Suture Zone, c) Menderes Massif, d) Lycian Nappes, and e) Taurides. These tectonic units were amalgamated by the closure of the northern branch of Neo Tethys (Vardar-İzmir-Ankara) in the Late Cretaceous-Eocene interval.

2.1. Pre-Neogene Basement Units

In Western Anatolia, pre-Neogene structural units with different geological features such as Sakarya
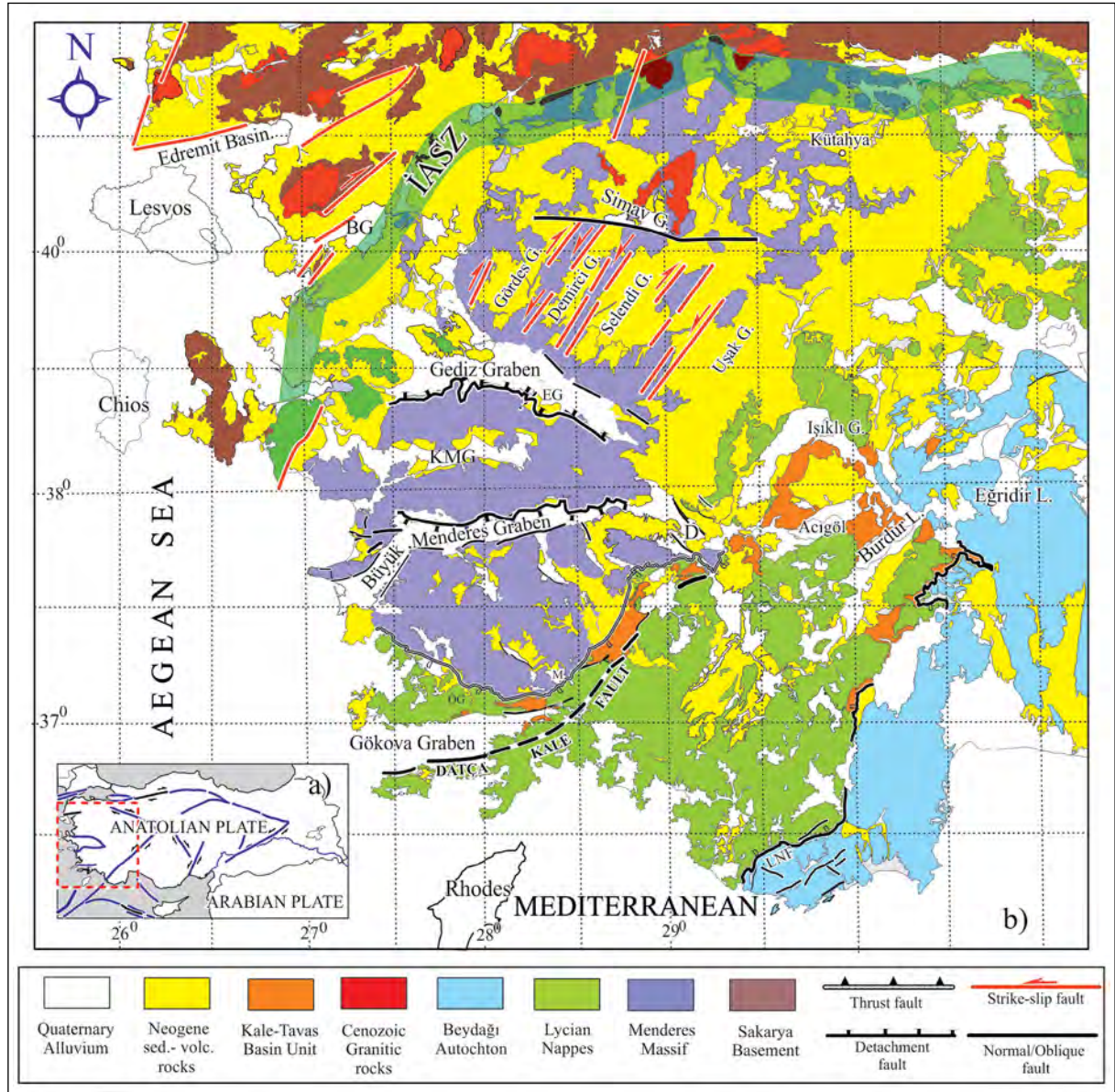
Figure 1- a) Outline map of Türkiye and b) Simplified geological map of Western Anatolia (simplified from Konak, 2002, Konak and Şenel, 2002). D: Denizli, M: Muğla, AH: Alaşehir Basin, KSH: Kuşadası-Söke Basin, ÖG: Ören Basin, BH: Bakırçay Basin, KMG: Küçük Menderes Graben, İAKZ: İzmir-Ankara Suture Zone.

Continent, İzmir-Ankara Suture Zone, Menderes Massif, Lycian Nappes, and Taurides are present. These structural units will be briefly introduced below, from north to south.

2.1.1. Sakarya Continent

Sakarya Continent is characterized by a strongly deformed Triassic basement with various metamorphics, namely the Karakaya Complex, which is covered by an extensive unconformity by Liassic conglomerate and sandstones, which pass to middle Jurassic-Lower Cretaceous carbonates and to Upper Cretaceous flysch (Bingöl et al. 1975; Okay, 1989; Genç and Yılmaz, 1995). Sakarya Continent is a unit bounded by the İzmir-Ankara Suture to the south and the Intra-Pontide Suture to the north. Based on consisting of several pre-Alpine sequences as tectonic assemblages presenting completely different geological ages in the basement, the unit is assumed as a composite terrane (Göncüoğlu et al., 1997).

2.1.2. İzmir-Ankara Suture Zone

İzmir-Ankara Suture Zone represents the northern branch of Neo-Tethys. This suture, which separates the Sakarya Zone from the Anatolide-Taurides, is generally accepted as the major Tethys suture in Türkiye (Yılmaz, 1981). The northern branch of Neo-Tethys was consumed beneath the Sakarya Continent by northward subduction during the Cretaceous-Eocene. This suture zone contains intense HP/LT blueschist facies metamorphism in some parts (Sherlock et al., 1999; Okay, 2002; Çelik et al., 2011). It also contains a number of fragmented ophiolite slices, which are interpreted to represent remnants of the Tethys oceanic lithosphere (Göncüoğlu et al., 2000). These oceanic lithosphere fragments were thrusted over the passive margin of Anatolide-Tauride platform (Şengör and Yılmaz, 1981; Gürer and Aldanmaz, 2002; Çelik et al., 2011).

2.1.3. Menderes Massif

The Menderes Massif is accepted as one of the metamorphic core complexes in which lower-middle crustal rocks outcrop (Bozkurt et al., 1993; Bozkurt and Park, 1994; Hetzel et al., 1995; Emre and Sözbilir, 1997; Gessner et al., 2001a, b; Ring et al., 2003; Seyitoğlu et al., 2004). This crystalline

complex is tectonically overlain by different tectonic units or zones such as the Lycian nappes in the south, and in the north and northwest by the Tavşanlı zone, Selçuk mélange, the Dilek Nappe, the Afyon zone, Ören Unit with high pressure metamorphism (Okay, 1981; Sherlock et al., 1999; Candan et al., 2001, 2005; Önen and Hal, 2000; Güngör and Erdoğan, 2001; Pourteau et al., 2010; Yılmaz, 2017a). In the west, the metamorphic rocks extending along the Dilek Peninsula are accepted as the eastern continuation of the Central Aegean Region Cycladic Massif, based on their geological and metamorphic characteristics (Candan et al., 2005; Rimmele et al., 2003, 2005; Gessner et al., 2001a, b; Van Hinsbergen and Schmid, 2012; Yılmaz, 2017a). The massif is covered by Neogene-Quaternary sedimentary/volcanic units in many areas.

The tectonic position and evolution of the Menderes massif is controversial. The ongoing debates about the massif concerns the type and timing of metamorphism, magmatism, and deformation (Yılmaz, 2017a), the overall structure of the massif, how and when the massif's lower-middle crustal rocks were exhumed, and the relationship of the massif to the other surrounding massifs (Whitney and Bozkurt, 2002). The debates are especially related to the structural position of the southern part of the Menderes Massif. Suggested models are mainly as follows: a series of north-vergent thrusts within the massif (Bozkurt and Park, 1994) (Figure 2a), southern Menderes sub-massif as a large north-vergent recumbent fold (Okay, 2001) (Figure 2b), a series of nappes stacked during south-directed thrusting (Ring et al., 1999; Gessner et al., 2001b). It has been suggested that the Menderes Massif, which was thought to have a simple structure in previous studies, presents a complex internal structure defined by the Late Alpine compressional tectonic product thrust faults (Partzsch et al, 1998; Candan and Dora, 1998; Gessner et al., 1998; Ring et al., 1999, 2003; Dora et al., 2001; Regnier et al., 2003; Ring and Collins, 2005; Bozkurt, 2007). The metamorphic rocks of the Central Menderes Massif consist of four nappes stacked during plate convergence from Late Cretaceous to Eocene along the İzmir-Ankara Suture Zone (Ring et al., 1999; Van Hinsbergen, 2010; Gessner et al., 2013). From the bottom to the top, these nappes include the Bayındır, Bozdağ, Çine and Selimiye nappes that are structurally overlain
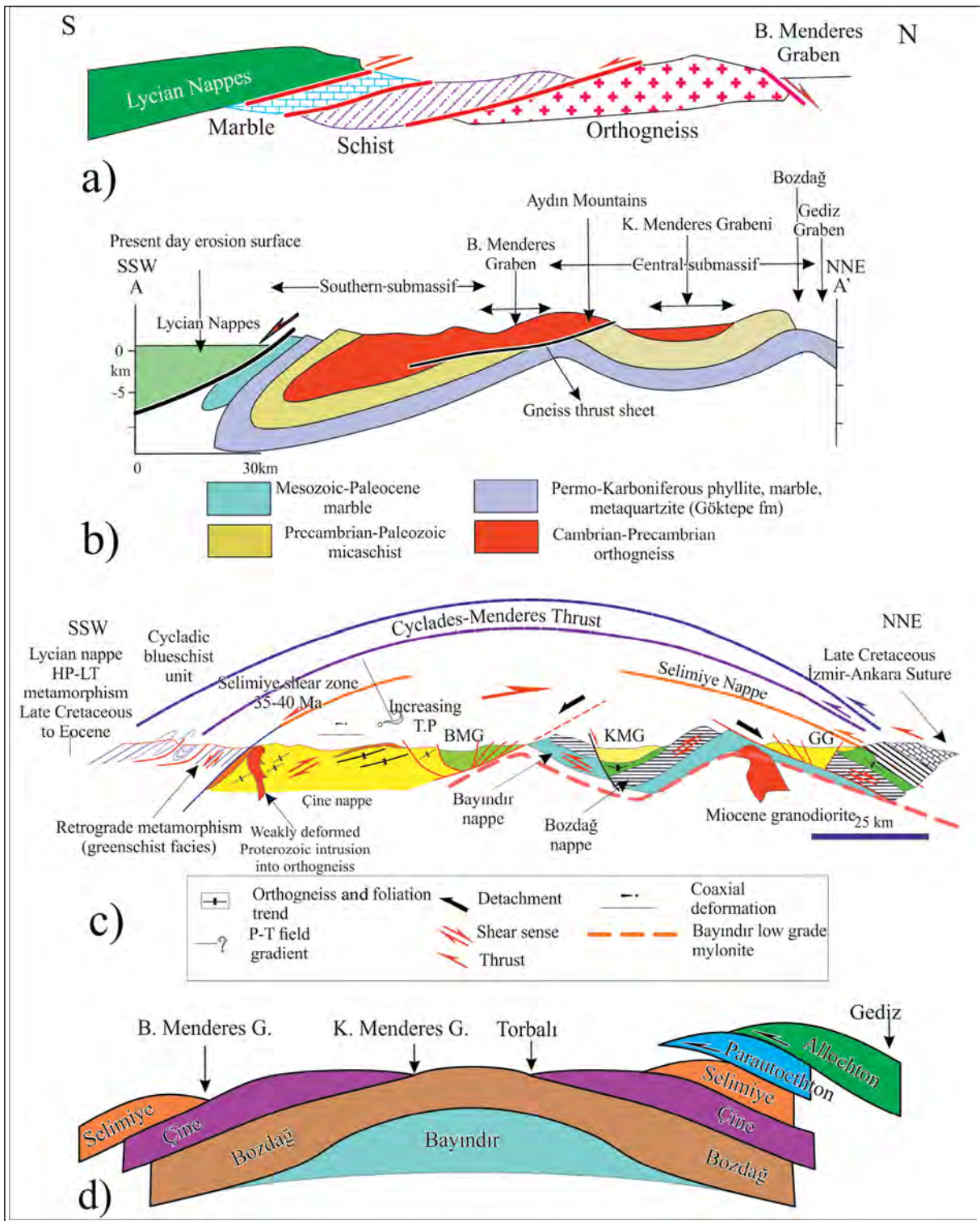
Figure 2- a) the north-vergent thrust model in the Menderes Massif (Bozkurt and Park, 1999), b) a schematic cross-section illustrating the recumbent fold in the Menderes Massif (Okay, 2001), c) the interpreted cross-section of the Menderes Massif by Gessner et al. (2001c), Lips et al. (2001), Regnier et al. (2007). $^{40}Ar/^{39}Ar$ white mica ages for the Selimiye shear zone were taken from Hetzel and Reischmann (1996). The Bayındır low-grade mylonite zone is shown with a thick dashed line. BMG: Büyük Menderes Graben, GG: Gediz Graben, KMG: Küçük Menderes Graben (Regnier et al., 2007) and d) an interpreted cross-section showing the positions of different thrust slices along the Menderes Massif (Yılmaz, 2017a).

by the Cycladic blueschist unit in the west (Ring et al., 1999; Gessner et al., 2013; Heineke et al., 2019). Regnier et al. (2007) demonstrated the napped internal structure of the massif by conducting a study focusing on metamorphic conditions along the contact of orthogneiss and surrounding metasedimentary rocks in the southern Menderes Massif (Figure 2c). According to Yılmaz (2017*a*), the Menderes Massif has been subjected to semi-brittle to brittle, N-S compressional deformation, which causes the shortening, thickening and imbrication in the entire region. Thick-skinned deformation has occurred in the Menderes Massif and its tectonic components have been structurally rearranged. Deep-seated metamorphic rocks (core rocks) were thrusted over the cover rocks (Figure 2d, Yılmaz, 2017*a*).

A large number of studies have been conducted on the metamorphisms and deformations of the Menderes Massif and its surrounding massifs (Table 1). In these studies, different opinions have been put forward about the deformation times of the massif. Ages varying from Eocene to Miocene for compression, while from Miocene to Pliocene for N-S trending extension in the massif have been suggested.

2.1.4. Lycian Nappes

The Lycian nappes form a nappe stack consisting of fragmented ophiolites forming the uppermost nappe, together with the slices of the Western Tauride metamorphic basement and the overlying Mesozoic platform carbonates. Lycian nappes are widespread in the south of the Menderes Massif (Figure 3). Lycian nappes as in tectonic slices tectonically overlie the Beydağı parautochthon of the Western Taurides at the south (Poisson, 1977, Gutnic et al., 1979; Ricou et al., 1979; Collins and Robertson, 1998; Ersoy, 1990). It has been accepted that the Lycian nappes were transported from the Neo-Tethys Ocean at the north of the Menderes Massif in the Late Cretaceous-Late Miocene interval as tectonic slices, over the massif from north to south and emplaced in the region (Şengör and Yılmaz, 1981; Şengör et al., 1985; Okay, 1989; Collins and Robertson, 1998).

2.1.5. Taurides

In the west of the Taurides, located in the south of Türkiye, rock units, which are mostly allochthonous,

developed in the Precambrian-Quaternary interval crop out. Beydağları autochthon is a carbonate platform during the Mesozoic and witnessed the emplacement of Antalya and Alanya nappes at the end of the Mesozoic and/or in Paleocene, and the Lycian nappes at the end of the Early Miocene and the beginning of the Middle Miocene (early Langhian). The first two of these nappes are south-originated, while the Lycian nappes of north-origin (Konak, 2007). The northern branch of the Neo-Tethys Ocean was closed in the Eocene as a result of the collision of the Sakarya zone in the north and the Tauride-Anatolide Platform in the south (Şengör and Yılmaz, 1981). The first thrusting of ophiolitic nappes and platform successions from north to south over the Tauride platform initiated in the Early Eocene, and its final emplacement lasted until the Middle Pliocene (Poisson, 1977; Yılmaz et al., 2000).

2.2. Neogene-Quaternary Basins

Neogene-Quaternary sequences are mainly found in basins in two different directions. The N-S trending basins are rhomboidal- or trough-shaped, with an average length of 20-25 km and a width of 5-10 km (Figure 1). The faults controlling the opening of the basins are generally oblique faults with a dominant strike-slip component (Yılmaz et al., 2000; Bozkurt 2003; Gürbüz et al., 2012; Gürer et al., 2001, 2009, 2013; Ersoy et al., 2011, 2014; Yılmaz 2017*a, b*). The basins, generally have similar stratigraphy, and are filled with terrestrial sediments and volcanics, presenting lateral and vertical changes within the facies and lithologies. The sediments were mainly deposited in alluvial fan, fluvial and lacustrine environments. The succession, which starts with blocky conglomerate and conglomerate at the basin margins, then passes into alternations of sandstone and mudstone, and into marl and limestones in the basin interior. In addition to the sediments, volcanics in andesite, latite and dacite composition and volcanoclastic rocks are commonly found in the northern basins (Yılmaz, 1989; Yılmaz et al., 2000). Basin fills can reach a thickness of 1500 m.

The N-S oriented basin sequences were influenced by syn- and post-depositional open-closed folds and reverse faults at different scales and were deformed. Miocene deposits of the basins located in the north of the Gediz Graben were deformed by wide folds with parallel axes to the basin margins (Yılmaz et al.,

Table 1- Views on the metamorphism and deformation of the Menderes Massif and its surrounding massifs.

Reference	Deformation Components	Metamorphism Conditions	Time of Deformation
Ring et al., 1999 **Samos**	D1-D2, WNW-ESE oriented nappe emplacement	Blueschist and blueschist-greenschist transitional metamorphism (M1) D2, Blueschist metamorphism in Kerketas nappe (M2)	Eocene-Early Oligocene
	D3, Oligocene-Miocene horizontal stretching,	Crustal horizontal stretching, then greenschist metamorphism (M3)	Early Oligocene
	D4, <8.6 and 9 My, E-W short-term compression	The cause of this event is unknown.	Miocene
	D5, <8.6-Recent N-S oriented normal faulting phase		Late Tortonian- Recent
Bozkurt and Park, 1999 **Southern Menderes Massif**	D1 related deformation; N-S	M1 Barrovian type regional metamorphism	Early Eocene-Early Oligocene
	D2, WNW-ESE trending	?	Late Oligocene-Early Miocene
Gessner et al., 2001*b* **Menderes Nappes**	D_{PA}, compression, top to the NE sense of shear	Amphibolite facies metamorphism	Pre-Alpine (Proterozoic)
	D_{A3+D4}, compression, top to the S	Greenschist facies	Late Oligocene
Gessner et al., 2001*a* **Menderes Massif**	First cooling phase	Temperature over 110ºC	Late Oligocene-Middle Miocene
	Second cooling phase	Temperature below 60ºC	Pliocene-Pleistocene
Rimmele et al., 2003 **South of Menderes Massif**	1st phase, top to the N sense of shear, compression	HP association magnesiocarpholite–kyanite	Late Cretaceous-Eocene
	2nd phase, top to the N sense of shear	AMM peak, gradual cooling (Late Eocene) HP metamorphism in the cover metaconglomerate. Northward thrust of the Lycian Nappes over the Menderes Massif, Reactivation of the Menderes-Lycian contact as a NE shear zone in the upper plate leading to the exposure of the Lycian HP rocks.	Paleocene-Eocene
	3rd phase	N-S bi-directional extension, Top to the SW shear sense in the chloritic shear bands in the late exhumation phase.	Oligo-Miocene
Rimmele et al., 2003 **South of Menderes Massif**	Top to the NE shearing concurrent with the syn-orogenic extension and exhumation of the Cyclades	HP-LT	Eocene
	Extension, NE trending shear in the regional upper plate		Miocene
Ring et al., 2003 **Gördes-Çine**	Napping		Late Cretaceous-Tertiary
	Extension, Rapid Cooling, southward movement of the upper plate		Late Oligocene (25My) - Miocene
	Extension, Cooling		Pliocene

Table 1- Continued.

Regnier et al., 2003 **South of Menderes Massif**	Selimiye shear zone, MM burial, top to the S shear sense	Greenschist and amphibolite facies, degree of metamorphism decreases from bottom to top in the Selimiye Nappe.	Eocene
	Çine Nappe	Max. P-T conditions, 8–11 kbar and 600–650º C	ca. 550 My was stated for the amphibolite facies metamorphism
	No evidence for the northward thrust of the upper plate for being an early Alpine phase.		
Ring et al., 2007 **Samos, Menderes Massif**	Ampelos/Dilek nappe was thrusted southward over the MM with greenschist facies, Cyclades-Menderes thrust, cutting a 30 to 40 km thick crust.		Detailed Rb-Sr and ^{40}Ar/^{39}Ar dating of mylonites indicate that both shear zones operated between 42-32 My.
	The upper contact of the Ampelos/Dilek wedge is the top to the NE Selçuk normal shear zone where the Ampelos/Dilek nappe exhumes about 30-40 km.		
	No evidence for a duration of 10 Myr episodic motion of shear zones, implying both shear zones worked steady, non-episodic manner (42-32 My).		
	Our data provide supporting evidence for that simultaneous thrusting and normal shear can result in early exposure of deep-seated rocks.		
Ten Veen et al., 2009 **Menderes Massif**	1st phase, detachment faulting in which the upper plate moves to the north in the uplift of Menderes Massif and accordingly the southeastward sliding of the Lycian Nappes. These faults reactivated in younger deformation stages.		Early-Middle Miocene
	2nd phase, NNE–SSE and ENE–WSW oriented extension, E-W trending main grabens		Late Miocene–Late Pliocene
	3rd phase, Stage 2 type of extensions are dominant in W Anatolian Graben Region and Lycian Taurids.		Post-Pliocene
Van Hinsbergen, 2010 **Menderes Massif**	MM formed a rectangular, NE-SW oriented, 150×100 km size tectonic window.		Early Miocene
Van Hinsbergen and Schmid 2012 **Aegean Region**	1st phase, 110 km extension		Between 25-15 My
	Most of the 2nd extension occurred		After 15 My (max. 290 km)
Cenki-Tok et al., 2016 **North of Menderes Massif**	Compression	Extensive amphibolite facies metamorphism reaching the peak. Approximately 625–670°C and 7–9 kbar	Eocene
	Extension		19.8-25.5 My
Ring et al., 2007 **South of Menderes Massif**	Menderes Nappes, Ören Nappe		Apatite fission-track dating 18-28 My, 31-42 My
	Menderes Nappes Cycladic blueschist unit Ören Nappe		Zircon fission-track dating 29-31 My 30-33 My 93 My and 129 My
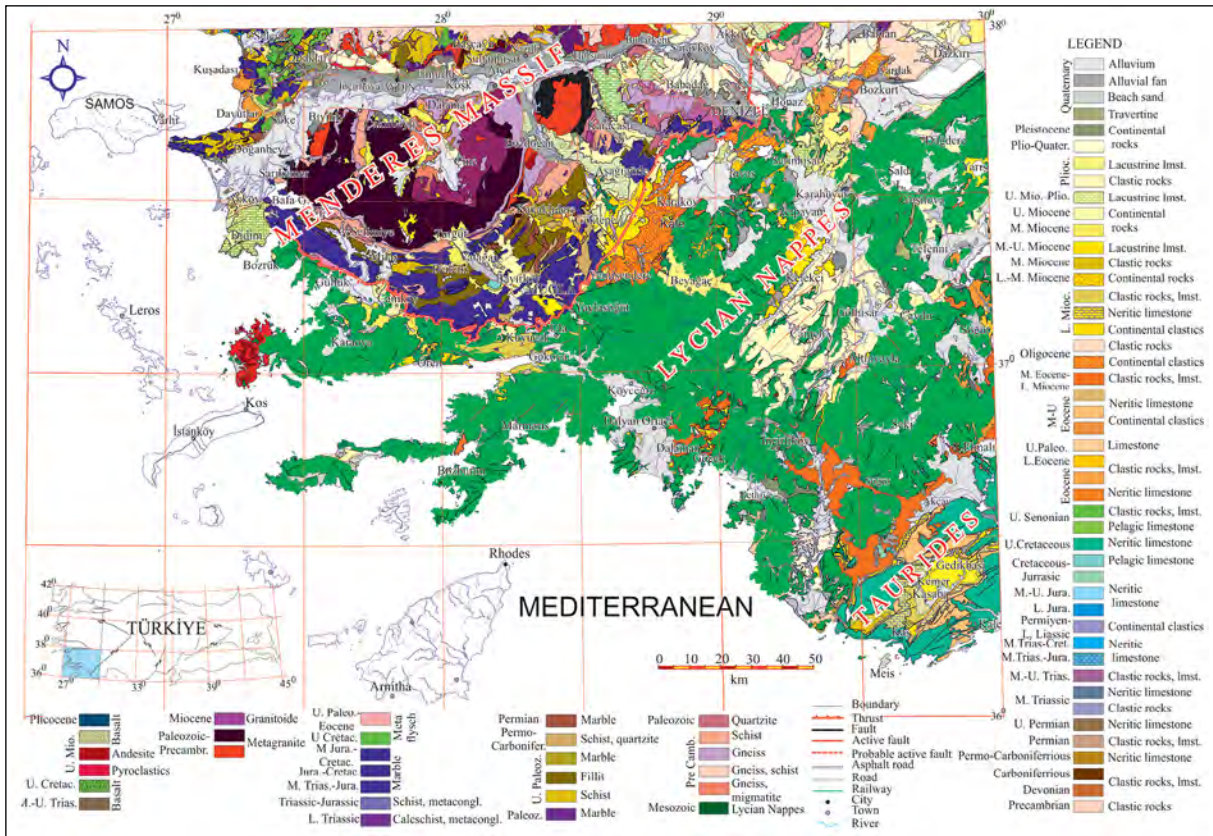
Figure 3- Simplified geological map of the SW Anatolia (simplified from Konak and Şenel, 2002).

2000; Sözbilir, 2002; Bozkurt, 2003) (Figures 4, 5). Some researchers associated the folds with the N-S extensional regime (Seyitoğlu et al., 2000; Sözbilir, 2001, 2002; Çemen et al., 2006), while some others does with the N-S compressional regime (Yılmaz et al., 2000; Gürer et al., 2009, 2013; Özburan and Gürer, 2012).

The youngest basins of western Anatolia are approximately E-W oriented, long and narrow (several km wide, tens of km long), asymmetrical, and generally arcuate (arc-shaped). One margin of each basin is characterized by steep topography associated with surface ruptures of active faults. Numerous closely spaced high-angle antithetic and synthetic faults developed in the footwall and hanging wall blocks of the basins. The horst and graben type morphology dominates the Western Anatolian landform and controls the major westward-flowing drainage system (Yılmaz, 2017b).

The faults of E-W oriented grabens cut and offset N-S oriented basins (Koçyiğit et al., 1999; Yılmaz et al., 2000; Sözbilir, 2001,2002; Bozkurt, 2001, 2003; Gürer et al., 2001, 2009, 2013; Westaway et al., 2004; Purvis and Robertson, 2004; Ersoy et al., 2011). Most of the N-S basins are generally observed as hanging basins on neighboring young uplifts. Gördes, Demirci and Selendi basins, for instance, are located in the horst block rising between the Gediz and Simav grabens. In addition, it was determined by the magnetotelluric method that the N-S trending basins in the Gediz Graben were trapped under the graben fill (Gürer et al., 2001, 2002).

E-W-oriented basins can be examined under two groups. The first group of basins (e.g., Simav, Gediz, Büyük Menderes) began to develop by a detachment fault and then continued evolving by high-angle antithetic and synthetic normal or oblique faults. Faults limiting the second group of basins (e.g., Bakırçay, Kütahya, Küçük Menderes, Gökova) are high-angle normal or oblique faults.

The basin fills are mainly terrestrial clastic deposits. The sequence, which starts with coarse clastics at
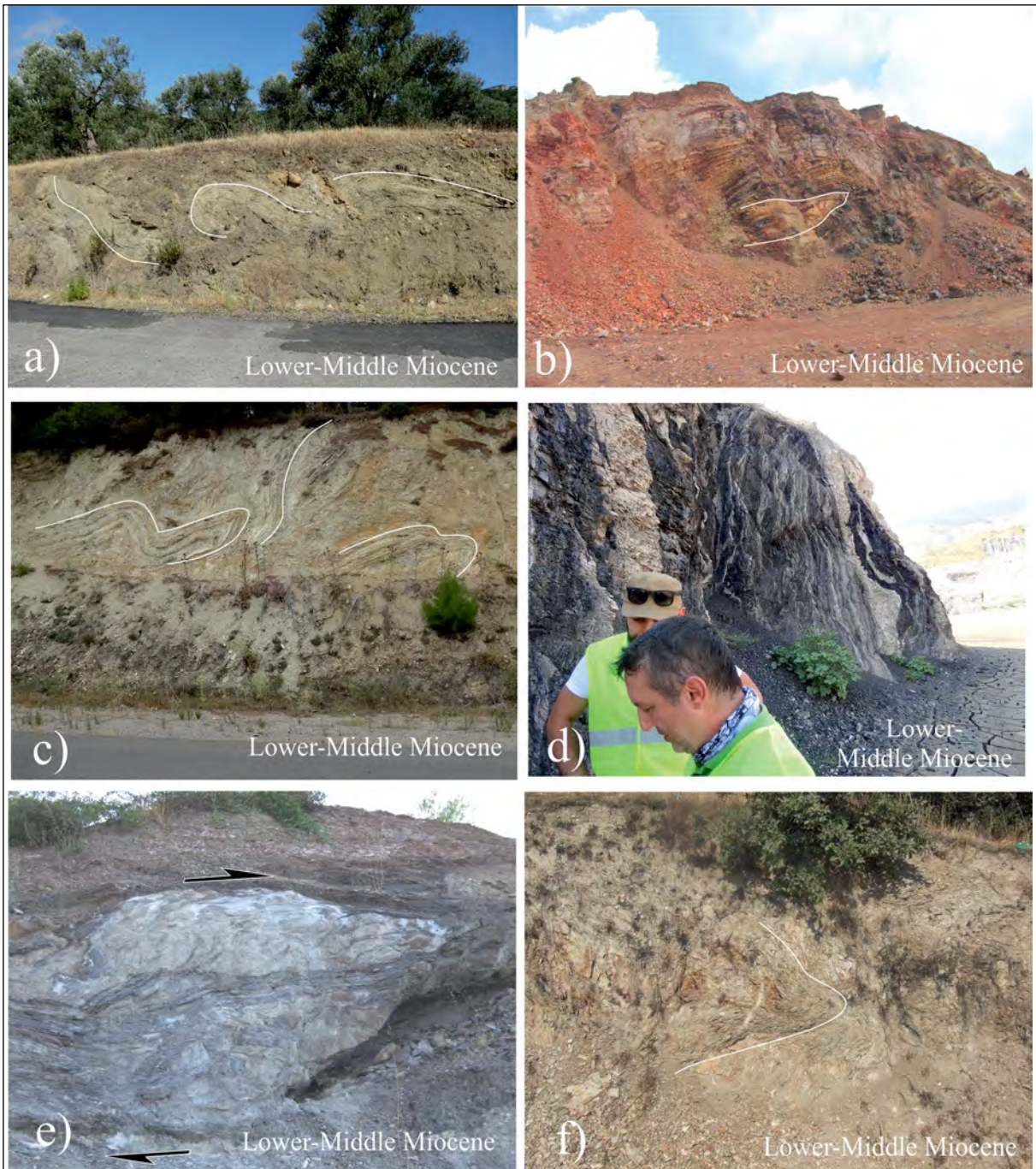
Figure 4- Examples of folds observed in Neogene successions in different parts of Western Anatolia; a) an overturned folding in the Küçükkuyu formation in the Bahçedere village (Edremit) road cut (39º 590685 N/ 26º 621073 E), b) a recumbent fold in the Tunçbilek formation in the Seyitömer coal pit (39º 35'12,28"N, 29º 53'04.40"E), c) examples of overturned and recumbent folds developed in the Lower-Middle Miocene succession in the east of Bergama (39º12'14.4"N, 27º40'46.6"E), d) vertical bedding in the Middle Miocene aged succession in the Soma Kısrakdere coal pit (39º6'41,5"N, 27º34'2,27"E), e) tectonic lens structure developed by compression in the Lower-Middle Miocene succession north of Ortaklar (37º56'19,73"N, 28º16'59,98"E) and f) recumbent folding developed in the Lower-Middle Miocene unit in the north of Nazilli (37º58'36,57N, 27º37'21,20E).
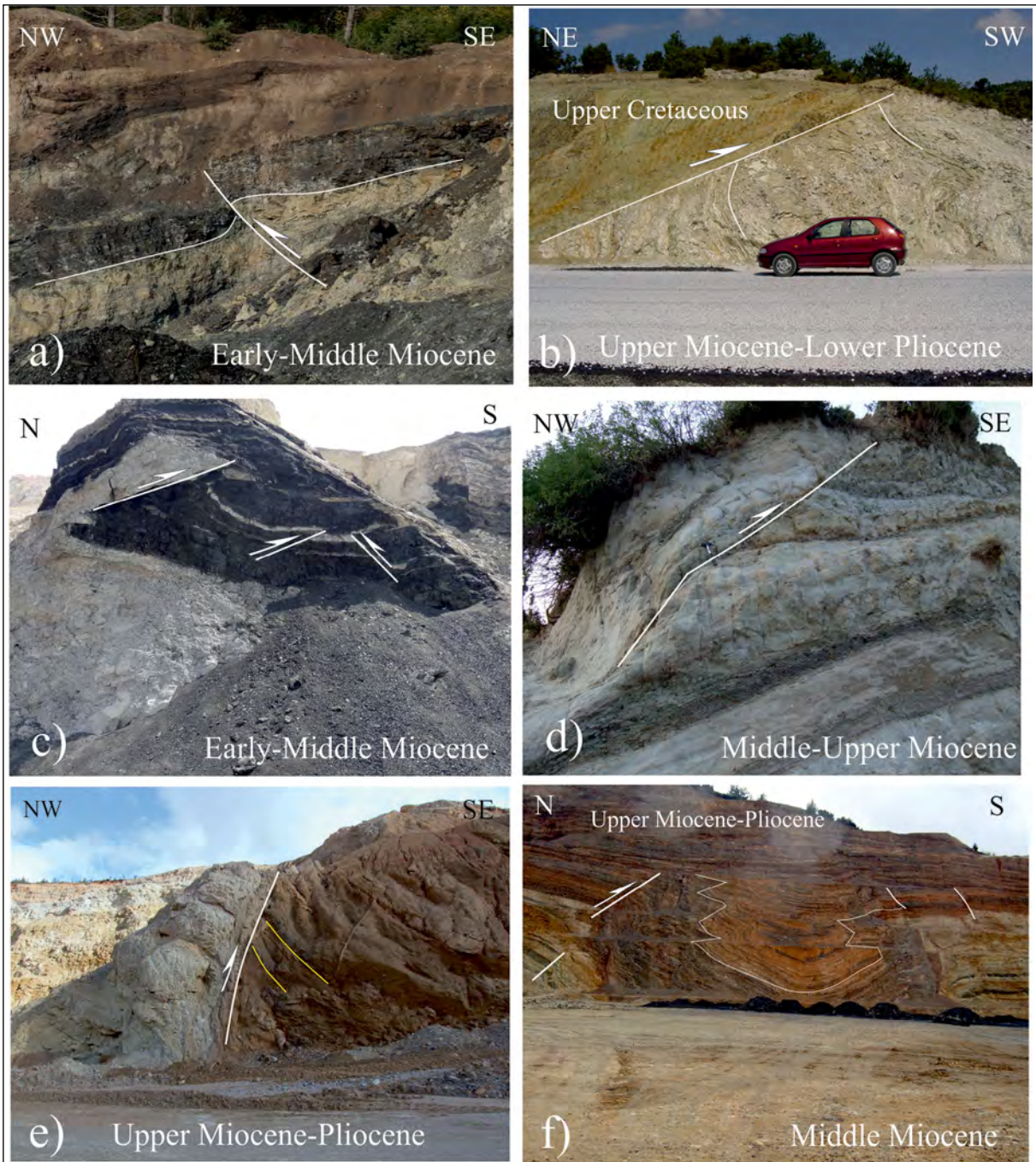
Figure 5- Examples of reverse faults observed in Neogene successions in different parts of Western Anatolia; a) a reverse fault observed in the Lower-Middle Miocene succession in the Çırpıköy coal pit, north of Kazdağ (39º 799565 N/ 27º 335935 E), b) ophiolite slice of the Tavşanlı Zone thrusted over the Emet formation on the Kütahya-Eskişehir highway (39º29'10,25"N, 30º02'41,17"E), c) reverse faults cutting the Lower-Middle Miocene succession in the Sevişler coal pit, north of Soma (39º5'39,3"N, 27º44'23,5"E), d) a reverse fault cutting the Middle-Upper Miocene succession in the southeast of Kuşadası (37º49'46,10"N, 27º17'29,48"E), e) A reverse fault developed in the Late Miocene-Pliocene aged Yatağan formation in the Tınaz Coal pit at the south of Yatağan (35º 606117, N/41º 21810E) and f) reverse faults and synclinal fold structure developed in the underlying Sekköy and overlying Yatağan formations, in the Tınaz coal pit (35º 4121395N/ 60º7818E).

the basin margins, continues with fine-coarse clastic alternations in the basin interior. The basin fill is generally horizontal; however folding and back tilting associated with stretching toward faults are observed (Sözbilir, 2002; Bozkurt and Sözbilir, 2004). Actual rivers such as Bakırçay, Gediz and Büyük Menderes flow through these basins.

The relations and origins of these two groups of basins in the region have long been controversial. In this study, based on our own observations and literature knowledge, brief information about the underlying structural units and Neogene-Quaternary basins will be given, and debates on their relationships and origins will be discussed. The readers can obtain detailed information about the basins from the related resources.

2.2.1. Edremit Basin and the Surroundings

Edremit Basin, the largest basin in Northwest Anatolia, extends into the sea towards the west by expanding (Figure 6). While the northern margin of the basin is steeper, linear, and distinct, the southern margin is gently inclined, indented, and indistinct. The structural and geometrical features of the basin indicate that it is a transtensional basin (Gürer et al., 2014, 2016. Koçyiğit and Gürboğa, 2021).

A basinal sequence represented by lacustrine deposition in the Early-Middle Miocene is present around Edremit. This clastic sequence consisting of bituminous shale, tuff, mudstone, sandstone, and limestone, which are mainly the products of lacustrine depositions, outcropping in the Küçükkuyu and the surroundings at the north and in the Ayvalık and its surroundings at the south are defined as Küçükkuyu Formation. The unit, mainly grey, brown, and green colored, is thin- to medium-bedded and is monotonous in terms of succession features (Gürer et al., 2016).

The Küçükkuyu formation was probably deposited in interconnected lacustrine environments in the central and eastern parts of the Biga Peninsula (Ayvalık, Küçükkuyu, Bayramiç, Çan, Yenice, Kalkım etc.). The sequence was developed mainly on the Çetmi mélange in the south of Kazdağ and rarely on the Asos volcanics. The succession, which started with conglomerate and sandstone alternation, then continued with alternation of sandstone, siltstone, and mudstone. Considering the lithology, facies distribution, geometry and structural position of the formation, it can be inferred that the basin margin rests against a high-angle rim and deepens from east to west (Yılmaz and Karacık, 2001). The formation, which is partially deformed in all areas where it outcrops, is the
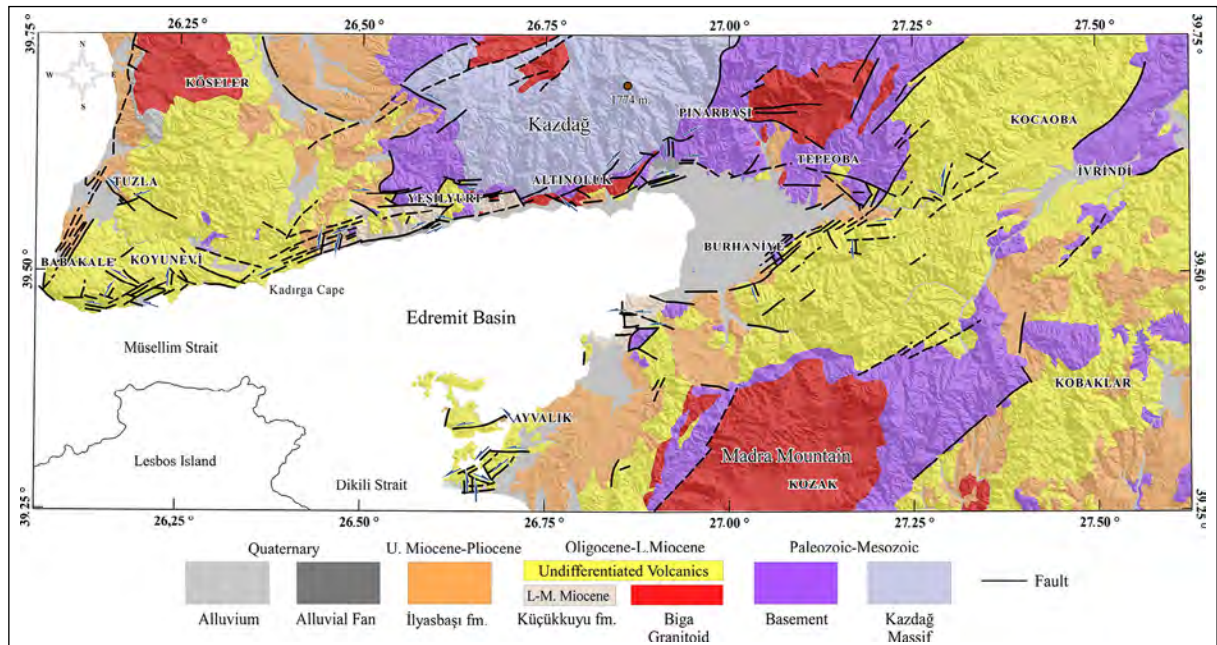
Figure 6- Simplified geological map of the Edremit Basin and its surroundings (adapted from Emre et al., 2012 (Gürer et al., 2016)).

equivalent of Early-Middle Miocene-aged lacustrine deposits widely exposed in Western Anatolia. The deformation developed as folding and faulting, and examples of overturned folds were observed as well as open folds (Figures 4a, 5a).

2.2.2. Kütahya Graben and the Surroundings

Kütahya and its surrounding area is one of the regions where the compressional and extensional system is well observed, exhibiting extensive Neogene-Quaternary successions, folds, reverse faults, uplifts and basin systems. The most prominent morphological element of the region is the Kütahya Graben with an approximately N65ºW orientation, 50 km length and 2-8 km width (Figure 7). The northern margin of this asymmetrical graben is indistinct and irregular, while the southern margin is more distinct, linear and high-angled. The boundary between the Graben and the Yellice horst located in its south is a normal fault zone with a left lateral component. Small-medium-sized alluvial fans developed between the horst and the graben.

To the north of the Kütahya graben, two NE-SW trending basins, Seyitömer and Sabuncupınar basins, extend. Seyitömer Basin is approximately 25 km long and 14 km wide. Both basins are filled with a sequence consisting of two successions belonging to the Lower-Middle Miocene and to the Pliocene. Stratigraphic and sedimentologic data indicate the presence of a significant angular unconformity between these two successions. The initial fillings of the basins are different from each other. Beke Formation (Lower Miocene) consisting of conglomerate, sandstone and siltstone and Tunçbilek Formation (Lower-Middle Miocene) consisting of coal seams intercalated with conglomerate, sandstone, siltstone, marl, claystone, tuff, limestone form the main filling of Seyitömer Graben. The Sabuncupınar Basin with an approximate N30º-35ºE orientation is filled with volcanics mainly composed of tuff and pyroclastics. Different fillings of these two parallel basins suggest that Karaöz Uplift located between them was a significant barrier in the Early-Middle Miocene period (Özburan, 2009; Özburan and Gürer, 2012).
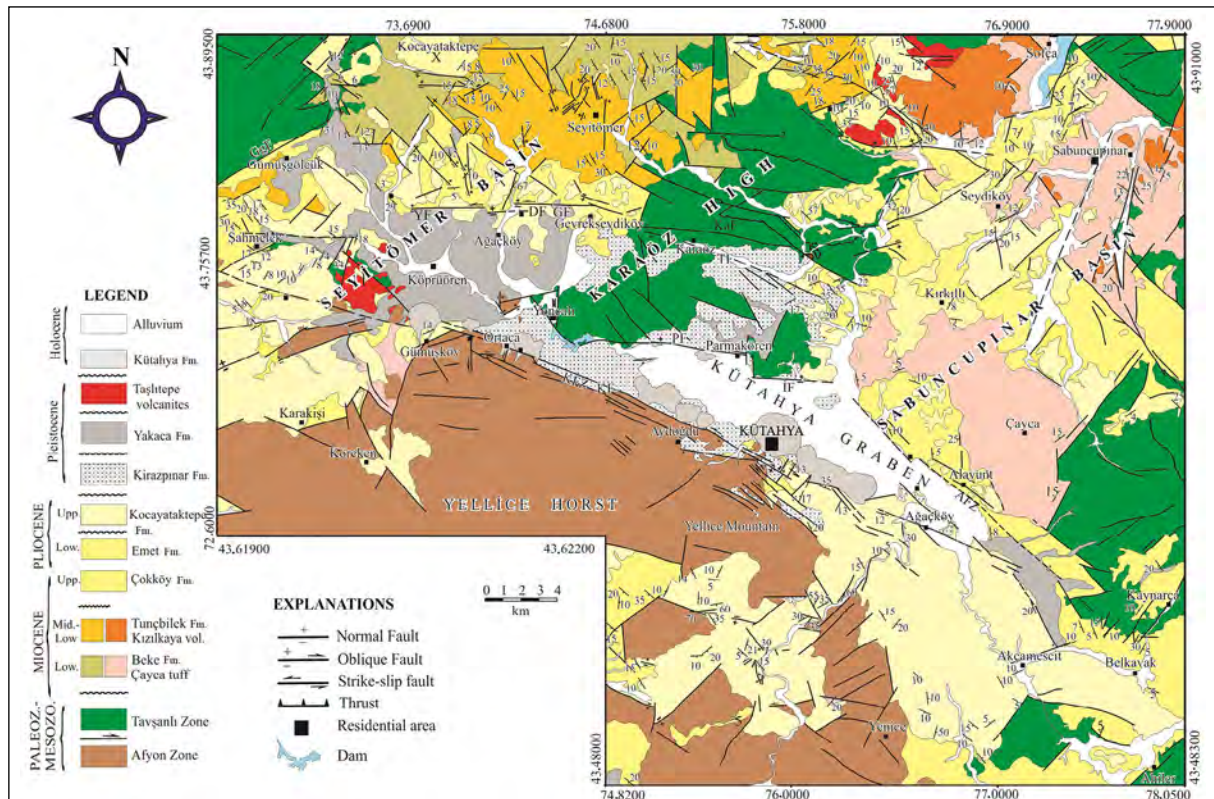
Figure 7- Geological map of the Kütahya graben and its surroundings (Özburan, 2009; Özburan and Gürer, 2012).

The common cover of these two basins and uplift is Late Miocene-Pliocene aged sequence that starts with an angular unconformity on the first succession in Seyitömer Basin and a parallel unconformity in Sabuncupınar Basin. The first unit of the sequence is the Çokköy Formation, which starts with conglomerate and later changes into alternating sandstone, siltstone and claystone. The overlying Emet Formation begins with an alternation of sandstone and claystone at the bottom and continues with mudstone, limestone and marl.

2.2.3. Bakırçay Basin and the Surroundings

Bakırçay Basin is a NE-SW trending, bow-tie shaped basin with a length of approximately 60 km and a width of 5 km (Figure 8). In the west of the basin, which has an asymmetrical morphology, the northern margin is steeper and linear than the southern margin. However, there is an opposite morphology in the east of the basin. The basin is located in a tectonically complex region where the N-S extensional regime of the Aegean extensional system and the NE-SW trending North Anatolian Fault System (NAFS) intersect. Therefore, it is accepted that these two factors concurrently control the neotectonic deformation of the region (e.g., Taymaz et al., 1991; Yılmaz et al., 2000; Pfister et al., 2000; Bozkurt, 2001a, b, 2003; Gürer et al., 2006, 2016; Yılmaz, 2017).

Three successions around the basin, separated by unconformable contacts between them, are as follows: The Early-Middle Miocene aged Dikili group, the Late Miocene aged Zeytindağ group and the Plio-Quaternary aged Bergama Basin fill. Early-Middle Miocene aged terrestrial sediments and the volcanics interfingering with them at all levels are located in the north and south of the basin. The sediments consist
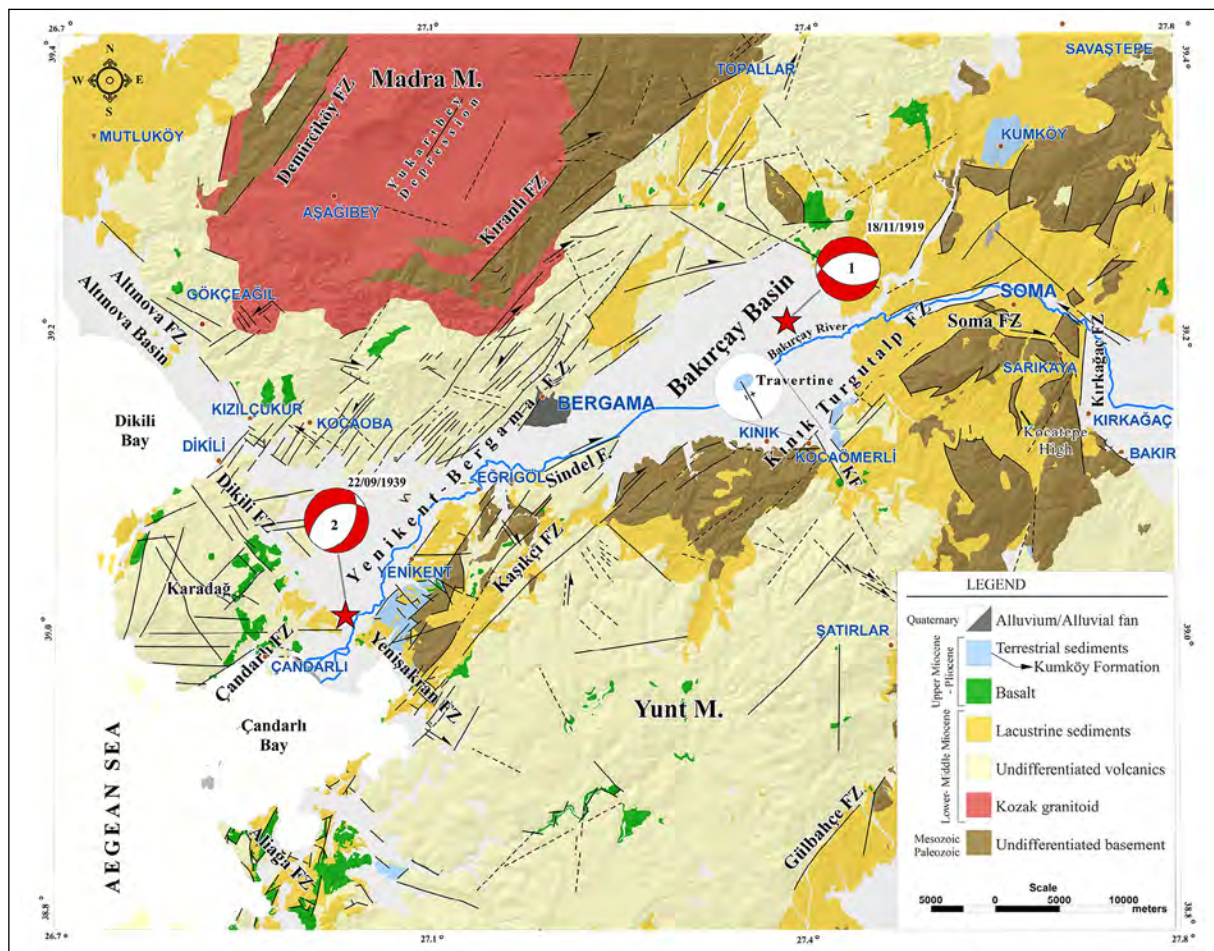
Figure 8- Simplified geological map of the Bakırçay Basin and its surroundings (modified from Konak, 2002). Two earthquake mechanisms in Bakırçay Basin are taken from Paradisopoulou et al. (2010) (Sangu et al., 2020).

of sandstone, mudstone, marl and shale alternations deposited in a lacustrine environment. Lacustrine deposits outcropping in NE-SW direction, especially in the east of the Çandarlı-Bergama line, exhibit widespread outcrops in the east of Bakırçay Basin and around Soma. In the sequence known as the Dikili group, open and closed folds and reverse faults have sporadically developed (Figures 4c, 5c).

2.2.4. Gediz Graben and the Surroundings

The Gediz Graben, one of the most developed grabens in Western Anatolia (Figure 9), has been studied in detail by many researchers in recent years (e.g., Cohen et al., 1995; Emre, 1996; Seyitoğlu and Scott, 1991, 1996; Koçyiğit et al., 1999; Yılmaz et al., 2000; Sözbilir, 2001; Işık et al., 2003; Çiftçi and Bozkurt, 2008, 2009; Öner and Dilek, 2011, 2012, 2013). The 140 km long and 10-15 km wide Gediz Graben, which has an arc-shaped geometry, is asymmetrical and its southern margin is steeper and more seismically active. Most of the graben fill outcrops around the southern margin. There are sedimentary basins developed in two different directions around the Gediz Graben. The NE-SW trending and Early-Middle Miocene aged ones are filled with younger clastic, volcanoclastic and volcanic rocks. The Gediz Graben, on the other hand,

is E-W trending and is mainly filled with clastic rocks (Yılmaz et al., 2000; Purvis and Robertson, 2004; Ersoy and Helvacı, 2007; Ersoy et al., 2010; Öner and Dilek, 2011, 2013).

The NE-SW trending major basins, mostly bounded by high-angle normal faults with strike-slip components, are Gördes, Demirci, Selendi, Uşak-Güre Basins (Yılmaz et al., 2000; Bozkurt, 2003; Ersoy et al., 2010). Gördes, Demirci and Uşak-Selendi basins are filled with a succession dominated by Early-Middle Miocene aged terrestrial clastic rocks, unconformably overlying the metamorphic rocks of the Menderes Massif and the İzmir-Ankara ophiolites. The stratigraphic and structural features of these basins have been introduced in detail in recent years (e.g., Seyitoğlu and Scott, 1994, Seyitoğlu et al., 1994; Seyitoğlu and Scott, 1996; Yılmaz et al., 2000; Purvis and Robertson, 2004; Ersoy et al., 2011).

The faults generating the Gediz Graben cut the NE-SW trending basins and slightly offset in a lateral sense (Yılmaz et al., 2000; Gürer et al., 2001). As a result, NE-SW trending basins remained as hanging grabens on the footwall blocks. This relationship indicate that NE-SW trending grabens were continuous before the development of the Gediz Graben.
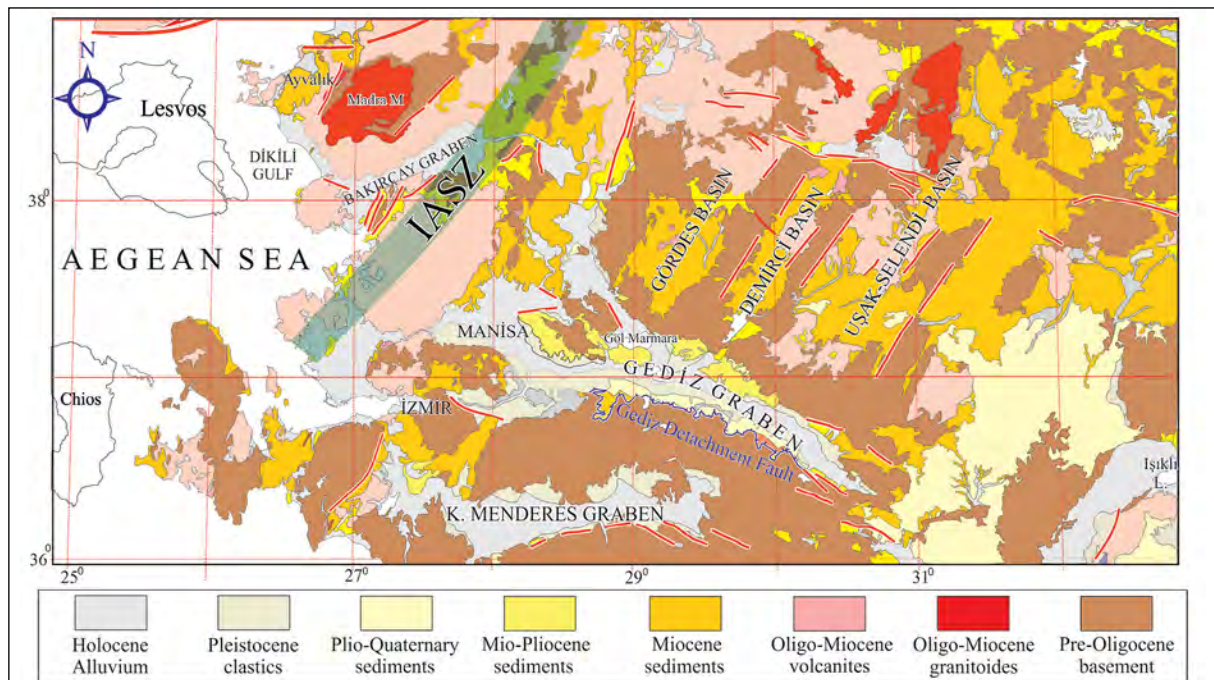
Figure 9- Simplified geological map of the Gediz graben and its surroundings (modified from Konak, 2002). IASZ: İzmir-Ankara Suture Zone.

2.2.5. Büyük Menderes Graben and the Surroundings

Büyük Menderes Graben bounded by the Menderes Massif from the north and south, is a 140 km long and 2.5-14 km wide graben with an arc-shaped structural geometry. The Graben extends approximately in an E-W direction until Ortaklar, and extends mainly in a NE-SW direction from there to the west (Figure 10). The northern margin of the graben is bounded by the linear mountain frontage of the Mount Aydın, which rises steeply from 50 m up to 1750 m, while the southern margin has a lower topography. These morphology and structural features indicate that the Büyük Menderes Graben is an asymmetrical graben (Gürer et al., 2009; Yılmaz, 2017a).

Two main rock groups, a basement consisting of the Menderes Massif and a Neogene-Quaternary sedimentary cover up to 2.5 km thick, are distinguished in and around the Büyük Menderes Graben. Interpretation of the data obtained from the cover units reveals the existence of three non-systematic lithostratigraphic units named A, B and C (Gürer et al., 2009). These three units outcrop on the northern margin of the graben, while units A and C outcrop on the southern margin. The relationship between the successions and the underlying metamorphic rocks is generally tectonic. Different tectonic processes produced diverse fault systems and basins in the region during the Neogene-Quaternary period.

The graben and its surroundings are cut by various fault groups ranging from oblique faults to high and low angle normal faults. Conjugate faults mainly strike NE and NW directions, while most of the normal faults strike E-W direction. Two fault systems have developed in the region: 1) Approximate NE and NW oblique faults adjacent to Unit A, 2) E-W trending faults adjacent to B and C units. The second group of faults can be subdivided into a) low-angle Büyük Menderes Detachment Fault with E-W direction and b) synthetic and antithetic en echelon normal faults (Yılmaz, 2017a).

The geological map of the Büyük Menderes Graben shows the existence of two structural basin systems of different ages and directions. The first
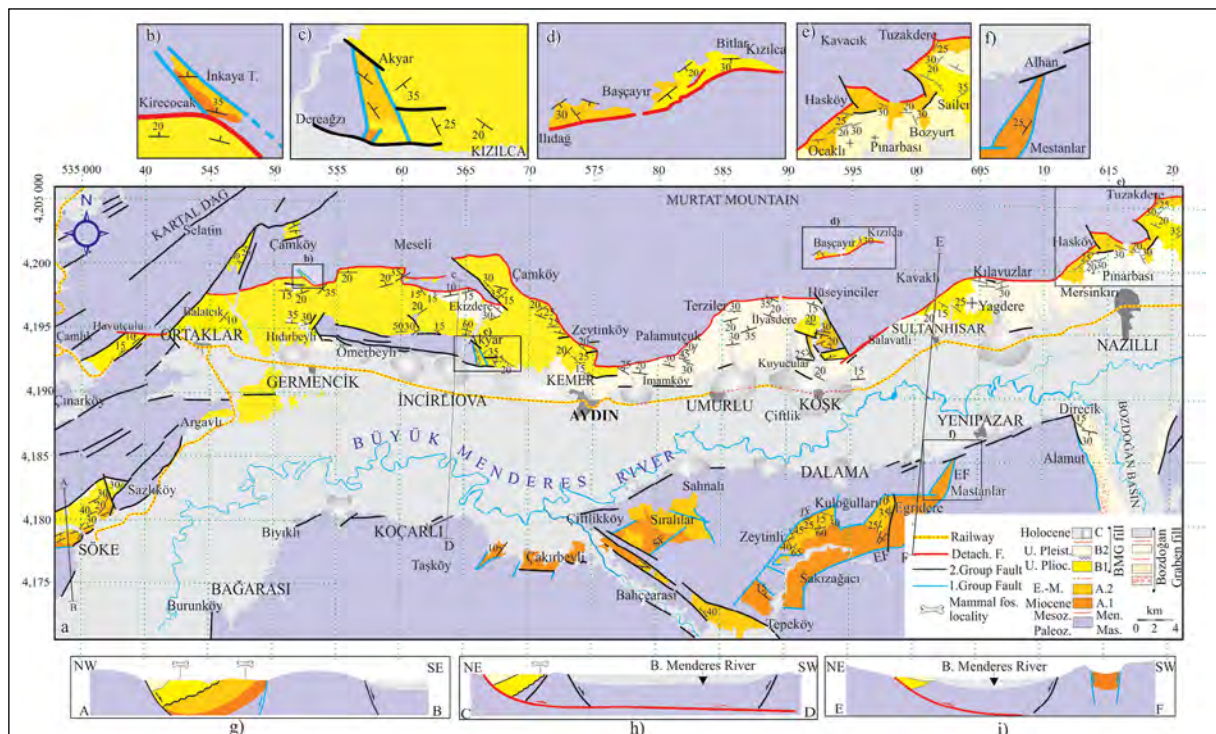
Figure 10- a) Geological map of the Büyük Menderes graben. BMDF: Büyük Menderes Detachment Fault, EF: Eğridere Fault, ZF: Zeytinli Fault, SF: Sıralılar Fault, b), c), d), e) and f) show the locations of the extended maps given in Figure 10. A-B, C-D and E-F represent the section lines given in Figure 10a (Gürer et al., 2019).

system is represented by N-S oriented structural depressions filled with Lower-Middle Miocene continental sediments. The second system cuts the preceding one and is represented by the E-W trending Büyük Menderes Graben filled with Plio-Quaternary terrestrial deposits. The synthesized data indicate that two different basin formations around the Büyük Menderes Graben, which developed in different structural environments, resulting from two successive and different tectonic regimes.

The Lower-Middle Miocene fillings (Unit A) of the NW and NE trending basins have been deformed in places by folds and reverse faults (Figures 4e, f, 5d). It has been suggested that folds and oblique faults correspond to a N-S compression in the region (Yılmaz et al., 2000; Gürer et al., 2009). It has been proven by fault kinematics studies that the N-S trending Bozdağan and Karacasu Basins, located in the south of the Büyük Menderes Graben, were deformed by N-S compression in Miocene and Early Pliocene (Ocakoğlu et al., 2014).

2.2.6. Gökova Graben and the Surroundings

Four groups of basins with different development periods and directions are present around the Gulf of Gökova, which is located in the southernmost part of the Western Anatolian Extensional Region. It has been suggested that the formation of the basins occurred in different structural environments and resulted from different consecutive tectonic regimes (Gürer and Yılmaz 2002; Gürer et al., 2013). Two different basement units, Lycian Nappes and Menderes Massif, coexist in the region (Figure 11). Gökova is a critical region for a better understanding of the transition from the compressional system to the extensional system.

The first group is represented by a NE-SW trending basin (Kale-Tavas Basin) filled with Oligocene-Lower Miocene shallow marine-terrestrial sediments. Kale-Tavas Basin extends in the E-W direction to the north and south of the Gulf of Gökova and NE-SW direction between the Gulf of Gökova and Denizli. The sequence of the Kale-Tavas Basin unconformably overlies the crystallized limestone and marbles of the Lycian nappes in the north of the Gökova Gulf, and the ophiolitic basement of the Lycian nappes around Acıpayam, Denizli and Burdur in the south and east of

the Gökova Gulf. The basin succession, which starts with a thick conglomerate, sandstone alternation at the base, and continues upward with conglomerate, sandstone and mudstone alternations, ends up with reefal limestone lenses.

The NE and NW trending structural depressions (Eskihisar and Tınaz Basins) in the second group are filled with Lower-Middle Miocene terrestrial deposits. Both of these basins bounded by oblique faults are geometrically L-shaped. In both basins, the successions start with conglomerate and sandstone alternation at the bottom (Turgut Fm.) and end up with sandstone, mudstone and marl alternation containing lignite intercalations (Sekköy Fm.). Fossils obtained from the limestones provide a Middle Astarasian age (Middle Miocene, 14 My) (Atalay, 1980; Gürer and Yılmaz, 2002).

The third group of basins in the region is the Yatağan Basin, which is located between Yatağan district and Gökova Bay. The NW-SE trending basin is 30 km long and 10 km wide, with unclear borders and geometry. The basement of the basin is the Menderes Massif in the north and the Lycian nappes in the south. The basin fill consists of brown, poorly sorted, thick-bedded alluvial conglomerate at the bottom, passes upwards into grayish-brown sandstone and mudstone, and ends up with light grey-white clayey limestone intercalations. Limestone and marl lenses, tuff intercalations and travertine are present at different levels of the succession. The succession is 300-500 m thick, and the red-colored beds provides a mammal fauna in the Muğla region representing the time interval spanning from the Middle Astaracian to the Turolian (Atalay, 1980). The basin has been interpreted as an intermountain basin developed without significant tectonic control (Gürer et al., 2013). Reverse faults were observed in places in the Miocene and Pliocene successions in the region (Figures 5e, f). The fourth group of basins in the Gökova region are Muğla, Paşapınarı, Yeşilyurt, Ula and Gökova Basins. These basins are filled with block-gravel, pebbly sand, sand and clays of the alluvium, colluvium and alluvial fan deposits. The sequence consists of marine sediments in the Gulf of Gökova. Muğla and Gökova basins are located at the altitudes of 650-700 m and 850 m respectively.
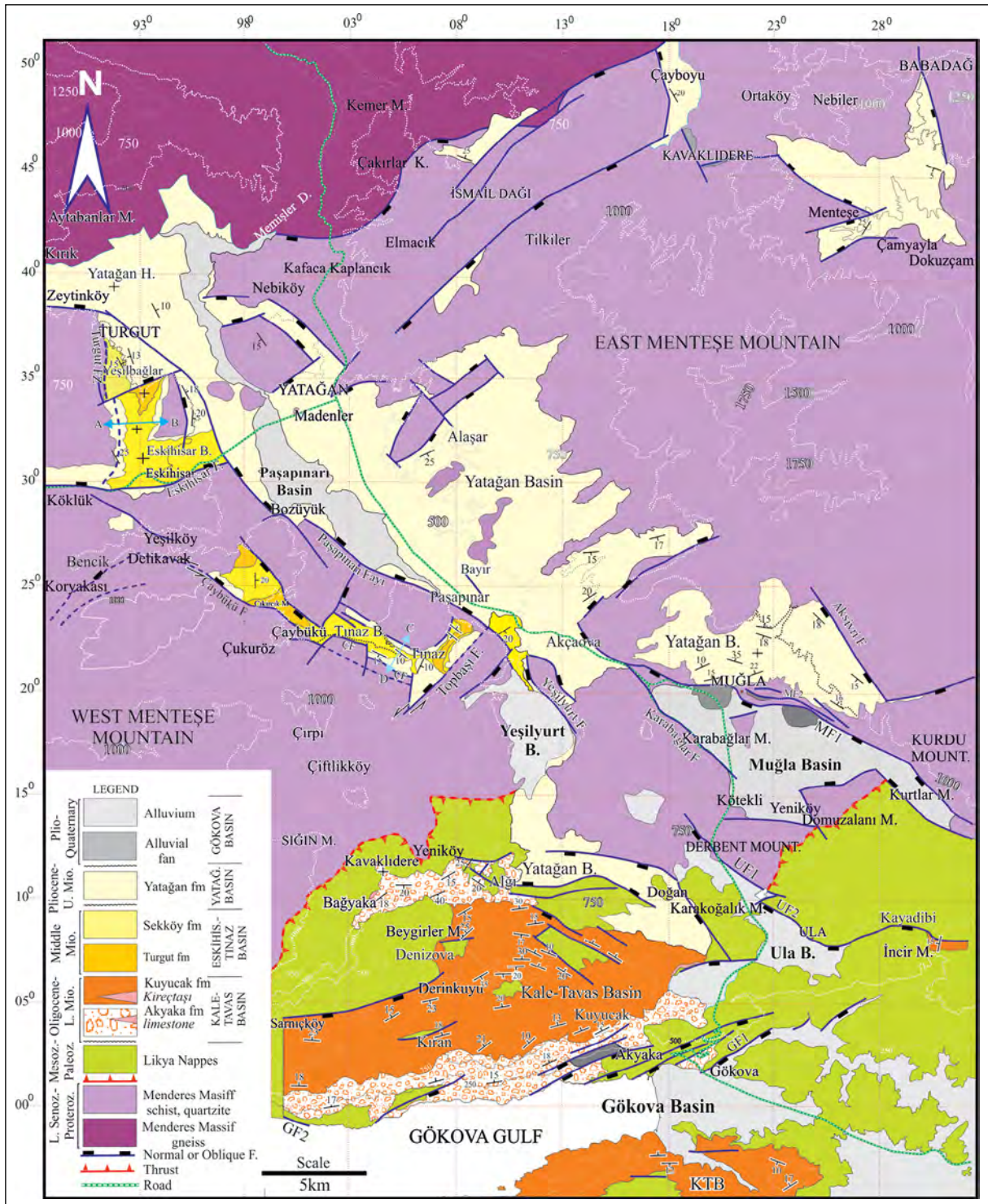
Figure 11- Geological map of the Gulf of Gökova and its surroundings (Gürer et al., 2013).

Çameli and Eşen Basins, placed within the Fethiye-Burdur Fault Zone in SW Anatolia, are also continental basins developed in the Neogene-Quaternary period. Compressional deformational structures were also observed in these basins bounded by oblique faults. Detailed information about these basins can be found in related studies (e.g., Alçiçek et al., 2004, 2005; Elitez and Yaltırak, 2014).

3. Discussions

In the evaluation of the above-mentioned studies on the Neogene-Quaternary basins in Western Anatolia, it is seen that there are disagreements, especially about the onset of the extension, the continuous or discontinuous nature of the extension, and the origin and evolution of the basins. In this section, the discussions about the compression and extension phases in the region will be briefly summarized.

The Late Cretaceous period marks the initiation of a convergent tectonic regime in and around Turkey and is particularly characterized by the emplacement of ophiolite nappes. These nappes were moved to large carbonate platforms that began to collapse by the onset of settlement (Yılmaz, 2017a, b). It has been suggested that the ophiolite slices derived from the closure of the northern branch of Neotethys, which was located between the Sakarya Continent and the Tauride-Anatolide continent in the Late Cretaceous-Eocene interval, progressed from north to south as nappes (Şengör and Yılmaz, 1981; Özgül, 1976, 1984; Hayward and Robertson, 1982; Dixon and Robetson, 1984; Şengör et al., 1985; Collins and Robertson, 2003; Okay, 2001; Ten Veen et al., 2009; Nemec et al., 2018). The nappes emplaced on the Taurides by moving over the Menderes Massif caused the deformation of the Taurides and the formation of thick nappe slices. Compression and the nappe slices have caused the continental crust in Western Anatolia to be thickened (Yılmaz, 2017a).

From the Oligocene period, on the other hand, the first uplift of the metamorphic complexes of the Aegean occurred and was partially exposed (Lacassin et al., 2007). Different opinions have been suggested on the uplift time and mechanism of the massifs, especially the Menderes Massif, in the region. Some researchers have claimed that the Menderes Massif

was uplifted by compression in the Oligocene-Middle Miocene interval and by the N-S extension after the Late Miocene or Plio-Quaternary (Yılmaz et al., 2000; Erkül et al., 2005a, b; Gürer et al., 2009, 2013). According to these researchers, during the Late Oligocene-Early Miocene, the Menderes Massif and all Western Anatolia underwent a compressional deformation in N-S direction. In addition, it has been suggested that the Thrace Basin and the Balkans were compressed in the NW-SE direction during the Late Oligocene-Early Miocene and thus folded (Erbil et al., 2021). As a result of this compression, the entire region was shortened, folded, imbricated, and thickened. This was followed by an extensional phase, probably due to the orogenic collapse (Seyitoğlu et al., 2004) or the rollback mechanism in the South Aegean Trench (Bozkurt, 2003; Gürer et al., 2009, 2013; Yılmaz, 2017a,b). Some researchers have suggested that the massif has been uplifted as an extensional core complex since the Late Oligocene (e.g., Ring et al., 2003; Seyitoğlu et al., 2004; Emre and Sözbilir, 1997; Sözbilir, 2005).

Various studies have been carried out associating the development of the basins in Western Anatolia with the uplift of the Menderes Massif (e.g., Gessner et al., 2001a; Ring et al., 2003; Seyitoğlu et al., 2004; Seyitoğlu and Işık, 2015). However, researchers working on the Menderes Massif have suggested different point of views about the geometry and movement directions of the nappes in the massif (Table 1). The northward movement of the upper plate has been suggested as pre-Alpine (Gessner et al., 2001b), pre-Eocene (Regnier et al., 2003), Eocene (Rimmele, 2003), Late Oligocene-Early Miocene (Bozkurt and Park, 1997; Seyitoğlu et al., 2004; Bozkurt et al., 2006).

Most of the researchers suggested that the Menderes Massif was uplifted by the core complex mechanism associated with the N-S directional extension in western Anatolia during the Late Oligocene-Miocene period. In general, metamorphic core complexes (MCCs) are interpreted as domal structures caused by ductile to brittle, high-stress metamorphic rocks extending under a high-stress detachment fault that undergo tens of kilometers of displacement in response to lithospheric extension. In such structures,

it has been argued that stress is the driving force that regulates uplift (Searle and Lamont, 2019).

Searle and Lamont (2019) stated that various core complexes such as the Himalayan, Karakoram and Pamir domes, completely occurred in compressional environments and are not related to the lithospheric extension. They suggested that many MCCs previously thought to have formed due to extension are related to compressional tectonics. According to the authors, low-angle normal faults due to regional Aegean extension previously generated contraction folds and metamorphic fabrics associated with crustal shortening and thickening in Naxos.

The exhumation mechanism of the Menderes Massif during the Late Oligocene-Early Miocene is a controversial issue. Has the uplift of the massif been caused by low-angle thrusts or normal faults commonly defined in the massif? Otherwise, considering its internal structure consisting of nappe slices where there is no consensus on the movement directions and times; the idea that the Menderes Massif may also be a compressional metamorphic complex, just as in the Himalaya, Karakoram, Pamir and Naxos examples proposed by Searle and Lamont (2019) becomes more likely.

Debates on the continental collision that started in the Late Cretaceous in Western Anatolia and the duration of the subsequent compression have been continuing. According to some researchers, the Lycian nappe stack advanced southward during the Early Miocene and finally emplaced on the Lower Miocene basin fill of the Antalya Basin prior to the Late Miocene (Okay, 1989; Collins and Roberston, 1998; Yılmaz et al., 2000, Gürer et al., 2009, 2013). According to some other researchers (Şengör, 1982; Hayward, 1984; Şengör et al., 1985), the compression lasted in the Western Taurides in the south and along the frontal thrust zone of the Lycian Nappes until the Late Miocene. It is claimed that the Taurides advanced over the younger Mediterranean basins in the south by carrying the Lower-Middle Miocene marine sediments on its back and started to uplift (Y. Yılmaz, personal communication). According to Seyitoğlu et al., (1992), on the other hand, the nappe movement from the Early Miocene in the north (in

Isparta) until the Late Miocene in the south and the west was attributed to the gravity sliding rather than N-S directional compression. This hypothesis was later supported by Collins and Robertson (1998), who suggested that the compressional shear zone at the base of the Lycian allochthon was reactivated as an extensional detachment during the Late Oligocene-Early Miocene extensional collapse.

The fluvial and lacustrine sediments, which were commonly developed in the Early Miocene, rest on the high-grade metamorphic rocks of the Menderes Massif, occasionally with an unconformable contact. The outcrops of the Menderes Massif observed from the northern margin (Demirci-Simav region) to the southern margin (Çine-Yatağan region) suggest that the main uplift of the Menderes Massif that resulted the exhumation of middle and lower crustal rocks occurred just before the Early Miocene, and removed approximately 20 km of material from the massif (Yılmaz et al., 2000a,b). Metamorphic and plutonic rocks and the minerals developed under the influence of faulting mechanism in Western Anatolia were dated by different methods, the geological/geodynamic evolution of the region was interpreted, and the plutonic rock emplacement related to the extension, the uplift rate and timing were discussed (Sümer et al., 2020). In addition to detailed structural and geochronological studies in the Menderes Massif, two models have mainly been proposed for N-S trending basins. The first is extensional type basins such as rifts (Figure 12b) (e.g., Görür et al., 1995) or supra-detachment basins (Figures 12a, c) (e.g., Lips et al., 2001; Sözbilir et al., 2011; Öner and Dilek. 2013). Low or high-angle normal faults are the main factor causing the stretching in such environments. Supra-detachment systems are characterized by significantly higher rates of crustal extension than that in the rift systems (Friedmann and Burbank, 1995). The second model is transtensional or transpressional basins specific to compressional environments. The differences between the N-S and E-W trending basins in Western Anatolia are presented in Table 2.

The Early-Middle Miocene aged basins in Western Anatolia developed on different basement rocks, from the Marmara Region in the north to the Mediterranean in the south. In the southern Marmara,
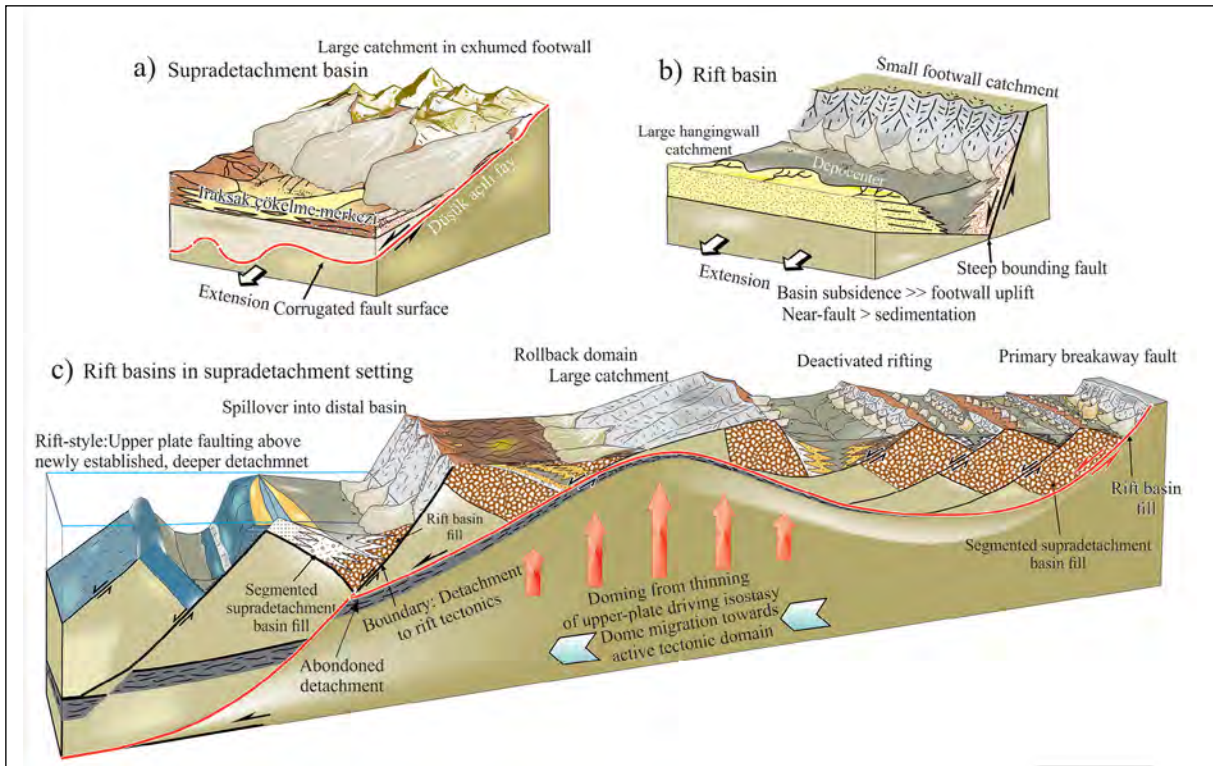
Figure 12- Block diagrams illustrating the characteristics of supra-detachment and rift basins (Modified from Serck et al., 2021).

Table 2- Comparison of the N-S and E-W trending basin characteristics.

	N-S trending basins	E-W trending basins
Geometry	Rhomboidal or trough shaped	Curved (arched), graben-half graben
Faults	Strike slip, oblique normal	Normal, oblique normal
Basin fill	Conglomerate, sandstone, marl, limestone interfingering with volcanics	Conglomerate, sandstone, mudstone with rare tuff intercalations
Basin symmetry	Variable	Generally asymmetric
Facies changes	E-W	N-S
Environment	Fluvial, alluvial fan, lacustrine	Fluvial, alluvial fan
Period	Early-Middle Miocene	Plio-Quaternary
Deformation	Open and closed folds, reverse faults	Open folds related to the extension, back-tilting, normal faults
Basement	Sakarya Continent, İzmir-Ankara Suture Zone, Menderes Massif, Lycian Nappes	Sakarya Continent, İzmir-Ankara Suture Zone, Menderes Massif, Lycian Nappes

Gönen and its surroundings (Gürer et al., 2003, 2006), Ayvalık-Altınova Basin (Yılmaz et al., 2000; Sangu et al., 2020), Soma and its surroundings, Urla Basin, Çubukludağ and Kocaçay basins (Genç et al., 2001; Uzel and Sözbilir, 2008; Göktaş, 2020), Seyitömer and Sabuncupınar basins in the northeast of Kütahya (Özburan and Gürer, 2012) are some of them. As can be seen, some of the basins were developed on or around the detachment faults, while others are distributed to the areas where detachment faults are not present. Thus, it is not possible to associate all basins with detachment faults or normal faults.

During the Early Miocene-Quaternary period, Western Anatolia has been approximately compressed in the N-S direction in different periods (Figures 4, 5). Several researchers working in Western Anatolia have displayed folds and reverse faults associated

with the compression (Koçyiğit et al., 1999; Yılmaz and Karacık, 2001; Kaya et al., 2004; Beccaletto and Steiner, 2005; Bozkurt and Rojay, 2005; Rojay et al., 2005; Erkül et al., 2005*a, b*; Çiftçi and Bozkurt, 2009).

The main basins that can develop in compressional environments are the foreland basin, piggy-back basin, transpressional or transtensional basins. Considering the geology of the region, N-S trending basins may be related to strike-slip basins, many of whose geological features are given by Nilsen and Sylvester (1995). If the characteristic features of the strike-slip basins are compared with the stratigraphic, sedimentologic, geometric and structural features of the N-S trending basins in Western Anatolia, it is thought that these basins may be pull-apart or transtensional pull-apart basins associated with strike-slip faults (Figure 13). However, detailed studies in the region will provide new approaches to the origins of N-S trending basins.

4. Conclusions

The main results obtained in the light of the arguments regarding the Neogene-Quaternary geology of Western Anatolia are listed below.

1- Although many studies have been carried out on the Menderes Massif, there are still debates about the exhumation age and mechanism of the massif. The internal structure of the Menderes Massif, consisting of nappe stacks, strengthens the idea that the massif may be a compressional core complex as shown in the Himalayan, Karakoram, Pamir and Naxos massifs. In the light of the data discussed in this article, it is possible to figure out this problem with a problem-focused approach.

2- Early-Middle Miocene aged N-S trending basins, which developed in a wide geography from Marmara to the Mediterranean, were opened on different basements. Therefore, since all of these
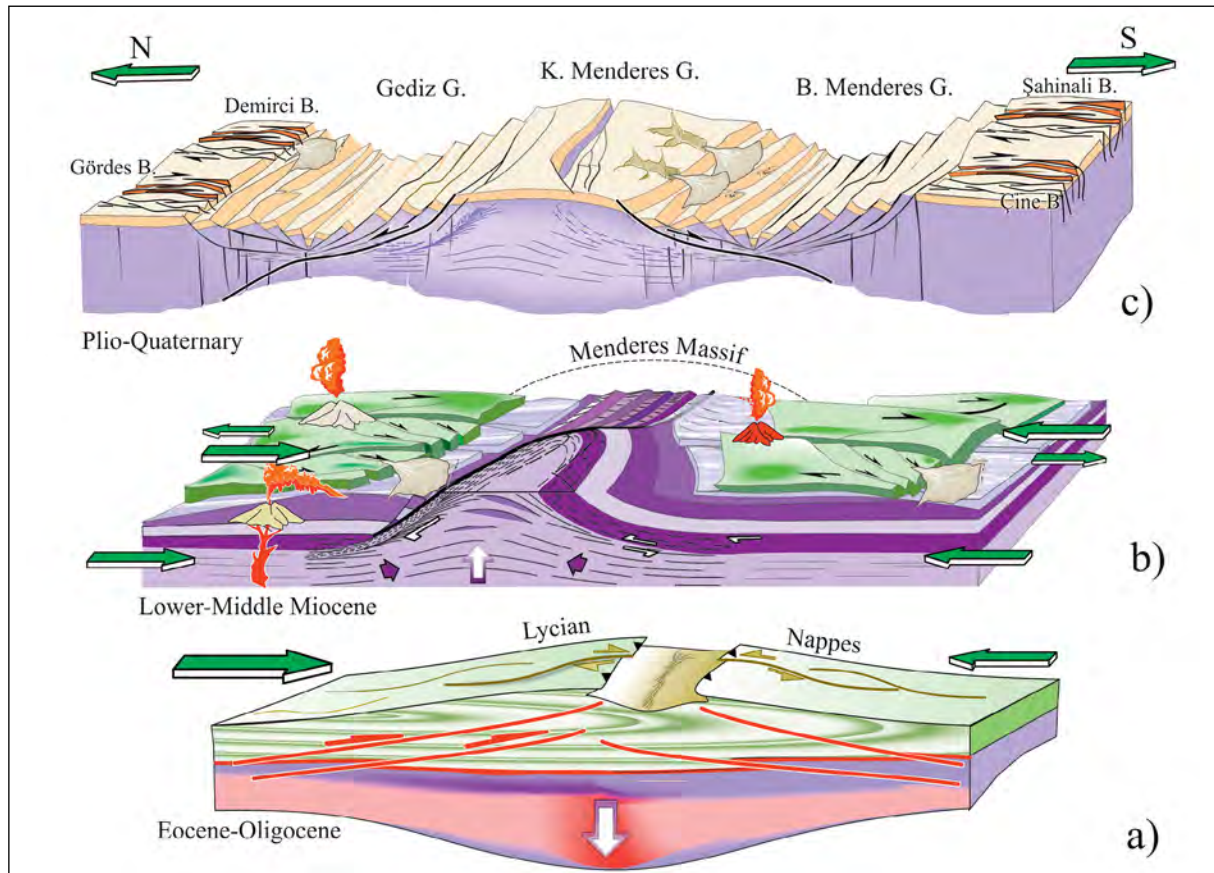
Figure 13- The sketch block diagrams proposed for the development of the N-S and E-W basins in Western Anatolia within a) the drawing of the internal structure of the Menderes Massif, b) the drawing of graben by Brunn et al. (2018) and c) adapted from Fossen (2010).

basins didn't develop on detachment faults, it is not possible to explain their origins only with the supra-detachment basin model as well.

3- The N-S trending basins are bounded by oblique faults with major strike-slip components. Volcanic and sedimentary sequences filling these basins were folded and faulted under the influence of syn- and post-sedimentary compressional tectonics. If the variety of the basement rocks in the region and the stratigraphic, geometric and structural features of the basins developed on them are evaluated together, it strengthens the idea that the N-S trending basins developed in a N-S directed compressional environment.

4- In the Miocene-Pliocene interval, Western Anatolia was also subjected to N-S directional compression, resulting folds and reverse faults. However, the transition from the compressional system to the extensional system in Western Anatolia occurred in the Plio-Quaternary. In contrast to the proposed single-phase extensional system, the obtained data suggest the existence of phases by consecutive compression and extension in the development of the region.

Acknowledgements

References

Alçiçek, M. C., Kazancı, N., Özkul, M., Şen, Ş. 2004. Sedimentary infill and geological evolution of the Çameli Basin, Denizli, SW Turkey. Bulletin of Mineral Research and Exploration of Turkey 128, 99-123.

Alçiçek, M. C., Ten Veen, J. H. 2008. The late Early Miocene Acıpayam piggy-back basin: Refining the last stages of Lycian nappe emplacement in SW Turkey. Sedimentary Geology 208, 3-4, 101-113.

Alçiçek, M. C., Kazancı, N., Özkul M. 2006. Multiple rifting pulses and sedimentation pattern in the Çameli Basin, southwestern Anatolia, Turkey. In: Kelling, G., Robertson, M. H. F., Van Buchem, F. H. P. (Ed.). Cenozoic Sedimentary Basins of South Central Turkey. Sedimentary Geology, Special Issue 173(1-4), 409-431.

Atalay, Z. 1980. Muğla-Yatağan ve yakın dolayı karasal Neojeninin stratigrafi araştırması. Türkiye Jeoloji Bülteni 23, 93-99.

Beccaletto, L., Steiner, C. 2005. Evidence of two-stage extensional tectonics from the northern edge of the Edremit Graben, NW Turkey. Geodinamica Acta 18(3-4), 283-297.

Bingöl, E., Akyürek, B., Korkmazer, B. 1975. Biga yarımadasının jeolojisi ve Karakaya formasyonunun bazı özellikleri (the geology of the Biga Peninsula and some features of the Karakaya Formation). Cumhuriyetin 50. Yılı Yerbilimleri Kongresi Tebliğleri, Bulletin of the Mineral Research and Exploration, 70-77.

Bozkurt, E. 2000. Timing of extension on the Büyük Menderes graben, Western Turkey, and its tectonic implications. Geological Society London of Special Publications 173, 385-403.

Bozkurt, E. 2001a. A Late Alpine evolution of the central Menderes Massif, western Turkey, International Journal of Earth Sciences 89, 728-744.

Bozkurt, E. 2001b. Neotectonics of Turkey-a synthesis. Geodinamica Acta 31, 3–30.

Bozkurt, E. 2003. Origin of NE trending basins in western Turkey. Geodinamica Acta 16, 61-81.

Bozkurt, E. 2004. Granitoid rocks of the southern Menderes Massif (southwestern Turkey): field evidence for Tertiary magmatism in an extensional shear zone. International Journal of Earth Sciences 93(1),52-71.

Bozkurt, E. 2007. Extensional contractional origin for the southern Menderes shear zone, SW Turkey: tectonic and metamorphic implications, Geological Magazine 144(01), 191-210.

Bozkurt, E., Park, R. G. 1994. Southern Menderes massif: an incipient metamorphic core complex in western Anatolia, Turkey. Journal of Geological Society London 151, 213-216.

Bozkurt E., Park R. G. 1997. Geochemistry and tectonic significance of augen gneisses from the Southern Menderes Massif (West Turkey). Geological Magazine 132(3), 287-301.

Bozkurt, E., Park, R. G. 1999. The structure of the Palaeozoic schists in the southern Menderes Massif, western Turkey: a new approach to the origin of the main Menderes Metamorphism and its relation to the Lycian Nappes. Geodinamica Acta 12(1), 25-42.

Bozkurt, E., Park, R. G., Winchester, J. A. 1993. Evidence against the core cover interpretation of the southern sector of the Menderes Massif, West Turkey. Terra Nova 5(5), 445-451.

Bozkurt, E., Sözbilir, H. 2004. Tectonic evolution of the Gediz Graben: field evidence for an episodic, two-stage extension in western Turkey. Geological Magazine 141(1), 63-79.

Bozkurt, E., Rojay, B. 2005. Episodic, two-stage Neogene extension and short-term intervening compression in western Turkey: field evidence from the Kiraz Basin abd Bozdağ Horst. Geodinamica Acta 18(3), 299-316.

Bozkurt, E., Winchester, J. A., Mittwede, S. K., Ottley, C. J. 2006. Geochemistry and tectonic implications of leucogranites and tourmalines of the southern Menderes Massif, SW Turkey. Geodinamica Acta 19(5), 363-390.

Brun, J. P., Sokoutis, D., Tirel, C., Gueydan, F., Van Den, D., Beslier, M. O. 2018. Crustal versus mantle core complexes. Tectonophysics 746, 22-45.

Candan, O., Dora, O. Ö. 1998. Menderes Masifi'nin genelleştirilmiş jeoloji haritası. DEU Jeoloji Mühendisliği Bölümü, Bornova, İzmir (unpublished).

Candan, O., Dora, O. Ö., Oberhänsli, R., Çetinkaplan, M., Partzsch, J. H., Warkus, F., Dürr, S. 2001. Pan-African high-pressure metamorphism in the Precambrian basement of the Menderes Massif, Western Anatolia, Turkey. International Journal of Earth Science 89(4), 793-811.

Candan, O., Çetinkaplan, M., Oberhansli, R., Rimmelé, G., Akal, C. 2005. Alpine high-pressure / low temperature metamorphism of Afyon Zone and implication for metamorphic evolution of western Anatolia, Turkey. Lithos 84, 102-124.

Cohen, H. A., Dart, C. J., Akyüz, H. S., Barka, A. 1995. Syn-rift sedimantation and structural development of the Gediz and Büyük Menderes graben, Western Turkey. Journal of the Geological Society of London 152, 629-638.

Collins, A. S., Robertson, A. H. F. 1998. Processes of Late Cretaceous to Late Miocene episodic thrust-sheet translation in the Lycian Taurides, SW Turkey. Journal of Geological Society 155, 759-772.

Collins, A. S., Robertson A. H. F. 2003. Kinematic evidence for late Mesozoic–Miocene emplacement of the Lycian Allochthon over the Western Anatolide Belt, SW Turkey. Geological Journal 38, 295-310.

Çelik, Ö. F., Marzoli, A., Marschik, R., Chiaradia, M., Neubauer, F., Öz, İ. 2011. Early-Middle Jurassic intra-oceanic subduction in the İzmir - Ankara - Erzincan Ocean, Northern Turkey. Tectonophysics 509(1-2), 120-134.

Çemen, İ., Catlos, E. J., Göğuş, O., Ozerdem, C. 2006. Post-collisional extensional tectonics and exhumation of the Menderes Massif in the Western Anatolia Extended Terrane, Turkey in Postcollisional Tectonics and Magmatism in the Mediterranean Region, edited by Y. Dilek and S. Pavlides, 353–379, Geological Society of America, Special Papers, 409.

Cenki-Tok, B., Expert, M., Işık, V., Candan, O., Monié, P., Bruguier, O. 2016. Complete Alpine reworking of the northern Menderes Massif, western Turkey. International Journal of Earth Sciences, 105, 1507-1524.

Çiftçi, N. B., Bozkurt, E. 2008. Folding of the Gediz Graben fill, SW Turkey: Extensional and/or contractional origin? Geodinamica Acta 21(3), 145-167.

Çiftçi, N. B., Bozkurt, E. 2009. Pattern of normal faulting in the Gediz Graben, SW Turkey. Tectonophysics 473, 234-260.

Dewey, J. F. 1988. Extensional collapse of orogens, Tectonics 7, 1123–1139.

Dewey, J. F., Şengör, A. M. C. 1979. Aegean and surrounding regions - Complex multi-plate and continuum tectonics in a convergent zone. Geological Society of America Bulletin 90(1), 84-92.

Dixon, J. E., Robertson, A. H. F. 1984. The geological evolution of the eastern Mediterranean. Geological Society of London, Special Publications 17.

Doglioni, C., Agostini, S., Crespi, M., Innocenti, F., Manetti, P., Riguzzi, F., Savaşçın, Y. 2002. On the extension in western Anatolia and the Aegean sea. In: Rosenbaum, G. and Lister, G. S. Reconstruction of the evolution of the Alpine-Himalayan Orogen. Journal of the Virtual Explorer 8, 161-176.

Dora, O. Ö., Candan, O., Kaya, O., Koralay, E., Dürr, S. 2001. Revision of the so-called leptite-gneisses in the Menderes massif: a supracrustal metasedimentary origin. International Journal of Earth Sciences 89(4), 836-851.

Elitez, İ., Yaltırak, C. 2014. Çameli Havzası'nın Miyosen-Kuvaterner Jeodinamiği, Burdur-Fethiye Makaslama Zonu (GB Türkiye). Türkiye Jeoloji Bülteni, 57(3), 41-67.

Emre, T. 1996. Gediz Graben'nin tektonik evrimi. Türkiye Jeoloji Bülteni 39(2), 1–18.

Emre, T., Sözbilir, H. 1997. Field evidence for metamorphic core complex, detachment faulting and accommodation faults in the Gediz and Büyük Menderes grabens (Western Turkey). In International Earth Sciences Colloquium on the Aegean Region, İzmir, Turkey.

Emre, Ö., Doğan, A., Yıldırım, C., 2012. Biga Yarımadası'nın diri fayları ve deprem potansiyeli, Biga Yarımadası'nın genel ve ekonomik jeolojisi, Erdoğan, Y., Gürkan, T. (Ed.). Maden Tetkik ve Arama Genel Müdürlüğü Özel YayınSerisi 28.

Erbil, U., Okay, A. İ., Hakyemez, A. 2021. Late oligocene-early miocene shortening in the Thrace Basin, northern Aegean. International Journal of Earth Sciences 110(6), 1921-1936.

Erkül, F., Helvacı, C., Sözbilir, H. 2005a. Evidence for two episodes of volcanism in the Bigadiç borate basin and tectonic implications for western Turkey. Geological Journal 40, 545-570.

Erkül, F., Helvacı, C., Sözbilir, H. 2005b. Stratigraphy and geochronology of the Early Miocene volcanics in the Bigadiç borate basin, western Turkey. Turkish Journal of Earth Science 14.

Ersoy, Ş. 1990. Batı Toros Naplarının yapısal öğelerinin ve evriminin analizi. Jeoloji Mühendisliği Dergisi 37, 5-16.

Ersoy, E. Y., Helvacı, C. 2007. Stratigraphy and geochemical features of the Early Miocene bimodal (ultrapotassic and calc-alkaline) volcanic activity within the NE-trending Selendi basin, western Anatolia, Turkey. Turkish Journal of Earth Science 16, 117-139.

Ersoy, E. Y., Helvacı, C., Sözbilir, H. 2010. Tectono-stratigraphic evolution of the NE-SW trending superimposed Selendi basin: implications for Late Cenozoic crustal extension in western Anatolia, Turkey. Tectonophysics 488, 210-232.

Ersoy, E. Y., Çemen, İ., Helvacı, C., Billor, Z. 2014. Tectono-stratigraphy of the Neogene basins in Western Turkey: Implications for tectonic evolution of the Aegean Extended Region. Tectonophysics 635, 33-58.

Ersoy, Y. E, Helvacı, C., Palmer M. R. 2011. Stratigraphic, structural Tectono-stratigraphy of the Neogene basins in western Turkey: Implications for associations of supra-detachment and transtensional strike-slip basin formation in extensional tectonic setting. Journal of Asian Earth Sciences 41, 159-183.

Fossen, H. 2010. Structural Geology. Cambridge University Press, New York.

Friedmann, S. J., Burbank, D. W. 1995. Rift basins and supradetachment basins - intracontinental extensional end-members. Basin Research 7-2, 109-127.

Gautier, P., Brun, J. P., Moriceau, R., Sokoutis, D., Martinod, J., Jolivet L. 1999. Timing, kinematics and cause of Aegean extension: a scenario based on a comparison with simple analogue experiments. Tectonophysics 315, 31-37.

Genç, Ş. C., Yılmaz, Y. 1995. Evolution of the Triassic continental margin, northwest Anatolia. Tectonophysics 243, 193-207.

Genç, Ş. C., Altunkaynak, Ş., Karacık, Z., Yazman, M., Yılmaz, Y. 2001. The Çubukludağ graben, South of Izmir: Its tectonic significance in the Neogene geological evolution of the western Anatolia. Geodinamica Acta 14, 45-55.

Gessner, K., Lackmann, W., Ring, U., Passchier, C. W., Güngör, T. 1998. Structure and crustal thickening of the Menderes Massif, southwest Turkey, and consequences for large-scale correlations between Greece and Turkey. Bulletin of Geological Society Greece 32, 145-152.

Gessner, K., Ring, U., Johnson, C., Hetzel, R., Passchier, C. W., Güngör, T. 2001a. An active bivergent rolling-hinge detachment system: Central Menderes metamorphic core complex in western Turkey, Geology 29 (7), 611–614.

Gessner, K., Piazolo, S., Güngör, T., Ring, U., Kröner, A. Passchier, C. W. 2001b. Tectonic significance of deformation patterns in granitoid rocks of the Menderes nappes, Anatolide belt, southwest Turkey. International Journal of Earth Sciences 89(4), 766-780.

Gessner, K., Ring, U., Passchier, C. W, Güngör, T. 2001c. How to resist subduction: evidence for large-scale out-of-sequence thrusting during Eocene collision in western Turkey. Journal of the Geological Society 158, 769-784.

Gessner, K., Gallardo, L. A., Markwitz, V., Ring, U., Thomson, S. N. 2013. What caused the denudation of the Menderes Massif: Review of crustal evolution, lithosphere structure, and dynamic topography in southwest Turkey. Gondwana Research 24(1), 243-274.

Göktaş, F. 2020. Çeşme Yarımadası'nın Neojen stratigrafisi ve bölgesel korelasyonu, Batı Anadolu. Bulletion of the Mineral Research and Exploration 162, 31-54.

Göncüoğlu, M. C., Dirik, K., Kozlu, H. 1997. Pre-Alpine and Alpine Terranes in Turkey: explanatory notes to the terrane map of Turkey. Annales Geologiques des Pays Helleniques 37, 515-536.

Göncüoğlu, M. C., Turhan, N., Şentürk, K., Özcan, A., Uysal, Ş., Yaliniz, M. K. 2000. A geotraverse across northwestern Turkey: tectonic units of the Central Sakarya region and their tectonic evolution. Geological Society, London, Special Publications, 173(1), 139-161.

Görür, N., Şengör, A. M. C., Sakınç, M., Tüysüz, O., Akkök, K. R., Yiğitbaş, E., Oktay, F. Y., Barka, A., Sarıca, N., Ecevitoğlu, B., Demirbağ, E., Ersoy, Ş., Algan, O., Güneysu, C., Aykol, A. 1995. Rift formation in the Gökova region, southwest Anatolia: implications for the opening of the Aegean Sea. Geological Magazine 132, 637-650.

Gutnic, M., Monod, O., Poisson, A., Dumont, I. F. 1979. Geologie- Des. Tauirides Occidentales (Turque).

Güngör, T., Erdoğan, B., 2001, Emplacement age and direction of the Lycian nappes in the Söke-Selçuk region, western Turkey. International Journal of Earth Sciences 89, 874-882.

Gürboğa, Ş., Koçyiğit, A., Ruffet, G. 2013. Episodic two-stage extensional evolutionary model for southwestern Anatolian graben-horst system: New field data from the Erdoğmuş-Yenigediz graben (Kütahya). Journal of Geodynamics 65, 176-198.

Gürbüz, A., Boyraz, S., İsmael, M. T. 2012. Plio-Quaternary development of the Baklan-Dinar graben: implications for cross-graben formation in SW Turkey. International Geology Review 54(1), 33-50.

Gürer, A., Gürer, Ö. F., Pinçe, A., İlkışık, O. M. 2001. Conductivity structure along the Gediz Graben, West Anatolia, Turkey: tectonic implications. International Geology Review 43(12), 1129-1144.

Gürer, A., Pinçe, A., Gürer, Ö. F., İlkışık, O. M. 2002. Resistivity distribution in the Gediz graben and its implications for crustal structure. Turkish Journal of Earth Sciences 10(1), 15-25.

Gürer, Ö. F, Bozcu, M., Yılmaz, K., Yılmaz, Y. 2001. Neogene basin development around Söke-Kuşadası (western Anatolia) and its bearing on tectonic development of the Aegean region. Geodinamica Acta 14, 57-69.

Gürer, Ö. F., Yılmaz, Y. 2002. Geology of the Ören and surrounding areas SW Anatolia. Turkish Journal of Earth Sciences 11, 1-13.

Gürer Ö. F., Aldanmaz, E. 2002. Origin of the Upper Cretaceous-Tertiary sedimentary basins within the Tauride-Anatolide platform in Turkey. Geological Magazine 139(2), 191-197.

Gürer, Ö. F., Sarıca-Filoreau, N., Özburan, M., Sangu, E. and Doğan, B. 2009. Progressive development of the Buyuk Menderes Graben based on new data, western Turkey. Geological Magazine 146, 652-673.

Gürer, Ö. F., Kaymakçı, N., Çakır, Ş. Özburan, M. 2003. Neotectonics of the southeast Marmara region, NW Anatolia, Turkey. Journal of Asian Earth Sciences 21(9), 1041-1051.

Gürer, Ö. F., Sangu, E., Özburan, M. 2006. Neotectonics of the SW Marmara region, NW Anatolia, Turkey. Geological Magazine 143(2), 229-241.

Gürer, Ö. F., Sangu, E., Özburan, M., Gürbüz, A., Sarıca-Filoreau, N. 2013. Complex basin evolution in the Gökova Gulf region: implications on the Late Cenozoic tectonics of southwest Turkey. International Journal of Erath Sciences, 102(8), 2199-2221.

Gürer, Ö. F., Sangu, E., Özburan, M., Gürbüz, A., Sinir, H., Gürbüz, E. 2014. Edremit Grabeni'ni Oluşturan Fayların Kinematiği ve Batı Anadolu Gerilmeli Sistemi İçindeki Yeri. TÜBİTAK, Rapor No: 111Y258, 249.

Gürer, Ö. F., Sangu, E., Özburan, M., Sinir H. 2016. Plio-Quaternary kinematic development and paleo stress pattern of the Edremit Basin, Western Turkey, Tectonophysics.

Gürer, Ö. F., Sangu, E., Gürer, A., Akın, M. 2021. Late Cenozoic shift from extension to strike-slip stress regime in the west of the Biga Peninsula, NW Turkey.Journal of Structural Geology 148,104-348.

Hayward, A. B., 1984. Sedimentation and basin formation related to ophiolite nappe emplacement, Miocene, SW Turkey. Sediemntary Geology, 40(1-3), 105129.

Hayward, A. B., Robertson, A. H. F. 1982. Direction of ophiolite emplacement inferred from Cretaceous and Tertiary sediments of an adjacent autochthon, the Bey Dağlari, SW Turkey. Geological Society of America Bulletin 93, 68-75.

Heineke, C., Hetzel, R., Nilius, N. P., Zwingmann, H., Todd, A., Mulch, A., Wölfler, A., Glotzbach,

C., Akal, C., Dunkl, I., Raven, M., Hampel, A. 2019. Detachment faulting in a bivergent core complex constrained by fault gouge dating and low-temperature thermochronology. Journal of Structural Geology 127(2019), 103865.

Hetzel, R., Passchier, C. W., Ring, U., Dora Ö. O. 1995. Bivergent extension in orogenic belts: the Menderes massif (southwestern Turkey). Geology 23 (5), 455-458.

Hetzel, R., Reischmann, T. 1996. Intrusion age of Pan–African augen gneiss in the southern Menderes Massif and the age of cooling Alpine ductile extensional deformation. Geological Magazine 133, 565-572.

Işık V., Seyitoğlu, G., Çemen, İ. 2003. Ductile-brittle transition along the Alaşehir detachment fault and its structural relationship with the Simav detachment fault, Menderes massif, western Turkey. Tectonophysics 374(1-2), 1-18.

İnci, U. 1998. Lignite and carbonate deposition in Middle Lignite sequence of the Soma Formation from Soma coalfield, western Turkey. International Journal of Coal Geology 37(3-4), 287-313.

İnci, U. 2002. Depositional evolution of the soma coalfield, western Turkey: a preliminary report. Polish Geological Institute Special Papers 7, 109–118.

Jackson, J., McKenzie, D. 1988. The relationship between plate motions and seismic moment tensors, and the rates of active deformation in the Mediterranean and Middle East. Geophysical Journal International 93(1), 45-73.

Jolivet, L. 2001. A comparison of geodetic and finite strain pattern in the Aegean, geodynamic implications. Earth and Planetary Science Letters187(1-2), 95-104.

Kaya, O., Ünay, E., Saraç, G., Eichhorn, S., Hassenrück, S., Knappe, A., Pekdeğer, A., Mayda S. 2004. Halitpaşa transpressive zone: Implications for an Early Pliocene compressional phase in central western Anatolia, Turkey. Turkish Journal of Earth Sciences 13, 1-13.

Kaymakçı, N. 2006. Kinematic development and paleostress analysis of the Denizli Basin (Western Turkish): implications of spatial varition of relative paleostress magnitudes and orientations. Journal of Asian Earth Sciences 27, 207–222.

Koçyiğit, A., Yusufoğlu, H., Bozkurt, E. 1999. Evidence from the Gediz graben for episodic two-stage extension in western Turkey. Journal of Geological Society, London 156(3), 605-616.

Koçyiğit, A. 2005. The Denizli graben-horst system and the eastern limit of western Anatolian continental extension: basin fill, structure, deformational mode, throw amount and episodic evolutionary history, SW Turkey. Geodinamica Acta, 18(3–4),167-208.

Koçyiğit A., Deveci Ş. 2007. A N-S-trending active extensional structure, the Suhut (Afyon) graben: Commencement age of the extensional neotectonic period in the Isparta Angle, SW Turkey. Turkish Journal of Earth Sciences 16(4), 391-416.

Koçyiğit, A., Gürboğa, Ş. 2021. Active tectonics of Gülpınar-Tuzla area (Biga peninsula, NW Turkey): the source of 6th February - 24th March 2017 earthquake cluster. Bulletin of the Mineral Research and Exploration 166, 85-111.

Konak, N. 2002. 1/500.000 ölçekli İzmir Paftası, Maden Tetkik ve Arama Genel Müdürlüğü, Ankara.

Konak, N. 2007. Menderes Masifinin Prekambriyen-Paleozoyik istiflerinin tektonik üniteler bazında tartışılması. Menderes Masifi Kolokyumu, İzmir, Genişletilmiş Bildiri Özleri Kitabı, 17-23.

Konak, N., Şenel, M. 2002. 1/500.000 ölçekli Denizli Paftası, Maden Tetkik veArama Genel Müdürlüğü,Ankara.

Lips, A. L. W., Cassard, D., Sözbilir, H., Yilmaz, H. 2001. Multistage exhumation of the Menderes Massif, western Anatolia (Turkey). International Journal of Earth Sciences 89, 781-792.

Lacassin, R., Arnaud, N., Leloup, P. H., Armijo, R., Meyer B., 2007. Synorogenic and postorogenic exhumation of metamorphic rocks in N Aegean. Earth 2, 51–63.

McClusky, S., Balassanian, S., Barka, A. A., Demir, C., Ergintav, S., Georgiev, I., Gürkan, O., Hamburger, M., Hurst, K., Kahle, H., Kastens, K., Kekelidze, G., King, R., Kotzev, V., Lenk, O., Mahmoud, S., Mishin, A., Nadariya, M., Ouzounis, A., Paradissis, D., Peter, Y., Prilepin, M., Reilinger, R., Sanli, I., Seeger, H., Tealeb, A., Toksoz, M.,Veis, G. 2000. Global positioning system constraints on plate kinematics and dynamics in the eastern Mediterranean and Caucasus. Journal of Geophysical Research 105(B3), 5695–5720.

McKenzie, D. P. 1978. Some remarks on the development of the sedimentary basins. Earth Planet Science Letters 40, 25-32.

Nemec, W., Alçiçek, M. C., Özaksoy, V. 2018. Sedimentation in a foreland basin within synorogenic orocline: Palaeogene of the Isparta Bend,Taurides, SW Turkey. Basin Research 30, 650–670.

Nilsen, T. H., Sylvester, A. G. 1995. Strike-slip basins. In: Busby, C. J., Ingersoll, R.V. (Eds.). Tectonics of Sedimentary Basins. Blackwell, Cambridge, 425–457.

Ocakoğlu, F., Açıkalın, S., Özsayın, E., Dirik, R. K., 2014. Tectonosedimentary evolution of the Karacasu and Bozdoğan basins in the Central Menderes Massif, W Anatolia. Turkish Journal of Earth Sciences 23, 361-385.

Okay, A. 1981, Kuzeybatı Anadolu'daki ofiyolitlerin jeolojisi ve mavişist metamorfizması (Tavşanlı - Kütahya). Türkiye Jeoloji Kurumu Bülteni 24, 85-95.

Okay, A. İ. 1989. Geology of the Menderes Massif and the Lycian nappes south of Denizli, western Taurides. Bulletin of Mineral Research and Exploration 109, 37-51.

Okay, A. İ. 2001. Stratigraphic and metamorphic inversions in the central Menderes massif: a new structural model. International Journal of Earth Sciences (Geol Rundschau) 89, 709-727.

Okay, A. İ. 2002. Jadeite-chloritoid-glaucophane-lawsonite blueschists in northwest Turkey: unusually high P/T ratios in continental crust. Journal of Metamorphic Geology 20(8), 757-768.

Önen, A. P., Hall, R. 2000, Sub-ophiolite metamorphic rocks from NW Anatolia, Turkey. Journal of Metamorphic Geology 18, 483-495.

Öner, Z., Dilek, Y. 2011. Supradetachment basin evolution during continental extension: the Aegean province of western Anatolia, Turkey. Geological Society of America Bulletin 123(11-12), 2115-2141.

Öner, Z., Dilek, Y. 2012. Fault kinematics in supradetachment basin formation, Menderes core complex of western Turkey. Tectonophysics 608, 1394-1412.

Öner, Z., Dilek, Y., 2013. Fault kinematics in supradetachment basin formation, Menderes core complex of western Turkey. Tectonophysics 608, 1394-1412.

Özgül, N. 1976. Some basic geological properties of Taurides. Türkiye Jeoloji Kurumu Bülteni 19, 65-78.

Özgül, N. 1984. Stratigraphy and Tectonic evolution of the central Taurus. In: Tekeli, O., Göncüoğlu, M. C. (Eds.). Geology of the Taurus Belt, Proceedings, 77-90.

Özburan, M. 2009. Kütahya ve çevresinin neotektonik incelemesi, Doktora Tezi, Kocaeli Üniversitesi, 227 (unpublished).

Özburan, M., Gürer, Ö. F. 2012. Late Cenozoic polyphase deformation and basin development, Kütahya region, western Turkey. International Geology Review 54(12), 1401-1418.

Paradisopoulou, P. M., Papadimitriou, E. E., Karakostas,V. G., Taymaz, T., Kilias, A., Yolsal, S. 2010. Seismic hazard evaluation in western turkey as revealed by stress transfer and time-dependent probability calculations. Pure and Applied Geophysics 167(8–9), 1013-1048.

Partzsch, J. H., Oberhänsli, R., Candan, O., Warkus, F. 1998. The Menderes Massif, WTurkey: A complex nappe pile recording 1.0 Ga of geological history. Third International Turkish Geology Symposium, Middle East Technical University, Ankara, 281.

Pfister, M., Greber, E., Schindler, C., Straub, C., Kahle, H.G., Rybach, L. 2000, Geodynamics of the Marmara Sea region recent tectonic activity and the role of fluids at the Western end of the North Anatolian fault zone. Bulletin of Applied Geology 5,155-176.

Poisson A. 1977. Re´cherches ge´ologiques dans le Taurus occidental, Turquie. The`se Doct d'E´ tat, University Paris-Sud Orsay, 795 (unpublished).

Pourteau, A., Candan, O., Oberhansli, R. 2010. High-pressure metasedimentsincentral Turkey: Constraintsonthe Neotethyan closure history. Tectonics 29, TC5004.

Purvis, M., Robertson, A. H. F. 2004. A pulsed extension model for the Neogene–Recent E–W-trending Ala¸ sehir Graben and the NE–SW-trending Selendi and Gördes Basins, western Turkey. Tectonophysics 391, 171–201.

Régnier, J. L, Ring, U., Passchier, C. W., Gessner, K., Güngör, T. 2003. Contrasting metamorphic evolution of metasedimentary rocks from the Cine and Selimiye nappes in the Anatolide belt, western Turkey. Journal of Metamorphic Geology 21(7), 699-721.

Régnier, J., Mezger, J. E., Passchier, C. 2007. Metamorphism of Precambrian-Palaeozoic schists of the Menderes core series and contact relationships with Proterzoic orthogneisses of the western Çine Massif, Anatolide belt, western Turkey. Geological Magazine 144, 67-104.

Ricou, L.-E., Marcoux, J., Poisson, A. 1979, L'allochtonie des Bey Dağları orientaux: Reconstruction palinspastique des Taurides occidentales. Bulletin de la Société Géologique de France 11, 125-133.

Rimmele, G. 2003. Structural and metamorphic evolution of the Lycian Nappes and the Menderes Massif

(Southwest Turkey): Godynamic implications and correlations with the Aegean domain. Doctoral Thesis, Institüt für Geowissenschaften, Universitat Potsdam, Deutschland, 243.

Rimmele, G., Oberhanslı, R., Goffe, B., Jolivet, L., Candan, O., Çetinkaplan, M. 2003. First evidence of highpressure metamorphism in the Cover Series of the southern Menderes Massif. Tectonic and metamorphic implications for the evolution of SW Turkey. Lithos 71,19–46.

Rimmele, G., Parra, T., Goffe, B., Oberhansli, R., Jolivet, L., Candan, O. 2005. Exhumation paths of high-pressure-low-temperature metamorphic rocks from the Lycian Nappes and the Menderes Massif (SW Turkey): a multi-equilibrium approach. Journal of Petrology 46(3), 641-669.

Ring, U., Laws, S., Bernet, M. 1999. Structural analysis of a complex nappe sequence and late-orogenic basins from the Aegean Island of Samos, Greece. Journal of Structural Geology, 21(11), 1575-1601.

Ring, U., Johnson, C., Hetzel, R., Gessner, K. 2003. Tectonic denudation of a Late Cretaceous-Tertiary collisional belt: regionally symmetric cooling patterns and their relation to extensional faults in the Anatolide belt of western Turkey. Geological Magazine 140(4), 421-441.

Ring, U., Collins, A. S. 2005. U-Pb SIMS dating of synkinematic granites: timing of core-complex formation in the northern Anatolide belt of western Turkey. Journal of the Geological Society 162, 289-298.

Ring, U., Will, T., Glodny, J., Kumerics, C., Gessner, K., Thomson, S., Güngör, T., Monié, P., Okrusch, M., and Drüppel, K. 2007. Early exhumation of highpressure rocks in extrusion wedges: Cycladic blueschist unit in the eastern Aegean, Greece, and Turkey. Tectonics, 26-2, TC2001.

Rojay, B., Toprak, V., Demirci, C. and Süzen L., 2005. Plio-quaternary evolution of the Küçük Menderes graben southwestern Anatolia, Turkey. Geodinamica Acta, 18, 317–331

Sangu, E., Gürer, Ö. F., Gürer, A. 2020. Fault kinematic and Plio-Quaternary paleostress evolution of the Bakırçay basin, western Turkey. International Geology Review 62, 1245-1261.

Sarıca, N. 2000. The Plio-Pleistocene age of Büyük Menderes and Gediz grabens and their tectonic significance on N–S extensional tectonics in West Anatolia: mammalian evidence from the continental deposits. Geological Journal 35,1-2.

Searle,M.P.,Lamont,T.N.2019.Compressionalmetamorphic core complexes, low-angle normal faults and extensional fabrics in compressional tectonic settings. Geological Magazine 157(1), 101-118.

Serck, C. S., Braathen, A., Olaussen, S., Osmundsen, P.T., Midtkandal, I., Van Yperen, A. E., Indrevaer, K. 2021. Supradetachment to rift basin transition recorded in continental to marine deposition; Paleogene Bandar Jissah Basin, NE Oman. Basin Research 33, 544–569.

Seyitoğlu, G., Scott, B. 1991. Late Cenozoic crustal extension and basin formation in west Turkey. Geological Magazine 128, 155-166.

Seyitoğlu, G., Scott, B. C., Rundle, C. C. 1992. Timing of Cenozoic extensional tectonics in west Turkey. Journal of the Geological Society London 149, 533-538.

Seyitoğlu, G., Scott, B. C. 1994. Late Cenozoic basin development in west Turkey. Gördes basin: tectonics and sedimentation. Geological Magazine, 131, 631-637.

Seyitoğlu, G., Benda, L., Scott, B. C. 1994. Neogene palynological and isotopic age data from Gördes basin, West Turkey. Newsletters on Stratigraphy, 31, 133-142.

Seyitoğlu, G., Scott, B. C. 1996. Age of Alaşehir graben (west Turkey) and its tectonic implications. Geological Journal 31, 1–11.

Seyitoğlu, G., Çemen, İ., Tekeli, O., 2000. Extensional folding in the Alaşehir (Gediz) graben, western Turkey. Journal of the Geological Society, London 157, 1097 -1100.

Seyitoğlu, G., Işık, V, Çemen, İ. 2004. Complete Tertiary exhumation history of the Menderes Massif, western Turkey: an alternative working hypothesis. Terra Nova 16,358–363.

Seyitoğlu, G., Işık, V. 2015. Batı Anadolu'da geç Senozoyik genişleme tektonği: Menderes çekirdek kompleksinin yüzeylemesi ve ilişkili havza oluşumu. Bulletin of the Mineral Research and Exploration 151, 49-109.

Sherlock, S., Kelley, S., Inger, S., Harris, N., Okay, A. 1999. 40 Ar-39Ar and Rb-Sr geochronology of highpressure metamorphism and exhumation history of the Tavsanli Zone, NW Turkey. Contributions to Mineralogy and Petrology, 137, 46-58.

Sözbilir, H. 2001. Extensional tectonics and the geometry of related macroscopic structures: field evidence

from the Gediz detachment, western Turkey. Turkish Journal of Earth Sciences 10 (2), 51-67.

Sözbilir, H. 2002. Geometry and origin of folding in the Neogene sediments of the Gediz Graben, western Anatolia, Turkey. Geodinamica Acta 15,277-288.

Sözbilir, H. 2005. Oligo-Miocene extension in the Lycian Orogen: evidence from the Lycian molasse basin, SW Turkey. Geodinama Acta, 18, 255-282.

Sözbilir, H., Sarı, B., Uzel, B., Sümer, Ö. Akkiraz, M. 2011. Tectonic implications of transtensional supradetachment basin development in an extension-parallel transfer zone: the Kocaçay Basin, western Anatolia, Turkey. Basin Research, 23(4), 423-448.

Sümer, Ö., Sözbilir, H., Uzel, B. 2020. Büyük Menderes Grabeni'nin Rolling Hinge (Yuvarlanan Reze) Modelinde Supra-Detachment (Sıyrılma Üstü) Havzadan Rift Havzasına Evrimi. Türkiye Jeoloji Bülteni 63, 241-276.

Şengör, A. M. C. 1979. The North Anatolian transform fault: its age, offset and tectonic significance. Journal of the Geological Society 136, 269-282.

Şengör, A. M C. 1982. Affects controlling the Neotectonic activity in Aegean region. Batı Anadolu'nun genç tektoniği ve volkanizması paneli. Türkiye Jeoloji Kurultayı 59-71.

Şengör, A. M. C. 1987. Cross-fault and differential stretching of hanging walls in regions of low- angle normal faulting: examples from western Turkey. Coward,M. P. , Deway, J. F., Hancock, P. L. (Ed.). Continental extensional tectonics. Geological Society Special Publication 28,575– 589.

Şengör, A. M. C., Yılmaz, Y. 1981. Tethyan evolution of Turkey: a plate tectonic approach. Tectonophysics 75, 181–241.

Şengör, A . M. C., Görür, N., Şaroğlu, F. 1985. Strike- slip faulting and related basin formation in zones of tectonic escape: Turkey as a case study. In: Biddle K. T., Christie-Blick N (Eds.) Strike-slip faulting and basin formation. Strike-Slip Deformation, Basin Formation and Sedimentation, Special Publications, SEPM Society for Sedimentary Geology 37, 227-264.

Ten Veen, J. H., Boulton, S. J., Alçiçek, M. C. 2009. From palaeotectonics to neotectonics in the Neotethys realm: The importance of kinematic decoupling and inherited structural grain in SW Anatolia (Turkey). Tectonophysics 473,261-281.

Taymaz, T., Jackson, J. McKenzie, D. 1991. Active tectonics of the north and central Aegean Sea. Geophysical Journal International 106(2), 433-490. Uzel, B. ve Sözbilir, H., 2008. A first record of a strikeslip basin in western Anatolia and its tectonic implication: The Cumaovasi basin. Turkish Journal of Earth Sciences, 17-3, 559-591.

Van Hinsbergen, D. J. J., Schmid, S. F. 2012. Map view restoration of Aegean–West Anatolian accretion and extension since the Eocene. Tectonics 31, TC5005.

Van Hinsbergen, D. J. J. 2010. A key extensional metamorphic complex reviewed and restored: The Menderes Massif of western Turkey. Earth-Sciences Reviews 102(1-2), 60-76.

Westaway, R., Pringle, M., Yurtmen, S., Demir, T., Bridgland, D., Rowbotham, G., Maddy, D. 2004. Pliocene and Quaternary regional uplift in western Turkey: the Gediz River terrace staircase and the volcanism at Kula. Tectonophysics 1-4, 121-169.

Whitney, D. L., Bozkurt, E. 2002., Metamorphic history of the southern Menderes Massif, western Turkey. Geological Society of America Bulletin 114, 829-838.

Yılmaz, Y. 1981. Sakarya kıtası güney kenarının tektonik evrimi. İstanbul Yerbilimleri 1, 33-52.

Yılmaz, Y. 1989. An Approach to the Origin of Young Volcanic Rocks of Western Turkey, Tectonic Evolution of the Tethyan Region. Springer, 159-189.

Yılmaz, Y. 2017a. Major Problems of Western Anatolian Geology. Edited by Çemen İ and Yılmaz, Y, Active Global Seismology: Neotectonics and Earthquake Potential of the Eastern Mediterranean Region, Book Series, Geophysical Monograph Book Series 225, 141-187.

Yılmaz, Y. 2017b. Morphotectonic Development of Anatolia and the Surrounding Regions. Çemen, İ.,Yılmaz, Y. (Ed.). Active Global Seismology: Neotectonics and Earthquake Potential of the Eastern Mediterranean Region, Book Series, Geophysical Monograph Book Series. John Wiley and Sons, Inc., 225, 11-91.

Yılmaz, Y., Genç, S. C., Gürer, Ö. F., Bozcu, M., Yılmaz, K., Karacık, Z., Altunkaynak, S., Elmas, A. 2000. When did the western Anatolian grabens begin to develop? Bozkurt, E., Winchester, J. A., Piper, J. D. A. (Ed.). Tectonics and Magmatism in Turkey and the Surrounding Area. Geological Society of London, Special Publication 173, 353- 384.

Yılmaz, Y., Karacık, Z. 2001. Geology of the northern side of the Gulf of Edremit and its tectonic significance for the development of the Aegean grabens. Geodinamica Acta 14,31–43.

Bulletin of the Mineral Research and Exploration

The importance of Confocal Raman Spectroscopy and mineral chemistry studies in the magma crystallization processes: Strandja Intrusives, NW Türkiye

Ezgi ULUSOY[a]* and Yusuf Kağan KADIOĞLU[b,c]

[a]General Directorate of Mineral Research and Exploration, Department of Geological Research, Ankara, Türkiye.
[b]Ankara University, Department of Geological Engineering, Ankara, Türkiye.
[c]Ankara University, Yerbilimleri Uygulama ve Araştırma Merkezi, Ankara, Türkiye.

Research Article

ABSTRACT

The Strandja Massif cropping out in NW Turkey is cut by Late Cretaceous intrusives. These are called Strandja Intrusives and they are felsic and mafic coeval intrusives. Felsic intrusives consist of granite, granodiorite, quartz monzonite and syenite, while mafic intrusives consist of diorite and gabbro composition. Main composition of felsic intrusives consists of quartz, alkali feldspar, plagioclase, biotite, amphibole ±pyroxene mineral association, while main composition of mafic ones consists of plagioclase, biotite, amphibole ±pyroxene ±olivine mineral association. Amphiboles hydrated double-chain mineral of the Strandja Intrusives observed in all rocks used as an index mineral in this study to understand the petrological evolution of the rocks. According to Confocal Raman Spectroscopy studies amphiboles were actinolite type and exhibited similar spectrum and results of mineral chemistry reveals that they were calcic/Mg-hornblende types. According to geothermobarometer calculations, amphiboles crystallize in felsic intrusives at a pressure range of 0.49-0.94 kbar and a temperature of 757.52-814.49°C temperature at a depth of approximately 1.34-4.93 km, while in mafic ones at 2.59 kbar pressure and 892.82°C temperature at 9.97 km depth. Different temperatures-depth conditions and overlaps in Raman shift obtained from amphiboles indicate that these intrusives are derived from different sources but crystallized in the same environment.

1. Introduction

The scattering of the beam reflected on a component occurs in two ways: elastic (Rayleigh) and inelastic (Raman) scattering. If the light absorption event does not occur during the reflection of a violent monochromatic beam on any component, the light scattering event occurs, and this scattering is defined as Rayleigh scattering (Young, 1981; Skoog et al., 1998; Akçe and Kadıoğlu, 2020). The energy of a large part of the light scattered during elastic Rayleigh scattering is equal to the energy of the light interacting with matter (Table 1). In addition, the fact that a very small part of the reflected light is absorbed by the molecule, and the wavelength of the scattered beam is different from the wavelength of the reflected light, is defined as inelastic Raman scattering (Raman and Krishnan, 1928). While Rayleigh scattering gives a single peak with 104-105 times intensity compared to Raman scattering, it does not give any information about vibrational transitions of molecules. In addition, Raman scattering, which is the scattering of light

interacting with a molecule, provides information about the vibrational energy levels of molecules (Raman and Krishnan, 1928; Skoog et al., 1998; Akçe and Kadıoğlu, 2020; Karacan, 2020).

Table 1- Scattering types of light reflected on a material (Raman and Krishnan, 1928; Young, 1981).

Types of Scatterring the ray		
Scatter Type		**Situation**
Rayleigh	Elastic	Wavelength of scattered ray = Wavelength of the incident ray
Raman	Inelastic	Wavelength of scattered ray > Wavelength of the incident ray Wavelength of scattered ray < Wavelength of the incident ray

Raman scattering is the basis of Confocal Raman Spectrometry (CRS) research. In Raman scattering, there is a difference between the wavelength of the beam reflected on a solid-liquid-gas molecule and the wavelength of the reflected rays back. Decoupled raman scattering is a reflection of a solid-liquid-gas molecule. These differences are defined as Raman shift and contain important information about the chemical structure of the molecule (McMillan and Hofmeister, 1988; Ferraro et al., 2003). Raman studies of liquid and solid phases can be identified with the individual,

the degree of crystallinity can be estimated with the result that many more of the data obtained can be used as a representative for temperature and density, and the abundance of each liquid component can be estimated, based on the characteristic of the Raman spectrum and in addition the ability to determine the molecular structure of a sample can be estimated due to polymerization (Bodnar and Frezzotti, 2020). Confocal Raman spectroscopy is a mineral that is sent with the wavelength of light emitted Raman shifts after the interaction with the molecule are called differences in the wavelength of light, and these spectra, which can reflect the identity of the mineral (Chukanov and Vigasina, 2020). The main vibration zones in the Raman spectrum according to mineral groups are generally shown in Figure 1. In addition, CRS studies show that minerals with a special solid solution (Ca-Mg carbonates, olivines, pyroxenes and tourmalines, etc.) also provides information about their chemical composition (Watenphul et al., 2016). Therefore, CRS analyses also provide useful data on qualitative phase identification and/or quantitative phase characteristics in mineralogical, crystallographic, geochemical, gemological and related sub-branches in the earth sciences (Nasdala and Schmidt, 2020; Ferrando, 2018).
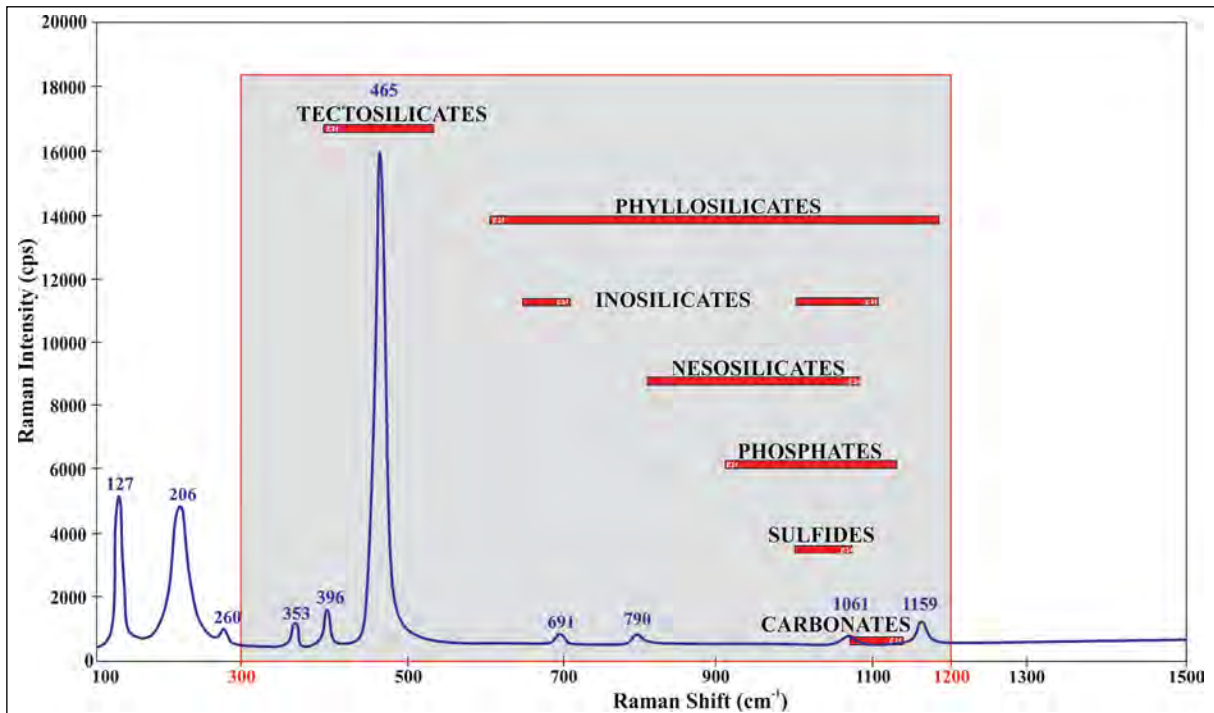
Figure 1- The main vibration zones of the most commonly observed mineral groups (Frezzotti et al., 2012; Ferrando, 2018).

Various approaches can be made about the crystallization processes of magma by performing CRS applications on the mineral components contained in intrusive rocks (Zoroğlu and Kadıoğlu, 2007; Deniz, 2010; Kadıoğlu et al., 2019; Akçe and Kadıoğlu, 2020; Ulusoy, 2021; Deniz, 2022). The differences in the Raman spectra obtained vary depending on the chemical structure of the molecules and thus minerals of different composition can be identified by distinguishing them according to their distribution and behavior in the Raman spectrum. For example, the fact that the mineral formed by elements/ions such as Na, Ca, Mg, Al and OH belonging to the amphibole group gives a different spectrum depending on the molecular structure may be due to the compositional difference of the amphibole mineral, and the size and uniformity in the spectrum may be due to the physical behavior and chemical purity of the amphibole mineral. In this way, it will be possible to distinguish the composition, type and different physical characteristics of the mineral that it has acquired during the crystallization period and/or later with the shift peaks in the Raman spectrum shown by the minerals.

Studies on the petrology and formation conditions of intrusive rocks outcropping in Anatolia, continue to be developed and updated, as well as useful studies conducted until today (Aydın et al., 2019; Kuşçu et al., 2019; Deniz and Kadıoğlu, 2019; Aydınçakır et al., 2020; Özdamar et al., 2021; Deniz, 2022). As first time in this study; By determining the changes in the crystallization processes of magma and the compositional behaviors of each rock group in the crystallization differentiation process by using the changes in the CRS spectra and the mineral chemistry data of the mafic mineral (amphibole) content common to all rock groups belonging to the Late Cretaceous Strandja Intrusions outcropped in NW Turkey, it is aimed to elucidate the petrological evolution of the region.

2. Geology of the Study Area

Turkey, located in the Alpine Himalayan Mountain Belt, consists of the amalgamation of many microcontinents and associations (Şengör and Yılmaz, 1981; Okay and Tüysüz, 1999). The rock units belonging to the Strandja Massif are outcropped from NW Turkey and expanding towards Bulgaria. The Strandja Massif is covered in the south by Tertiary sediments belonging to the Thracian Basin, while in the west it is cut by the strike-slip, N-S trending Western Black Sea fault (Okay et al., 2001) (Figure 2). The basement rocks of the Strandja Massif consist of pre-Permian aged crystalline rocks that lately metamorphosed and Late Variscan intrusions that cut the metamorphic basement (Aydın, 1982; Sunal et al., 2006; Okay et al., 2008; Natal'in et al., 2016). All the basement units underwent metamorphism and deformation under the conditions of the greenschist-amphibolite facies during the Variscan orogeny (Okay and Yurtsever, 2006). The bassement units are overlain by Triassic-Jurassic sedimentary cover units, that changes from clastic to carbonated, were metamorphosed under the lower amphibolite-upper greenschist conditions (Aydın, 1974, 1982; Chatalov, 1988; Okay et al., 2001; Okay and Yurtsever, 2006; Natal'in et al., 2005; Bedi et al., 2022), these units finally underwent regional metamorphism and compressional deformation during the Late Jurassic (Aydın, 1988). During the Alpine Orogeny, the Late Cretaceous aged intrusions are cut the Massif as a result of the closure of the Neotethys Ocean (Figure 3) (Aydın, 1974, 1982, 1988; Aykol, 1979; Moore et al., 1980; Ohta et al., 1988; Üşümezsoy, 1990; Aykol and Tokel, 1991; Çağlayan and Yurtsever, 1998; Karacık and Tüysüz, 2010; Ulusoy, 2012; Ulusoy, 2021; Ulusoy and Kadıoğlu, 2021; Bedi et al., 2022). According to geochemical data, these intrusions have a subduction-related origin (Aykol and Tokel, 1991; Karacık and Tüysüz, 2010). Biotite-hornblende-whole rock K-Ar and Ar-Ar ages indicate that the age of intrusions are in the Santonian-Campanian range (Moore et al., 1980; Ohta et al., 1988; Kuşçu et al., 2019; Ulusoy, 2021). All units belonging to the massif are unconformably covered by Upper Cretaceous sedimentary, volcano-sedimentary and volcanic units that are not metamorphosed (Aydın, 1982; Okay and Yurtsever, 2006). These volcanics belonging to the volcanic-plutonic complex in the Eastern Srednogorie zone are the product of the same system and are associated with Late Cretaceous aged intrusions (Okay and Yurtsever, 2006).

3. Analytical Methods

Strandja Intrusions are divided into two main groups as felsic and mafic intrusive rocks according
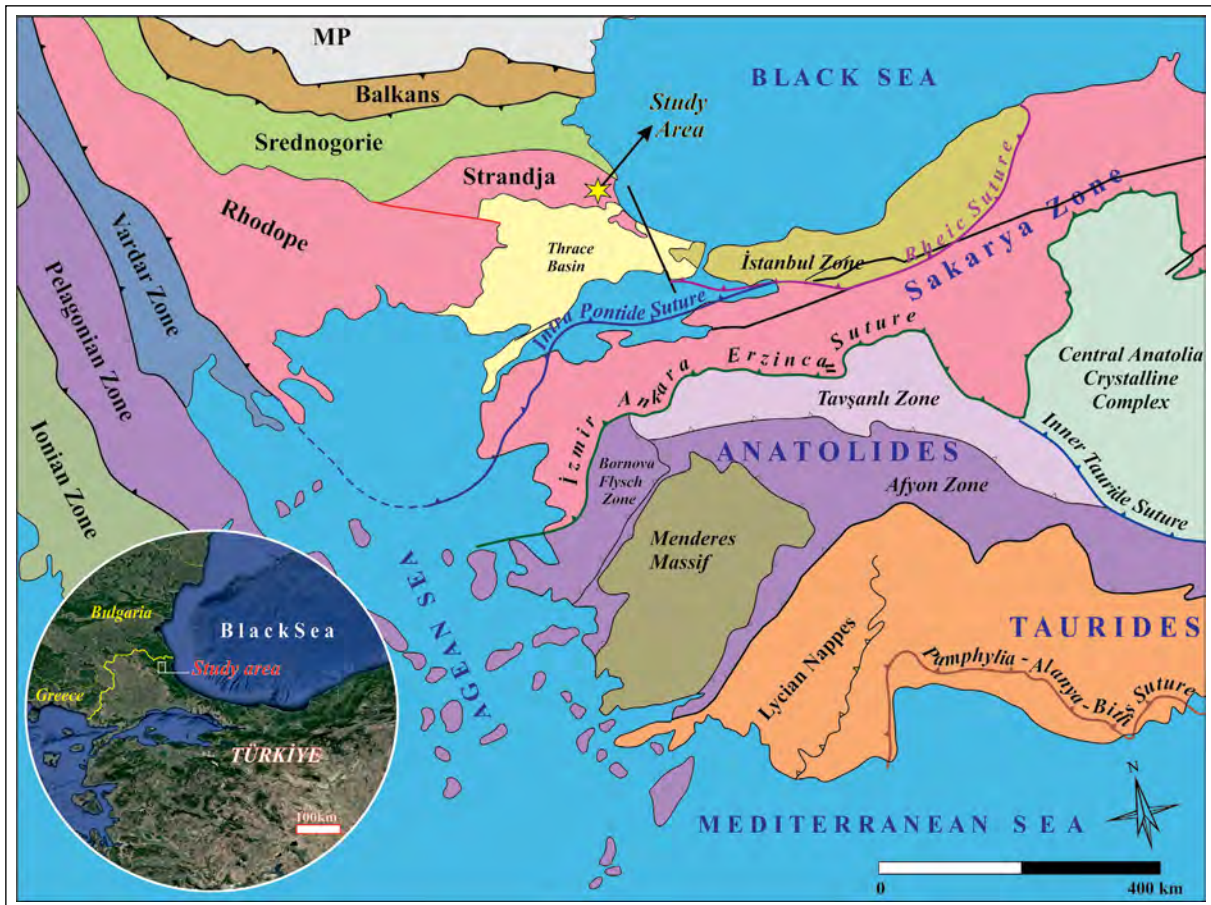
Figure 2- Location of the study area within the tectonic units of Türkiye (MP: Moezya Platform) (Map is modified from Okay and Tüysüz, 1999; Catto et al., 2018; and Candan et al., 2016).

to their compositional differences (Ulusoy, 2021). Detailed textural and mineralogical investigation of the representative samples selected from the rocks belonging to these groups were performed under a polarizing microscope and instrumental analyzes were performed.

Semi-qualitative CRS analyses and quantitative electron probe microanalysis (EPMA) of amphibole minerals from samples representing each rock group belong to the Strandja Intrusions were performed at the Ankara University Geosciences Application and Research Center. CRS examinations were performed with Thermo brand DXR model CRS device. The main components of the CRS measurement system consist of a laser, an electrically cooled charge-coupled device detector (CCD), an optical microscope. The device calibration was tested using polystyrene film.

Raman spectra with a resolution of 2 cm^{-1} in the range of 0-1200 cm^{-1} were obtained by using 633 cm^{-1} laser from the open thin sections of the samples. Mineral identification was made according to the spectra. After the polished sections of the same rocks were coated with carbon with Qurorum Q150TES device, the selected crystals were analyzed with JEOL brand JXA 8230 model Super Probe equipped with five wavelength dispersive spectrometer with a current of 20 kV and an acceleration voltage of 20 nA. Natural oxide and mineral reference materials were used for calibration and measurements. The conditions of the sample preparation and analysis process were carried out as defined in Deniz (2022). In the obtained data, matrix effects were corrected with the software provided by JEOL and corrections were made for atomic number (Z), absorption (A) and fluorescence (F) effects.
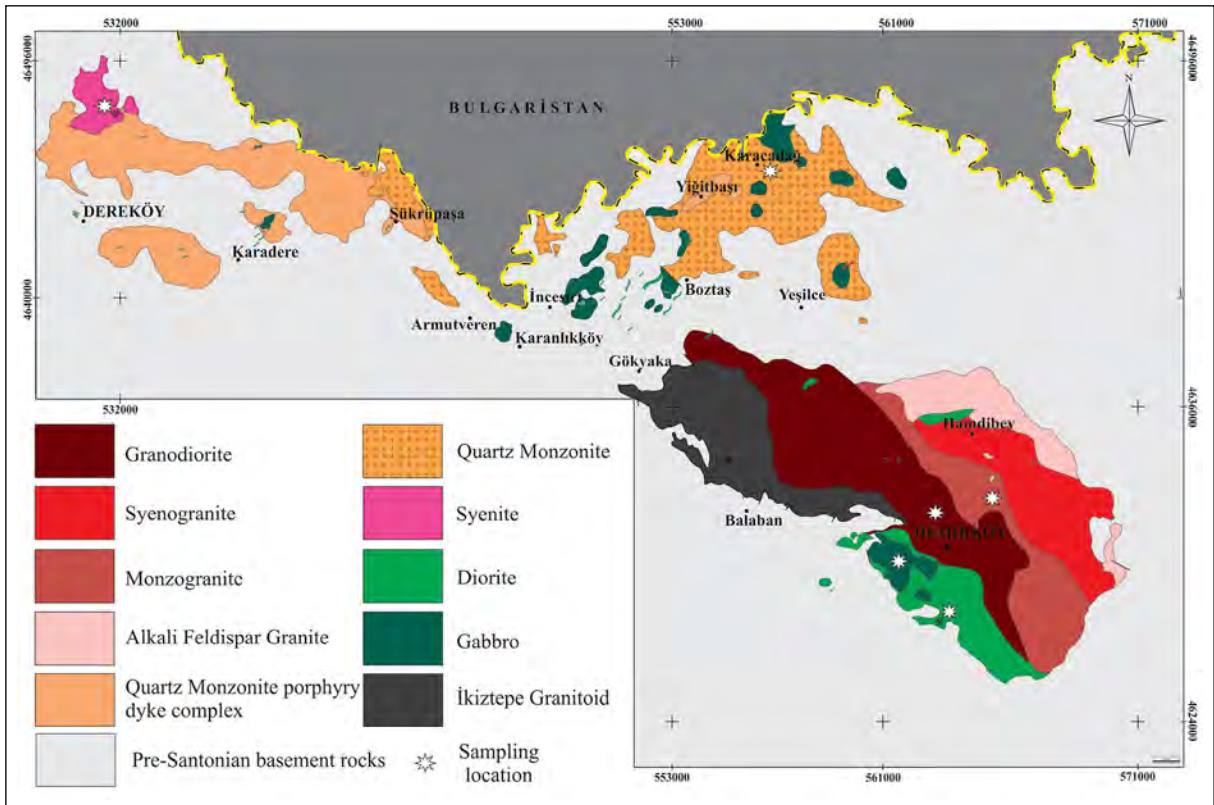
Figure 3- Compositional and positional distribution map of Late Cretaceous aged Strandja Intrusions outcropped in the study area (Ulusoy, 2021).

4. Results

4.1. Mineralogy - Petrography

The Late Cretaceous aged Strandja Intrusions that cut through the Strandja Massif are divided into two main groups as felsic and mafic. Macroscopically, the rocks are generally observed to be coarse-grained, phaneritic textured; microscopically, they exhibit holocrystalline hypidiomorph granular texture (Figure 4). The felsic intrusions are composed of granite, granodiorite, quartz monzonite and syenite. The main mineral content of the felsic group is quartz +plagioclase (oligoclase-andesine) +orthoclase in varying proportions depending on its composition. Varying amounts of biotite +amphibole in granites and granodiorites; in addition to these minerals,

	1 Granite	2 Granodiorite	3 Quartz Monzonite	4 Syenite	5 Diorite	6 Gabbro
Texture	Holocrystalline hypidiomorphic	Holocrystalline hypidiomorphic	Holocrystalline hypidiomorphic	Holocrystalline hypidiomorphic	Holocrystalline hypidiomorphic	Holocrystalline hypidiomorphic
Main minerals	KF, Q, PLG	PLG, Q, KF	PLG, KF, Q	KF, PLG, Q	PLG ± Q ±KF	PLG ± Q ±KF
Mafic minerals	Biotite, amphibole	Biotite, amphibole	Biotite, amphibole, clinopyroxene	Biotite, amphibole, clinopyroxene	Biotite, amphibole, clinopyroxene	± Biotite, amphibole, clinopyroxene ± olivine
Accessory minerals	Titanite, rutile, apatite, zircon, opaque min.	Titanite, rutile, apatite, zircon, opaque min.	Titanite, rutile, apatite, zircon, opaque min.	Titanite, rutile, apatite, zircon, opaque min.	opaque min.	opaque min.

Figure 4- Summary of petrographic characteristics of rock groups belonging to Strandja intrusions (AF: alkali feldspar, K: quartz: Plj: plagioclase, red highlighted mineral represents the mafic phase common to all rock groups).

clinopyroxene constitutes the mafic mineral composition in quartz monzonite and syenite. In addition, the syenite in the study area, unlike monzonite, contains less nepheline, which is another distinguishing feature. Some fine-grained titanite, allanite, apatite, zircon crystals and scattered magnetite crystals are located secondary to the rock groups. Mafic intrusions are composed of diorite and gabbro and cut felsic intrusions. In the field observations, dioritic compositional rocks have been evaluated in mafic intrusions due to their gradual transition with gabbro. The main composition of mafic rocks is plagioclase, amphibole, clinopyroxene ±biotite ±olivine ±orthoclase ±quartz. Magnetite, ilmenite and pyrite are scattered in varying proportions in mafic intrusions. In the studied rocks belonging to Strandja Intrusions, zoning in plagioclases and partially in coarse-grained minerals (orthoclase, plagioclase, amphibole, etc.), while poikilitic texture is observed. The coexistence of poikilitic and zoned texture indicate that crystallization may have continued in an irregular temperature range. Kaolinization and sossuritization in feldspars; magmatic uralitization observed in some of the clinopyroxenes and defined by the transformation only to amphibole group minerals from the crystal rim,

as well as epidotization and chloritization observed in some parts of mafic components.

4.2. Confocal Raman Spectroscopy

Within the scope of this study, CRS investigations of mafic component amphiboles, which are found in varying proportions in all rock groups constituting the felsic and mafic components of the Strandja Intrusions, were carried out. During the investigations, care was taken to select the amphibole crystals from euhedral and/or subhedral amphibole crystals that do not decompose as much as possible. The distribution of numerical values of characteristic Raman shifts of amphibole minerals crystallized in Strandja intrusions according to spectral regions is given in Table 2.

Ranges in the amphibole spectrum; the region of vibrations from the interactions between the cation and oxygen (M-O), internal Si_4O_{11} consists of band vibrations and OH molecule vibrations (Apopei and Buzgar, 2010). Raman shift spectrum of amphibole is $625 cm^{-1}$ the underlying spectral fields consist of the bending (deformation) field of the double chain silicate and vibrations in various M regions containing cations (Kloprogge et al., 2001; Rinaudo et al., 2004;

Table 2- Characteristic Raman shift values of amphibole minerals crystallized in the Strandja Massif.

	Spectral Region	Si-O-Si	O-Si-O	Si-O-Si	Si	SiO₄O₁₁-OH	T-M- OH (M: Mg,Fe)
	Raman Shift (cm⁻¹)	*1200-1021*	*1021-735*	*735-500*	*500-383*	*383-173*	*173-50*
Rock Types	Gabbro	•1020.27	•818.36	•661.43	•535.12	•366.70 •319.34	•155.22
	Diorite			•667.17	•526.50	•383.93 •358.09 •218.38	•173.41 •152.35
	Syenite	•1021.16	•922.72 •735.74	•665.78 •564.86 •524.00	•406.99 •383.46	•359.93 •291.21 •216.91	•171.10 •150.05 •134.57 •112.28
	Quartz Monzonite	•1049.02		•728.93 •665.78 •561.15 •526.48	•408.84 •385.93	•363.65 •292.45 •217.53 •173.57	•151.90 •115.38
	Granodiorite		•1014.35 •917.15	•728.31 •663.92 •527.72	•383.46	•362.41 •289.97 •217.53 •174.19	•153.14
	Granite	•1045.31	•927.67	•668.88 •528.33	•388.41	•366.12 •220.63 •176.67	•155.00

Petry et al., 2006). 300-420cm^{-1} spectral region between T (M-OH), 420-610 cm^{-1} the spectral region is composed of Si-O-Si bending vibrations (Makreski et al., 2006). T denotes the transition mode and M denotes the Ca-Fe-Mg cations. 625-1130cm^{-1} the spectral region is caused by the internal vibrations of the crystal and consists of symmetrical (Vs) and asymmetric (Vas) vibrations of the Si-O-Si and O-Si-O bonds that make up the crystal (Kloprogge et al., 2001; Rinaudo et al., 2004).

As a result of CRS investigation of amphiboles contained in rocks of different compositions in the study area, it was determined that the amphiboles are in the composition of actinolite. When the spectra of actinolite amphiboles detected in the samples are examined, it is observed that the spectra overlap with each other in general (Figure 5). When the raman shifts of Mg-hornblend and Na-amphibole (riebeckite) are compared with the Raman shifts of the Strandja Intrusion amphiboles, it is observed that the amphiboles of the Strandja Intrusions differ significantly from the Na-amphibole (riebeckite) reference member, while they clearly show similarity to the Mg-Hornblend reference member. Raman shift peaks observed between 420-10 cm^{-1}, expressing OH release and lattice transition, show a change from felsic intrusives to mafic intrusives. The peaks of OH release and lattice transition show low amplitude in the early phase of magmatism and increase in later phases (Kadıoğlu et al., 2019; Güllü et al., 2019). Amphiboles representing the high temperature mineral in granites give relatively low amplitude peaks, while amphiboles in gabbros give higher amplitude peaks due to relatively being a lower temperature mineral. Güllü et al. (2019) stated that the Si4O11 bending mode OH bond amplitudes of amphiboles crystallized in the late phase are higher in amphibole minerals crystallized in the early phase.

Similarly, the high amplitude OH bond developed in such amphiboles in the Strandja Intrusives may also be related to the H2O concentration in the late stage residual magma. In this context, the rock groups evaluated as early stage in the study area represent rocks with gabbro-diorite composition, while the late stage rock groups are represented by granite and granodiorites.

In addition, the presence of magma mixing processes in intrusive rocks that outcropped in the study area can be supported by the similarity of the raman spectra of amphibole contained in granite and amphibole contained in gabbro-composed rock. Amphiboles are determined as hornblende under the optical microscope and mineral chemistry analyzes as actinolites in CRS investigation can similarly be explained by magma mixing processes. It is observed that the composition of the intrusions in the study area varies from mafic to intermediate and felsic composition. According to the geological, petrographic and spectroscopic data obtained, magma mixing is observed in all rocks (Ulusoy and Kadıoğlu, 2021; Ulusoy, 2021). In this context, it is observed that a certain part of the amphiboles exhibits changes from actinolite to chermachite as a result of magmatic uralitization. In mafic minerals crystallizing from the source magma of gabroic rocks, OH bonding cannot be expected under normal conditions, but crystallization of hydrous silicates (amphibole group minerals) can occur by mixing with felsic magmas during the crystallization periods of such magmas and interacting acidic and mafic elements.

When the Raman shift spectra of all amphiboles were compared, it was determined that they were distributed in 6 separate bands (Figure 5). It was determined that the Raman shift spectra of all the rocks in the group showed significant overlap and showed a broader spectrum range, especially by expanding in the SiO_4O_{11}-OH release band from gabbro to granite. The liberalization of the spectrum in the OH band can be explained by the increase in the water content of magma from gabbro to granite and, as a result, the crystallization of hydrous mafic (actinolite) silicates (Figure 5 and Table 2).

4.3. Chemistry of Amphiboles

Amphiboles, which are hydrous, double chain silicate minerals, are the most common mafic mineral among all rock groups in the study area. Amphibole minerals of varying crystal size are semi-octagonal and octagonal in shape, and partially coarse-grained crystals exhibit poikilitic texture. In general, amphiboles in rocks belonging to Strandja Intrusions display a homogeneous structure under microscope. Serial point measurements were made from amphibole
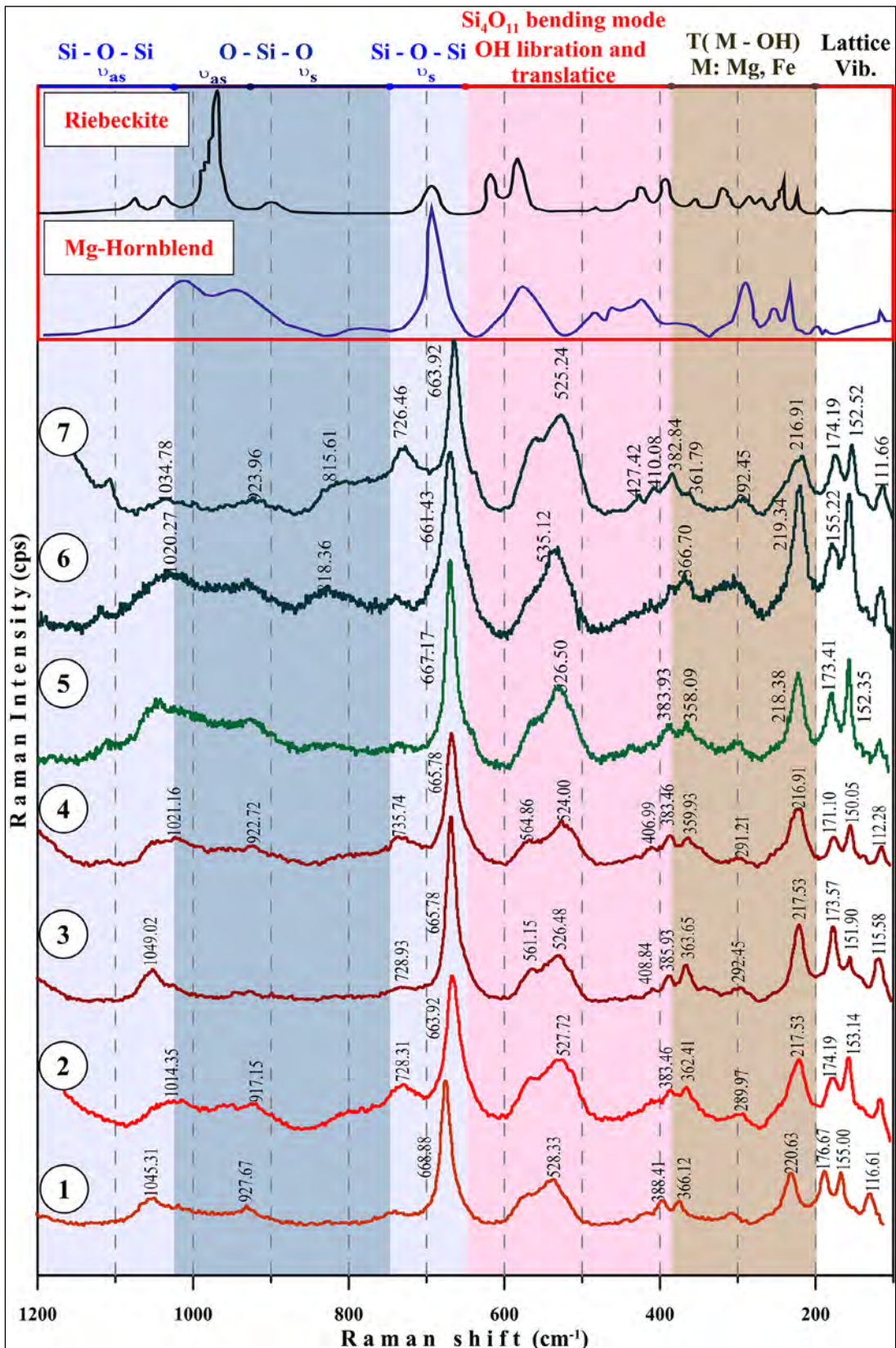
Figure 5- Comparison of the Raman spectra of amphibole crystals selected from each rock group with the Raman shift peaks of sodic and calcic amphibole minerals taken as reference (*: RRUFF, 2021; Ruff.info Riebeckite taken from the site and MG-Hornblende reference peaks) (1: Granite (Monzogranite), 2: Granodiorite, 3: Monzonite Quartz, 4: Syenite, 5: Diorite, 6: Gabbro).

crystals selected from felsic and mafic rock groups along a line from the rim to the core.

According to the obtained anoxide values, stoichiometric calculations were performed and the number of cations contained in each point was determined. The cation numbers and mineral structure were calculated according to Leake (1997) by taking 23 O. The representative mineral chemistry of the amphiboles belonging to the rock groups examined, the anoxide values and the calculated cation values as a result of the analysis are given in Table 3.

In the Al^{vi} versus Al^{vi} variation diagram, all amphiboles fall into the unaltered calcic magmatic amphibole fields (Figure 6a). According to the distribution of the points where the (Ca + Na) B values are greater than 1 on the BCa + BNa versus BNa exchange diagram, all of the samples have a calcic composition (Figure 6b). In the distribution of points where CaB is greater than 1.50 and (Na+K)A and CaA values are less than 0.50 in the $Mg/(Mg+Fe+2)$ versus Si exchange diagram, it is observed that most of the amphiboles fall into the Mg-hornblende area, and a small number of points is located at the border of actinolite and chermakite (Figure 6c). The distribution

Table 3- Representative mineral chemistry analysis results of the samples belonging to the studied rock groups.

Sample	Granite			Granodiorite			Quartz Monzonite			Syenite			Gabbro		
	1	*2*	*3*	*1*	*2*	*3*	*1*	*2*	*3*	*1*	*2*	*3*	*1*	*2*	*3*
SiO_2	48.30	49.71	50.97	47.84	46.11	49.38	50.64	51.18	50.23	51.51	51.23	49.49	43.68	50.58	43.41
TiO_2	0.84	0.69	0.55	0.64	1.75	0.57	0.69	0.84	0.94	0.45	0.56	1.06	2.14	0.20	2.18
Al_2O_3	6.36	4.97	4.50	5.91	8.13	5.11	4.05	3.86	4.23	3.27	3.41	4.85	10.33	4.62	11.07
FeO	15.58	14.86	14.26	17.48	15.29	15.95	13.78	13.41	13.95	13.21	12.95	14.18	16.42	15.64	15.14
MgO	14.04	14.81	15.24	13.06	13.97	14.34	15.66	16.06	15.47	16.16	16.17	15.44	12.89	14.5	12.92
CaO	10.80	10.84	10.99	10.75	10.58	10.67	10.71	10.74	10.81	11.57	11.52	11.29	10.94	11.65	10.97
MnO	0.74	0.77	0.81	0.74	0.32	0.71	1.09	1.10	1.06	0.61	0.66	0.66	0.30	0.25	0.30
Na_2O	1.19	0.96	0.74	1.03	1.61	0.93	1.27	1.13	1.19	0.91	1.04	1.40	1.71	0.68	1.82
K_2O	0.44	0.39	0.29	0.46	0.47	0.37	0.34	0.34	0.39	0.25	0.32	0.50	0.59	0.19	0.63
Total	98.41	98.00	98.35	97.90	98.20	98.03	98.22	98.65	98.28	98.87	98.35	98.67	98.99	98.36	98.43
O	23	23	23	23	23	23	23	23	23	23	23	23	23	23	23
Cation	15	15	15	15	15	15	15	15	15	15	15	15	15	15	15
Si	6.99	7.20	7.31	7.03	6.70	7.18	7.32	7.29	7.34	7.45	7.42	7.17	6.33	7.27	6.32
Al^{iv}	1.01	0.80	0.69	0.97	1.30	0.82	0.68	0.71	0.66	0.55	0.58	0.83	1.67	0.73	1.68
Al^{vi}	0.08	0.05	0.07	0.05	0.09	0.05	0.02	0.02	0.03	0	0	0	0.10	0.05	0.22
Ti	0.09	0.08	0.06	0.07	0.19	0.06	0.09	0.10	0.07	0.05	0.06	0.12	0.23	0.02	0.24
Fe^{+2}	1.18	1.23	1.12	1.44	1.09	1.28	1.37	1.39	1.35	1.30	1.33	1.44	1.05	1.19	1.08
Fe^{+3}	0.62	0.44	0.49	0.59	0.61	0.50	0.16	0.14	0.17	0.16	0.12	0.11	0.84	0.61	0.67
Mg	3.03	3.20	3.26	2.86	3.02	3.11	3.37	3.35	3.38	3.48	3.49	3.34	2.78	3.12	2.80
Mn	0.09	0.09	0.10	0.09	0.04	0.09	0.12	0.13	0.13	0	0	0	0.04	0.03	0.04
Ca	1.68	1.68	1.69	1.69	1.65	1.66	1.69	1.68	1.66	1.79	1.79	1.75	1.70	1.79	1.71
Na	0.15	0.10	0.12	0.09	0.16	0.09	0.03	0.03	0.05	0	0.01	0	0.16	0.10	0.15
K	0.08	0.07	0.05	0.09	0.09	0.07	0.07	0.07	0.06	0.05	0.06	0.09	0.11	0.03	0.12
Total	14.99	14.95	14.96	14.96	14.93	14.91	14.91	14.91	14.91	14.84	14.85	14.84	15.01	14.96	15.02
CaB	1.68	1.66	1.68	1.69	1.65	1.66	1.69	1.68	1.66	1.79	1.79	1.75	1.70	1.79	1.71
NaB	0.15	0.14	0.10	0.09	0.16	0.09	0.03	0.03	0.05	0	0.01	0	0.16	0.10	0.15
NaA	0.19	0.14	0.17	0.20	0.30	0.17	0.29	0.30	0.31	0.25	0.29	0.40	0.32	0.09	0.36
KA	0.08	0.14	0.17	0.20	0.30	0.17	0.07	0.07	0.06	0.05	0.06	0.09	0.11	0.03	0.12
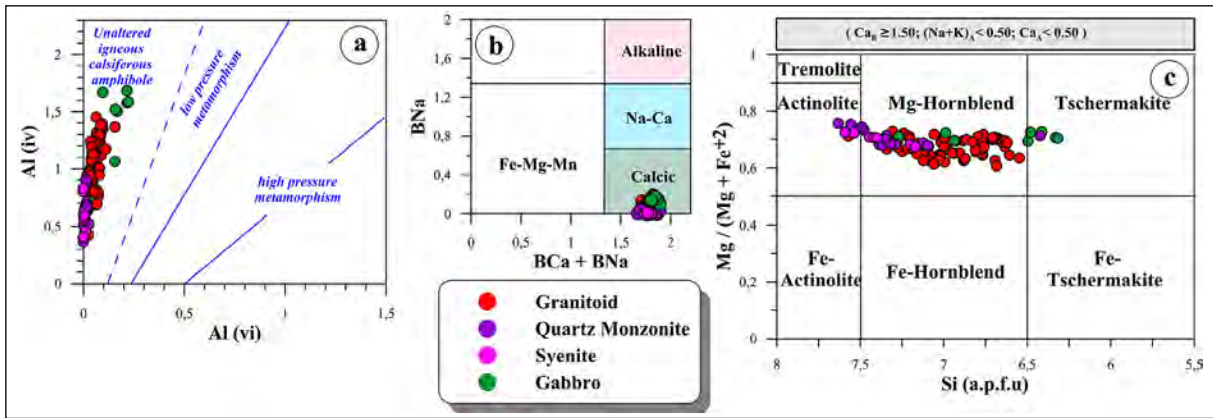
Figure 6- Amphiboles belong to the rock groups in the study area; a) Al^{iv} versus Al^{vi} change (Fleet and Barnett 1978), b) BNa versus BNa + BCa change and c) Species naming of crystals in the Mg/(Mg+Fe+2) versus Si diagram (Leake et al., 1997).

in the aforementioned diagram can be interpreted as the amphibole composition is concentrated in the Mg-hornblende area in samples belonging to rocks where the magma mixing/crust interaction is excessive. Accordingly, it is possible to say that mafic intrusions show homogeneous and less magma mixing effect, while felsic intrusions (granite, granodiorite, quartz monzonite and syenite) show more magma mixing effect.

As suggested by Ridolfi et al. (2010), pressure and temperature calculations were made in amphiboles. Accordingly, it was determined that it crystallizing of amphiboles in granites 0.56-1.19 kbar pressure, 745.25-799.62^{o}C temperature; 0.37-1.28 kbar pressure, 704.07-872.33^{o}C temperature in granodiorites; pressure of 0.42-0.56 kbar, temperature of 738.15-772.79^{o}C in quartz monzonites; pressure range of 0.35-0.63 kbar, temperature range of 738.15-772.79^{o}C in syenites; In the gabbros, the pressure range of 1.82-3.34 kbar and the temperature range of 862.15-919.61^{o}C. Based on thid, it has been theoretically calculated that amphiboles in felsic intrusions crystallize between 3.61 km and 1.88 km on average, and amphiboles in mafic intrusions crystallize at an average depth of 9.97 km (Table 4). It is concluded that felsic intrusive rocks crystallize mostly in the upper crust and have a similar origin in that they come from similar depths. It has been shown that gabroic rocks derived from different sources may have crystallized at deeper depths (9.97 km) compared to granitoids by coming from deeper depths (lower crust-mantle). In addition, it is observed that both the

crystallization temperatures observed in felsic rocks and the excess of overlaps in the pressures of the medium in which they are formed may be due to the mixing of magma.

Table 4- Crystallization conditions and depths of intrusive rocks in the Strandja massif based on the chemical composition of minerals in amphiboles (Ridolfi et al., 2010).

Rock Types		Temperature (T) (C^o)	Pressure (P) (kbar)	Depth (km)
Granite	*min*	745.25	0.56	2.16
	max	799.62	1.19	4.58
	ort	779.74	0.81	3.12
Granodio-rite	*min*	704.07	0.37	1.42
	max	872.33	1.28	4.93
	ort	814.49	0.94	3.61
Syenite	*min*	710.34	0.35	1.34
	max	797.49	0.63	2.42
	ort	761.57	0.51	1.96
Quartz Monzonite	*min*	738.15	0.42	1.61
	max	772.79	0.56	2.15
	ort	757.52	0.49	1.88
Gabbro	*min*	862.15	1.82	7.01
	max	919.61	3.34	12.86
	ort	892.82	2.59	9.97

5. Conclusion

Late Cretaceous aged subduction-related intrusions of in Strandja Massif have been studied in two groups as felsic and mafic intrusions. Felsic intrusions consist of granite, granodiorite, quartz monzonite and syenite, while mafic intrusions consist of diorite and gabbro. Markers of coeval magma mixing processes

are observed in Strandja intrusions with macroscopic and microscopic evidences. Mineral chemistry and Confocal Raman Spectrometry studies were carried out on amphibole crystals, which are common among all rock groups in the Strandja Intrusions, which are the product of magma mixing. According to the results of mineral chemistry of amphiboles, which are hydrous silicate minerals, calcic is Mg-hornblende type. According to P-T-d calculations made in amphibole crystals, felsic intrusions were crystallized under the pressure range of 0.35-1.28 kbar, 704.07-872.33°C temperature, at a depth of about 4.93 km to 1.34 km; mafic intrusions were crystallized at pressure of 1.82-3.34 kbar, at temperature of 862.15-919.61°C and at depth of 7.01-12.86 km. The fact that the felsic intrusions have similar and overlapping conditions both in the thermobarometric conditions of crystallization and in the depths where they crystallize at a higher rate of magma mixing, whereas the mafic intrusions exhibit different thermobarometric relationships and crystallize at different depths, which means that they originate from different sources and exhibit proportionally less magma mixing. In spectroscopic investigation performed with CRS, it was determined that felsic and mafic magma mixing was effective in the formation of amphiboles and that actinolite amphiboles crystallized more. As a result, amphibole minerals in the Strandja Intrusions, As a result, mineralogy, petrography, CRS and EPMA data of amphibole minerals in Strandja Intrusions point to similar petrological results, reflecting that felsic intrusions have similar origins and are formed as a result of magma mixing, whereas mafic intrusions are originated from deeper depth and are less affected by magma mixing.

Acknowledgement

References

Akçe, M. A., Kadıoğlu Y. K. 2020. Raman Spektroskopisinin İlkeleri ve Mineral Tanımlamalarında Kullanılması. Nevşehir Bilim ve Teknoloji Dergisi 9 (2), 99-115.

Apopei, A. I., Buzgar, N. 2010. The Raman study of amphiboles. Analele Stiintifice de Universitatii AI Cuza din Iasi, Section 2. Geologie 56 (1), 57.

Aydın, Ü., Şen, P., Özmen, Ö., Şen, E. 2019. Petrological and geochemical features of Biga Peninsula granitoids, NW Anatolia, Turkey. Bulletin of the Mineral Research and Exploration 160 (160), 81-115.

Aydın, Y. 1974. Etude pétrographique et géochimique de la partie centrale du Massif d'Istranca (Turquie). Thsede Docteur, Universit de Nancy, 131, Ingnieur.

Aydın Y. 1982. Yıldız Dağları (Istranca) Masifi'nin jeolojisi. Doçentlik Tezi, İstanbul Teknik Üniversitesi, 106, İstanbul.

Aydın Y. 1988. Yıldız Dağları Masifi'nin Jeolojisi. Selçuk Üniversitesi Mühendislik Mimarlık Fakültesi Dergisi 2, 61-74.

Aydınçakır, E., Gündüz, R., Yücel, C. 2020. Emplacement conditions of magma (s) forming Jurassic plutonic rocks in Gümüşhane (Eastern Pontides, Turkey). Bulletin of the Mineral Research and Exploration 162 (162), 175-196.

Aykol, A. 1979. Kırklareli Demirköy Sokulumu'nun petroloji ve jeokimyası. Doktora Tezi, İTÜ, Maden Fakültesi, 204.

Aykol, A., Tokel, S. 1991. The geochemistry and tectonic setting of the Demirköy pluton of the Srednogorie–Istranca granitoid chain, NW Turkey. Mineralogical Magazine 55 (379), 249-256.

Bedi, Y., Ulusoy, E., Yusufoğlu H., Boncheva, I., Vasilev, E., Dabovski, C., Sachanski, V., Ivanova, D., Lakova, I. 2022. Istranca Kristalen Kompleksinin Tektonostratigrafik Özellikleri ve Bulgaristan'daki İstiflerle Korelasyonu Sonuç Raporu. Maden Tetkik ve Arama Genel Müdürlüğü, Ankara, 835.

Bodnar, R. J., Frezzotti, M. L. 2020. Microscale chemistry: Raman analysis of fluid and melt inclusions. Elements: an International Magazine of Mineralogy, Geochemistry, and Petrology 16 (2), 93-98.

Candan, O., Akal, C., Koralay, O. E., Okay, A. I., Oberhänsli, R., Prelević, D., Mertz-Kraus, R.

2016. Carboniferous granites on the northern margin of Gondwana, Anatolide-Tauride Block, Turkey–Evidence for southward subduction of Paleotethys. Tectonophysics 683, 349-366.

Catto, S., Cavazza, W., Zattin, M., Okay, A. I. 2018. No significant Alpine tectonic overprint on the Cimmerian Strandja Massif (SE Bulgaria and NW Turkey). International Geology Review, 60(4), 513-529.

Chatalov, G. 1988. Recent developments in the geology of the Strandzha Zone in Bulgaria. Bulletin Technical University of İstanbul, 41, 433-466.

Chukanov, N. V., Vigasina, M. F. 2020. Vibrational (Infrared and Raman) spectra of minerals and related compounds. Springer, Cham, Switzerland, 1-1376.

Çağlayan, M. A., Yurtsever, A. 1998. Burgaz-A3, Edirne-B2 ve B3; Burgaz-A4 ve Kırklareli-B4; Kırklareli-B5 ve B6; Kırklareli-C6 Paftaları, 1:100 000 ölçekli açınsama nitelikli Türkiye jeoloji Haritaları No: 20, 21, 22, 23. Maden Tetkik ve Arama Genel Müdürlüğü, Ankara.

Deniz, K. 2010. Buzlukdağı (Kırşehir) alkali magmatik kayaçların jeolojisi, petrolojisi ve konfokal raman spektrometresi ile incelenmesi. Yüksek Lisans Tezi, Ankara Üniversitesi Fen Bilimleri Enstitüsü Jeoloji Mühendisliği Ana Bilim Dalı, 138.

Deniz, K. 2022. Mica Types as Indication of Magma Nature, Central Anatolia, Turkey. Acta Geologica Sinica-English Edition, 96 (3), 844-857.

Deniz, K., Kadıoğlu, Y.K. 2019. Investigation of feldspar raw material potential of alkali feldspar granites and alkali feldspar syenites within Central Anatolia. Bulletin of the Mineral Research and Exploration 158 (158), 265-289.

Ferrando, S. 2018. Raman spectroscopy in Earth Sciences. GNM-SIMP "Physical Properties of Minerals" School, 12-15 February 2018, Brixen.

Ferraro J. R., Nakamoto, K., Brown, C. W. 2003. Introductory Raman Spectroscopy 2nd Ed. Academic Press. San Diego, 434.

Fleet, M. E., Barnett, R. L. 1978. Al iv/Al vi partitioning in calciferous amphiboles from the Frood Mine, Sudbury, Ontario. The Canadian Mineralogist 16 (4), 527-532.

Frezzotti, M. L., Tecce, F., Casagli, A. 2012. Raman spectroscopy for fluid inclusion analysis. Journal of Geochemical Exploration 112, 1-20.

Güllü, B., Kadıoğlu, Y. K., Koralay, T., Deniz, K. 2019. Raman characteristics of Gucunkaya (Aksaray)

gabbroic rocks, central Anatolia-Turkey. International Multidisciplinary Scientific GeoConference: SGEM, 28.06-07.07.2019, Albena, 475-482.

Kadıoğlu, Y. K., Deniz, K., Korala, T., Güllü, B. 2019. Nature of the gabbro in Central Anatolia: Geological observation and spectroscopic applications, Turkey. International Multidisciplinary Scientific GeoConference: SGEM, 28.06-07.07.2019, Albena, 377-384.

Karacan, M. S. 2020. "Enstrümental Analiz" Ders Notları, Ankara (unpublished).

Karacık, Z., Tüysüz, O., 2010. Petrogenesis of the Late Cretaceous Demirköy Igneous Complex in the NW Turkey Implications for the magma genesis in the Strandja Zone. Lithos, 114 (3-4), 369-384.

Kloprogge, J. T., Case, M. H., Frost, R. L. 2001. Raman microscopic study of the Li amphibole holmquistite, from the Martin Marietta Quarry, Bessemer City, NC, USA. Mineralogical Magazine 65 (6), 775-785.

Kuşcu, İ., Tosdal, R. M., Gençalioğlu-Kuşcu, G. 2019. Episodic porphyry (Cu-Mo-Au) formation and associated magmatic evolution in Turkish Tethyan collage. Ore Geology Reviews 107, 119-154.

Leake, B. E., Woolley, A. R., Arps, C. E., Birch, W. D., Gilbert, M. C., Grice, J. D., Hawthorne, F. C., Kato, A., Kısch, J. H., Krivovichev, G. V., Linthout, K., Laird, J., Mandarino, S. A., Maresch, V. W., Nickel, E. H., Schumacher, C. J., Smith, D. C., Stephenson, N. C. N., Ungaretti, L., Whittaker, E. J. W., Youzhi, G. 1997. Nomenclature of amphiboles; report of the subcommittee on amphiboles of the International Mineralogical Association, Commission on New Minerals and Mineral Names. Mineralogical Magazine, 61 (405), 295-310.

Makreski, P., Jovanovski, G., Gajović, A., Biljan, T., Angelovski, D., Jaćimović, R. 2006. Minerals from Macedonia. XVI. Vibrational spectra of some common appearing pyroxenes and pyroxenoids. Journal of Molecular Structure 788 (1-3), 102-114.

McMillan, P. F., Hofmeister, A. M. 2018. Infrared and Raman spectroscopy. In Spectroscopic Methods in Mineralogy and Geology, 99-160.

Moore, W. J., McKee, E. H., Akıncı, Ö. 1980. Chemistry and chronology of plutonic rocks in the Pontid mountains, northern Turkey. Inc Symposium European Copper Deposits congress 18-22

September, Belgrade, 209-216.

Nasdala, L., Schmidt, C. 2020. Applications of Raman spectroscopy in mineralogy and geochemistry. Elements: an International Magazine of Mineralogy, Geochemistry, and Petrology 16 (2), 99-104.

Natal'in B.A., Satir M., Sunal G., Toraman E. 2005. Structural and metamorfic evolution of the Stradja masif. Türkiye Bilimsel Teknik Araştırma Kurumu, Yer Deniz Atmosfer Bilimleri ve Çevre Araştırma Grubu, Ankara.

Natal'in, B. A., Sunal, G., Gün, E., Wang, B., Zhiqing, Y. 2016. Precambrian to Early Cretaceous rocks of the Strandja Massif (northwestern Turkey): evolution of a long lasting magmatic arc. Canadian Journal of Earth Sciences, 53 (11), 1312-1335.

Ohta, E., Doğan, R., Batık, H., Abe M. 1988. Geology and mineralization of Dereköy porphyry copper deposit, northern thrace, Turkey. Bulletin of the Geological Survey of Japan 39 (2), 115-134.

Okay, A. I., Bozkurt, E., Satır, M., Yiğitbaş, E., Crowley, Q. G., Shang, C. K. 2008. Defining the southern margin of Avalonia in the Pontides: Geochronological data from the Late Proterozoic and Ordovician granitoids from NW Turkey. Tectonophysics, 461 (1-4), 252-264.

Okay, A. I., Satır, M., Tüysüz, O., Akyüz, S., Chen, F. 2001. The tectonics of the Strandja Massif: Late-Variscan and mid-Mesozoic deformation and metamorphism in the northern Aegean. International Journal of Earth Sciences, 90 (2), 217-233.

Okay, A. I., Tüysüz, O. 1999. Tethyan sutures of northern Turkey. Durand, B., Jolivet, L., Horvath, F. Serrane, M. (Ed). The Mediterranean Basins Tertiary Extension within the Alpine Orogene. Geological Society of London, Special Publications 156, 475-515.

Okay A. I., Yurtsever, A. 2006. Trakya Bölgesi litostratigrafi birimleri: Stratigrafi komitesi litostratigrafi birimleri serisi-2. Maden Tetkik ve Arama Genel Müdürlüğü Yayınları, 1-41.

Özdamar, Ş., Roden, M. F., Zou, H., Billor, M. Z., Hames, W., Georgiev, S., Dunkl, I. 2021. Petrogenesis of oligocene plutonic rocks in western Anatolia (NW Turkey): Insights from mineral and rock chemistry, Sr-Nd isotopes, and U-Pb, Ar-Ar and (U-Th)/He geochronology. Geochemistry, 81 (2), 125747.

Petry, R., Mastalerz, R., Zahn, S., Mayerhöfer, T. G., Völksch, G., Viereck-Götte, L., Kreher-Hartmann, B., Holz, L., Lankers, M., Popp, J. 2006. Asbestos mineral analysis by UV Raman and energy-dispersive X-ray spectroscopy. Chemphyschem: a European Journal of Chemical Physics and Physical Chemistry, 7 (2), 414-420.

Raman, C. V., Krishnan, K.S., 1928. The Negative Absorption of Radiation. Nature 122 (3062), 12–13.

Ridolfi, F., Renzulli, A., Puerini, M. 2010. Stability and chemical equilibrium of amphibole in calc-alkaline magmas: an overview, new thermobarometric formulations and application to subduction- related volcanoes. Contributions to Mineralogy Petrology, 160 (1), 45-66.

Rinaudo, C., Belluso, E., Gastaldi, D. J. M. M. 2004. Assessment of the use of Raman spectroscopy for the determination of amphibole asbestos. Mineralogical Magazine, 68 (3), 455-465.

RRUFF (Database of Raman spectra, X-ray diffraction and chemistry data for minerals). http://rruff.info/. 27.02.2021

Skoog D. A., Holler F. J., Nieman T. A. 1998. Principles of Instrumental Analysis. Saunders College Publishing, 849.

Sunal, G., Natal'in, B.A., Satır, M., Toraman E. 2006. Paleozoic magmatic events in the Strandja Massif, in NW Turkey. Geodinamica Acta, 19 (5), 283- 300.

Şengör, A. C., Yılmaz, Y. 1981. Tethyan evolution of Turkey: a plate tectonic approach. Tectonophysics, *75* (3-4), 181-241.

Ulusoy, E. 2012. Demirköy (Kırklareli) intrüzif kayaçlarının jeolojisi ve petrolojisi. Yüksek Lisans Tezi, Ankara Üniversitesi Fen Bilimleri Enstitüsü Jeoloji Mühendisliği Ana Bilim Dalı, 135.

Ulusoy, E. 2021. Istranca Masifindeki Mesozoyik intrüziflerinin tektonomagmatik evrimi, KB Türkiye/Tectonomagmatic evolution of Mesozoic intrusives of Strandja Massif, NW Turkey. Doktora Tezi, Ankara Üniversitesi, Fen Bilimleri Enstitüsü, Jeoloji Mühendisliği Ana Bilim Dalı, 258.

Ulusoy, E., Kadıoğlu, Y. K. 2021. Petrography and geochemical decomposition parameters of crystalline rocks; Demirköy intrusive body (DIB), NW Turkey. Bulletin of the Mineral Research and Exploration 165 (165), 253-365.

Üşümezsoy, Ş. 1990. Istranca orojeni; Karadeniz çevresi Kimmerid orojen kuşakları ve masif sülfit yatakları. Türkiye Jeoloji Bülteni 33 (1), 17-28, Ankara.

Watenphul, A., Burgdorf, M., Schlüter, J., Horn, I., Malcherek, T., Mihailova, B. 2016. Exploring the potential of Raman spectroscopy for crystallochemical analyses of complex hydrous silicates: II. Tourmalines. American Mineralogist, 101 (4), 970-985.

Young, A. T. 1981. Rayleigh scattering. Applied Optics, 20 (4), 533–535.

Zoroğlu, O., Kadıoğlu, Y. K. 2007. Behavior of amphiboles in the determination of magma zoning using confocal Raman spectrometry: Beypazarı Oymaağaç granitoid-Ankara Turkey. In Second International Conference on Geo-Resources in The Middle East and North Africa (GRMENA-2), 24-28 February 2007, Egypt, 110-111.

Bulletin of the Mineral Research and Exploration

http://bulletin.mta.gov.tr

Evaporate salt exploration by two dimensional (2D) seismic reflection method: Ankara-Polatlı region, Türkiye

Recep GÜNEY[a]*, Zeynep Rezzan ÖZERK[a], Erdener IZLADI[a], Salih ERDEN[b], Esra AK[a], Erdi APATAY[a], Erdoğan ERYILMAZ[c], Batuğhan YIKMAZ[c], Sami Aytaç ÖZDEMİR[c], Sermet GÜNDÜZ[a], Tuğçe CAN[a], İmam ÇELİK[d], Abdullah GÜRER[e], Sinem AYKAÇ[a], Muzaffer Özgü ARISOY[a], Esra Burcu KÖSE[a] and Büşra Bihter DEMİRCİ[a]

[a]General Directorate of Mineral Research and Exploration, Department of Geophysical Studies, Ankara, Türkiye
[b]General Directorate of Mineral Research and Exploration, Western Black Sea Regional Directorate, Zonguldak, Türkiye
[c]Turkish Petroleum International Company, Department of Mining and Drilling, Ankara, Türkiye
[d]Çiçekli Mahallesi, Akten Caddesi, 58/8, İncirli, Keçiören, Ankara, Türkiye
[e]Akpınar Mahallesi, 850. Cadde, 10/19, Çankaya, Ankara, Türkiye

Research Article

ABSTRACT

The presence of the evaporate salt zone in Ankara-Polatlı region has been determined by the drillings. It is thought to be the largest reserve in Türkiye. The seismic reflection method was used to determine the top-bottom levels of the region; its depth; its thickness and extent boundaries; the horst-graben structures; base depth and tectonic movements affecting the study area. Data were collected on three seismic lines. The near-surface tomographic velocity sections were compatible with the top-of-the-zone depth observed in the drillings. As a result of the study, the depth and thickness of the top-bottom of the zone were determined along the lines. Within the scope of the study, a combined interpretation was made on the lines by using gravity and seismic data. The extent of the ore zone was determined only in the E-W direction section, but not in the north-south direction lines since they are outside the license area and the seismic lines. The closest point of the evaporate zone to the surface is approximately 150 m, the deepest point is approximately 310 m, the average thickness is approximately 100 m and the maximum thickness is 185 m.

1. Introduction

Evaporate minerals (salts) used in many industrial areas are easily soluble formations. Due to this feature, they do not outcrop under the influence of atmospheric conditions and must be covered with cover layers (clays) in order not to be affected by atmospheric conditions (Kırtıl et al., 2020).

The study area is located in the district of Polatlı, approximately 80 km southwest of Ankara (Figure 1). Evaporates in the study area were determined to deposit in the playa lake complex developed effectively in paleoclimatic conditions, periodic terrestrial volcanism with tectonism, and depositional systems with different lithologies (Güngör, 2005). Sodium sulfate (42.64% grade), polyhalite (23.74%

Corresponding author: Recep GÜNEY, recep.guney@mta.gov.tr

Figure 1- Study area (yellow box) and license area (black line).

grade), and Halite (36.30% grade) mineralization were detected intensively in the drillings carried out in the region between 2017-2019 (Kırtıl et al., 2020).

Although many geological studies are carried out in the license area, geophysical studies; are only limited to regional gravity data and ground electrical study. Geological data indicate that the Evaporite zone was deposited in a lacustrine environment and the tectonic regime of the region was characterized by a series of horst and graben formations; geophysical studies support this information. However, no high-resolution geophysical survey has been carried out in the region.

Determining the depth, thickness, and extent limits of the ore-bearing zone are extremely important for mining operations. Therefore, detailed imaging of the underground is required. The seismic reflection method has been frequently used in investigating evaporitic salt zones (Gendzwill, 1978; Tay et al., 2002; Leveille et al., 2011; Butler et al., 2014; Jones and Davison, 2014; Yamamoto et al., 2017; Protasov et al., 2017).

The aim of this study with the seismic reflection method is to determine the closest point to the earth's

surface, top-bottom levels, depth, thickness, and spreading limits of the evaporate salt zone, as well as the depth of the basement topography of the study area, the horst-graben structures formed throughout the basin and the tectonic movements affecting the study area. In this context, seismic reflection studies were carried out on 3 critical lines determined in the license area, in the light of the prior information available.

2. Geology of the Study Area

The study area is located within the Tethys belt, in the west of Central Anatolia, in the Central Anatolian Plain Regime under the effect of N-S direction stress tectonics according to Şengör (1979). Tertiary and Quaternary volcanism have been very effective in the study area. Most of the volcanic units in the area are related to young plate tectonics that developed from the Eurasian-Arabic plates (Gözler et al., 1996). Arıkan (1975) stated that the Haymana-Polatlı basin extends to the southeast and connects with Salt Lake. In the NW-SE direction in the Polatlı-Haymana Basin, sediments extending from Triassic to Quaternary were observed (Ünalan et al., 1976; Turgay and Kurtuluş,

1985). The study area is covered by Miocene, Pliocene aged volcano-sedimentary, evaporitic, carbonate, clastic units, and young sediments (Gözler et al., 1996). In general, most of the Miocene sediments are covered with Pliocene lacustrine deposits and outcrops in a limited area (west of the study area). It was stated that evaporitic and palustrine deposition on a vertical and lateral scale in a partially closed system in the lake sedimentary deposition had occurred several times, and the thickening in the basin margin sequences was under the control of block faults controlling the geodynamic structure of the basin (Varol et al., 2005).

The geological map and the stratigraphic units of the study area are illustrated in Figure 2 and Figure 3, respectively.

3. Preliminary Studies

Many geological studies have been carried out on the Evaporate salt zone in the study area (Aydoğdu, 2004; Varol et al., 2005; Güngör, 2005; Zeybek, 2007; Kırtıl, 2008). Kırtıl (2008) revealed the deposition phases of the evaporate sequences (Figure 4). The Bouguer gravity data calculated from the variation of the gravitational field studies, measured within
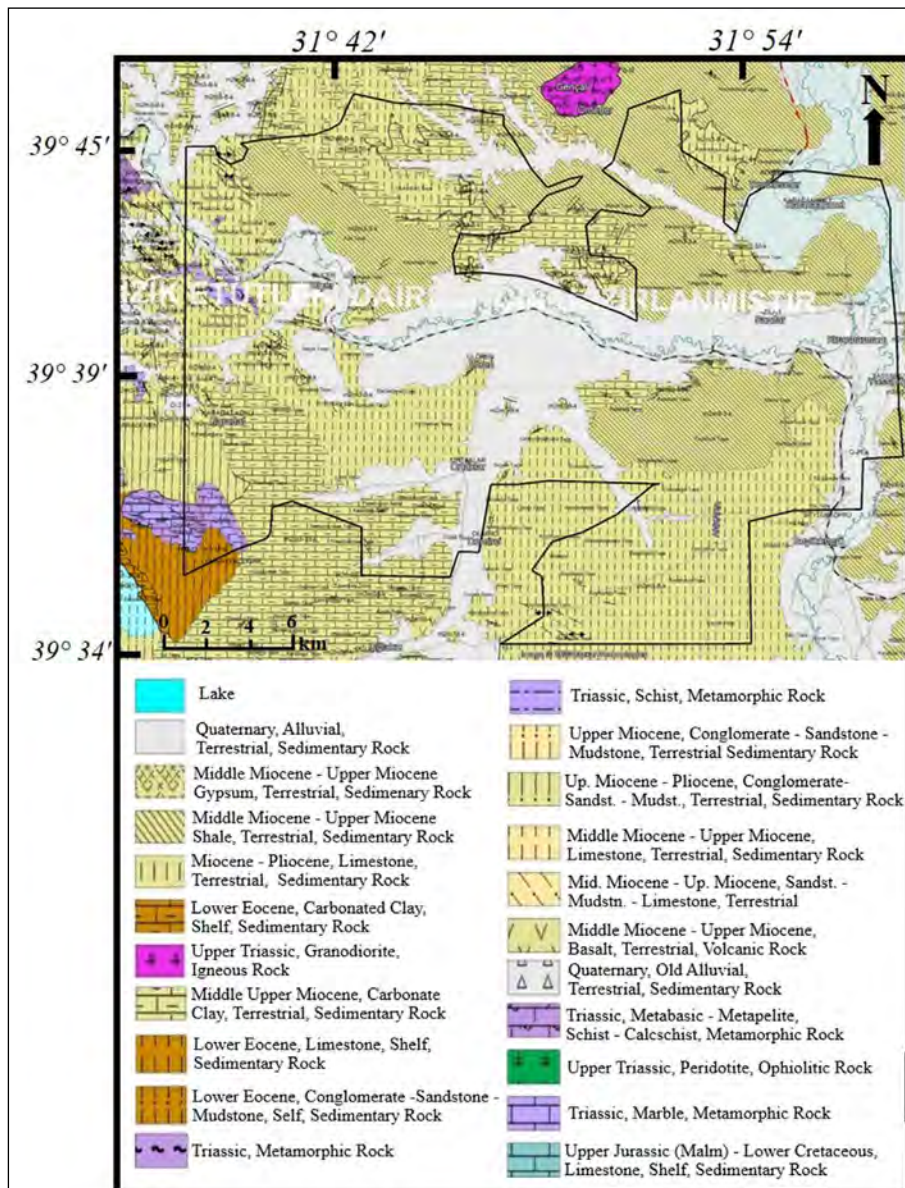
Figure 2- Geological map of the study area (modified from MTA, 2012; Kırtıl et al., 2020).
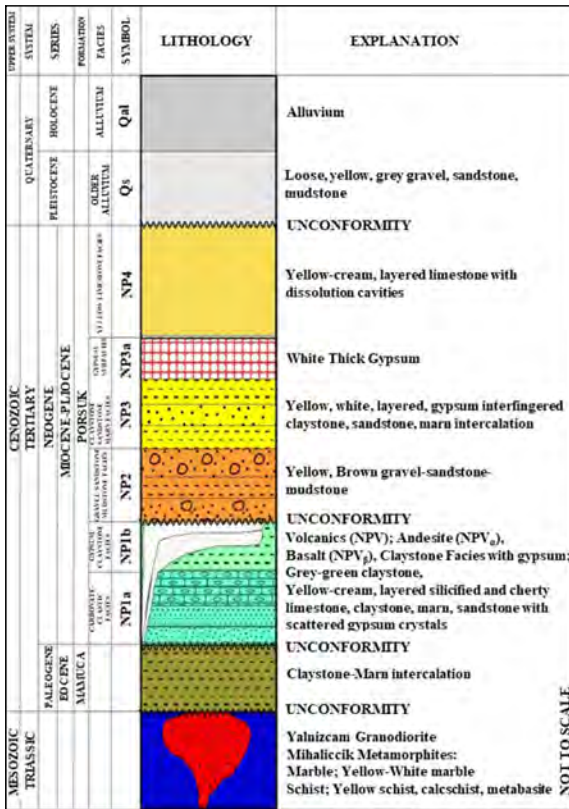
Figure 3- Stratigraphic section of the study area (modified from Gözler et al., 1996; Kırtıl et al., 2020).

the scope of many projects, primarily the Türkiye Geophysical Regional Gravity Maps Project between 1973-2021 by the General Directorate of Mineral Research and Exploration (MTA), can be seen in Figure 5. Türkiye Bouguer gravity dataset have tidal, declination, latitude, free air, topography and Bouguer corrections. The presentation of the gravity data was prepared as 2D profile graphs, interpolated with a sampling interval of 100 m in order to adapt to the geometry of the seismic data and to enable easier visual inspection. In addition, the total horizontal derivative filter, which is widely used in the evaluation of potential field data, was applied to all gravity profile data for the purpose of visualizing near-surface subsurface structures/bodies and discontinuities. Ataman et al. (2019) stated that the basin, in general, is the main graben and that there are many horst and graben structures within the main basin.

4. Data and Methods

Considering the information given above, three seismic lines were designed in the license area. One of the lines is approximately E-W, and the other two are approximately N-S directional lines (Figure 6). The
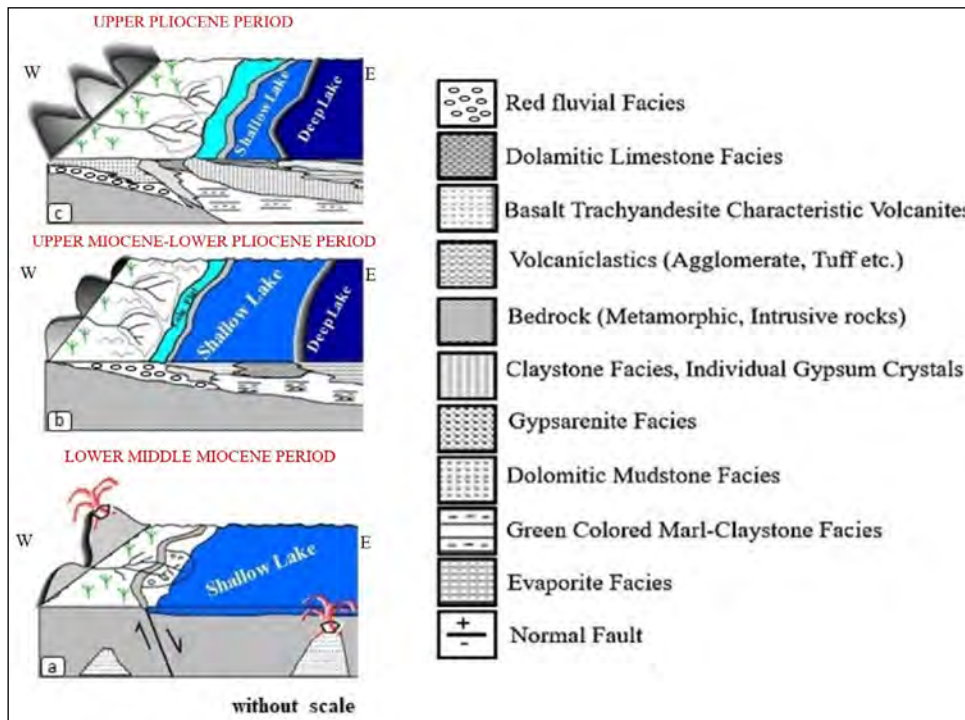
Figure 4- Sedimentation phases of evaporate sequences (Kırtıl, 2008); a) Lower-Middle Miocene, b) Upper Miocene – Lower Pliocene, and c) Upper Pliocene.
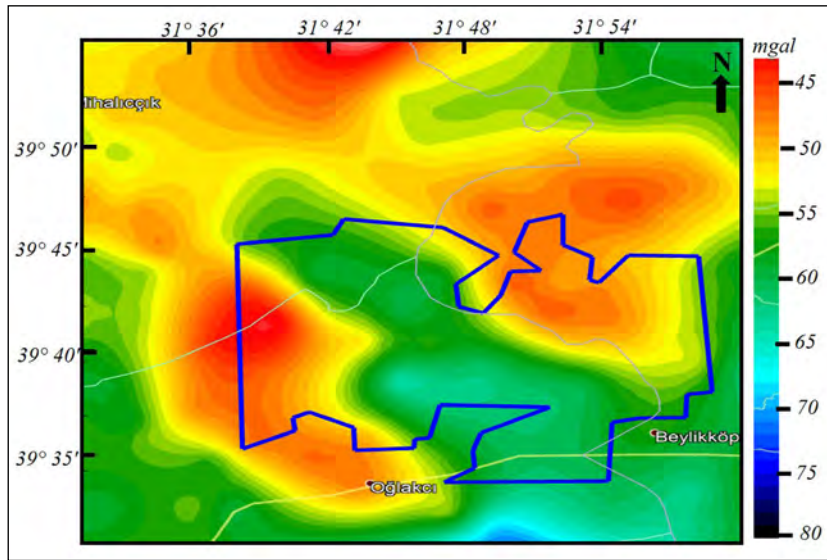
Figure 5- Regional gravity anomaly map of the license area.

purpose of the study, imaging the evaporate salt zone estimated at 20-500 m depth (the primary purpose), and the schist bedrock estimated to be at about 1500 m depth. The seismic studies carried out in this context were tested and carried out with the determined parameters (Özerk et al., 2021).

During the data acquisition, Sercel 428 XL acquisition equipment and two vibro (12000 pounds each) as active seismic energy sources (Mini Vib II) were deployed. Field recording parameters were decided based on the depth target, the purpose of the study, the expected horizontal-vertical resolution, and obtaining high data quality (Table 1). Within the scope of the project, the most ideal seismic sections were attempted to be obtained by processing the data collected in the field (Table 2). ToModel software for
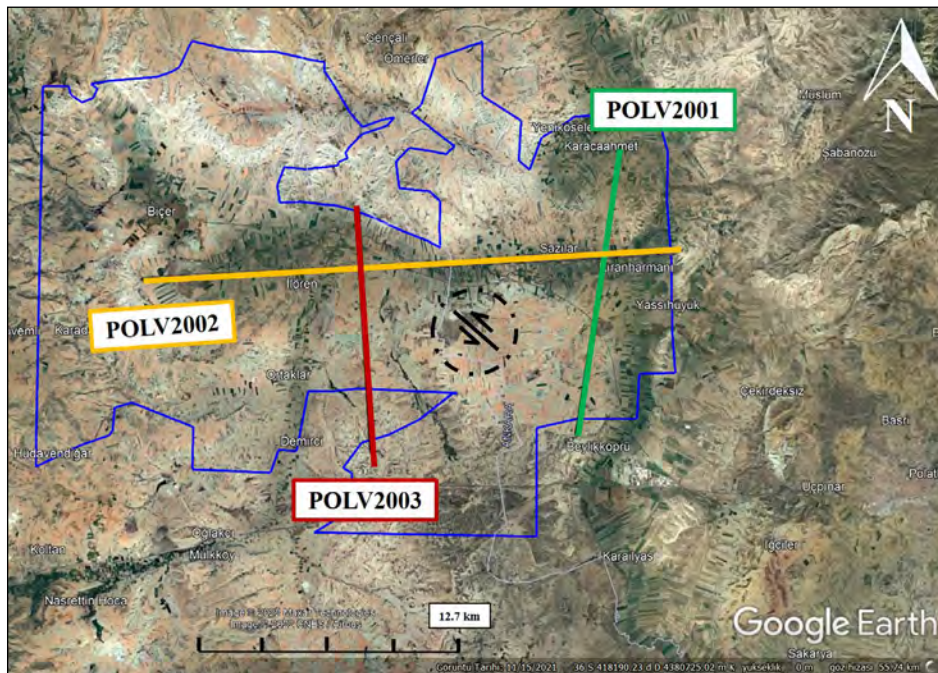
Figure 6- Licensed area, seismic lines, and left-lateral strike-slip fault (black dashed line area, Kandemir and Kanar, 2018).

static correction of seismic data; Disco Focus 5.4 and SeisSpace ProMAX software for data analysis and processing; and Petrel software for data interpretation were used.

Table 1- Acquisition parameters used in seismic reflection study.

Near Offset (m)	5
Far Offset (m)	2495
Live Channel Number	350
Start Frequency (Hz)	12
Stop Frequency (Hz)	126
Number of Vibro	2
Number of Sweep	6
Sweep Time (sn)	14
Sweep Type	Logarithmic -3dB
Taper (ms)	400
Shot Interval (m)	10
Group Interval (m)	10
Receiver Interval (m)	0.9
Spread Type	100-250 (Asymmetric)
Record Length (ms)	4095
Sampling Interval (ms)	1

Table 2- Data processing flowchart.

Data Input
Geometry Definition
Trace Edit/Kill
Static Correction (Datum: 1000 m, Velocity: 1500 m/sn)
True Amplitude Recovery
Ground Roll Attenuation (FK Domain, Coherent Filter)
Predictive Deconvolution (Prediction lag: 36 ms, Operator length: 400 ms)
Bandpass Filter (Cutting Frequencies: 15-50 Hz)
CDP Sort
Velocity Analysis -1 (250 m, 50 CDP)
NMO
Brut Stack-1
Residual Static Correction -1
Velocity Analysis -2 (125 m, 25 CDP)
Brut Stack-2
Residual Static Correction -2
Final Stack (Datum : 1000 m)
FX Migration (15-50 Hz)

5. Research Findings

On the POLV2001 line, 14550 m seismic reflection data were acquired in approximately N-S direction. Near-surface tomographic velocity sections were also created using refractive tomography from the data. Evaporate zone top level - seen in the drillings that were previously made in the region and with a maximum 100 m distance to the seismic line (19/28, 18/103, 18/70, 18/44, 18/47-6, 18/4, 18/19, 18/11, and 18/12) - were marked on the tomographic sections (Figure 7). The levels where the seismic velocity increases in the near-surface tomographic velocity section are consistent with the evaporate salt zone top level. Five different horizons were followed in the seismic time section (Figure 8a). By utilizing nearby drilling data, the uppermost horizon (green) between 450-500 ms was interpreted as claystone-gypsum claystone, the second horizon (turquoise) between 500-600 ms as the top of evaporate salt zone, the third one (blue) between 650-700 ms as claystone-glauberite-gypsum, fourth horizon (dark green) between 900-1000 ms as claystone-siltstone, and the last one (brown) between 1050-1250 ms as basalt. The first three horizons were inspected by the boreholes close to the area. All faults are marked as yellow. Additionally, in the seismic section, the area near the CDP numbered 22200 was interpreted as horst, and the fault near the surface around CDP numbered 20675 was interpreted as a thrust fault. Since the region is in the extensional regime, it may be interesting to see the thrust fault. This thrust fault is most likely associated with the strike-slip fault in the region (Figure 6). According to the regional Bouguer gravity data, a soft rise is observed in the Bouguer gravity amplitudes (Figure 8b) from south to north depending on the topography for the POLV2001 line that cuts through the basin in S-N direction from the eastern border. Especially deep faults drawn on the interpreted seismic section are clearly observed in the gravity total horizontal derivative graph (Figure 8c).

On the POLV2002 line, approximately 26510 m of seismic reflection data in the E-W direction was acquired. A refractive tomographic section of the data was created (Figure 9). In the tomography section, a deformation thought to be due to fracture is observed between approximately 18000-22000 m. By utilizing nearby drilling data (20/02, 20/20, 19/18,
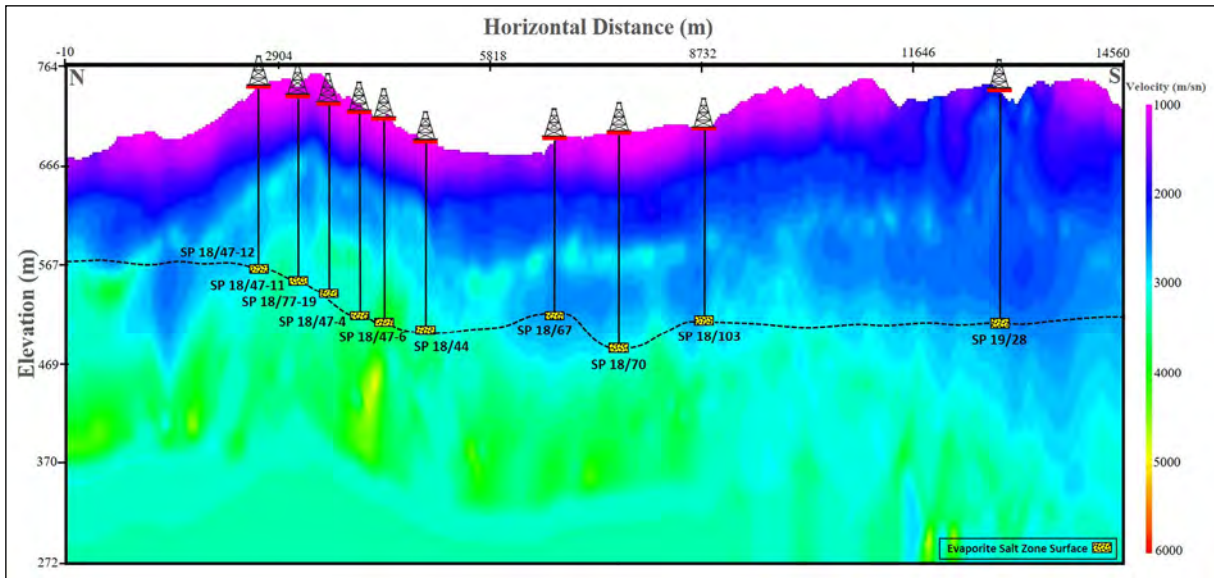
Figure 7- Near surface tomographic velocity section of POLV2001 line and the elevation to the top of evaporate salt zone obtained from the boreholes close to the line.
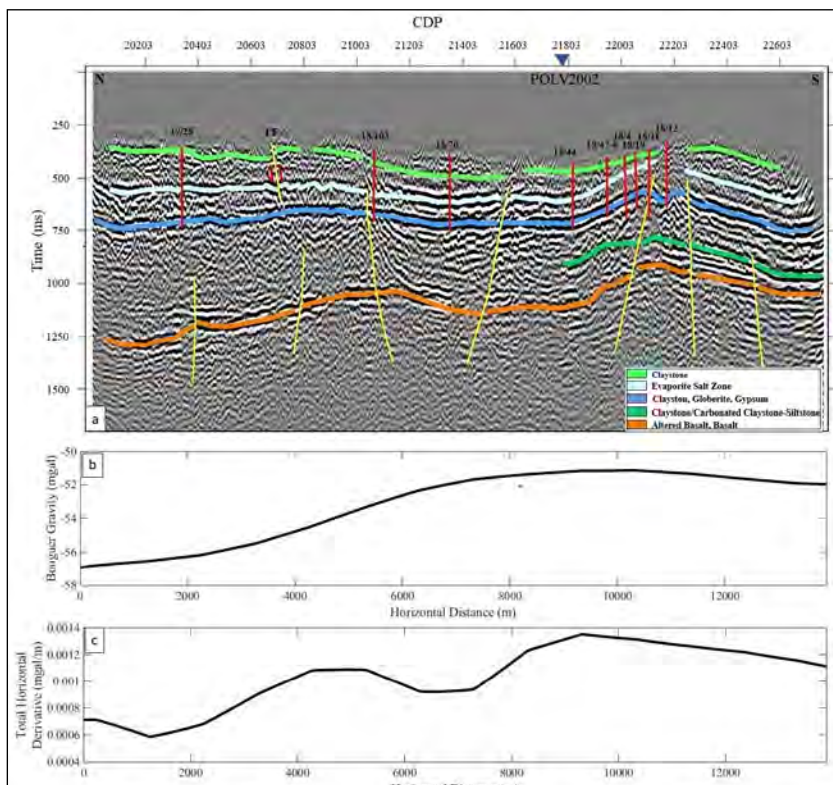
Figure 8- a) Interpreted seismic time section of the POLV2001 line, boreholes (red) and numbers of boreholes, faults (yellow), and interpreted horizons in the area, b) Bouguer gravity graph and c) total horizontal derivative graph.

19/125, 19/118, 18/143, 18/90, 18/89, 18/86, 19/138, 19/151, 19/123, 19/153, 19/141, 18/47-3, 18/44), six horizons could be followed in the seismic time section (Figure 10a). Seismic reflection horizons which are the uppermost horizon (green) as claystone-gypsum claystone, the second horizon (turquoise) as the evaporate salt zone, and the third horizon (blue) as claystone were interpreted. The fourth horizon (dark
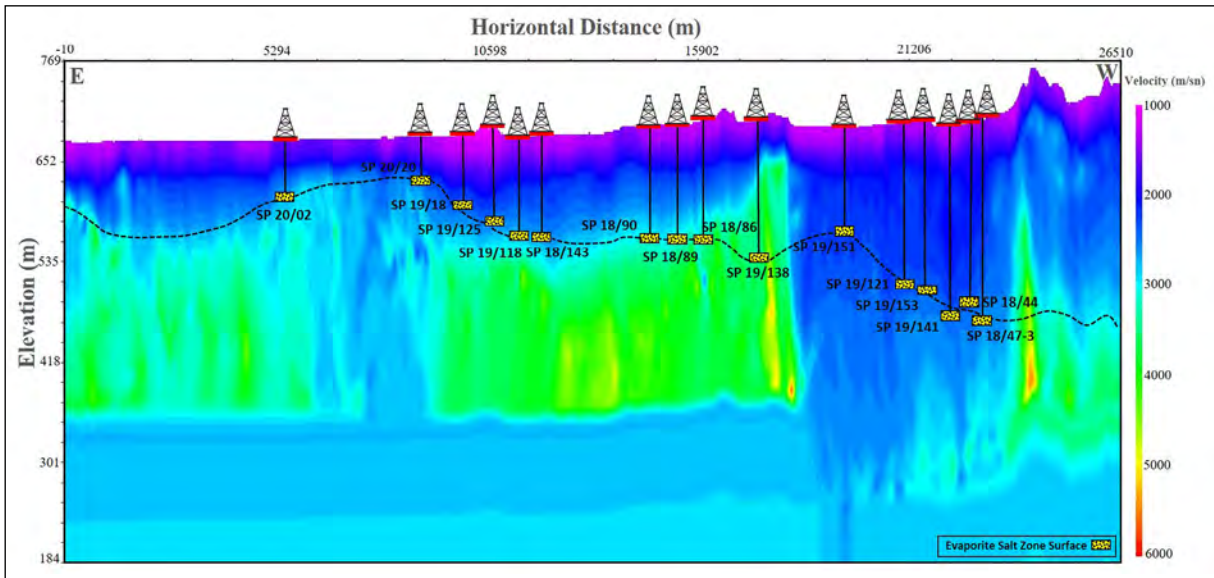
Figure 9- Near surface tomographic velocity section of POLV2002 line and the elevation to the top of evaporate salt zone obtained from the boreholes close to the line.
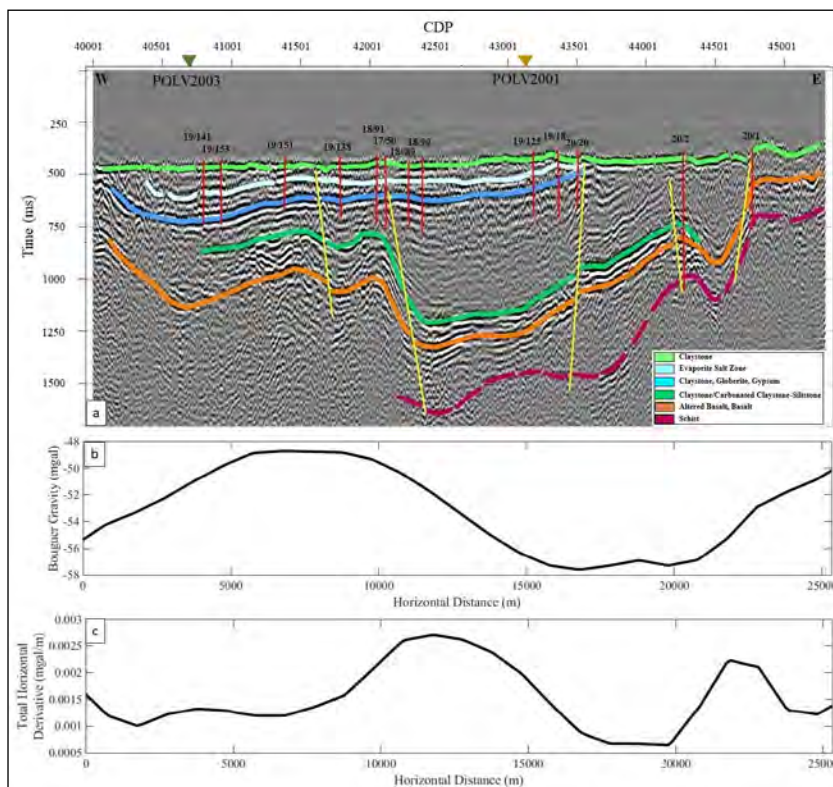
Figure 10- a) Interpreted seismic time section of the POLV2002 line, boreholes (red) and numbers of boreholes, faults (yellow), interpreted horizons in the area, b) Bouguer gravity graph and c) total horizontal derivative graph.

green) was interpreted as claystone-siltstone, the fifth one (brown) as basalt, and the last one (purple) as metamorphic basement schist. It is seen that the extensional boundaries of the evaporate salt zone

continue for approximately 18000 m (CDP numbered 43600) from the beginning of the line (CDP numbered 40000). Evaporate salt was not seen in the boreholes numbered 20/1 and 20/2. Faults defining the basin

structure are shown in the seismic section. Moreover, horst structures were observed around CDP numbers 42100 and 44200. In the Bouguer gravity profile graph presented in Figure 10b for the POLV2002 line that intersects the basin in the E-W direction, it has been interpreted that the basin boundaries may be between 10-23 km of the line horizontally from east to west. The faults observed in the interpreted seismic section (Figure 10a) can also be observed in the Bouguer gravity profile graph (Figure 10b). However, this situation can be controlled much more clearly in the total horizontal derivative profile curve given in Figure 10c.

On the POLV2003 line, 12020 m of seismic reflection data were collected in the approximately N-S direction. In the tomographic velocity section (Figure 11), although the resolution is poor in the southern part of the line, it is seen that the top of evaporate salt zone matches the high-velocity zone in the northern part of the line. By utilizing nearby drilling data (17/129, 20/18, 19/36, 20/48, 19/69, 20/49, 19/82, 19/41, 19/35), six levels are interpreted in the seismic time section (Figure 12a). Although the first three levels are interrupted in some parts, they can be followed throughout the line. The uppermost

seismic reflection horizon (green) was interpreted as claystone-gypsum claystone, the second horizon (turquoise) as the evaporate salt zone, the third horizon (blue) as claystone, the fourth horizon (dark green) as claystone-siltstone, the fifth one (brown) as basalt and the last one (purple) as metamorphic basement schist. Approximately 61100 CDP area of the line has been interpreted as horst. In the Bouguer gravity profile graph presented in Figure 12b for the POLV2003 line, which intersects the basin almost from the middle of it approximately in the N-S direction, it is observed that the amplitude values from north to south decrease towards the middle of the basin and then increase towards the southern border of the basin. As expected, the total horizontal derivative method (Figure 12c) showed signs of sudden changes in gravity values and it was seen that these symptoms were caused by faults as in the other two profiles.

The level interpreted as metamorphic basement schist was not observed in the POLV2001 line. The basalt level monitored continuously in all seismic sections could be partially observed in the POLV2001 line. The schist level, traced in POLV2002 and POLV2003 seismic sections, has been correlated utilizing the lithology information of boreholes 20/1
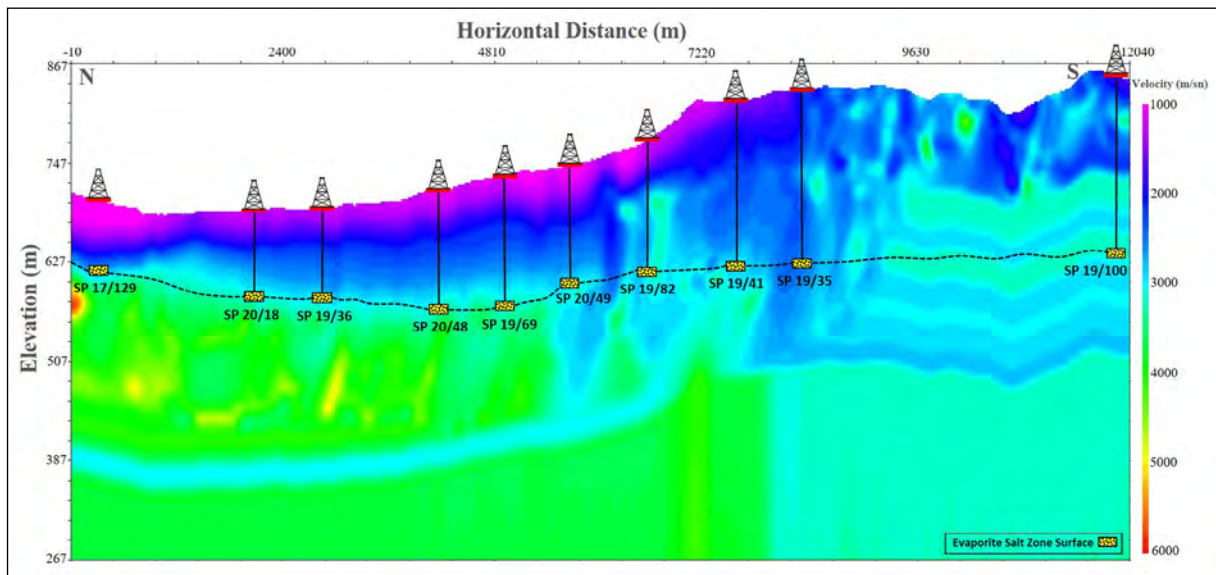
Figure 11- Near surface tomographic velocity section of POLV2003 line and the elevation to the top of evaporate salt zone obtained from the boreholes close to the line.
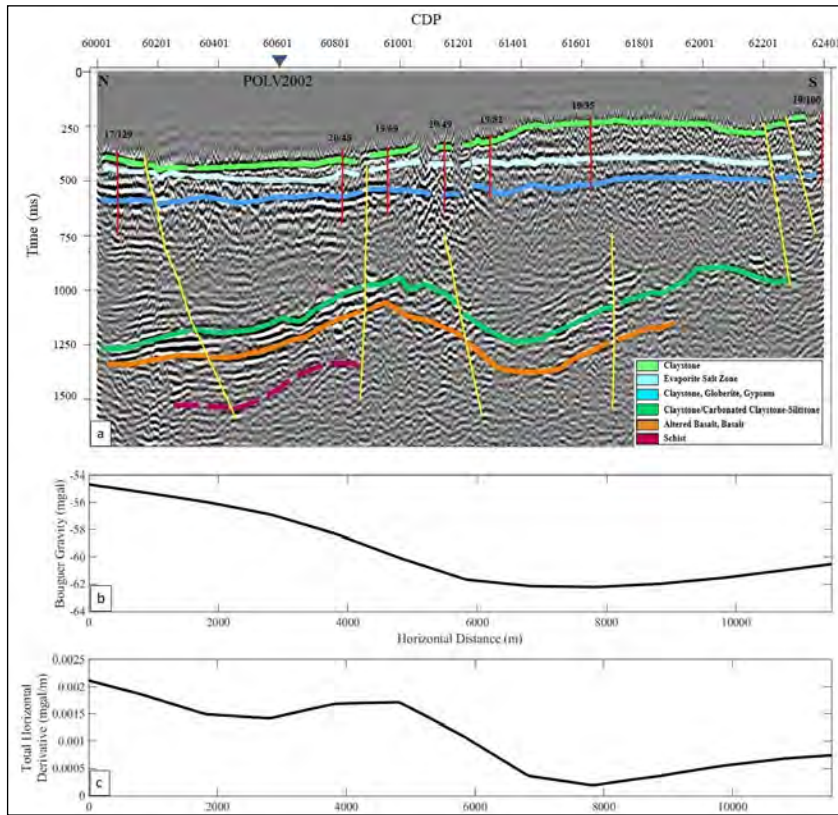
Figure 12- a) Interpreted seismic time section of the POLV2003 line, boreholes (red) and numbers of boreholes, faults (yellow), and interpreted horizons in the area, b) Bouguer gravity graph and c) total horizontal derivative graph.

and 20/2 (Figure 10). Figure 13 shows the 3D views of the tomographic velocity sections and the seismic time sections.

6. Discussion

The evaporate salt zone, located in the tectonically not very complex region, was deposited in a lacustrine environment. It is known that the seismic reflection method produces good results in such sedimentary basins. Such basins, where the geological layers can be observed clearly, can be illuminated by seismic reflection studies and fewer drilling data.

Evaporate salt zone, which is extensive in the study area, was attempted to illuminate with three seismic lines. Evaporate salt zone was visualized along the seismic lines, but the extent limit of the salt zone could not be determined in the N-S directional lines as the ore zone across the license area.

In the near-surface velocity models obtained by refraction tomography, it is seen that the approximate
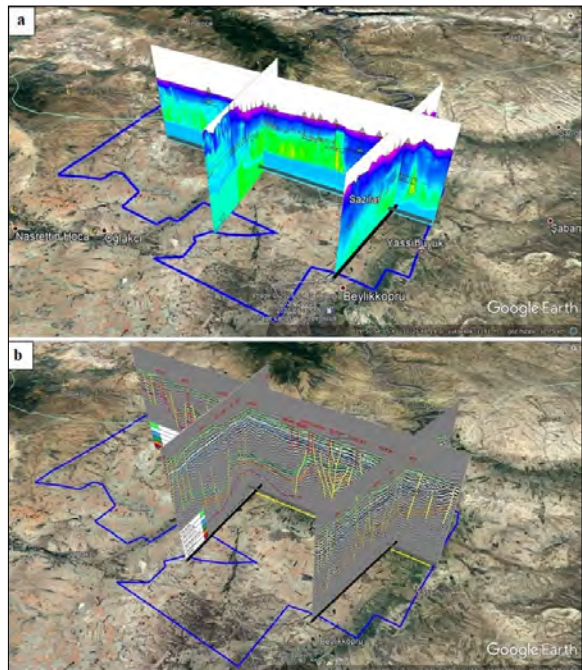
Figure 13- a) The 3D view of the near-surface tomographic velocity sections and b) the 3D view of the interpreted seismic time sections.

velocity of the evaporate salt zone is 3500 m/s and it is compatible with the depth of the evaporate zone determined in the boreholes close to the study area. However, discontinuities are observed in the tomographic velocity sections in some parts because of disruption at the arrivals of refracted data resulting in inconsistencies during the tomographic inversion.

The low-density anomaly seen in the gravity map of the region (Figure 5) supports the presence of salt in the basin. It is seen that especially the 2D total horizontal derivative data derived from the Bouguer gravity map show quite compatible changes with the faults observed in the seismic section. Thus, both methods inspected and supported each other.

Seismic lines remain within the main graben and there are many fracture lines. In addition, there are horst-graben structures in the basin (Ataman et al., 2019). Around CDP number 22200 of the POLV2001 line, around CDP number 42100 and 44200 of the POLV2002 line, and around CDP point 61100 of the POLV2003 line were evaluated as horst structures in the basin.

On the POLV2001 line, there is a thrust around the CDP number 20675 (Figure 10). Considering that the study area was formed by an extension in the horst-graben system, the presence of a thrust fault in the region is extremely interesting. Moreover, there is a left-lateral strike-slip fault in the geological map of the region (Figure 2). It is thought that the mentioned fault may have a reverse component at the point where it intersects the POLV2001 line. Since there are not many earthquakes in the region, no focal mechanism solution has been reached. So previous geological and geophysical studies have predicted that there are horst-graben systems in the basin. However, the horst-graben system was imaged as high resolution with seismic reflection study.

7. Results

In this widely spread sedimentary basin in which many drilling study have been carried out, seismic reflection studies were conducted only along three lines and a total of 53080 m of geophysical seismic reflection data were collected. Near-surface tomographic velocity models were produced and found to be consistent with the top depth of the evaporate salt zone. The schist level, which is the metamorphic basement rock (locally in POLV2002 and POLV2003 lines); and the depth of the Evaporate salt zone in the three seismic lines were determined. The evaporate salt zone thickness and depth were presented with the help of these seismic lines and the drilling data previously obtained in the field. However, the extent limit of the salt zone could only be determined on the POLV2002 line in the E-W direction. On the lines in the N-S direction (POLV2001 and POLV2003), the evaporate salt zone exceeds the license area.

By utilizing previously obtained drilling data in the field, on the POLV2001 seismic line, there are 5 interpreted horizons: claystone-gypsum claystone, evaporate salt zone, claystone-glauberite-gypsum, claystone-siltstone (partly), and basalt. The seismic line remained within the Evaporate salt zone and its boundaries could not be determined. And one of the faults on the line was interpreted as a thrust fault. On the POLV2002 seismic line, there are 6 interpreted horizons: claystone-gypsum claystone, evaporate salt zone, claystone-glauberite-gypsum, claystone-siltstone, basalt, metamorphic basement schist (partly). On this line, the western and eastern boundaries of the evaporate salt zone could be determined. On the POLV2003 seismic line, there are 6 interpreted horizons: claystone-gypsum claystone, evaporate salt zone, claystone-glauberite-gypsum, claystone-siltstone, basalt (partly), metamorphic basement schist (in a very short space). The seismic line remained within the evaporate salt zone like the POLV2001 seismic line and its boundaries could not be determined.

According to the interpreted seismic lines, the ore thickens towards the north and the thickest point (approximately 185 m) is the beginning of the POLV2001 line. Based on seismic lines, the average thickness of the ore is around 100 m. The points where the ore is closest (approximately 150 m) to the surface are on the POLV2002 line. The furthest point of the ore from the surface is about 310 m.

In addition, the basement topography and faults seen in the seismic section were inspected with the 2D Bouguer gravity and total horizontal derivative graphs derived from Bouguer gravity maps. In particular,

the changes in the total horizontal derivative graphs fit very well with the faults and basement topography interpreted in the seismic sections.

The fault, marked at the CDP point approximately 20675 of the POLV2001 section and cuts the first two levels, was evaluated as a thrust fault. In such large basins, it would be beneficial to design narrow more seismic profiles so that the interpretation of geological structures and the fault correlation with each other could be more accurate. Planning of more efficient and beneficial drilling with detailed seismic reflection studies is an important step for underground illumination.

Acknowledgements

References

Arıkan, Y. 1975. The geology and petroleum prospects of the Tuz Gölü basin. Bulletin of the Mineral Research and Exploration 85, 17-37.

Ataman, O., Duman, Ö., Gülşen, H. 2019. Orta Anadolu Tersiyer Havzaları endüstriyel tuz aramaları projesi Ankara ili Polatlı ilçesi (Ömerler-Sazılar-Kıranharmanı) ruhsat sahaları jeofizik özdirenç etüt raporu. General Directorate of Mineral Research and Exploration, Ankara (unpublished).

Aydoğdu, M. N. 2004. The Sedimentology of the Upper miocene age of evaporitic units around Oğlakçı and Demirci villages (NE Sivrihisar). Master Thesis, Ankara University, Graduate School of Natural and Applied Sciences, Ankara (unpublished).

Butler, R. W. H., Maniscalco, R., Sturiale, G., Grasso, M. 2014. Stratigraphic variations control deformation patterns in Evaporite basins: Messinian examples, onshore and offshore Sicily (Italy). Journal of the Geological Society 172, 113–124.

Gendzwill, D. J. 1978. Winnipegosis Mounds and Prairie evaporite formation of Saskatchewan-seismic study. The American Association of Petroleum Geologists Bulletin 62(1), 73-86.

Gözler, M. Z., Cevher, F., Ergül, E., Asutay, H. J. 1996. Orta Sakarya ve güneyinin jeolojisi. Mineral Research and Exploration, Report No: 9973, Ankara, Turkey.

Güngör, P. 2005. Geochemistry and origin of evaporites in the Demirci village around (NE Sivrihisar). Master Thesis, Ankara University, Graduate School of Natural and Applied Sciences, Ankara (unpublished).

Jones, I. F., Davison, I. 2014. Seismic imaging in and around salt bodies. Interpretation 2, SL1-SL20.

Kandemir, Ö., Kanar, F. 2018. Türkiye jeoloji haritaları serisi: Ankara i-27 Paftası, No: 27. General Directorate of Mineral Research and Exploration of Turkey, Ankara.

Kırtıl, M. 2008. Sedimentology of evaporite units in neogene age near aronud Sazak and Biçer villages. Master Thesis, Ankara University, Graduate School of Natural and Applied Sciences, Ankara (unpublished).

Kırtıl, M., Kocaherzen, A., Kırbaş, H., Yılmaz, M., Işık, A. E., Ergun, Z. 2020. Ankara-Polatlı yöresindeki S:201700027 (Er: 3351092) No'lu IV. grup ruhsat sahasının buluculuğa ait maden jeolojisi ve kaynak tahmini raporu, sodyum sülfat (tenardit, globerit)-polihalit-halit. General Directorate of Mineral Research and Exploration of Turkey, Ankara (unpublished).

Leveille, J. P., Jones, I. F., Zhou, Z. Z., Wang, B., Liu, F. 2011. Subsalt imaging for exploration production and development: A review. Geophysics 76(5), 1SO-Z122.

MTA. 2012. 1/25000 ölçekli Türkiye jeoloji haritası, i27 paftası. General Directorate of Mineral Research and Exploration, Ankara.

Özerk, R. Z., Güney, R., Aykaç, S., Izladı, E., Köse, E. B., Erden, S., Ak, E., Can, T., Gündüz, S., Apatay, E., Demirci, B. B. 2021. Orta Anadolu Tersiyer Havzaları globerit ve tenardit aramaları projesi Ankara-Eskişehir 2020 yılı jeofizik sismik

yansıma etüdü raporu. General Directorate of Mineral Research and Exploration, Ankara.

Protasov, M., Kolyukhin, D., Rostomyan, S., Landa, E. 2017. Subsalt imaging in the presence of saltbody uncertainty. The Leading Edge 36(2), 110-192.

Şengör, A. M. C. 1979. The North Anatolian Transform Fault: its age, offset, and tectonic significance. Journal of the Geological Society of London 136, 269-282.

Tay, P. L., Lonergan, L., Warner, M., Jones, K. A. 2002. Seismic investigation of thick evaporite deposits on the central and inner unit of the Mediterranean Ridge accretionary complex. Marine Geology 186(1–2, 5), 167-194.

Turgay, M. I., Kurtuluş, C. 1985. Seismic reflection studies in Polatlı region, Turkey. Bulletin of the Mineral Research and Exploration 103-104, 45 - 55.

Ünalan, G., Yüksel, V., Tekeli, T., Gönenç, O., Seyirt, Z., Hüseyin, S. 1976. The stratigraphy and paleogeographical evolution of the Upper Cretaceous-Lower Tertiary sediments in the Haymana-Polatlı region (SW of Ankara). Bulletin of the Geological Society of Turkey 19, 159-176.

Varol, B., Tekin, E., Ayyıldız, T., Karakaş, Z. 2005. Sedimentology of Lacustrine Neogene evaporitic deposits of Polatlı-Sivrihisar Basin (Central Anatolian Basin). 58th Geological Congress of Turkey, 113-117, Ankara.

Yamamoto, T., Maul, A., Martini, A., Born, A., Gonzalez, M. 2017. Evaporitic section characterization using inversion and Bayesian classification. Society of Exploration Geophysicist, Global Meeting Abstracts 17-22.

Zeybek, B. 2007. Geochemical studies of Porsuk Formation (Pliocene) Evaporites, Middle Sakarya Region, Central Anatolia, Turkey. Master Thesis, Ankara University, Graduate School of Natural and Applied Sciences, Ankara.

Bulletin of the Mineral Research and Exploration

Determination of the coal-bearing zones and the alteration zones containing uranium ore by using two dimensional (2D) seismic reflection method in Thrace Basin

Sinem AYKAÇ[a]*[iD], Abdullah GÜRER[b][iD], İmam ÇELİK[c][iD], Batuğhan YIKMAZ[d][iD], Erdoğan ERYILMAZ[d][iD], Erdi APATAY[a][iD], Sami Aytaç ÖZDEMİR[d][iD], Sermet GÜNDÜZ[e][iD], Tuğçe CAN[a][iD], Esra AK[a][iD], Erdener IZLADI[a][iD], Salih ERDEN[f][iD], Zeynep Rezzan ÖZERK[a][iD], Recep GÜNEY[a][iD], Esra Burcu KÖSE[a][iD] and Büşra Bihter DEMİRCİ[a][iD]

[a]*General Directorate of Mineral Research and Exploration, Department of Geophysical Studies, Ankara, Türkiye*
[b]*Akpınar Neighborhood, 850. Street, 10/19, Çankaya, Ankara, Türkiye*
[c]*Çiçekli Neighborhood, Akten Street, 58/8, İncirli, Keçiören, Ankara, Türkiye*
[d]*Turkish Petroleum International Company, Ankara, Türkiye*
[e]*General Directorate of Mineral Research and Exploration, Directorate of Aegean Regional, İzmir, Türkiye*
[f]*General Directorate of Mineral Research and Exploration, Western Black Sea Regional Directorate, Zonguldak, Türkiye*

Research Article

ABSTRACT

It is aimed to reveal the basement topography, the coal-bearing levels, the alteration zones containing uranium ore, and the tectonic structure prevailing by using two dimensional (2D) seismic reflection method in the Thrace Paleogene-Neogene Basin. In this context, seismic data collected on the six profiles were interpreted by correlating with the data of 97 wells. In the seismic lines, respectively, the metamorphic basement-Eocene boundary, the top of the coal-bearing zone and the boundary of the Danişmen-Ergene formations were confirmed by using the borehole data. By evaluating seismic data, the coal propagation is modeled with three dimensional (3D) figures. Moreover, coal accumulation starts from the southwest of the field and continues towards the northeast, and it is supported by the results obtained from the borehole data. The presence of uranium ore in some of the alteration zones and borehole data indicated that all alteration zones determined should be inspected for uranium ore. In addition to normal and reverse faults, positive and negative flower structures formed in the strike-slip fault zones were determined, and lignite deposits were cut in the flank of these structures. Finally, it is recommended to carry out seismic studies before drilling, to investigate potential coal and uranium areas and to plan more seismic lines.

1. Introduction

The Thrace Basin is a Paleogene-Neogene Basin bounded by the metamorphic Rhodope Massif within the borders of Greece and Bulgaria in the west, the Strandja Massif consisting of metamorphic-granitic rocks in the north within the borders of Bulgaria and Türkiye, the Marmara Sea in the south and the İstanbul Zone in the east. The Thrace Basin located within these geographical boundaries lies across Greece to the west, Saros Bay to the southwest and the Aegean Sea. Paleozoic and Mesozoic aged metamorphic and

Corresponding author: Sinem AYKAÇ, sinem.aykac@mta.gov.tr

magmatic rocks constitute the base of the Thrace Basin. The basement rocks in the basin are seen in the Strandja Mountains in the north, in the Rhodope Massif in the west, in the North Anatolian Fault Zone and Sakarya Continent in the south, and around the Bosphorus in the east (Sezen and Taşkıran, 2020).

Strandja is located in the north of the Thrace Basin, the Rhodope Massif in the west, and the Sakarya continent in the south. The Strandja Massif is represented by gneissic rocks at the bottom and metamorphosed Paleozoic Mesozoic aged sedimentary rocks in greenschist facies above them (Üşümezsoy, 1982; Taner and Çağatay, 1983; Çağlayan and Yurtsever, 1998). Sedimentary rocks were cut by Late Cretaceous granitoid rocks and partly covered by a Late Cretaceous volcano-sedimentary unit (Taner and Çağatay, 1983). Metagranitic rocks are outcropped on the southern slope of the Strandja Massif (Öztunalı and Üşümezsoy, 1979). In the north of the Thrace Basin, lignites are generally located on the southern slopes of the Strandja Massif. The lignites outcropping in the north and south of the basin gradually deepen towards the middle of the basin and are located at depths exceeding 600 meters in a sedimentary sequence that reaches approximately

10 km in the middle parts of the basin. . In the Northern Thrace region, a lobata type delta formation with fluvial dominant characteristics was detected in the Middle Eocene (Sonel and Büyükutku, 1998). With the regression that occurred in the basin, completely deltaic and lacustrine conditions were formed in the Oligocene. Coals of the Thrace Basin are also included in the units deposited in these environments. The high sedimentation rate caused the sediment thickness to be high but made the correlation of coal seams difficult (Şengüler, 2010). However, coal exploration, production, and development activities continue in the region. Kangal et al. (2018) produced high-calorie (5036 Kcal/kg) clean coal from fine coal processing 14.3% amount in a coal preparation plant in the region.

As a result of the drillings carried out by the General Directorate of Mineral Research and Exploration in the Thrace Basin, it was determined that uranium mineralization took place in the Süloğlu formation. As a result of the evaluations made about the mineralization in the study area, igneous rocks with acidic character are thought to be the source rocks of uranium. The uranium ore in these rocks is transported in solution under suitable conditions and stored in sedimentary environments (Sezen and Taşkıran, 2020; Figure 1).
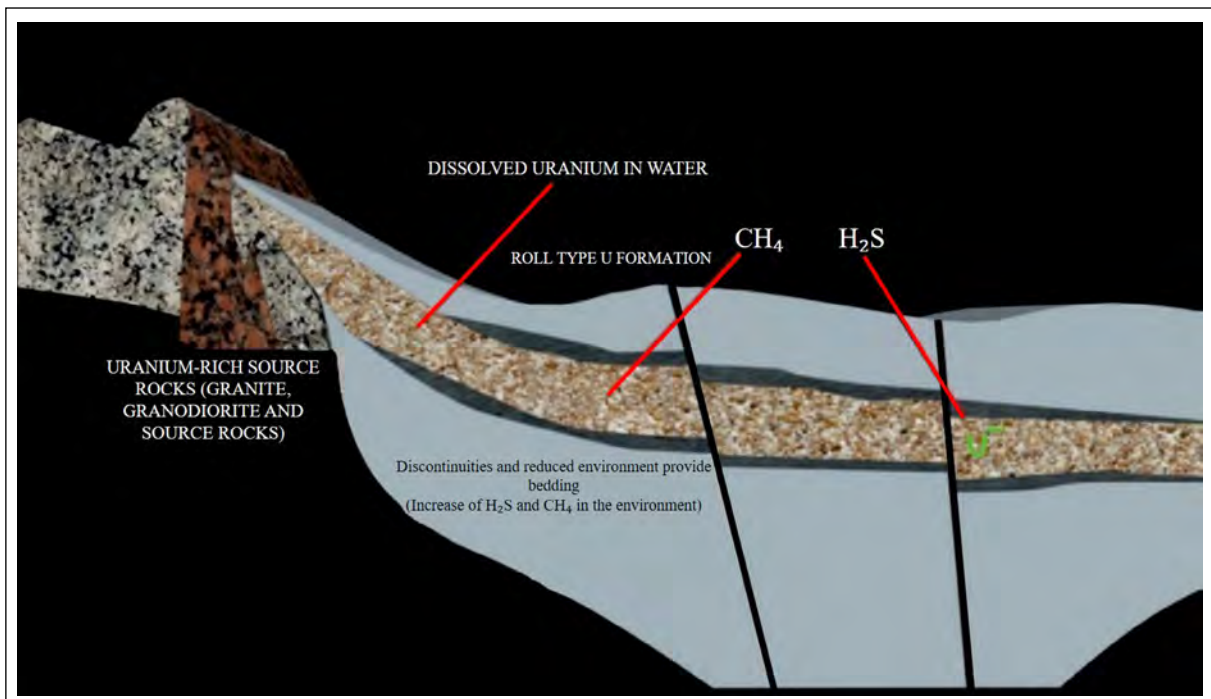
Figure 1- The general conceptual model of uranium mineralization in the study area (Sezen and Taşkıran, 2020).

Considering the study site, the necessary conditions for uranium formation have been shown below:

i) Source rock: There are granitoids and similar depth rocks rich in radioactive elements (uranium, thorium, etc.) in the Strandja Massif.

ii) Transport: Paleo-current channels extending from the Strandja Massif to the Thrace sedimentary basin carry out the transport of radioactive minerals (uranium, thorium, etc.) dissolved in water.

iii) Subsidence: Based on the assumption that alteration zones are formed as a result of tectonic movements affecting the site, oxidation-reduction takes place in these zones, and the organic materials required for chemical reaction are supplied from the lignite layers, it is thought that the uranium in solution in the alteration zone precipitated into the sandstones, which is the reservoir rock in the field.

iv) Cap rock: The lithological required system for the storage of uranium is the alternation of permeable layers (sandstone) with non-permeable (claystone) layers. Sandstone-claystone alternation can be given as an example. Since claystone is not permeable, it acts as a stratigraphic cap rock and directs uranium-containing melts to subside uranium in sandstone.

Except for geophysical radiometric methods, other geophysical methods are indirect methods for uranium exploration. The seismic method, like all geophysical methods, is successful if there are physical differences to be detected in the field. Structural elements, lithological sequence, alteration zones, basement topography, and paleochannels are the most important elements for uranium exploration.

The study area is located in the area between the center of Edirne Province and the center of Kırklareli, the southeast of Süloğlu, and the north of Kocahıdır (Figure 2).
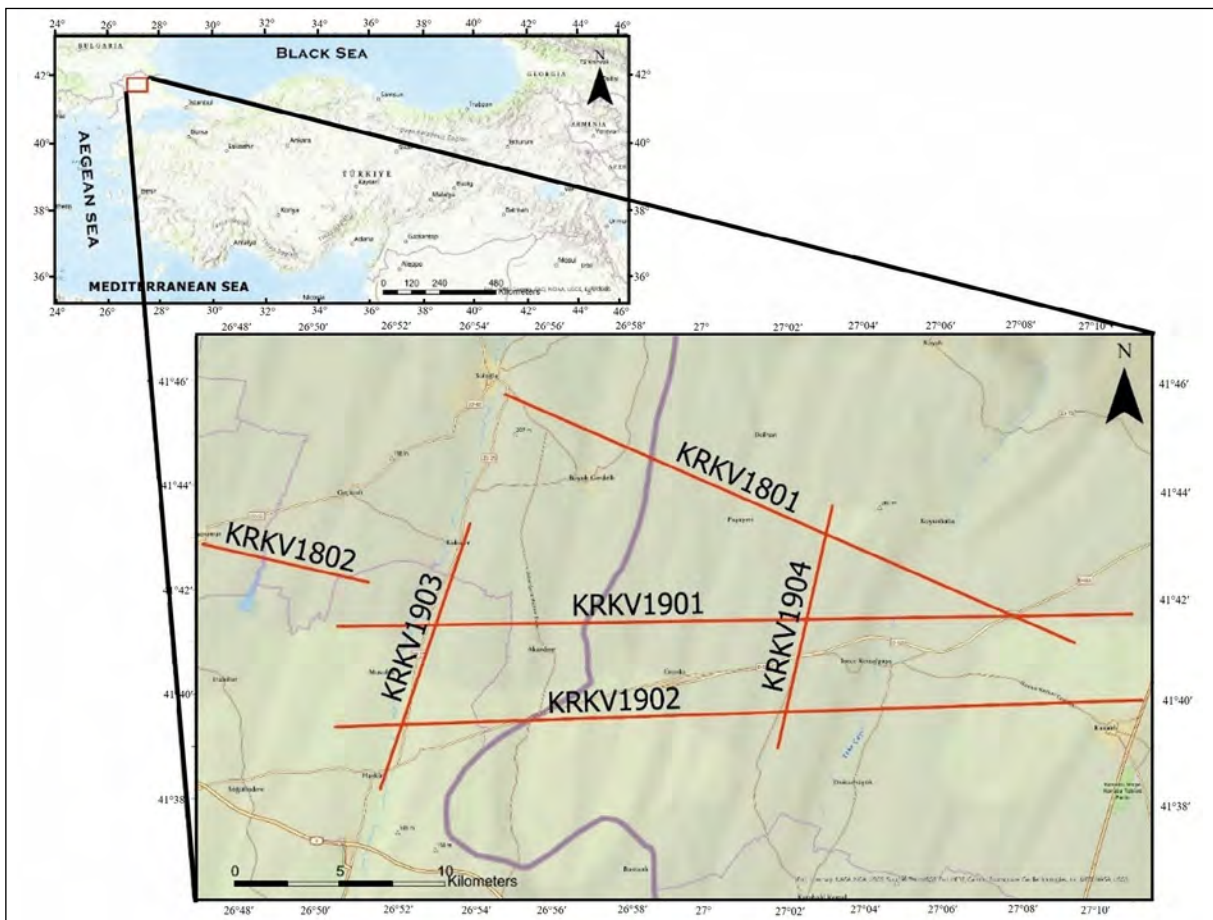
Figure 2- The location of the study area and the seismic reflection lines on the map. The collected seismic reflection lines are indicated by the red line. The KRKV1801 and KRKV1802 lines were collected in 2018, while the other seismic lines were collected in 2019.

In this study, with the application of the seismic reflection method; it is aimed to determine the basic topography of the area, the extent of the spread of the coaly layers, the alteration zones containing uranium ore, and the tectonic movements that contribute to the formation of these structures. In this context, seismic reflection data were collected and 6 profiles were interpreted; 2 east-west (E-W) (KRKV1901, KRKV1902), 2 northeast-southwest (NE-SW) (KRKV1903, KRKV1904), 2 NW-SE (KRKV1801, KRKV1802) in the study area.

The seismic method is based on the reflection of acoustic waves emitted from active (earthquake) or passive sources (dynamite, vibroseis, etc.) between two layers in accordance with the laws of physics as they move through the subsurface. These waves are recorded by receivers (geophones) laid along a certain profile (2D or 3D space) on the surface. From these recorded waves, a seismic image of the subsurface is obtained by using various seismic data processing techniques. With the obtained seismic images, the layer/formation boundaries, faults, slopes, and angles of the layers are determined and the geological model of the seismic cross-sections is revealed (Güreli, 2021).

2. Geological Settings

The Tekedere Group (Çağlayan and Yurtsever, 1998), which consists of various Paleozoic gneisses and schists, and the Şeytandere Metagranite (Çağlayan and Yurtsever, 1998), which consists of meta granites containing pink, white-colored, large feldspar crystals, are located at the base of the study area (Okay et al., 2001). Şeytandere metagranite shows a distinctive steep slope morphology. Isotopic dating using the single zircon Pb-Pb evaporation method shows two magmatic events: One occurred in a short time interval between 312 ± 2 and 315 ± 5 Ma, and the other was dated as 257 ± 6 Ma (Sunal et al., 2008).

İslambeyli formation (Keskin,1966) which consists of Middle Eocene aged, beige, white, yellow, gray colored, volcanic clastic at the base, sandy, clayey limestone, sandstone, and marl overlies the basement units with an angular unconformity. Moreover, Kırklareli limestone (Keskin, 1966) consisting of late Eocene aged white, grayish white, gray, cream,

yellow-colored, abundantly fossiliferous, sandy-clay, reef limestone overlies the basement units with an angular unconformity (Şengüler, 2010).

The Eocene units are also the reservoirs of the geothermal system. Pınarhisar Formation consists of white-colored oolitic limestone and beige-colored, thick-bedded, abundant Congeria tuffite, sand, clay, and marl interlayer limestone on Kırklareli limestone in an angular unconformity and yellow, gray, light brown colored, locally coal banded, sand, Süloğlu formation, which consists of alternating silt and clay (Şengüler, 2010). Overlying these units with angular unconformity, the Sinanlı Member (Boer, 1954) is composed of late Miocene-aged white, yellowish gray colored muddy sandstone and carbonate claystone intermediate level, lacustrine limestones. In addition, the Ergene Formation also consists of yellowish-white, white-colored, cross-bedded sandstone, clayey sandstone, and reddish, greenish, laminated claystone and slightly attached conglomerate lenses, cropping out in a small area in the study area. This unit is unconformably overlain by the Pliocene-aged Thrace formation, which is red, brown, light brown, yellow, locally white and cross-bedded, poorly sorted, reddish clay-mil matrix, unconsolidated conglomerate, pebble, sandstone and claystone (Kirk, 1936; Gürsoy et al., 1996; Günaydın and Çolak, 2010, 2011). Quaternary-aged alluviums cover all these units with angular unconformity, especially in stream beds (Figures 3 and 4; Sezer and Taşkıran, 2020).

2.1. Tectonics

The tectonic evolution of the Thrace Basin began as a result of the movements between the macro plates in the region. The tectonic development took place as a consequence of the interaction of the African, Anatolian, and Eurasian plates during the Late Cretaceous and Miocene (Şengör and Yılmaz, 1981). With the compression in Eastern Anatolia and the opening event expressed by grabens in Western Anatolia, the Thrace Basin was uplifted and eroded in this period, and as a result, the Late Miocene aged Ergene Formation (Umut et al., 1983; Umut et al., 1984) covering the entire Oligocene succession was formed. The Intra-Pontide Suture Belt was also affected by these movements and became the North Anatolian Fault (NAF) (Şengör, 1979). The Thrace
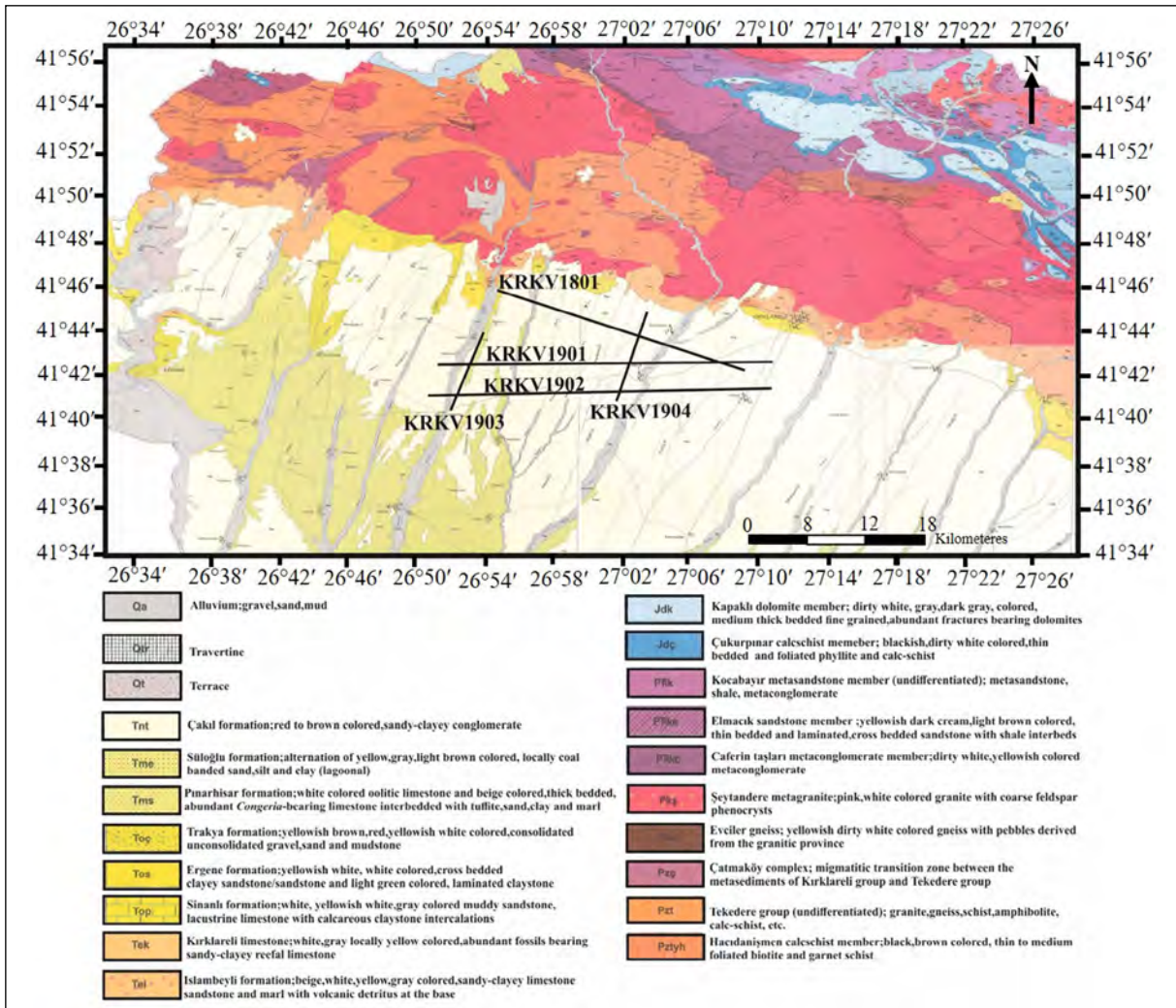
Figure 3- Geological map of the study area covering the Edirne-e17 and Kırklareli-e18 sheets with a scale of 1/100.000 (Çağlayan and Yurtsever, 1998).

Basin was intersected by the young NAF in the south, within the Marmara Sea. The NAF is a strike-slip fault located between the Anatolian and Eurasian plates (Şengör, 1979). As a result of the activity of the fault, porosity, permeability, and dolomitization developments were observed in the structural trap types and reservoir units in the basin (Perinçek, 1987; Coşkun, 1998). As a result of the NAF and ongoing plate movements, abundant clastic material from the Strandja and Rhodope Massifs comes to the Thrace Basin as a result of erosion and transport (Erten and Çubukçu, 1998).

The general tectonic regime of the region is shown by NW-SE trending normal faults as seen in Figure 5

(Turgut et al., 1991). The North Osmancık Fault Zone is an important fault zone that provides facies distribution in the region. Strike-slip faults appear during the middle Miocene (Perinçek, 1991). In the middle of the basin, the greatest displacement occurred in the Terzili Fault Zone. This fault zone reflects the characteristics of strike-slip faults defined by positive and negative flower structures in seismic data. This fault zone extends from the south of the Hamitabat area towards the Turkish-Greek border.

As a result of the studies carried out using seismic cross-sections and subsurface data, strike-slip fault zones were determined through the basin. These are Kırklareli Fault Zone (KFZ), Lüleburgaz Fault Zone (LFZ) and Babaeski Fault Zone (BFZ). These faults, which developed in the Thrace Basin,

UPPER SYSTEM	SYSTEM	SEQUENCE	GROUP	FORMATION	SYMBOL	LITHOLOGY	DESCRIPTIONS
CENOZOIC	QUATERNARY				Qal		Alluvium including gravel, sand, mud
CENOZOIC	PLIOCENE		Trakya		Tnt		Yellowish brown, red, yellowish white colored, consolidated/unconsolidated gravel sand and mudstone
CENOZOIC	NEOGENE MIOCENE	UPPER	Sinanlı Ergene		Tme		Ergene formation; yellowish white, white colored,cross bedded clayey sandstone/sandstone and light green colored, laminated claystone Sinanlı formation,white, yellowish white, gray colored muddy sandsone, lacustrine limestone withcalcareous clatstone intercalations
CENOZOIC	NEOGENE MIOCENE	UPPER			Tms		
CENOZOIC	PALEOGENE OLIGOCENE		Pınarhisar	Süloğlu	Tos		Süloğlu formation;alternation of yellow,gray,light brown colored, locally coal banded sand,silt and clay (lagoonal)Pınarhisar formation;white colored oolitic limestone and beige colored,thick bedded, abundant *Congeria*-bearing limestone interbedded with tüffite,sand,clay and marl
CENOZOIC	PALEOGENE OLIGOCENE		Pınarhisar		Top		
CENOZOIC	PALEOGENE EOCENE UPPER		Kırklareli Limestone		Tek		Kırklareli limestone;white, gray locally yellow colored, abundant fossil bearing sandy-clayey reefal limestone
CENOZOIC	PALEOGENE EOCENE MIDDLE		Islambeyli		Tei		Islambeyli formation; beige, white,yellow, gray colored, sandy-clayey limestone sandstone and marl with volcanic detritus at the base
PALEOZOIC	PERMIAN	Kırklareli Group	Şeytandere Metagranite		Pkş		Şeytandere metagranite; pink, white colored granite with coarse feldspar phenocrysts
PALEOZOIC	PRE-PERMIAN	Tekedere Group			Pzt		Gnays and schist

Figure 4- Generalized stratigraphy of the study area (modified from Sezen and Taşkıran, 2020).

caused improvements in the reservoir properties of the reservoir Osmancık sandstone (Ünal, 1967) and Kırklareli limestones in the basin. Flower structures and fault traps formed due to these faults are important geological structures that allow hydrocarbon accumulation in the basin.

3. Two-Dimensional (2D) Seismic Reflection Method

Elastic waves produced from any energy source propagate in the subsurface and reach the surface again by reflecting from the interfaces of units with different acoustic impedances. The seismic waves reaching the surface are recorded by receivers called geophones on land with the help of a seismic recording unit. The important point of the method is to record the amplitudes against the time of elastic waves emitted from an energy source. The main physical parameters that are effective in the seismic reflection method are velocity and density.

The seismic method is based on the reflection of acoustic waves emitted from active (earthquake) or passive sources (dynamite, vibroseis, etc.) between two layers in accordance with the laws of physics as they move through the subsurface. These waves are recorded by receivers (geophones) laid along a certain profile (2D or 3D space) on the surface. From these recorded waves, a seismic image of the subsurface
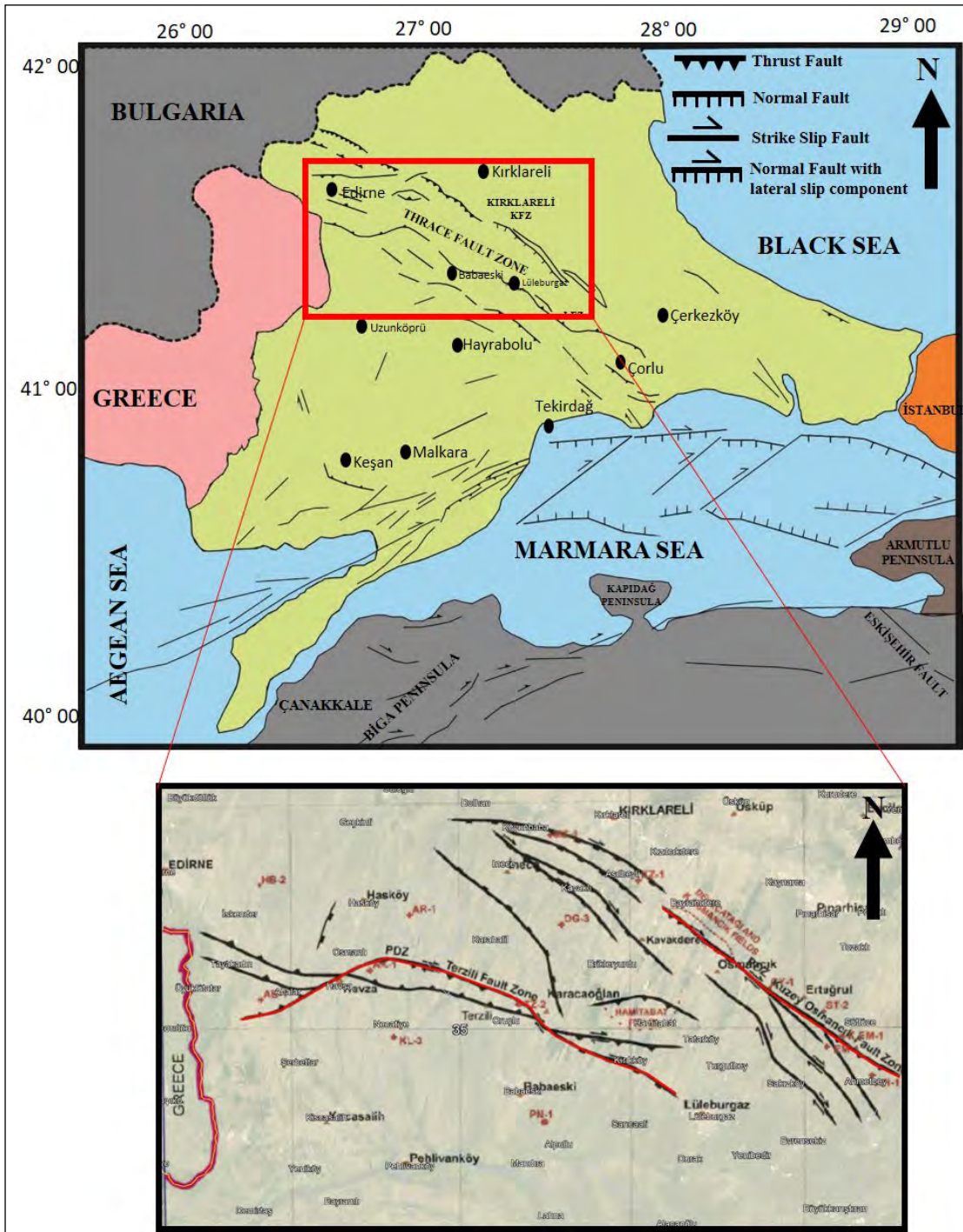
Figure 5- Structural map of the Thrace region and its surroundings (modified from Sakınç et al., 1999).

is obtained by using various seismic data processing techniques. With the obtained seismic images, the layer/formation boundaries, faults, slopes, and angles of the layers are determined and the geological model of the seismic cross-sections is revealed (Güreli, 2021).

3.1. Seismic Reflection Data Acquisition and Methodology

The seismic reflection profiles designed within the scope of this study were obtained using Sercel 428 XL data acquisition equipment and 2 vibroseis

seismic energy sources (Mini Vib II). The recording parameters used in the seismic reflection profiles in Table 1 were determined as a result of the parameter test studies carried out in the study field according to the target depth to be obtained from the subsurface. While the seismic data of the KRKV1801 and KRKV1802 lines were collected in 2018, the seismic data of the KRKV1901, KRKV1902, KRKV1903, and KRKV1904 lines were collected in 2019. The number of shots and profile lengths in meters of each of these seismic lines are shown in Table 2. Thus, a total of 89165 m of seismic reflection data was collected.

Table 1- Data acquisition parameters.

Parameters	Value
Near Offset (m)	17,5
Initial Frequency (Hz)	24
End Frequency (Hz)	180
Number of Vibroseis	2
Number of Sweep	3
Sweep Length (s)	8
Sweep Type	Logarithmic 2 dB
Taper (ms)	350
Group Interval (m)	5 (2 String-12 geophones)
Shot Interval (m)	10
Spread Length (m)	662.5
Spread Type	130+130 (Symmetric)
Record Length (s)	2
Sampling Interval (ms)	1

Table 2- Number of shots and lengths of seismic lines.

Name	Number of Shots	Line Length (m)
KRKV1801	1137	11975
KRKV1802	319	1670
KRKV1901	2592	27240
KRKV1902	2596	27280
KRKV1903	863	9950
KRKV1904	973	11050
Total	8480	89165

3.2. Processing of Seismic Reflection Data

Seismic data processing is making the collected data meaningful and interpretable with various processes. At the data processing stage, the aim is to process the data in the best way and make it ready for the interpretation stage. Within the scope of the project,

the most ideal seismic cross-section and geological model were tried to be obtained by processing the data collected in the field.

The data recorded in the field were collected in SEGD format, and the Disco Focus 5.4 seismic reflection data processing software was used for the purpose of analysis and processing of the data. Transforming the data collected in the field into meaningful and interpretable seismic cross-sections depends on determining the correct data processing parameters by performing signal analysis. With the determined parameters, the data processing steps in Table 3 were applied and the seismic cross-sections were prepared for interpretation.

Table 3- Main seismic data processing steps.

Data Loading
Geometry Definition
Trace Edit (Kill-Mute)
Gain (500 ms)
Deconvolution [Prediction Lag:12 ms; Operation length:200 ms]
Filter [25-100 Hz]
Static Correction
Ground Roll Attenuation
CDP Sort
Velocity Analysis1
NMO and Stack (Brute1) (Vel1&NMO&Stack)
Residuel Statics1 (Brute2) Res1 and NMO and Stack
Velocity Analysis2 (Brute3) Vel2 and NMO and Stack
Residuel Statics2(Brute4) Res2 and NMO and Stack
Final Stack (Final Datum)
Migration

In order to increase the seismic resolution (S/N ratio), several different data-processing steps can be applied to the seismic data. The data processors applied a series of parameter tests to the input data for each step to determine the suitable parameters.

In this context, the gain was applied to remove the absorption in the seismic data. Afterward, deconvolution was applied to compress the wavelet and increase the resolution. Then, the low-velocity layer and variations in elevation were eliminated by applying a static correction process. The Ground

Roll Attenuation process was applied to weaken the surface wave. With the first velocity analysis, the brut stack section was created and NMO data were produced, and residual statics were calculated and applied to the data. Now, velocity analysis can be done more effectively for the second time after the residual static process. With the velocity information obtained from the second velocity analysis, the residual static correction process was applied again. After these processes, the final stack section was prepared and the migration process was applied.

3.3. Interpretation of Seismic Reflection Data

Seismic interpretation is the process of revealing the detailed geological model from the seismic cross-sections obtained as a result of data processing. Although the interpretation studies are carried out on the seismic cross-section, the studies that will be the basis for the interpretation are started while the seismic cross-sections are being planned. For this, first of all, the geology of the study area, the general geological structure, and the structural elements of the region are investigated. All kinds of geological information belonging to the geological units spreading in the field are compiled and the structural positions of these formations in the surrounding areas are revealed.

Professional seismic interpretation applications are used for the interpretation of seismic cross-sections. The boundary of the geological formations on the seismic cross-sections is defined by transferring well information to the interpretation software. Simultaneously, all structural elements (fold, fault, thrust, etc.) that can be identified in seismic cross-sections are marked. Finally, by correlating the seismic cross-section with the information obtained from the well logs, the geological model of the subsurface, the surface maps of each level, and the isometric maps are revealed. Within the scope of the study, seismic reflection cross-sections were interpreted using the Schlumberger Petrel 2019.2 interpretation software.

4. Findings

With the seismic reflection study conducted around Kırklareli and Edirne-Süloğlu districts in the Thrace Region, 4 seismic reflection profiles (KRKV1901, KRKV1902, KRKV1903, and KRKV1904) were

fulfilled in 2019 in order to determine the uranium formation areas and coal-bearing zones in the region and to reveal the uranium ores. In addition, two seismic reflection profiles (KRKV1801, KRKV1802), which are thought to contribute to the interpretation and intersect with the study area from the lines collected in the Thrace Basin in 2018, were included in the data set. Sections 4.1, 4.2, 4.3, and 4.4 contain the findings of the seismic cross-sections that modeled the study area in the best way. The seismic horizons determined on the evaluated seismic cross-sections were interpreted by using borehole lithology. The correlation of seismic horizons with the borehole data was made using the stack velocities obtained from the seismic data processing. While evaluating the seismic cross-sections, data from a total of 97 wells located near and/or on top of the lines were utilized.

4.1. KRKV1801 Seismic Reflection Cross-Section

In this seismic line, which starts near Edirne–Süloğlu and continues in the northwest-southeast direction, the level observed around 400 ms at the northwest and goes 1200 ms at the southeast of the seismic cross-section has been determined as the Metamorphic Basement-Eocene boundary. The seismic horizon observed between the 20125 and 28120 CDP numbers above the basement is called the Eocene-Oligocene boundary. The Danişmen-Ergene formations boundary, which was marked by utilizing the lithology levels of the borehole logs, and the reflection surfaces drawn between the CDP numbers approximately 21353 - 21962 were also determined as the surface of the coal zone (the top of the coal). While the seismic cross-section was examined, it was determined that the reasons why the boreholes drilled in the northwest of the seismic cross-section did not intersect the coal were the thinning of the coal-bearing zone, ending towards the Ergene formation and the rising of the basement throughout the northwest. It is thought that the discontinuities observed on the interfaces correspond to the fractures (yellow faults) intersecting the basement. The basin shows a stepped structure and deepens from northwest to southeast due to fracture lines (Figure 6). Boreholes were drilled mainly around Süloğlu, near CDP numbers 20123 and 22170 and in the north and south of the seismic cross-section. Uranium ore with low ppm values was observed in the borehole approximately 550 m
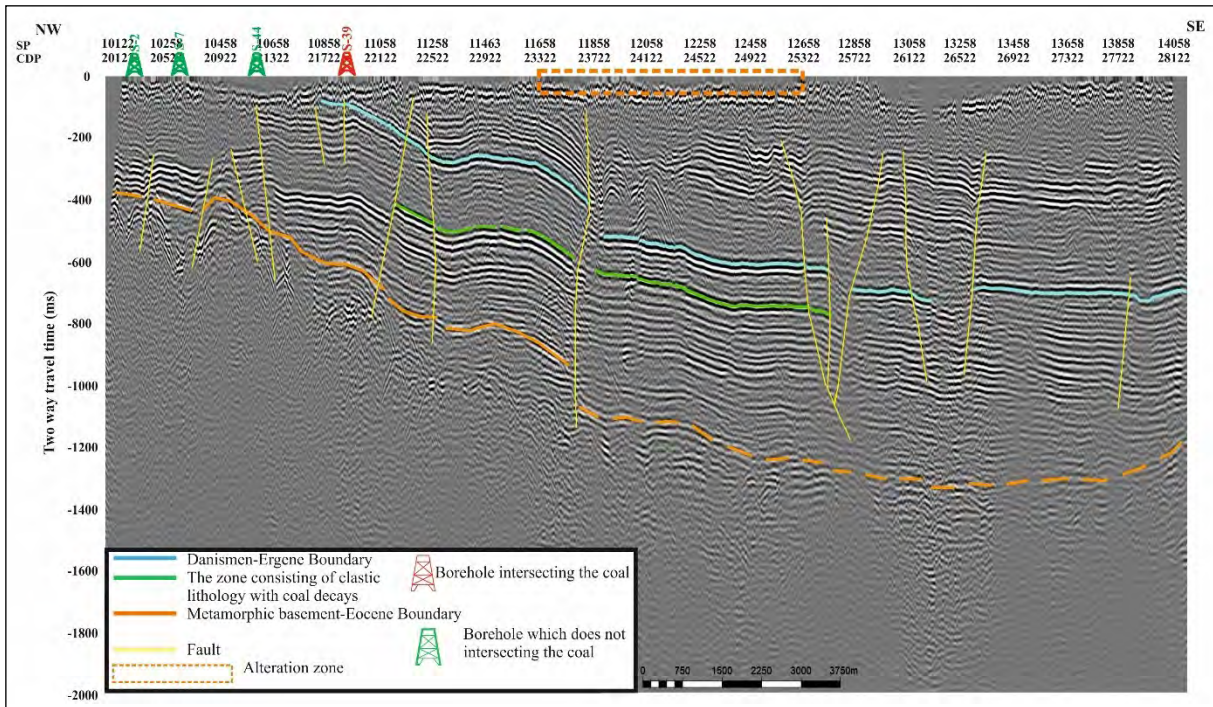
Figure 6- Interpreted KRKV1801 seismic cross-section. The small and large-scale faults that are not named and dominate throughout the region are shown in yellow. The location of the borehole intersecting the coal (S-39) is shown with a red symbol in the figure. The location of the boreholes which does not intersect the coal (S-2, S-7, and S-44) is shown with a green symbol in the figure. The boundary of the alteration zone is shown with the orange dashed line.

southwest of CDP number 20688 and in the borehole approximately 850 m northeast of CDP number 20424.

4.2. KRKV1901 Seismic Reflection Cross-Section

The basin deepens in the east direction towards the CDP number 24132 due to the fractured structures that intersect the basement and cap layer in a stepped way and continues horizontally between CDP numbers 24132-28132. Then, after CDP number 28132, it rises again and continues towards the east (Figure 7). Faults interpreted with yellow lines are unnamed in Figure 7 since normal faults are common throughout the seismic cross-section. With the effect of these normal faults, the seismic horizons deepen in the middle of the seismic line.

One of the drilled boreholes is approximately 14 m away from the 21364 CDP number in the seismic cross-section. The Danişmen-Ergene formation boundary and coal-bearing zone were seen at 77.3 m (~260 ms) and 194.6 m (~380 ms) respectively while 302.3 ppm uranium was observed at 131.3 m (~320 ms) in the well. Considering its proximity to

the seismic line, the well data and the seismic cross-section were correlated, and the interpretation was started from this seismic cross-section.

It was observed that a coal-bearing unit was not found in some boreholes close to the KRKV1901 seismic line. Depth conversion was made using data processing velocities (± 5% margin of error) and it was seen that the coal-bearing unit could not be observed due to the suspension of the borehole.

According to the geological interpretation of seismic cross-section; the metamorphic basement-Eocene boundary, which can be followed throughout the seismic line, the uppermost layer of the coal-bearing zone and Danişmen-Ergene formations have been identified from oldest to youngest with the help of borehole logs.

Areas indicated by orange dashed rectangles on the seismic cross-section were determined as alteration zones. The first alteration zone was observed at the intersection of KRKV1901 and KRKV1903 lines, approximately between CDP numbers 20640-21720,
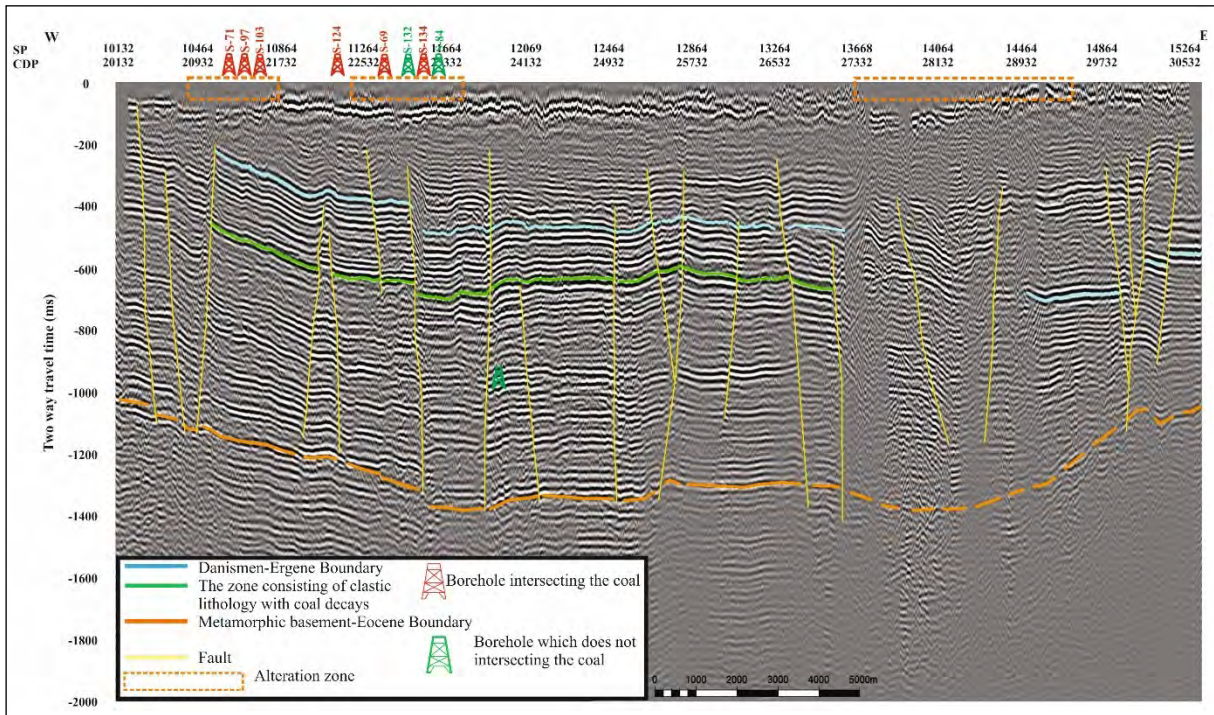
Figure 7- Interpreted KRKV1901 seismic cross-section. The small and large-scale faults that are unnamed and dominate throughout the region are shown in yellow. The location of the borehole intersecting the coal (S-71, S-97, S-103, S-124, S-69, S-134) is shown with a red symbol in the figure. The location of the boreholes which does not intersect the coal is shown with a green symbol (S-132 and S-84). The boundary of the alteration zone is labeled with the orange dashed line. It is seen that the seismic levels, which are colored blue, green, and orange, are followed approximately along the line.

the second alteration zone is between CDP numbers 22245 - 23520 and the third alteration zone is also at the intersection of KRKV1901, KRKV1904 and KRKV1801 lines, approximately between CDP numbers 26732-29232. It is seen that the interpreted alteration zones are compatible with the topography seen on the seismic cross-section (Figure 7).

4.3. KRKV1903 Seismic Reflection Cross-Section

KRKV1903 seismic line is one of the lines collected in the NE-SW direction. The horizon shown between approximately 1460 ms in the south and 960 ms in the north of the seismic cross-section has been interpreted as the Metamorphic Basement-Eocene boundary. This boundary and the upper layer of the coal-bearing zone (determined by the information of borehole and intersections of seismic cross-sections) interpreted on the KRKV1903 seismic cross-section can be followed to the end of this section, while the Danişmen-Ergene formations boundary can be followed up to CDP number 62810. In this section, it is observed that the geological structures, especially the interface of the

Danişmen-Ergene formations, are inclined towards the south (Figure 8). The discontinuity surfaces that intersect the reflection surfaces and the basement were interpreted as fracture lines (normal and strike-slip fault systems).

Two different flower structures formed by the strike-slip fault were defined on the seismic cross-section. The first of these is the positive flower structure observed in the CDP range of 60810 to 61710. It has been observed that the folding causes reverse fault uplift with the effect of the compression formed in this strike-slip fault zone, resulting in a positive flower structure. While the probability of lignite layers in the center of positive flower structures based on folding is very low, the coal-bearing units are much more likely to be seen on the flanks of the structure. In this context, the observation of coal-bearing horizons with an average thickness of 30-150 m in the boreholes was carried out on the flanks of the positive flower structure. This structure can be clearly seen on the KRKV1903 seismic line.
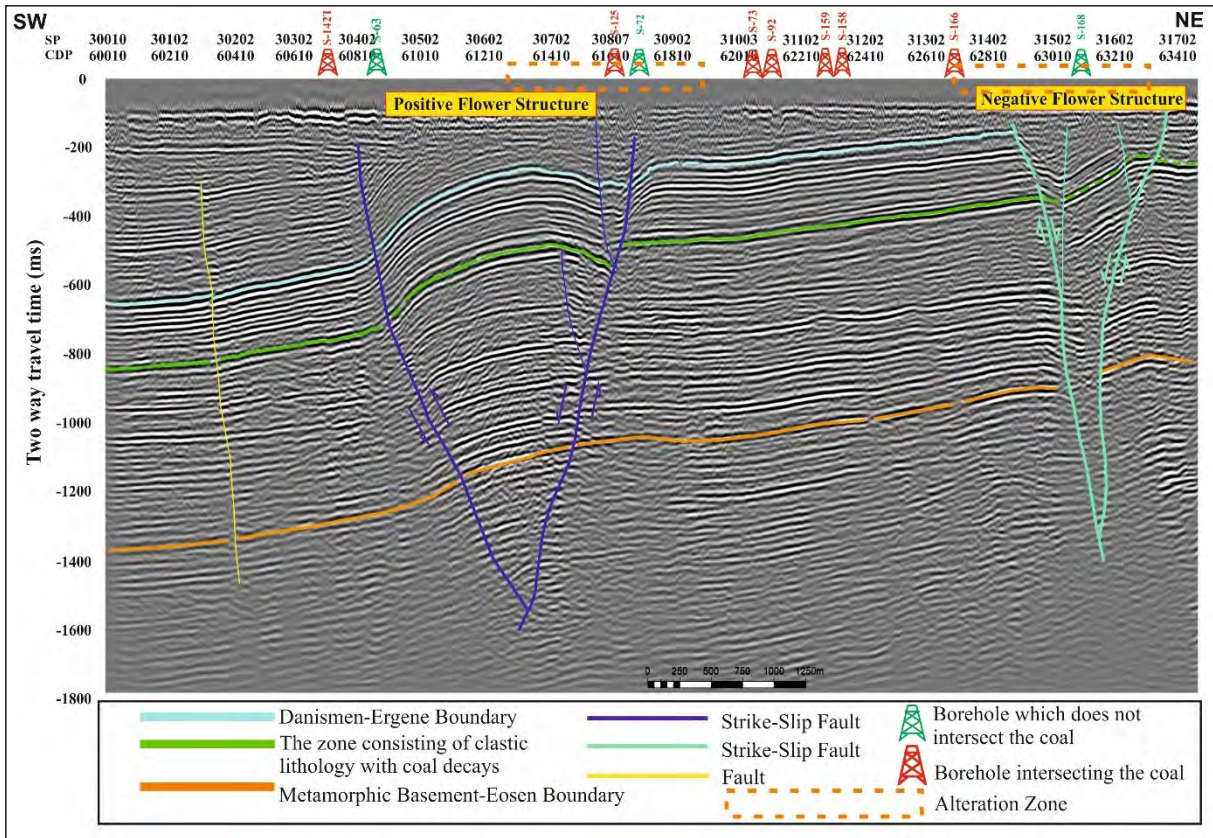
Figure 8- Interpreted KRKV1903 seismic line. One of the strike-slip faults is represented by a blue color, and the other is represented by a green color. The fault that is not named and dominate throughout the region are shown in yellow. The alteration zones observed above the positive and negative flower structures are shown with orange dashed lines. The location of the borehole intersecting the coal (S-142T, S-125, S-73, S-92, S-159, S-158, S-166) is shown with a red symbol in the figure. The location of the boreholes which does not intersect the coal (S-63, S-72, and S-168) is shown with a green symbol in the figure. It is seen that the seismic horizons, which are colored blue, green, and orange, are followed along the line.

A negative flower structure interpreted with green color is another structure that is located in the CDP range of 62810 and 63400 in the northeast of the seismic line. The negative flower structure was formed by the effect of normal faults developing in the strike-slip fault zone. Lignite and uranium ores were not discovered since the boreholes on this structure could not reach sufficient depth. In addition, it was observed that some boreholes drilled before the seismic study did not intersect the coal-bearing sequences because they coincided with the fault zones seen in the seismic cross-section. For this reason, the determination and consistent interpretation of strike-slip fault systems in hydrocarbon exploration are important for future borehole studies.

The areas indicated by the orange rectangular box on the seismic cross-section were determined as the alteration zones. The first alteration zone is approximately between 61260 - 61910 CDP numbers, and the second alteration zone is between 62710-63314 CDP numbers. It was thought that these alteration zones should be investigated, indicating the presence of uranium ore, and a borehole was suggested in this area (Figure 8). In light of all the findings obtained with these suggestions, uranium ore was observed in the boreholes at the intersection of the KRKV1901 and KRKV1903 seismic lines. The presence of alteration zones in this area indicates that alteration zones in other seismic lines should also be discovered and may indicate the presence of uranium ore.

4.4. KRKV1904 Seismic Reflection Cross-Section

The KRKV1904 seismic profile is designed in the NE-SW direction and it intersects the KRKV1901

line at the receiver point 40845 (CDP 81690) and the KRKV1801 line at the receiver point 41425 (CDP 82850). The level labelled at approximately 1580 ms in the south and approximately 820 ms in the north of the seismic cross-section has been interpreted as the Eocene-Metamorphic basement boundary. The Metamorphic Basement-Eocene boundary interpreted on the seismic cross-section and the upper layer of the coal-bearing zone (determined by the information of borehole data and intersections of seismic lines) and the Danişmen-Ergene formations boundary are continuously observed up to the CDP number 82100 (Block A) (Figure 9). Up to this CDP number the quality of the seismic cross-section is quite good. Beginning from the CDP number 82700, only Danişmen-Ergene boundary and the Metamorphic Basement-Eocene boundary have been approximately marked (A¹ Block). When the KRKV1904 seismic cross-section is investigated, it is seen that the geological structures, especially the Danişmen-Ergene formations boundary, are inclined towards the southwest.

The discontinuity surfaces intersecting the reflections observed in the seismic cross-section were interpreted as fracture lines (yellow and pink faults). The region where there are reflective surfaces that can be observed horizontally is interpreted as Block A and A¹, and the region where the levels cannot be observed clearly is interpreted as Block B. Considering the seismic reflection packages, the discontinuity and deterioration of the reflections in the B block can be explained by the presence of a strike-slip fault. However, due to the few number of seismic lines in the region, the existence of this fault could not be clearly demonstrated.

In the seismic cross-section, two areas thought to be alteration zones were identified. The first alteration zone is approximately between 80200–80620 and the second alteration zone is between CDP numbers 82140 – 82860. It is known that in the second alteration zone, which coincides with the intersection of KRKV1901, KRKV1904, and KRKV1801 lines, a subsidence area was formed due to tectonism and provides a suitable environment for uranium ore. For this reason, it is thought that alteration zones should be investigated in detail and these zones may have very high-grade ppm uranium (Figure 9).
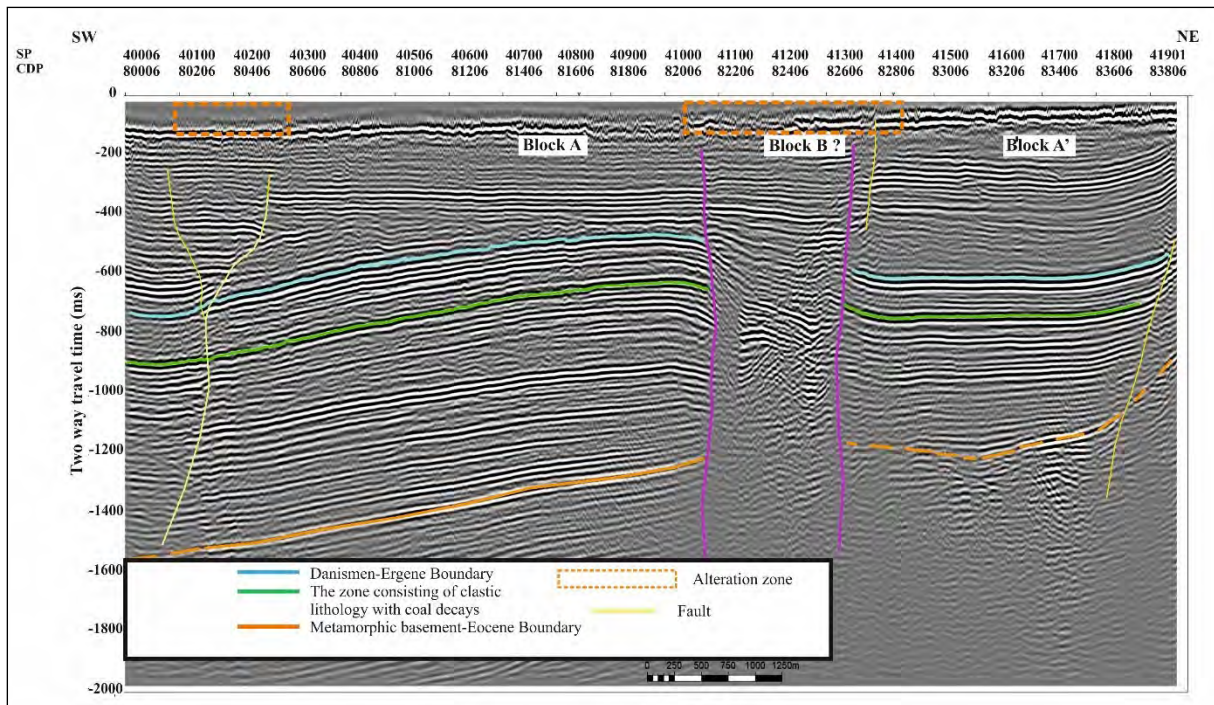
Figure 9- Interpreted KRKV1904 seismic cross-section. A possible strike-slip fault is shown in pink and the fault that is not named is shown in yellow. The boundary of the alteration zone is shown with the orange dashed line. It is seen that the seismic levels, which are colored blue, green, and orange, are followed along the line in blocks A and A' but in block B these seismic levels are deteriorating.

5. Discussion

Coal formations in the Thrace Cenozoic Basin are located within the Oligocene-aged Danişmen Formation (Şengüler, 2013). Lignite outcropping in the north and south of the basin gradually deepens towards the middle of the basin and is observed at depths exceeding 600 m in a sedimentary succession reaching 10.000 m in the middle parts of the basin (Şengüler, 2013). The coal reserve of the Thrace-Ergene Basin has exceeded 1 billion tons with the studies initiated by the General Directorate of Mineral Research and Exploration (MTA) in 2005 and still continues (Şengüler, 2013). According to the 2011 coal reserve preliminary study report of the General Directorate of Energy Affairs, the possible coal reserve in the Süloğlu field located within the study area was determined as 14.5 million tons. This result was obtained according to the results of the boreholes drilled in the region. The boundary of the coal spread, which was determined by evaluating the lines obtained as a result of the seismic study conducted in 2019, was

modelled in a 3D environment and it was determined that the boundary of the coal spread started from the southwest of the study area and continued towards the northeast (Figure 10). It was observed that some boreholes were suspended as a result of the determined coal-bearing layers transported deeper with tectonic movements (Figure 8). This supports the argument that the calculated coal reserve ratio may be higher for the Süloğlu field.

Perinçek (1987, 1991) argues that the faults in the Thrace fault system were formed before the deposition of the Ergene formation and were right-lateral strike-slip (Figure 11a). Perinçek (1991) in his study stated that the NAF was active before the late Miocene in the Thrace Basin and named the aforementioned fault zone as Kırklareli, Babaeski, and LFZ extending from southeast to northwest. In the previous seismic studies carried out in the Thrace Basin, the positive flower structure formed by the effect of the LFZ, one of the fault zones mapped as a continuation of the NAF, was determined on the seismic cross-sections (Figure 11b).
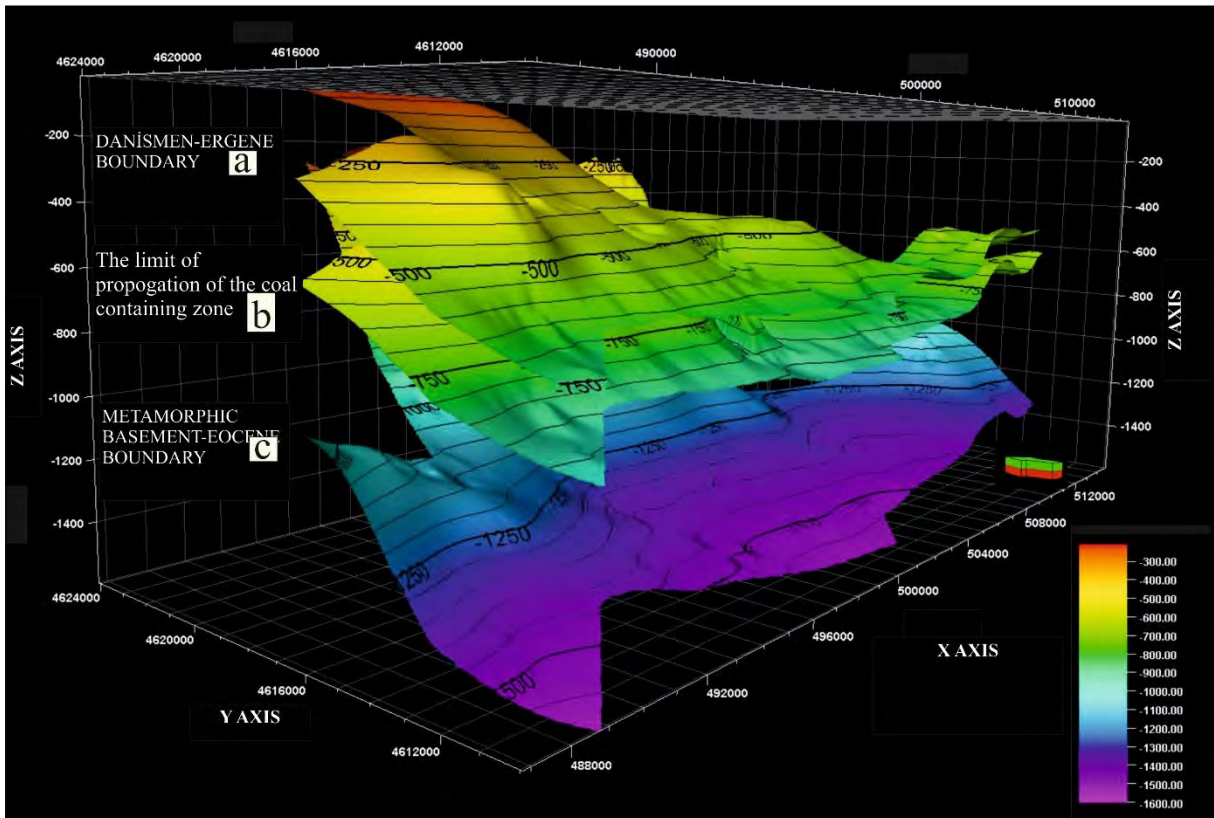
Figure 10- 3D view of; a) Danişmen-Ergene boundary, b) extensions of the coal-containing zone and c) metamorphic Basement-Eocene boundary. All boundaries are plotted on a millisecond (ms) scale.
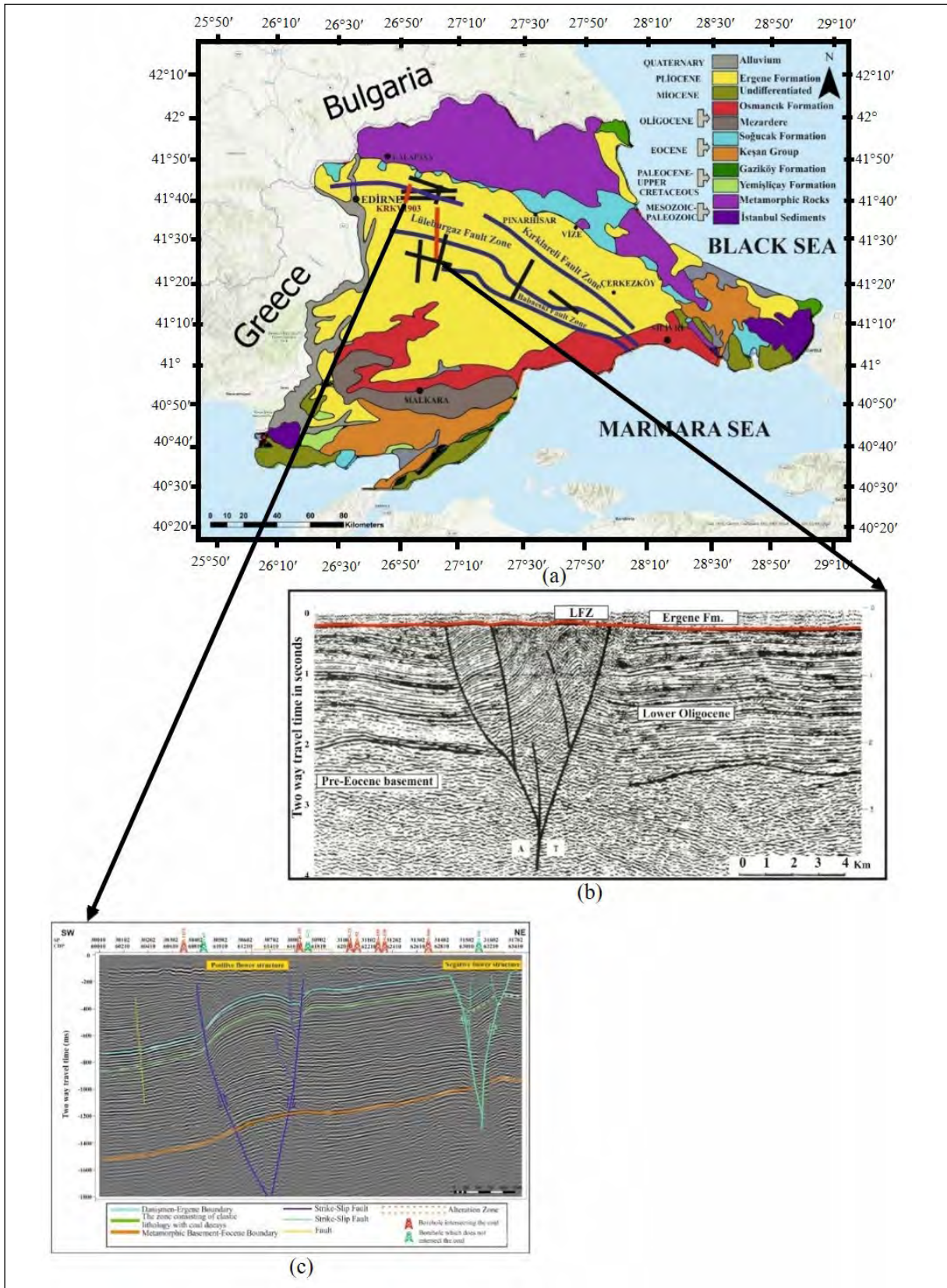
Figure 11- a) Geological map of Thrace Basin and Thrace fault zones (geological map; Kasar et al., 1983; modified from Perinçek, 1991; Perinçek et al., 2015), b) positive flower structure near the western part of the Lüleburgaz Fault Zone (LFZ) (Perinçek, 1991; Perinçek et al., 2015) and c) fault systems observed on the KRKV1903 seismic cross-section.

When the seismic lines studied by MTA in 2018-2019 are placed on the map drawn from Perinçek (1991), it is thought that the positive flower structure determined on the KRKV1903 seismic cross-section was formed by the effect of the northern branch of the KFZ (Figure 11c).

By using a high-resolution seismic reflection method, it is possible to detect small-size ores and alteration zones with low acoustic impedance in terms of mining (Hajnal et al., 1997). In light of this information, the existence of zones was tried to be determined in all seismic lines carried out in the field. The tectonic structure in which the presence of uranium ore observed in the determined alteration zone is similar to the structure observed in the east of the line suggests that it may indicate the presence of uranium ore in this region as well (Figure 8). For this reason, it is important to give priority to this area in the drilling plans to be carried out in the future.

6. Results

As a result of the study, the basic topography of the area, the alteration zones assumed to be important for uranium deposition, the extension of the coal-bearing zones, and the tectonic structures affecting the area were determined, and 3D surface maps were created.

After the evaluation made by showing the 2D seismic cross-sections in a 3D block diagram, it was determined that the thin Ergene formation was deposited in the uplift areas developed due to faulting in the basin, and the formation was thicker in the synclines in the trough areas. In addition, it has been observed that the geological formations, especially the Danişmen-Ergene formations boundary, are inclined in the NW-SE direction. In some areas in the east of the basin, the unconformity surface at the base of the Ergene formation was folded due to the compression created by the fault activity. The probability of seeing lignite layers in the center of areas with positive flower structures is rare due to folding. It is recommended to drill on the flanks of these structures so as to detect the lignite layer.

The extension coal-bearing zone determined by evaluating the seismic lines collected in the study area was modeled with a 3D image. In light of these obtained data, it has been determined that the extension of coal continues from the southwest of the basin to the northeast, and the borehole information have also supported this model.

This study was carried out for radioactive purposes, as an example, it is recommended to conduct seismic reflection studies before coal-targeted drilling for level monitoring and determination of target zones in coal exploration areas.

The uranium ore in the alteration zones determined at the intersection of the seismic cross-sections KRKV1901 and KRKV1903 indicates that the alteration zones in the other seismic cross-sections should also be explored in this respect. The seismic reflection method contributes to the identification of geological structures that are not outcropped, the determination of the inclination angles of the formations, and detailed site characterization with new boreholes. In order to obtain more detailed information about the study area, the seismic reflection method should be performed before drilling activities and more frequent seismic lines should be planned. In addition, with the data obtained as a result of the study, it is recommended to drill new boreholes in areas with coal and uranium potential.

References

Boer, N. P. 1954. De report on a geological reconnaissance in Turkish Thrace. Hague Petroleum Office, Report No: 25373.

Coşkun, B. 1998. Triple junction zone-North Anatolian Fault relationship and implications on petroleum exploration Saros Gulf, northern Aegean Sea Turkey. 3rd International Turkish Geology Symposium, Ankara.

Çağlayan, M. A., Yurtsever, A. 1998. Burgaz-A3, Edirne-B2 ve B3; Burgaz-A4 ve Kırklareli-B4; Kırklareli-B5 ve B6; Kırklareli-C6 maps, 1:100000 scaled geological maps of Turkey, No: 20, 21, 22, 23. General Directorate of Mineral Research and Exploration, Ankara.

Erten, T., Çubukçu, A. 1998. Petrographic-sedimentological features, tectonic environmental models, nutritional sources, hydrocarbon and reservoir properties of the Eocene-Oligocene aged deposits of the Northern Thrace Basin. Turkish Petroleum Company, Research Group Report No: 1217, 66 (unpublished).

Günaydın, A. B., Çolak, T. 2010-2011. Industrial raw material exploration prospecting report in the Strandja Massif (E19 and E20 sheets) and Thrace Tertiary (F19 sheets). General Directorate of Mineral Research and Exploration, Report No: 11833, Ankara (unpublished).

Güreli, O. 2021. Application and success of seismic methods in mineral exploration. Architects and Engineers Group 120, 98-101 (in Turkish).

Gürsoy, B., Tuncalı, E., Kara H., Narin, R., Dümenci, S. 1996. Thrace Tertiary coal basin report. General Directorate of Mineral Research and Exploration, Report No: 9974, Ankara (unpublished).

Hajnal, Z., Annesley, I. R., White, D., Matthews, R. B., Sopuck, V., Koch, R., Leppin, M., Ahuja, S. 1997. Sedimentary-hosted mineral deposits: A high-resolution seismic survey in the Athabasca Basin. Fourth Decennial International Conference on Mineral Exploration GEO/FX, 421-432.

Kangal, M. O., Özer, M., Burat, F., Akın, S. 2018. Evaluation of Thrace region fine coal tailings. Bulletin of the Mineral Research and Exploration 157, 219-227.

Kaşar, S., Bürkan, K., Siyako M., Demir, O. 1983. Geology and hydrocarbon possibilities of Tekirdağ-Şarköy-Keşan-Enez region. Turkish Petroleum Corporation Research Group, Archive Report No: 1771, 71, Ankara (unpublished).

Keskin, C. 1966. Pınarhisar reef complex microfacies investigation: Rev. Fac. Scien. Univ. İst, Serial B, 31 / 3-4;109-146 (in Turkish).

Kirk, H. M. 1936. The first summary about the geology of Thrace. General Directorate of Mineral Research and Exploration, Report No: 235, Ankara (unpublished).

Okay, A. I., Satır, M., Tüysüz, O., Akyüz, S., Chen, F. 2001. The tectonics of the Strandja Massif: late-Variscan and mid-Mesozoic deformation and metamorphism in the northern Aegean. International Journal Earth Science 90, 217-233.

Öztunalı, Ö., Üşümezsoy, Ş. 1979. Core rocks of the Strandja Massif and their petrogenetic evolutions. Altınlı Symposium, Turkish Geology Institute İstanbul University Faculty of Earth Sciences, 37-44.

Perinçek, D. 1987. Seismic characteristics of the wrench fault zone in the Thrace Basin. Proceedings of 7th Turkish Petroleum Congress, 11-21.

Perinçek, D. 1991. Possible strand of the North Anatolian Fault in the Thrace Basin, Turkey - An interpretation. AAPG Bulletin 75, 241-257.

Perinçek, D., Ataş, N., Karatut, Ş., Erensoy, E. 2015. Stratigraphy of Danişmen formation and distribution of lignite levels in the unit in the basin, Thrace Basin, Turkey. Geological Bulletin of Turkey 58(1), 19-62 (in Turkish).

Sakınç, M., Yaltırak, C., Oktay, F. Y. 1999. Palaeogeographical evolution of the Thrace Neogene Basin and the Tethys Paratethys relations at northwestern Turkey (Thrace). Paleogeography, Palaeoclimatology, Palaeoecology 153, 17-40.

Sezen, E., Taşkıran, L. 2020. Evaluations of the drilling studies carried out within the scope of the radioactive raw material exploration project of the Thrace region. Mineral Research and Exploration Natural Resources and Economy Bulletin 29, 131-137.

Sonel, N., Büyükutku, A. 1998. Reservoir rock properties of Middle Eocene sandstones in Northern Thrace Basin. Bulletin of the Mineral Research and Exploration 120, 259-268.

Sunal, G., Satır, M., Natal'in, B. A., Toraman, E. 2008. Paleotectonic position of the Strandja Massif and surrounding continental blocks based on Zircon Pb-Pb age studies. International Geology Review 50, 519-545.

Şengör, A. M. C. 1979. Mid-Mesozoic closure of Permo-Triassic: Tethys and its implications. Nature 279, 590- 593.

Şengör, A. M. C., Yılmaz, Y. 1981. Tethyan evolution of Turkey: A plate tectonic approach. Tectonophysics 75, 181-241.

Şengüler, İ. 2010. Thrace basin TKİ coal drillings project report. General Directorate of Mineral Research and Exploration, Report No: 11286, Ankara (unpublished).

Şengüler, İ. 2013. Geology and coal potential of Ergene (Thrace) Basin. Mineral Research and Exploration Natural Resources and Economy Bulletin 16, 109-114 (in Turkish).

Taner, F., Çağatay, A. 1983. Geology and mineralogy of mineral deposits in the Stradja Massif. Bulletin of the Turkish Geological Institute 26, 31-40, Ankara (in Turkish).

Turgut, S., Türkaslan, M., Perinçek, D. 1991. Evolution of the Thrace sedimentary basin and its hydrocarbon prospectivity. In A. M. Spencer, Generation, Accumulation, and Production of Europe's Hydrocarbons 1, 415-437.

Umut, M., Kurt, Z., İmik, M., Özcan, İ., Sarıkaya, H., Saraç, G. 1983. Geology of Tekirdağ, Silivri İstanbul), Pınarhisar area. Mineral Research and Exploration, Report No: 7349, Ankara (unpublished).

Umut, M., İmik, M., Kurt, Z., Özcan, İ., Ateş, M., Karabıyıkoğlu, M., Saraç, G. 1984. Geology of Edirne province-Kırklareli province-Lüleburgaz (Kırklareli province)-Uzunköprü (Edirne province) vicinity. Mineral Research and Exploration, Report No: 7604, Ankara (in Turkish).

Ünal, O. T. 1967. Thrace geology and oil possibilities. Turkish Petroleum Corporation Search Group Archive, Report No: 391, 80, Ankara (unpublished).

Üşümezsoy, Ş. 1982. Igneous and metamorphic geology and mineralization of Istranca region (geotectonic setting and mineralization of the Istranca Massif). İstanbul University Earth Sciences Review 3(1-2), 227-294.

Publication Rules for the "Bulletin of the Mineral Research and Exploration"

1. Purposes

• To contribute to the establishment of scientific communication issues in earth sciences both in Turkey and internationally.

• To contribute to economic (mining, oil and gas, geothermal etc.), environmental and social (geoheritage etc.) studies in Turkey and in the World.

• To make the earth science scientific research and applications made by the MTA on publicly known,

• To use the bulletin as an effective tool in the international publication exchange by keeping it at a high level in terms of quality, scope and format,

2. Scope-Attribute

In order for manuscripts to be published in the Bulletin of the Mineral Research and Exploration, they must have at least one of the following qualifications:

2.1. Research Articles and Reviews

2.1.1. Original Scientific Researches

• Such articles cover original scientific research and its results that contribute to the fundamental issues of earth sciences, research and evaluation of underground resources, and examine the environmental problems in terms of earth sciences,

• It covers research that apply new approaches and methods in solving problems related to earth sciences.

2.1.2. Review Articles

• They cover studies that compile previous research on subjects of earth sciences with a critical approach and put forward a new opinion on that subject.

2.2. Criticism and Response Articles

• Articles that criticize all or part of an article of the bulletin in the latest issue are published in the following first issue, if submitted within six months at the latest from the date of publication digitally.

• Before the publication, review articles are sent to the responsible author of the criticized article to make a response.

• If the criticism is not responded within foreseen time, the criticism letter is published alone, subsequent replies are not published. Replies are not allowed to be re-criticized.

• In criticizing and replying, scientific discussion and ethical rules should be followed. Criticism and response manuscripts should not exceed four pages, including figures, if available.

2.3. Brief Notes

• In "Brief Notes" section of the Bulletin of the Mineral Research and Exploration, the brief, objective and concise articles reflecting the data obtained from scientific researches and applications carried out in the area of earth sciences or new findings related to previously unknown geosciences in Turkey are given place.

• The articles arranged in the "Brief Notes" section are published without waiting in the first or in the second issue the latest, after the date they are sent to the Chair of the Editorial Board in order to ensure rapid communication.

• Articles requested to be published in the "Brief Notes" section should not exceed four pages, including all figures and tables.

3. Submission and Acceptance for Manuscripts

• The manuscripts submitted to be published in the Bulletin of the Mineral Research and Exploration should be prepared in ENGLISH in accordance with the Publishing Rules of the Bulletin of the Mineral Research and Exploration, and submitted via electronic application at http://dergi.mta.gov.tr/index.php.

• The manuscript must not have been previously published partially or completely elsewhere (except in abstract form).

• Manuscripts submitted with the request for publication in the Bulletin of the Mineral Research and Exploration should not exceed 30 pages, including all illustrations. The articles exceeding 30 pages can be published if deemed appropriate by referees and editors.

• In the submitted manuscript, the number of figures and tables should be given in proportion to the main text in a ratio of 1/3.

• Corresponding author is asked to suggest at least three referees for the evaluation of the manuscript. (The proposed referees and the authors should not have any joint work within the last two years).

- Manuscripts that do not comply with the Publishing Rules for the Bulletin of the Mineral Research and Exploration in terms of quality and form are directly returned without being examined in terms of content.

- Manuscripts deemed appropriate in terms of format are sent to at least two expert referees for review by the Editorial Board of the Bulletin of the Mineral Research and Exploration.

- Authors should make the referee corrections and suggestions sent to them within 20 days and upload to the system.

- Comments from referees are evaluated by the Editors and associated editors. Manuscripts deemed necessary to be corrected are sent back to the authors with a request for correction. Whether the suggested corrections have been made or not is checked by the Editorial Board.

- In the revision proposals given by the editors and referees, if there are suggestions that are not accepted by the author and have not been corrected, a report explaining the reason for rejecting these suggestions by the author should be sent to the Editorial Board together with the corrected copies.

- After the last control at the printing stage, the pre-print of the manuscript is sent to the authors in pdf format and the printing control is requested.

- Articles, not accepted for publication are not returned to the authors, for the unpublished articles, a letter is written to the responsible author indicating the reason for rejection.

4. Language and Period of Publication

- The Bulletin of the Mineral Research and Exploration is published three times a year, each issue as being in English (printed and online) and in Turkish (online) languages.

- The spelling rules of the Turkish Language Association are valid for the spelling rules for the Turkish issue. However, in spelling of the words related to earth sciences, the spelling forms of technical terms are used in accordance with the decision of the Editorial Board (For example; underground, ground, earth's crust, etc.).

5. Spelling Draft

- The text of the manuscripts to be sent for the first review with the request to be published in the Bulletin of the Mineral Research and Exploration should be written in A4 (29.7 x 21 cm) size, word format, Times New Roman 10 pt., normal with 2.0 line spacing.

- At the bottom, top, left and right of the page 2.5 cm indent must be left. Formulas that require the use of special letters and symbols should be presented in computer media.

- In all subtitles, the initials of all words must be capital. First degree headings to be used in the article should be written in Times New Roman, 10 pt., bold and left aligned by giving numbers. Secondary headings should be written in Times New Roman, 10 pt., normal font and left aligned by giving numbers. Third-degree headings should be written in Times New Roman, 10 pt., italic font and left-aligned by giving numbers. Fourth-order headings should be written in Times New Roman, 10 pt., italic, aligned to the left, without giving numbers, and the text should continue after the title without a colon and a paragraph (see example article: www.dergi.mta.gov.tr).

- One blank line should be left after paragraphs in the text.

- Paragraph headings should be written 0.5 mm indentation.

- One article should respectively contain;

  -Title

  -Author's Name and Surname and * sign

  - Abstract

  - Keywords

  - Introduction

  - Main Text

  - Discussion

  - Results

  - Acknowledgements

  - Reference sections.

- Line and page numbers must be added to the article text.

5.1. Title of the Article

- The title should reflect the subject of the article as briefly, clearly and adequately as possible. Subjects that are not sufficiently covered in the article should not be included in the title. The first letter of the title

should be capitalized and the other words should be in lowercase letters (except for proper names) in Times New Roman, 10 pt. and bolded.

5.2. Author Name, Address and E-Mail Address

• The first name of the authors should be in lowercase (except the first letter), and the surname should be in capital letter and without any title.

• Only the name of the organization should be specified in the occupational address after the name and surname of the authors (position should not be specified).

• ORCID number should be taken from www.orcid.org and placed under the address.

• In articles written by more than one author, numbers should be placed on surnames of the authors, the address information should be included in the bottom line with a single line spacing. In this section, the corresponding author of the article should be indicated by using an asterisk (*) and the corresponding author's e-mail, telephone and other contact information must be provided.

• Abbreviations should not be used in writing the author's name and address. Addresses should be given in Turkish in Turkish publication (online) and in English in English publication (printed).

5.3. Abstract

• Abstract should be written at a level that can be understood without referring to the other parts of the article.

• The abstract should be organized as a brief presentation of the sections in the article, reflect the purpose of the article, be informative, and should be written in a way to emphasize new data and results on the subject.

• Short and simple sentences should be used in writing the abstract.

• In the abstract, there should not be any reference to other parts and illustrations of the article or to other articles.

• Information not mentioned in the main text should not be included in the abstract.

• The abstract should not exceed approximately 200 words and should be written as a single paragraph.

• Abstract should be written in Times New Roman, 10 pt., normal text with single line spacing.

• "ABSTRACT" should not be placed for the articles to be included in "Brief Notes" section.

• The English abstract should be given under the heading "ABSTRACT".

5.4. Keywords

In order to facilitate searches, five keywords that will indicate the general content of the article should be selected and specified in this section. Words used in the title should not be repeated.

5.5. Introduction

• In this section, the necessary information for preparatory and facilitative to understand the article such as the purpose of the study, its location, methods of study and previous reviews on the subject should be given.

• If an unusual way is followed in naming, classification and abbreviations within the text of the manuscript, its reason should be stated in this section.

• Each of the topics to be included in this section can create a separate paragraph or a subtitle can be given for each of them when necessary (e.g. method, material, terminology and etc.).

• This section can again be used when reminder information is needed to facilitate the understanding of the article (e.g. statistical information, formulas, experimental or application methods and etc.).

5.6. Main Body of Article

• Constitutes the main body of the article.

• In this section, the data, findings and opinions that are intended to be transferred to the reader on the subject are mentioned.

• The data used in other parts of the article such as "Abstract", "Discussions", "Results" originate from this part.

• Care should be taken not to deviate from the purpose stressed in the "Introduction" section of the article when dealing the topics. Information that does not contribute to the achievement of the purpose of the article or that is not used to reach the conclusion should not be included.

• All data used in this section and all opinions put forward should be proven by the findings obtained from the studies or based on a source by reference.

- The way and method to be followed in handling the topics vary according to the characteristics of the topics covered.

- Subject headings in necessary numbers with different stages should be used in this section.

5.7. Discussions

- The data and findings objectively conveyed in the "Main Text" section of the article should be discussed by the author in this section. Discussions should be separate from the "Results" section.

5.8. Results

- New data and findings obtained from the review that constitutes the subject of the article should be stated concisely and concretely in this section.

- Subjects that are not adequately addressed and / or covered in the main text should not be included in this section.

- The results can be given as items in order to emphasize the research results and make the expression understandable.

5.9. Acknowledgements

- In this section, important contributions in the realization of the study, which is the subject of the article, are indicated. An attitude that will distract this section from its main purpose should not be taken in the Acknowledgements.

Contribution should be stated as short and concise as possible to the persons and/or organizations that provided assistance (reading, writing, language assistance, etc.) during the research, and should not take an attitude that would distract this section from its main purpose.

5.10. References

- In this section, only the documents mentioned in the article should be included in complete.

- Abbreviations should be avoided in naming the publications and journals.

- The mentioned documents should be written in Times New Roman and 9 pt.

- The first line of the references should be written as justified to the left margin of the page, and the other lines should be written by giving a hanging indent value of 1.25.

- The references should be listed in alphabetical order, taking into account the surnames of the authors.

- If one author has more than one work in the same year, lowercase alphabet letters should be used right after the year of publication and the letters should be italic (e.g. Saklar, 2011*a, b*).

- If more than one document of the same author is cited, first his / her single-name publications in chronological order, then double-names according to the chronological order, and then multi-names according to chronological order should be given.

For example:

Corradini, C. 2007. The conodont genus Pseudooneotodus Drygant from the Silurian and Lower Devonian of Sardinia and the Carnic Alps (Italy). Bollettino-Societa Paleontologica Italiana 46 (2/3), 139-148.

Corradini, C., Serpagli E. 1999. A Silurian conodont biozonation from late Llandovery to end Pridoli in Sardinia (Italy), In Serpagli (Ed.), Studies on conodonts: Proceedings of the 7th European Conodont Symposium. Bollettino della Società Paleontologica Italiana 37 (2-3) (1998), 255-273.

Corradini, C., Corriga, M. G. 2010. Silurian and lowermost Devonian conodonts from the Passo Volaia area (Carnic Alps, Italy). Bollettino della Società Paleontologica Italiana 49 (3), 237-253.

Corradini, C., Corriga, M. G. A. 2012. Pridoli – Lochkovian conodont zonation in Sardinia and the Carnic Alps: implications for a global zonation scheme. Bulletin of Geosciences 87 (4), 635-650.

Corradini, C., Leone, F., Loi, A., Serpagli, E. 2001.Conodont Stratigraphy of A Highly Tectonised Silurian-Devonian Section in The San Basilio Area (Se Sardinia, Italy). Bollettino Della Societa Paleontologica Italiana 40 (3), 315-323, 1 Pl.

Corradini, C., Pondrelli, M., Serventi, P., Simonetto, L. 2003. The Silurian cephalopod limestone in the Monte Cocco area (Carnic Alps, Italy): conodont biostratigraphy. Revista Española de Micropaleontologia 35 (3), 285-294.

Corradini, C., Corriga, M. G., Männik, P., Schönlaub, H. P. 2015. Revised conodont stratigraphy of the Cellon section (Silurian, Carnic Alps). Lethaia 48 (1), 56-71.

- If documents of different authors with the same surname are mentioned, they should be written in alphabetical order, considering their first names.

- If documents of different author(s) with the same surname are mentioned in the same year, they should be cited as given below. Same publication rule should be applied for the single author.

For example:

"Usta, M., Yetiş, C., Nazik, A. 2018. Anamur (Mersin) dolayının stratigrafisi ve Kambriyen yaşlı kuvarsitler ile dolomitlerin endüstriyel hammadde potansiyeli. Çukurova Üniversitesi Fen ve Mühendislik Bilimleri Dergisi 35, 6, 11-22, Adana"

should be cited as (Usta, M. et. al., 2018)

"Usta, D., Ateş, Ş., Çoban, M., Deveci, Ö, Sağlam, F.M. 2014. Adıyaman-Sincik-Hilvan arasındaki bölgenin stratigrafisi ve kaya türü özellikleri. 67. Türkiye Jeoloji Kurultayı Bildiri Özleri, Ankara, 98-99"

should be cited as (Usta, D. et. al., 2018)

"Usta, M. 2018. Anamur (Mersin) dolayının stratigrafisi ve Kambriyen yaşlı kuvarsitler ile dolomitlerin endüstriyel hammadde potansiyeli. Çukurova Üniversitesi Fen ve Mühendislik Bilimleri Dergisi 35, 6, 11-22, Adana"

should be cited as (Usta, M., 2018)

"Usta, D. 2014. Adıyaman-Sincik-Hilvan arasındaki bölgenin stratigrafisi ve kaya türü özellikleri. 67. Türkiye Jeoloji Kurultayı Bildiri Özleri, Ankara, 98-99"

should be cited as (Usta, D., 2018)

- If the document is in a periodical publication (if it is an article), information about the document is given in the following order: Authors ' surname, first letters of the authors' first names. Year of publication. The name of the article. The name of the publication in which the article was published, volume number and / or issue number with the first letters in capital, the numbers of the first and last page of the document.

Punctuation marks like comma and etc. after journal names should not be used.

- In the examples below, the information about the mentioned documents is organized according to different document types, taking into account the punctuation marks.

For example:

Gürsoy, M. 2017. Munzur Dağları Alt Miyosen çökelleri mollusk topluluğu ve paleoekolojisi (Doğu Anadolu, Türkiye). Maden Tetkik ve Arama Dergisi 155, 75-99.

Pamir, H. N. 1953. Türkiye'de kurulacak bir Hidrojeoloji Enstitüsü hakkında rapor. Türkiye Jeoloji Bülteni 4 (1), 63-68.

Robertson, A. H. F. 2002. Overview of the genesis and emplacement of Mesozoic ophiolites in the Eastern Mediterranean Tethyan region. Lithos 65, 1-67.

- If the document is a book: authors' surnames, authors' first names. Year of publication. Title of the book with capital letters. The name of the publishing organization or the name of the publication in which the document was published, the volume and / or issue number, and the total number of pages of the book should be specified, respectively.

For example:

Einsele, G. 1992. Sedimentary Basins. Springer Verlag, 628.

Ketin, İ., Canıtez, N. 1956. Yapısal Jeoloji. İTÜ, 308.

Meriç, E. 1983. Foraminiferler. Maden Tetkik ve Arama Genel Müdürlüğü Eğitim Serisi, 26, 280.

- If the document is published in a book containing the articles of various authors, the usual order for the document included in a periodical publication is followed until the end of the document title. Then the editors' surnames and initials and the abbreviation of the editor word "Ed." is written in parentheses. Then, the title of the book in which the document is located is written with the first letters in capital letters. Name of publishing organization. The place of publication, the volume number of the publication in which the document was published, and the numbers of the first and last pages of the document should be written.

For example:

Anderson, L. 1967. Latest information from seismic observations. Gaskell, T. F. (Ed.). The Earth's Mantle. Academic Press. London, 335-420.

Göncüoğlu, M. C., Turhan, N., Şentürk, K., Özcan, A., Uysal, S., Yalınız, K. 2000. A geotraverse across northwestern Turkey. Bozkurt, E., Winchester, J. A., Piper, J. D. A. (Ed.). Tectonics and Magmatism in Turkey and the Surrounding Area. Geological Society of London. Special Publication, 173, 139-162.

• If it is desired to specify the name of a book in which the writings of various authors are collected as a document; following the surnames and names of the book's editors, in parentheses the "Ed." statement is written. Year of publication. Title of the book with capital letters. The name of the publishing organization or the name of the publication in which the document was published, the volume and / or issue number and the total number of pages of the book should be specified.

For example:

Gaskel, T. F. (Ed.). 1967. The Earth's Mantle. Academic Press, 520.

• If the document is "published abstract", information about the document is given in the following order: Authors' surnames, authors' first names. Year of publication. Name of the document (paper). The name, date and place of the meeting where the paper is published, and the first and last page numbers in the book containing the abstract should be written.

For example:

Öztunalı, Ö., Yeniyol, M. 1980. Yunak (Konya) yöresi kayaçlarının petrojenezi. Türkiye Jeoloji Kurumu 34. Bilim Teknik Kurultayı, Ankara, 36.

Yılmaz, Y. 2001. Some striking features of the Anatolian geology. 4. International Turkish Geology Symposium, 24-28 Eylül 2001, Adana, 13-14.

• If the mentioned document has not been published like report, lecture notes and etc., the word "unpublished" should be written at the end of the information about the document in parentheses after the information about the document is given in the usual order for the document in a periodical publication.

For example:

Akyol, E. 1978. Palinoloji ders notları. EÜ Fen Fakültesi Yerbilimleri Bölümü, 45, İzmir (unpublished).

Özdemir, C., Biçen, C. 1971. Erzincan ili, İliç ilçesi ve civarı demir etütleri raporu. Maden Tetkik Arama Genel Müdürlüğü, Rapor No: 4461, 21, Ankara (unpublished).

• For unpublished courses, seminars and similar notes, the course organizer after document name. The place of the meeting. Title of the book and relevant page numbers should be given.

For example:

Walker, G.R., Mutti, E. 1973. Turbidity facies and facies associations. Society for Sedimentary Geology Pacific Section Short Course. Annaheim. Turbitides and Deep Water Sedimentation, 119-157.

• If the document is a thesis; author's surname, initial of the author's first name. Year of publication. Name of the thesis. The type of the thesis, the university where it was given, the total number of pages, its province and the word "unpublished" are written in parentheses.

For example:

Akıllı, H. 2019. Polatlı-Haymana (Ankara) civarı sıcak sularının izotop jeokimyası ($\delta18O$, δD, 3H, $\delta13C$, $\delta34S$, 87Sr/86Sr) ve ana iz element bileşimleri ile incelenmesi. PhD Thesis, Ankara University, 255, Ankara (unpublished).

Argun Aktan, Ö. 2019. Marmara Denizi Batı Kıta Sahanlığı Yüzeysel Çökellerinde Jeojenik ve Antropojenik Ağır Metal Zenginleşmesine Yönelik Araştırmalar (Şarköy Kanyonu, KB Türkiye). MSc Thesis, Ankara University, 179, Ankara.

• Anonymous works should be arranged according to the publishing institution.

For example:

MTA. 1964. 1/500.000 ölçekli Türkiye Jeoloji Haritası, İstanbul Paftası. Maden Tetkik ve Arama Genel Müdürlüğü, Ankara.

• For the documents that are in print, no date is put after the name of the author, the name of the article and the source to be published should be specified and the word "in print" and / or "in review" should be written at the end (in parentheses).

For example:

Ishihara, S. The granitoid and mineralization. Economic Geology 75th Anniversary (in press).

• Information downloaded from the Internet should be given in the form of the name of the institution, its web address, and the date on which the web address was accessed. Turkish references should be given directly in Turkish and should be written in Turkish characters.

For example:

ERD (Earthquake Research Department of Turkey). http://www.afad.gov.tr. 3 March 2013.

• While citing the source, the original language should be adhered to, and the title of the article should not be translated.

6. Illustrations

• All of the drawings, photographs, plates and tables used in the article are referred to as "illustrating".

• Illustrations should be used when their use is unavoidable or when they make the subject easier to understand.

• In the selection and arrangement of the format and size of the illustrations, an attitude should be made to prevent loss of space as much as possible considering the page length and layout of the bulletin.

• The number of illustrations used should be proportional to the size of the text.

• All illustrations should be submitted in separate files regardless of the text.

• Abbreviations should not be used in illustration explanations in the text and should be numbered in the order of mention within the text.

• Photographs and plates must be submitted as a computer file in which all details can be seen for the examination of the article, with EPS, TIFF or JPEG extension and at least 300 dpi resolution.

6.1. Figures

• Drawings and photographs other than the plate to be included in the article are evaluated together as "Figure" and numbered in the order of mention in the text.

• The figures should be prepared in computer considering the dimensions of a single column width as 7.4 cm or double column width as 15.8 cm. The figure area with its caption should not exceed 15.8x21 cm.

• While preparing the figures, unnecessary details should not be included and care should be taken not to use more space than necessary for the transfer of information.

• In figure descriptions, a space should be left after the word "Figure" is written, and the number is given in the usual sequence number, followed by a hyphen (-) and a space again, and a description of the relevant figure should be written. If the figure legend exceeds the bottom lines, the following lines should to be written after the "Figure 1-" statement alignment. Figure descriptions should be created as follows, without exceeding the edges of the figure and justified on both sides.

For example:

Figure 1- The district of Sandıklı (Afyon); a) geological map of the southwest, b) the general vertical section of the study area (Seymen, 1981), c) Turkey's most important neotectonic structures (modified from Koçyiğit, 1994).

• Drawings should be drawn in computer properly, clean and with care.

• The use of thin lines that may disappear when minimized in figures should be avoided.

• Symbols or letters used in all drawings should not be less than 2 mm (7 pt.) in Times New Roman.

• All standardized symbols used in the drawings should preferably be explained in the drawing, if they are too long then they should be explained in the figure below.

• Bar scale should be used in all drawings and the north direction should be indicated on all maps.

• The name of the author, description of the figure, figure number should not be included in the drawing.

- Photographs should reflect the aims of the subject and should be in adequate numbers.
- Figures should be framed.

6.2. Plates

- Plates should be used in cases where multiple photographs are required to be printed together on a special paper.
- Plate dimensions must be equal to the size of the bulletin's usable area of the page.
- Figure numbers should be written under each of the figures on the plate and bar scale should be used.
- Original plates must be attached to the final copy to be submitted in the case of acceptance of the manuscript.
- Figures and plates should be numbered among themselves and independently. Figures should be numbered with Latin numerals and plates with Roman numerals (eg Figure 1, Plate I).
- There should be no explanation text on the figures inside the plate.

6.3. Tables

- All tables should be arranged in word format and should be prepared in Times New Roman.
- Tables should not exceed the size of 15x8 cm together with the table caption.
- Table explanations should be created without exceeding the edges of the figure and justified as in the example below.

For example:

Table 1- Hydrogeochemical analysis results of geothermal waters in the study area.

7. Nomenclature and Abbreviation

- Abbreviations must be in the accepted international or national form. Unusual nomenclature and abbreviations that are not standardized in the article should be avoided. In cases where it is deemed necessary to use such nomenclature and abbreviations, the way and method followed should be explained.
- There should not be a dot between the words initials used in standard abbreviations (such as MTA, DSİ).
- Abbreviations of geography aspects should be made in English (N, S, E, W, NE and etc.).

The word group to be abbreviated should be written clearly where it is mentioned first time and the abbreviation should be given in parentheses, then only the abbreviated form should be written throughout the article.

- Systems with international validity (m, inch, etc.) should be used as the unit of measure. Decimals should be separated with commas in Turkish articles and with a period in English articles.
- The names of figures, plates and tables in the article should not be abbreviated. For example, "As seen in the generalized stratigraphic section of the region (Figure 1) …….".

7.1. Chronostatigraphic and Geochronologic Nomenclature

- "International Chronostratigraphic Chart" (https://stratigraphy.org/chart), which is updated annually by the International Stratigraphic Committee, should be taken into consideration in chronostratigraphic and geochronological nomenclature.
- Position within a chronostratigraphic unit can be expressed in adjectives indicating the position, for example: lower, middle, upper and etc. When using these adjectives, it should be decided whether the lower, middle and upper distinction is formal / informal in the International Chronostratigraphic Chart.

For example:

lower Miocene, Upper Holocene and etc.

- When stating the time where a geochronological unit is, temporal adjectives such as; early, middle, late and etc. are used. When using these adjectives, the International Chronostratigraphic Chart should be taken into consideration to decide whether the adjectives begin with capital or lowercase letters.

For example:

early Miocene, Late Holocene etc.

7.2. Paleontological Nomenclature and Spelling of Fossil Names

- Original names of fossils should be used.

For example:

Nummulites with limestone

• Fossil genus and species names are written in italics, cf., aff. and gr. etc. expressions are written as normal (perpendicular). When writing fossil names for the first time, the surnames of the people who identify them and the year in which they were first defined should be written. In later uses, the surnames and the year in which they are defined may not be written. The surnames and dates of identifiers coming at the end of the fossil names are not references, they should not be included in the mentioned documents.

For example:

Alveolina aragonensis Hottinger, 1960 not a reference.

Alveolina cf. *aragonensis* Hottinger, 1960 not a reference.

Alveolina aff. *aragonensis* Hottinger, 1960 not a reference.

Alveolina gr. *aragonensis* Hottinger, 1960 not a reference.

• After the first use of the same genus in the text is written clearly, it can be abbreviated as in the example so that it will not be confused with another genus in later use.

For example:

Alveolina aragonensis, A. polathensis, A. ellipsoidalis etc.

• If the date is in parentheses after the person describing it after the name of the fossil in the text, this is a reference and should be included in the mentioned documents.

For example:

Alveolina aragonensis Hottinger (1960) is a reference.

• The following rules should be taken into account when writing the systematic paleontologic section.

a. First of all, genus, species and subspecies to be identified should be written in hierarchical order like the order, upper family, family type species and so on. Later, the species to be described should be written together with the surnames and date of the people who defined the subspecies name. If there is a photograph of the described fossil, the plate or figure with the photograph should be added under the fossil name. The names of the authors listed here are not references, so they are not included in the reference.

For example:

> Order: Foraminiferida Eichwald, 1830
>
> Superfamily: Alveolinacea Ehrenberg, 1839
>
> Family: Alveolinidae Ehrenberg, 1839
>
> Type Genus: *Borelis* de Montfort, 1808
>
> Type Species: *Borelis melenoides* de Montfort, 1808 = *Nautilus melo* Fichtel and Moll, 1798
>
> *Borelis vonderschmitti* (Schweighauser, 1951)
>
> (Plate II, Figure 3-5 or Figure 3A-H).

b. Similar or synonyms (synonym) list should be left-aligned in chronological order. The page and figure number of the synonymous fossil in the relevant study should be included in the synonymous list. Authors in the synonymous list are references and must be included in the references.

For example:

1951 *Neoalveolina vonderschmitti* **Schweighauser**, page 468, Figures 1-4.

1974 *Borelis vonderschmitti* (Schweighauser), **Hottinger**, page 67, plate 98, Figures 1-7.

c. After the synonymous list is given, the definition, explanations (similarities and differences), dimensions, material, stratigraphic distribution (according to the characteristics of the fossil) should be written.

d. If the fossil is defined for the first time (new species) in the systematic paleontology section, the origin of the name, holotype, type locality, material, description, explanation (similarity and differences), age and geographical distribution, dimensions (according to the features that define the fossil) should be written. Photographs of the fossil identified for the first time by the authors must necessarily be placed in plates or figures.

e. Bar scale indicating the size of fossils must be used definitely in plates / figures.

8. References

• In the references to be made in the Main Text, only the surnames of the authors and the publication year of the mentioned article should be specified. Referencing should be arranged according to one of the following examples:

• Referring to a publication with a single author (in chronological order):

-Altınlı (1972, 1976) defined the Bilecik sandstone in detail.

It is known that the fold axes of the Devonian and Carboniferous units around İstanbul are N-S trending (Ketin, 1953, 1956; Altınlı, 1999).

• Referring to a publication with two authors:

- The upper parts of the unit include Ilerdian fossils (Sirel and Gündüz, 1976; Keskin and Turhan, 1987, 1989).

• Referring to a publication with more than two authors:

- According to Caner et al. (1975), the Alıcı formation reflects the conditions of fluvial environment.

- Unit disappears by wedging towards E (Tokay et al., 1984).

• Referring to a reference in another publication:

It is known that Lebling mentioned about the existence of Liassic around Çakraz (Lebling, 1932; Charles, 1933).

• When referring to the works of the authors with the same surname in the same year, referring the authors' first names by writing their initials:

- Many studies have been done in the field of structural geology in the study area (Gutnic et al., 1979; Yılmaz A., 1983; Yılmaz, İ., 1983; Poisson et al., 1984 etc.).

9. Prints Sent to Authors

Two copies of the relevant issue published in the Bulletin of the Mineral Research and Exploration are sent to the authors.

10. Terms of Publication and Copyrights

• Some or all of the articles to be published in the Bulletin of the Mineral Research and Exploration should not have been published before.

• Authors who submit a publication to the Bulletin of the Mineral Research and Exploration are deemed to have accepted the bulletin's publication rules in advance.

• The copyright of the manuscripts accepted for publication and converted into publications belongs to the General Directorate of Mineral Research and Exploration (MTA).

The authors of the study sign the relevant forms within the scope of the provisions specified in the Regulation of the Editorial Board regarding the transfer of copyright and submit them to the Editorial Board. After the publication of the article, MTA may pay royalty fees to the authors of the article for their declarations within the scope of the "Regulation on the Editorial and Processing Fees to be paid by the Public Organizations and Institutions".

NOTE: Information and forms about Bulletin of the Mineral Research and Exploration can be accessed from the website: http://dergi.mta.gov.tr/index.php.